



HAL
open science

Towards a unified description of quantum liquid and cluster states in atomic nuclei within the relativistic energy density functional framework

Petar Marević

► **To cite this version:**

Petar Marević. Towards a unified description of quantum liquid and cluster states in atomic nuclei within the relativistic energy density functional framework. Nuclear Theory [nucl-th]. Université Paris Saclay (COMUE), 2018. English. NNT : 2018SACLS358 . tel-01915952

HAL Id: tel-01915952

<https://theses.hal.science/tel-01915952>

Submitted on 8 Nov 2018

HAL is a multi-disciplinary open access archive for the deposit and dissemination of scientific research documents, whether they are published or not. The documents may come from teaching and research institutions in France or abroad, or from public or private research centers.

L'archive ouverte pluridisciplinaire **HAL**, est destinée au dépôt et à la diffusion de documents scientifiques de niveau recherche, publiés ou non, émanant des établissements d'enseignement et de recherche français ou étrangers, des laboratoires publics ou privés.

Towards a unified description of quantum liquid and cluster states in atomic nuclei within the relativistic energy density functional framework

Thèse de doctorat de l'Université Paris-Saclay
préparée à l'Université Paris-Sud

Ecole doctorale n°576 Particules, Hadrons, Énergie, Noyau, Instrumentation, Imagerie,
Cosmos et Simulation (PHENIICS)
Spécialité de doctorat : Structure et réactions nucléaires

Thèse présentée et soutenue à Orsay, le 2 octobre 2018, par

PETAR MAREVIĆ

Composition du Jury :

| | |
|--|-----------------------|
| M. Peter Schuck Directeur de Recherche Émérite, <i>IPN Orsay, France</i> | Président |
| M. Luis Robledo Professeur, <i>Autonomous University of Madrid, Spain</i> | Rapporteur |
| M. Matko Milin Professeur, <i>University of Zagreb, Croatia</i> | Rapporteur |
| M. Nicolas Schunck Chargé de Recherche, <i>LLNL Livermore, the United States</i> | Examineur |
| M. Dario Vretenar Professeur, <i>University of Zagreb, Croatia</i> | Examineur |
| M. Elias Khan Professeur, <i>IPN Orsay, Université Paris-Saclay, France</i> | Directeur de thèse |
| M. Jean-Paul Ebran Chargé de Recherche, <i>CEA, DAM, DIF, France</i> | Co-directeur de thèse |

Acknowledgements

Messieurs les officiers, je vous remercie.

Toréador Escamillo, Act 2, *Carmen* by G. Bizet

Le doctorat dure trois ans, un peu comme l'amour¹. The past three years have arguably been, both professionally and personally, the most eventful and intense period of my life. While I hope that the manuscript before you will remain as a lasting evidence of the work done during this period, some of the interesting stories and events - that seem to be of an almost equal importance in forming of a young scientist and person - will likely remain untold. In paragraphs that follow, however, I would like to express my gratitude to people that partook in some of them and that have thereby, in one way or another, influenced my life and work during this exciting journey.

Time and place: Oct31 2015, CDG Airport, Paris. *My level of French:* Bonjour, merci. Luckily, my thesis advisor Jean-Paul was there, together with his wife and children, to welcome me on my arrival to France. Even though (as he will reveal publicly years later, during my thesis defense) I did not sufficiently appreciate the food that he himself cooked for me on the day, I will always stay grateful for his presence and assistance during those first weeks in a completely new environment. Having such a talented physicist by my side during this thesis was a real privilege and it provided me with a great amount of confidence in my everyday work. Moreover, I feel impelled to say that Jean-Paul's (predominantly) kind personality, uncommon sense of humor, and cheerful spirit made me - as time passed by - start considering him as less of a boss and more of an older bro (though, to be fair, the one who is living abroad and can be encountered only on rare family gatherings). Furthermore, thanks are due to my other advisor, Elias (Emranuzza-man) Khan, a non-owner of the *Researchgate* profile, Laurate of the CNRS Silver Medal 2016, and a skillful basketball player (verified by yours truly on an usually hot and tiring day in Perpignan, summer 2016). Even though Croatia virtually never managed to beat France in any of the sports competitions that we permanently bantered about², it was a real pleasure to work under Elias, both for his relaxed but effective approach to work and for always having *my guy* in the university administration who can help me resolve any bureaucratic struggle. The extent of my gratitude to Tamara Nikšić, my masters thesis advisor and PhD *advisor in charge*, cannot be overstated. Tamara's competence, calmness, and dedication to work remain a source of perpetual inspiration for me, while

¹For more details on the latter subject an interested reader is referred to F. Beigbeder, *L'amour dure trois ans*, Éditions Grasset & Fasquelle (1997).

²It was not a penalty.

countless e-mail and Skype exchanges that we had over the past years testify to the major role she played in making of this thesis and in making of this physicist.

I would like to extend my sincere gratitude to all the members of the committee. Firstly, many thanks to Peter Schuck, an experienced master of the field, for presiding over the committee and for continuously reminding me to keep an eye on the Hoyle state. Special thanks go to two referees, Luis Robledo and Matko Milin, who authorized for the thesis defense to happen in the first place. Luis' extraordinary contributions to the field of beyond mean-field models remain one of my favorite scientific reads and they indeed represents an important pillar of the present thesis. While Matko's experimental work on clusters remains somewhat less transparent to my theoretical mind, his unusually kind personality and deep physics knowledge - dating in my personal calendar as far back as *General Physics* classes in 2011 - had a very strong influence on my scientific career. Finally, thanks are due to two examiners. I am grateful to Nicolas Schunck for traveling from the US to take part in my committee and, even more, for enabling my future travel to the US to take part in our common project. Thanks to Dario Vretenar, for taking interest and care in my professional development and for using his immense knowledge and experience to better the research that I try to perform. Having my work verified by such an exceptional group of physicists was both honoring and humbling experience.

During the past three years I had a privilege of working at two of the best nuclear physics institutions in France. I would like to thank the people of my laboratory in Bruyères-le-Châtel for taking a Croatian guy among their ranks. Je suis navré que nous n'ayons pas pu passer plus de temps ensemble et j'espère que le futur nous en offrira l'opportunité. On the other hand, I am immensely grateful to the entire scientific, administrative, and informatics staff of IPN Orsay for welcoming me in their nest and allowing me to make our lab my second home (which was, during the last months of writing this manuscript, admittedly true also in a literal sense). Dear Bira, David R., Denis, Gai, Guillaume, Jean-Philippe, and Marcella, it was a pleasure to share theory corridor and CESFO table with you, and I hope to see you all around in the near future. Special thanks go to the funniest member of the group, Paolo, for numerous cheerful and silly conversations we had, as well as to the head of the group Michael, for making me a full-fledged group member and helping me with hardware issues prior to my long postdoc interview. Thanks to our group secretary Valérie, pour son aide toujours aimable et pour m'avoir aidé à organiser mon pot de thèse.

Upon my arrival to IPN, I had to take the least attractive desk in the office 101a. I would like to thank Noël for letting me inherit his desk after his departure, as well as for introducing me to and sharing many drinks at my favorite Parisian bar. I raise a cup of *Café Raoul* to Raphaël, my travel companion to York and Galveston and an extraordinarily bright young mind: it was a real pleasure to share an office, advisors, and an official thesis title with him. I wish the best of luck to younger PhD students that I am leaving behind at the battlefield: Antoine (look down!), David D., Haşim, and Melih. Significant amount of luck will also be needed by Jean-Paul's remaining students - a new apprentice Kilian, whose driving and translation services were highly appreciated, and Julien, whom I've shared rooms with on our *Gogny* adventure in Madrid. I am grateful to IPN colleagues and friends that I have spent numerous entertaining out-of-the-office hours with: the *tressette* master Alice, data scientist, drummer and Nature Physics author Aurélie, my first PRL co-author and the most stylish guy of IPN Clément, my tattooed Slav-sis Jana, our salsa instructor Liss, as well as the vigilante hero Olivier, the *Pheniicsman*. The past three years were cheerful largely due to the presence of my dear friend and *amourette* Anastasia, whom I shared a million of laughter-filled adventures with. Naturally, she was

particularly thrilled that I also shared my amazing friend Marc with her, and all three of us are very excited about the upcoming Greek wedding in the summer of 2019. Special mention goes to my meanest friend Florent, who is - let's face it - much better volleyball than a beer pong player. I am grateful for his not-so-kind guidance through the hell of French language and bureaucracy, many late afternoon sandwich expeditions, and more than anything for throwing the best birthday parties I have ever seen.

Spending mid-twenties in Paris is arguably not the worst destiny that can fall upon a young human being, and I was additionally blessed with the opportunity to travel rather regularly over the past three years. Naming all of the people who made my time in Paris and abroad pleasant would surely be an impossible task. Nevertheless, I would like to give special thanks to Ariel, Alessandra, Benjamin, Dinko, Giulia, Luka, Niki, Pierre, Robert, and Xixi, for entertaining and precious time we spent together. A huge shout-out and 100% thanks to my Croatian gang - Jure, Marko, Matija, Pave, and Saša - for our exciting yearly eurotrips and for their warm welcomes every time I would get back home to Zagreb. Special mention goes to the *Losos* department of the gang, who visited Paris for my defense and honored me with a captain armband to lead them in our Parisian adventures. My Croatian roommate (Cimer) of three years and, to use his mother's words, *almost a brother* Branimir stayed close to me despite the Atlantic that is currently separating us. 6161 thanks are due to him and his wife Lauren for traveling from DC to Paris to witness my defense. Somewhere along the way I was lucky enough to stumble upon my dude and brave warrior Bařak, whose gentle and (overly) pleasant company, particularly when there was a *sh*tty pizza* to share, made my mind calm and my time unusually joyful.

There are people that may seem peripheral to the uninformed observer, but deep inside, at the very absolute minimum of your potential energy surface, you just know that you should acknowledge them. To start with, I want to thank all of my French language teachers, for largely enhancing my survival odds in this wild world. Some of my happiest hours were spent in *Hurling Pub* of the 5th arrondissement, at the bar or in front of the dartboard, and it is largely due to the two of the coolest bartenders. Furthermore, I occasionally enjoyed very tasteful pastries at the bakery of *Orsay* RERB station, prepared by an anonymous baker who always appeared to me as someone who once agreed to jump in for a friend-baker that had an emergency but then, by a weird twist of fate, had to stay ever since. Special recognition goes to the anonymous referee of my first first-author paper, whose insightful remark *Results are very interesting (...). However, the authors are overoptimistic and the overall tone should be lowered* probably strikes a general chord more loudly than I would be willing to admit.

Finally, I want to thank my entire family, for tolerating and supporting a family black sheep who is interested in studying some weird stuff that no sane person cares about. To my mom and dad, for deciding it was a good idea to have and raise one mischievous boy who grew up to become a doctor. To my sister and my brother in law, for making their home mine whenever I needed so. And to my sweet nephews Boris and Dino, for periodically reminding about the things in life that really matter.

In the end, I thank you, my dear reader, for taking your precious time to read this manuscript. I wish you a very pleasant journey through the realm of breaking and restoring symmetries, and may your personal symmetries never need to be restored.

Orsay, October 26, 2018.

*"The ponies run, the girls are young
The odds are there to beat.
You win a while and then it's done
Your little winning streak.
And summoned now to deal
With your invincible defeat.
You live your life as if it's real
A thousand kisses deep."*

L. Cohen, "A Thousand Kisses Deep"

Contents

| | |
|---|-----------|
| An Overture | 1 |
| I Theoretical Framework | 9 |
| 1 The Nuclear Energy Density Functional Method | 11 |
| 1.1 Relativistic Mean-Field Theory | 13 |
| 1.1.1 Basic Building Blocks of the RMF Theory | 13 |
| 1.1.2 The DD-PC1 Effective Interaction | 15 |
| 1.1.3 The Separable Pairing Force | 20 |
| 1.2 Relativistic Hartree-Bogoliubov Model | 22 |
| 1.2.1 The Independent Quasiparticle Picture | 22 |
| 1.2.2 Relativistic Hartree-Bogoliubov Equation | 24 |
| 1.2.3 Constrained RHB Calculation | 27 |
| 1.3 Nuclear Clustering within the RMF Framework | 29 |
| 2 Restoration of Symmetries and Configuration Mixing | 37 |
| 2.1 Restoration of Broken Symmetries | 39 |
| 2.1.1 Breaking and Restoring Symmetries | 39 |
| 2.1.2 Rotational Symmetry | 42 |
| 2.1.3 Particle Number Symmetry | 43 |
| 2.1.4 Parity Symmetry | 45 |
| 2.1.5 Translational Symmetry | 46 |
| 2.2 Configuration Mixing Scheme | 47 |
| 2.2.1 Basic Principles of the Hill-Wheeler-Griffin's Method | 47 |
| 2.2.2 Mixing of Symmetry-Restored Configurations | 48 |
| 2.2.3 Structural Properties of Collective States | 51 |
| 2.2.4 Evaluation of Norm Overlap and Hamiltonian Kernels | 52 |
| II Microscopic Description of Clustering in Light Nuclei | 57 |
| 3 A Computational Interlude | 59 |
| 3.1 Convergence of Mean-Field Calculation | 60 |
| 3.2 Convergence of Symmetry-Restoring Calculation | 62 |
| 3.2.1 Convergence of Projected Energies | 62 |

| | | |
|----------|---|------------|
| 3.2.2 | Some Convergence Issues | 66 |
| 3.3 | Configuration Mixing and Linear Dependencies | 68 |
| 3.4 | Concluding Remarks | 69 |
| 4 | Quadrupole-Octupole Collectivity and Clusters in Neon Isotopes | 71 |
| 4.1 | Ground-State Properties of Neon Isotopes | 73 |
| 4.1.1 | The Mean-Field Analysis | 73 |
| 4.1.2 | The Effect of Collective Correlations | 75 |
| 4.2 | Excited-State Properties of Neon Isotopes | 80 |
| 4.2.1 | Systematics of the Low-Lying States | 80 |
| 4.2.2 | Structure of the Neutron-Rich Isotopes | 84 |
| 4.3 | Structure of the Self-Conjugate ^{20}Ne Isotope | 87 |
| 4.3.1 | Spectroscopy of Collective States | 87 |
| 4.3.2 | Cluster Structures in Collective States | 90 |
| 4.4 | Concluding Remarks | 92 |
| 5 | Cluster Structures in ^{12}C Isotope | 95 |
| 5.1 | Structure of the ^{12}C Isotope | 97 |
| 5.1.1 | Potential Energy Maps | 97 |
| 5.1.2 | Spectroscopy of Collective States | 99 |
| 5.1.3 | Structure of Collective States in the Intrinsic Frame | 101 |
| 5.1.4 | Electron Scattering Form Factors | 103 |
| 5.2 | Concluding Remarks | 106 |
| | Conclusion and Outlook | 109 |
| A | The Single-Particle Bases | 113 |
| A.1 | A Brief Note on Second Quantization | 113 |
| A.2 | Coordinate Representation of the Harmonic Oscillator Basis | 115 |
| A.3 | The Simplex-X Basis | 118 |
| A.4 | Bogoliubov States in the Simplex-X Basis | 120 |
| A.5 | Rotation Operator in the Simplex-X Basis | 124 |
| B | Calculation of Electric Observables | 129 |
| B.1 | Spectroscopic Moments and Transition Strengths | 129 |
| B.2 | Electron-Nucleus Scattering Form Factors | 132 |
| C | Résumé en Français | 139 |
| C.1 | Introduction | 139 |
| C.2 | La Fonctionnelle de la Densité pour l'Énergie | 140 |
| C.3 | Structures en Agrégats dans les Isotopes de Néon | 141 |
| C.4 | Structures en Agrégats dans le ^{12}C | 143 |
| C.5 | Conclusion | 144 |

| | |
|-----------------|-----|
| Bibliography | 147 |
| Abbreviations | 163 |
| List of Figures | 165 |
| List of Tables | 167 |

An Overture

After sleeping through a hundred million centuries we have finally opened our eyes on a sumptuous planet, sparkling with colour, bountiful with life. Within decades we must close our eyes again. Isn't it a noble, an enlightened way of spending our brief time in the sun, to work at understanding the universe and how we have come to wake up in it? This is how I answer when I am asked – as I am surprisingly often – why I bother to get up in the mornings. To put it the other way round, isn't it sad to go to your grave without ever wondering why you were born? Who, with such a thought, would not spring from bed, eager to resume discovering the world and rejoicing to be a part of it?

Richard Dawkins, "Unweaving the Rainbow: Science, Delusion and the Appetite for Wonder"

Atomic nucleus is a quantum many-body system comprised of the lightest baryons, protons and neutrons, that are bound together on a femtometer scale by a residual strong interaction. Due to the fact that the underlying gauge theory for quarks and gluons, quantum chromodynamics, is highly non-perturbative in the low-energy regime, the exact analytical form of the nuclear interaction still remains elusive. Treatment of the nuclear many-body problem is further complicated by the fact that a number of nucleons in typical nucleus is both too large to be tackled with the exact methods and too small to be solved by employing statistical models. These difficulties, among others, propelled development of different theoretical nuclear models over the past decades, the most successful of which include various implementations of the ab initio methods [NQH⁺16], the configuration interaction method [CMPN⁺05], and the nuclear energy density functional [BHR03, NVR11, RRR18]. All of these models assume the unenviable task of ultimately having to describe a vast richness of nuclear phenomena, ranging from the structure and reactions in finite nuclei to the complex processes in neutron stars.

Historically, a wide success of the semi-empirical liquid-drop model [Wei35] showed that, to a perhaps surprisingly good approximation, atomic nucleus can in fact be described as a drop of incompressible and dense liquid whose properties are determined by a fine balance between macroscopically-derived cohesive and repulsive forces. Further introduction of the nuclear shell model [May48, HJS49] provided a more microscopically-founded picture of atomic nucleus, accounting simultaneously for the experimentally observed stability of certain configurations by introducing a concept of shell-like structure. On the other hand, as early as 1938, Hafstad and Teller proposed the description of structure of light nuclei in terms of bound states of clusterized α -particles [HT38],

which lead to a development of microscopic models based on the effective α - α interaction [Mar41, AB66]. In stark contrast to the homogeneous quantum-liquid picture, spatial localization of α -particles gives rise to a molecule-like picture of atomic nucleus, with any excess neutrons playing a role of covalent bonding between clusterized structures. Today, formation of cluster states in nucleonic matter, stellar matter, and finite nuclei represents a very active topic of experimental and theoretical research in nuclear physics and astrophysics [Bec10, Bec12, Bec14, HIK12, FHKE+18, THSR17, EKNV17]. Particularly favorable conditions for formation of cluster structures are found in light self-conjugate nuclei, where exotic configurations such as linear chains and compact triangular arrangements are thought to be formed [FHKE+18]. Hoyle state, the famous second 0^+ state in ^{12}C isotope which plays a crucial role in stellar nucleosynthesis and - consequently - appearance of life on Earth, is predicted to display precisely a three- α structure [THSR01, F+05]. Another manifestation of clustering in atomic nuclei is cluster radioactivity, first discovered in early 80s by Rose and Jones [RJ84]. The range of experimentally observed radiated clusters varies between ^{14}C and ^{32}S , while the heavy mass residue is always a nucleus in the neighborhood of a doubly-magic ^{208}Pb isotope [WR11]. Recently, a new form of clustering in heavy systems was discovered in terms of $\alpha+^{208}\text{Pb}$ states in ^{212}Po isotope that are decaying to the yrast band via enhanced dipole transitions [APP+10]. All of these experimental advances necessitate a thorough theoretical understanding of the nuclear clustering phenomenon.

Among theoretical models that aim to describe nuclear clustering, the antisymmetrized molecular dynamics (AMD) [KEH01, KEHO95, KEKO12] and the fermionic molecular dynamics (FMD) [Fel90, FBS95, NF04] certainly belong to the most successful ones. Starting from the single-nucleon Gaussian-like wave functions, these models have been able to describe various kinds of cluster structures, as well as the shell-model-like features of nuclear systems [FHKE+18]. Numerous other theoretical models have been employed in a description of clustering phenomena, including the Tohsaki-Horiuchi-Schuck-Röpke (THSR) wave function and container model [THSR01], the no-core shell model [NVB00], the continuum quantum Monte-Carlo method [CGP+15], the nuclear lattice effective field theory [EHM09], as well as the self-consistent mean-field theories [ASPG05, MKS+06]. Recently, the Bruyères-Orsay-Zagreb collaboration has carried out studies within the relativistic energy density functional (EDF) framework that unveiled some interesting results on the origin of nuclear clustering, linking the appearance of clusters to the depth of the underlying single-nucleon potential [EKNV12, EKNV13, EKNV14a, EKNV14b].

The framework of nuclear EDFs currently provides the most complete and accurate description of ground-state and excited-state properties of atomic nuclei over the entire nuclide chart [BHR03, NVR11, Egi16, RRR18]. In practical implementations, nuclear EDF is typically realized on two distinct levels. The basic implementation, which is usually referred to as either the self-consistent mean-field (SCMF) method or the single-reference energy density functional (SR-EDF), consists of constructing a functional of one-body nucleon density matrices that correspond to a single product state of single-particle or single-quasiparticle states. Modern functionals are typically determined by about ten to twelve phenomenological parameters that are adjusted to a nuclear matter equation of state and to bulk properties of finite nuclei. The obtained functional can then be employed in studies of ground-state properties of atomic nuclei, such as binding energies,

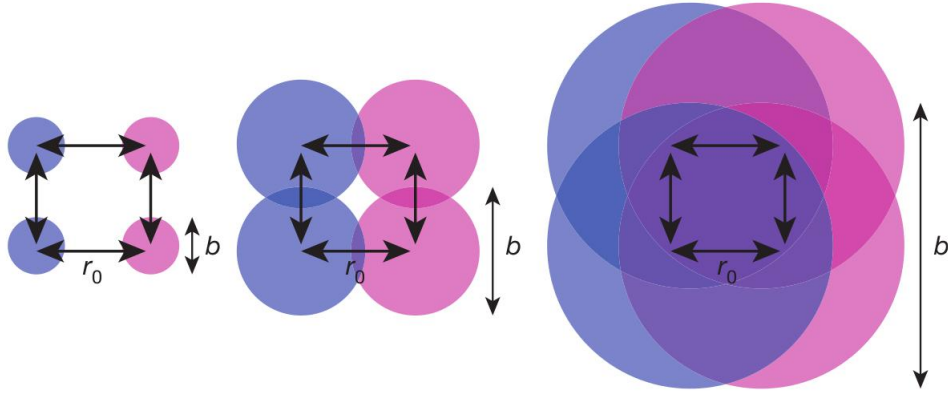


FIGURE 1: Schematic representation of clustering in atomic nuclei. Localization parameter α corresponds to a ratio between the spatial dispersion of nucleon wave function b and the average internucleon distance r_0 . Large and small values of α correspond to the quantum-liquid and solid phases of atomic nucleus, respectively. For values $\alpha \approx 1$ a hybrid cluster phase between quantum liquid and solid phases is formed. Figure taken from Ref. [EKNV12].

charge radii, and equilibrium shapes. However, in order to obtain an access to nuclear spectroscopy, it is necessary to extend the basic mean-field picture by taking into account collective correlations that arise from symmetry restoration and configuration mixing. The second level of implementation, which is usually referred to as either the beyond mean-field (BMF) method or the multi-reference energy density functional (MR-EDF), provides a description of excited nuclear states, including the electromagnetic transitions between them. In practice, it consists of recovering symmetries of intrinsic configurations that have been broken on a mean-field level, and further mixing the symmetry-restored states in order to build a collective state of atomic nucleus with good quantum numbers. Both non-relativistic and relativistic realizations of the framework have so far been successfully applied in various structure and reactions studies, from relatively light systems to superheavy nuclei, and from the valley of β -stability to the particle drip-lines (see Refs. [BHR03], [NVR11], [Egi16] and references therein). Some of the advantages of using manifestly covariant functionals involve the natural inclusion of nucleon spin degree of freedom and the resulting spin-orbit potential, the unique parameterization of nucleon currents, as well as the natural explanation of empirical pseudospin symmetry in terms of relativistic mean-fields [Men16]. In addition, J.-P. Ebran and collaborators have recently shown that, when compared to non-relativistic functionals which yield similar values of ground-state observables, it is the relativistic formulation of a framework that predicts the occurrence of significantly more localized intrinsic densities, thus favoring formation of clusters [EKNV12].

On a more fundamental level, the appearance of clusters can be considered as a transitional phenomenon between quantum liquid and solid phases in atomic nuclei. Situation is rather similar to the one encountered in mesoscopic systems such as quantum dots [FW05] and bosons in a rotating trap [YL07], or to the superfluid-insulator phase transitions in gases of ultracold atoms held in three-dimensional optical lattice potentials [GME⁺02].

The problem of quantum-liquid-to-crystal transitions was already addressed by Mottelson, who introduced the quantality parameter to describe a phase of infinite and homogeneous quantum systems [Boe48]. In order to take into account the finite-size effects in atomic nuclei, the localization parameter α was recently introduced [EKNV12]. This parameter corresponds to a ratio between the spatial dispersion of nucleon wave function b and the average internucleon distance r_0 , as schematically depicted in Figure 1. For large values of α nucleons are delocalized and nucleus behaves as a quantum liquid. At the opposite end, when the average internucleon distance significantly exceeds the nucleon spatial dispersion, nucleons localize on the nodes of a crystal-like structure. The intermediate values of α are marked by a hybrid phase of cluster states which are, in a first approximation, expected to appear for $\alpha \approx 1$ values. Comprehensive study of α values in light self-conjugate nuclei has shown that the relativistic functionals systematically yield smaller α values as compared to their non-relativistic counterparts, thus favoring formation of clusters [EKNV13]. In fact, even though non-relativistic and relativistic functionals predict very similar values of ground-state binding energies, deformations and charge radii, the relativistic framework was demonstrated to predict much more localized intrinsic densities [EKNV12]. This phenomenon was successfully linked to the pronouncedly larger depth of the underlying single-nucleon potential, which in the relativistic case arises naturally as a sum of the large attractive scalar and repulsive vector Lorentz fields [EKNV12]. Subsequent studies have examined the role of saturation, deformation and degeneracy of single-nucleon levels in formation of clusters [EKNV14a, EKNV14b], and interesting cluster structures have been predicted in excited configurations of light self-conjugate nuclei [EKNV14b]. However, in order to carry out a more quantitative analysis of the excited states, it is necessary to extend the static mean-field picture by including configuration mixing of symmetry-restored configurations.

In this thesis, we build upon the work of Refs. [EKNV12, EKNV13, EKNV14a, EKNV14b, EKNV17, EKL18] by developing a symmetry-restoring collective model based on the relativistic EDF framework. Starting point of our calculation is the relativistic Hartree-Bogoliubov (RHB) model [VALR05, MTZ⁺06], which provides a unified description of particle-hole and particle-particle correlations on a mean-field level. In the particle-hole channel, we will be using the density-dependent point-coupling DD-PC1 functional [NVR08] whose parameters have been fitted to the experimental binding energies of a set of 64 deformed nuclei in the mass regions $A \approx 150 - 180$ and $A \approx 230 - 250$. The DD-PC1 functional has been further tested in calculations of ground-state properties of medium-heavy and heavy nuclei, including binding energies, charge radii, deformation parameters, neutron skin thickness, and excitation energies of giant multipole resonances. In the particle-particle channel, we will be using the non-relativistic pairing force that is separable in a momentum space [Dug04, TMR09a]. By assuming a simple Gaussian ansatz, two parameters of the force were adjusted to reproduce density dependence of the gap at the Fermi surface in nuclear matter, as calculated with the Gogny D1S parameterization [BGG91]. The separable pairing force reproduces pairing properties in spherical and deformed nuclei calculated with the original Gogny force, while significantly reducing computational cost. The RHB equations are solved numerically by expanding nuclear spinors in the basis of an axially symmetric harmonic oscillator. Both axial and time-reversal symmetry of the intrinsic states are imposed, while nucleus is allowed to deform

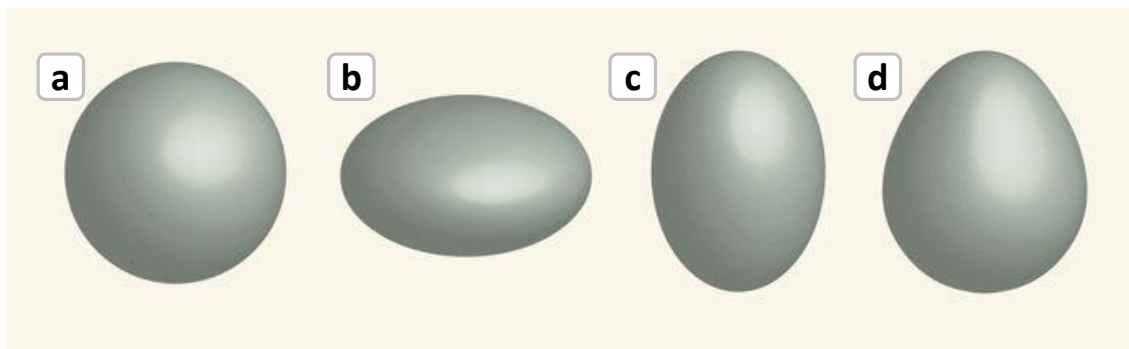


FIGURE 2: Different nuclear shapes that are taken into account in this study. State which preserves all spatial symmetries corresponds to the spherical shape (a). By allowing rotational symmetry to be broken, we obtain oblate (pancake-like) shape (b) or prolate (cigar-like) shape (c). Additionally, breaking of parity symmetry leads to the octupole-deformed (pear-like) shape (d). Figure adopted from Ref. [LB13].

into prolate (cigar-like) and oblate (pancake-like) shape, as well as to the octupole-deformed parity-breaking (pear-like) shape. Various nuclear shapes that are taken into account in this study are shown in Figure 2. This kind of analysis provides an access to nuclear configurations in the entire plane spanned by the axially-symmetric quadrupole and octupole deformations. In the next step, we will be recovering the most relevant symmetries that are broken on a mean-field level. In particular, the rotational symmetry, the particle number symmetry, and the parity symmetry are all simultaneously restored. Additionally, a simple center-of-mass correction that accounts for the violation of translational symmetry is included in the model [BHR03]. The symmetry-restored states are subsequently used as a basis for the configuration mixing scheme, rooted in the generator coordinate method (GCM) by Hill, Wheeler, and Griffin [HW53, GW57]. Solving the corresponding Hill-Wheeler-Griffin equation yields the excitation spectra and collective wave functions that can be used to calculate various observables, such as spectroscopic quadrupole moments and electromagnetic multipole transition strengths. These quantities can then serve as a testing ground for the performance of our model in comparison with the experiment, as well as with the predictions of other theoretical models. Furthermore, we have implemented into our model the beyond-mean-field techniques for studies of elastic and inelastic electron scattering off nuclei, that have recently been developed within the Skyrme-based EDF framework by J. M. Yao and collaborators [YBH15]. By using collective wave functions of the symmetry-restored states, we are therefore able to calculate laboratory densities and transition densities between the low-lying states, as well as both the elastic and inelastic scattering form factors.

From a computational point of view, this study has commenced with the axially symmetric version of the DIRHB package [NPVR14] which computes ground-state properties of even-even nuclei using the framework of relativistic self-consistent mean-field models [Rin96, RGL97]. During the course of this thesis, the existing code was first extended by including the axially symmetric octupole degree of freedom, which enabled us to perform self-consistent calculations in the entire axially symmetric quadrupole-octupole plane. Furthermore, restoration of rotational, parity, and particle number symmetry were all

added, as well as mixing of these configurations within the GCM framework. Since the obtained code was significantly time-consuming, it was parallelized with the OpenMP techniques in order to make it computationally feasible. Finally, a recently developed method for studies of electron scattering off nuclei was implemented in the model. This provided us with the state-of-the-art tool for nuclear structure studies that can, together with the eventual extensions, be applied in analyses of various phenomena over the entire nuclide chart, particularly in the heavy-mass region where the framework of EDFs still remains unrivalled among theoretical nuclear models.

In this thesis, particularly, the developed model will be applied in a study of clustering phenomena in light atomic nuclei. As the first application of the model, we chose to focus our attention on a structure of neon and carbon isotopes. Generally speaking, light systems are arguably the most demanding test for nuclear EDF models, not least because few-body systems are marked by a gradual breaking of the mean-field picture and by increasing necessity of the exact restoration of translational symmetry. On the other hand, one of the main advantages of using the EDF framework in studies of clusters is its feature that no localized structures are *a priori* assumed within the model. In fact, the framework incorporates both the quantum-liquid and cluster aspects of nuclear systems on the same footing, and clusterization may eventually appear only as a consequence of the self-consistent procedure on a mean-field level and/or the subsequent configuration mixing. In addition, parameters of the effective interaction were fitted to data on very heavy nuclei, and therefore the interaction itself does not bear any information whatsoever about the light systems that we aim to tackle. Of course, globality of the approach does not come without a price, and the employed interaction may not be able to describe all particularities determined by shell evolution in specific mass regions. Nevertheless, in spite of the mentioned drawbacks, it is the underlying credo of this manuscript that the employment of such a global framework, even at (or, in some sense, especially at) the verge of its applicability, represents a meaningful endeavor and a valuable contribution to the lively field of nuclear cluster physics. It is left to the reader to decide for himself on the validity of this assumption.

This manuscript is organized as follows. Part I contains detailed description of the employed theoretical framework. In Chapter 1, we will describe the single-reference implementation of relativistic EDF theory. The RHB model, a particular realization of the theory that encompasses both mean-field and pairing correlations, will be introduced, and effective interactions in both the particle-hole and particle-particle channels will be discussed. Additionally, we will summarize recent results obtained by the Bruyères-Orsay-Zagreb collaboration on the origin and phenomenology of nuclear clustering within the relativistic mean-field framework. In Chapter 2, the multi-reference implementation of EDF theory will be laid out, encompassing a procedure of symmetry restoration and configuration mixing. Furthermore, relations most pertinent for calculation of correlated densities and form factors will be displayed. Part II contains first results obtained within the described framework. We will start with an introductory Chapter 3 in which we will address computational aspects of a study. In Chapter 4, a comprehensive analysis of quadrupole-octupole collectivity and cluster structures in neon isotopes will be carried out. Special attention will be paid to the case of the self-conjugate ^{20}Ne isotope, where cluster structures are thought to form already in the ground state. In Chapter 5, the

framework will be applied in a description of low-lying structure of ^{12}C isotope, focusing particularly on a structure of the $K^\pi = 0^+$ bands that are known to manifest a rich variety of shapes. Finally, a concluding chapter will briefly summarize the results of the present study and suggest possible extensions and improvements to the model.

Part I

Theoretical Framework

The Nuclear Energy Density Functional Method

Use the Force¹, Luke.

Jedi Master Obi-Wan Kenobi, "Star Wars Ep. IV"

The nuclear energy density functional (EDF) method currently provides the most complete and accurate description of ground-state and excited-state properties of atomic nuclei over the entire nuclide chart [BHR03, NVR11, RRR18]. Among microscopic approaches to the nuclear many-body problem, it is arguably the one which maintains an optimal compromise between global accuracy and feasibility of computational cost. It is very similar² in form to the density functional theory (DFT) [HK64, KS65, Koh99], a method which is widely used in condensed matter physics and quantum chemistry. In resemblance to DFT framework, nuclear EDF models effectively map the many-body problem onto a one-body problem by introducing relatively simple functionals of powers and gradients of ground-state nucleon densities and currents, representing distributions of matter, spin, momentum, and kinetic energy. In this way, a complex system of strongly-interacting particles is substituted by a much simpler and more intuitive system of independent particles that move in a self-consistent mean-field generated by all the other particles. On the other hand, and in contrast to the situation encountered in electronic many-body systems, derivation of highly accurate functionals from first principles is yet

¹If you are already wondering which one, this is the right chapter for you.

²The main conceptual difference between EDF and DFT lies in their relation to symmetry breaking. While EDF method minimizes energy of the system with respect to the symmetry-breaking trial wave function, DFT is built on an energy functional that is to be minimized with respect to a density which possesses all symmetries of the actual ground-state density [Dug14]. Even though, more recently, DFT framework has been extended to account for breaking of translation symmetry [Eng07], more involved symmetries (such as rotational or particle number) are yet to be included to the framework. The relation between DFT and nuclear EDF method still remains under debate [Dug14, Men16, Nak12, LDB09].

to be achieved in nuclear systems. Meanwhile, a hybrid approach is routinely employed: (i) form of the EDF is motivated by the underlying fundamental theory and relevant symmetries of the nucleon-nucleon force are respected, but (ii) additional free parameters are introduced to a model. Modern functionals are typically determined by about ten to twelve such parameters that are adjusted to a nuclear matter equation of state and to ground-state properties of finite nuclei. The most popular phenomenological functionals can be broadly divided into three separate classes:

- Non-relativistic Skyrme interaction. Originally introduced by T. H. R. Skyrme in the late 50s [Sky56, Sky58] as a combination of momentum-dependent two-body contact forces and momentum-independent three-body contact force, Skyrme functionals are probably the most widely used effective interaction in studies of low-energy nuclear structure up to date. This interaction is zero-range and quasilocal, which makes it particularly attractive from a computational point of view. On the other hand, pairing term is not included in the central part of an interaction and it is therefore typically added by hand. A general overview of Skyrme formalism can be found in Ref. [BHR03] and references cited therein.
- Non-relativistic Gogny interaction. In the late 60s, D. M. Brink and E. Boeker introduced a finite-range nuclear interaction [BB67]. A bit over a decade later, J. Dechargé and D. Gogny proposed a new parameterization of nuclear interaction [DG80] that became known as the Gogny force. Since within Gogny's framework mean-field and pairing terms have a common origin, this force is marked by a consistent treatment of all parts of the interaction. Finite range of the force guarantees a proper cut-off in momentum space, but the resulting pairing field is non-local which can render numerical implementations rather time-consuming. Over the past decades, various parameterizations of the force have been successfully applied in numerous nuclear structure studies. A general overview of Gogny formalism can be found in Refs. [Egi16, RRR18] and references cited therein.
- Relativistic interactions. Building upon a pioneering work of B. D. Serot and J. D. Walecka from the mid-80s [SW86], manifestly covariant approaches to the nuclear many-body problem have been developed [VALR05, NVR11, Men16]. Starting from a field theoretical Lagrangian that obeys Lorentz symmetries, these models have been able to match the performance of conventional non-relativistic models, while naturally accounting for purely relativistic effects such as the spin-orbit potential or the pseudospin symmetry [Gin97, MSTY+98]. Even though the relativistic Hartree-Fock-Bogoliubov model has been introduced quite recently [LRGM10, EKAV11], the vast majority of relativistic models is explicitly built as Hartree theories. In other words, the exchange terms of nuclear interaction are usually not taken into account explicitly and their effect is implicitly included through the free parameters of the model. Finally, non-relativistic pairing force is typically added to the functional.

All of the listed formulations have their own advantages and drawbacks, and the choice of interaction in each study often comes down to a particular problem in question and/or

to a personal taste and formational tradition of a researcher. Due to a nature of the problem in question, as well as the personal taste and formational tradition of the author of these lines³, the present study will be carried out within the relativistic framework. This means that a discussion of the non-relativistic framework will be completely omitted from the manuscript. For more information on recent applications of the non-relativistic framework an interested reader is referred to the review papers on the Skyrme [BHR03] and the Gogny [Egi16, RRR18] techniques. We will start this chapter with a brief overview of the relativistic mean-field (RMF) theory. It goes almost without saying that an intention or a capacity of this manuscript is not to give a comprehensive theoretical account of the framework. Much more detailed discussions can be found in a recently published book on relativistic EDFs [Men16] and in various review articles on the subject [Rin96, VALR05, NVR11]. For the purposes of this thesis, in Section 1.1 we will first lay out the basic building blocks of the RMF theory, introducing the meson-exchange and point-coupling pictures of a covariant framework. We will then proceed to describe particular effective interactions that will be used in the particle-hole (ph) and particle-particle (pp) channels throughout the study, that is, the density-dependent point-coupling DD-PC1 functional and a non-relativistic force separable in the momentum space, respectively. Relativistic Hartree-Bogoliubov model, which enables a unified description of ph and pp correlations on a mean-field level, will be discussed in Section 1.2. In Section 1.3, we will summarize recent results on the origin and phenomenology of nuclear clustering within the RMF framework that are relevant for the present work.

1.1. Relativistic Mean-Field Theory

1.1.1 Basic Building Blocks of the RMF Theory

Relativistic mean-field theory is a phenomenological, Lorentz-invariant approach to the nuclear many-body problem. It is based on a picture of atomic nucleus as a relativistic system of nucleons that are coupled to exchange mesons and photons through an effective Lagrangian. Basic assumptions of the theory are [Rin96, Men16]:

- RMF is a semi-classical field theory and the effective mesons serve only to introduce classical fields that carry appropriate relativistic quantum numbers. Consequently, rather than being treated as dynamical degrees of freedom, the meson-field operators are replaced by their expectation values in the nuclear ground state. More formally, effective mesons can be thought of as collective bosonic degrees of freedom that parameterize the non-vanishing bilinear combinations of local nucleon fields in the Hubbard-Stratonovich sense [Hub59].
- Nucleons are treated as point-like particles and their complex substructure including quarks and gluons is not explicitly taken into account. This approximation is

³And his respective doctoral advisors as well.

justified by considerations rooted in the effective field theory (EFT), since in the low-energy regime characteristic for nuclear structure the detailed substructure of nucleons cannot be resolved. Therefore, the explicit contribution from quarks and gluons can be integrated out, while their effect is being completely accounted for through the free parameters of effective Lagrangian.

- Vacuum polarization is not taken into account explicitly, that is, contributions from the Dirac sea are neglected (the so called *no-sea* approximation). However, effects of vacuum polarization are taken into account implicitly, through a phenomenological adjustment of free parameters of a model.
- In order to correct for too large incompressibility and properly describe the nuclear surface properties, a density-dependence of the interaction is introduced. This feature is not specific to relativistic interactions only, since a large majority of parameterizations of both Skyrme and Gogny interactions includes density-dependent terms as well.

Starting point of RMF calculations is a Lagrangian density that includes coupling of nucleons on effective mesons and photons, as well as the meson self-coupling. The attractive part of effective interaction is mediated by the exchange of scalar mesons. In fact, the spin-zero positive-parity σ -meson, which provides the mid- and long-range attractive part of nuclear interaction, can be understood as an approximation to the two-pion exchange in the mesonic picture [Rin96]. The repulsive part of interaction is determined by the exchange of vector mesons, the most important of which is the isoscalar-vector ω -meson. Finally, isospin dependence of the nuclear force is accounted for through the exchange of isovector-vector ρ -meson. The isoscalar-scalar σ -meson, the isoscalar-vector ω -meson, and the isovector-vector ρ -meson build a minimal set of meson fields that is, together with the electromagnetic field, necessary for a description of bulk and single-particle nuclear properties [NVR11]. In principle, one could also introduce to a model the isovector-scalar δ -meson, which would lead to a minor difference of scalar nuclear potentials in two isospin channels. However, it was demonstrated that the effect of inclusion of δ -meson can be completely absorbed in the readjusted coupling constant of ρ -meson [RMVC⁺11]. Therefore, δ -meson is omitted from majority of successful parameterizations. One should bear in mind that RMF is a phenomenological theory and that properties of the effective mesons do not necessarily have to coincide with properties of actual mesons known from the experiment.

In order to take into account the higher-order many-body effects, which are needed for a quantitative description of nuclear matter and finite nuclei, it is necessary to include a medium dependence of the effective interaction. This can be done either by introducing non-linear meson self-couplings or by allowing for the explicit density-dependence of the meson-nucleon couplings. Both the former [LKR97, LMGZ04, TRP05] and the latter [HKL01, NVFR02, LNVR05] approach have so far been employed in building successful phenomenological interactions. In the next step, the very exchange of effective mesons in each channel (scalar-isoscalar, vector-isoscalar, scalar-isovector, and vector-isovector) can be replaced by the corresponding local four-point (contact) interactions

between nucleons. The main motivation for this step is a fact that the exchange of heavy mesons is associated with short-distance dynamics which is unresolvable at low energies that are characteristic for nuclear systems. The main practical advantage, on the other hand, is reducing the computational cost considerably by rendering the interaction zero-range. It has been argued that other advantages of the point-coupling picture include a possibility of studying the role of naturalness in effective theories for nuclear structure-related problems [FS00], an easier inclusion of the Fock term, as well as the transition to a framework which is more convenient to investigate relationship between relativistic and non-relativistic models. Within the point-coupling picture, finite range effects of the nuclear force are typically taken into account by local derivative terms, similar to the situation encountered within the Skyrme framework. On the other hand, medium dependence is accounted for either through density-dependent coupling constants in two-body interactions or by including many-body contact terms. Over the past two decades, point-coupling functionals [BMMR02, NVR08, ZLYM10] have been developed whose performance matches that of the meson-exchange functionals. Throughout this study we will use the density-dependent point-coupling (DD-PC1) functional [NVR08] that was formulated in 2008 and employed in numerous studies ever since.

1.1.2 The DD-PC1 Effective Interaction

Basic building blocks of the point-coupling functional are densities and currents bilinear in the Dirac spinor field ψ of a nucleon:

$$\bar{\psi}\mathcal{O}_\tau\Gamma\psi, \quad \mathcal{O}_\tau \in \{1, \vec{\tau}\}, \quad \Gamma \in \{1, \gamma_\mu, \gamma_5, \gamma_5\gamma_\mu, \sigma_{\mu\nu}\}, \quad (1.1)$$

where $\vec{\tau}$ represents Pauli isospin matrices and Γ denotes 4×4 Dirac matrices. An effective Lagrangian is then built by forming the four-fermion (contact) combinations that behave like scalars under Lorentz transformations and under rotations in isospin space. Possible combinations in various isospace-space channels read:

- (i) isoscalar-scalar: $(\bar{\psi}\psi)(\bar{\psi}\psi)$,
- (ii) isoscalar-vector: $(\bar{\psi}\gamma^\mu\psi)(\bar{\psi}\gamma_\mu\psi)$,
- (iii) isovector-scalar: $(\bar{\psi}\vec{\tau}\psi) \cdot (\bar{\psi}\vec{\tau}\psi)$,
- (iv) isovector-vector: $(\bar{\psi}\vec{\tau}\gamma^\mu\psi) \cdot (\bar{\psi}\vec{\tau}\gamma_\mu\psi)$.

Vectors in isospin space are denoted with arrows, and vectors in coordinate space will be marked in bold throughout the manuscript. In principle, a general effective Lagrangian can be written as a power series of these terms and their derivatives, with higher-order terms representing in-medium many-body correlations. However, the currently available empirical data constrains only a limited set of parameters in such general expansion.

Therefore, an alternative approach is usually employed where the effective Lagrangian includes only second-order interaction terms, while all of the many-body correlations are built into a density-dependence of coupling constants. Total effective Lagrangian density of DD-PC1 interaction reads:

$$\mathcal{L}^{\text{DD-PC1}} = \mathcal{L}^{\text{free}} + \mathcal{L}^{4\text{f}} + \mathcal{L}^{\text{der}} + \mathcal{L}^{\text{EM}}. \quad (1.2)$$

Here, the first term corresponds to a Lagrangian density of free nucleons:

$$\mathcal{L}^{\text{free}} = \bar{\psi}(i\gamma_\mu\partial^\mu - m)\psi, \quad (1.3)$$

while the four-fermion point-coupling part reads:

$$\mathcal{L}^{4\text{f}} = -\frac{1}{2}\alpha_S(\rho)(\bar{\psi}\psi)(\bar{\psi}\psi) - \frac{1}{2}\alpha_V(\rho)(\bar{\psi}\gamma^\mu\psi)(\bar{\psi}\gamma_\mu\psi) - \frac{1}{2}\alpha_{TV}(\rho)(\bar{\psi}\vec{\tau}\gamma^\mu\psi)(\bar{\psi}\vec{\tau}\gamma_\mu\psi). \quad (1.4)$$

In full analogy with the meson-exchange picture, contact part of the interaction includes the isoscalar-scalar, isoscalar-vector and isovector-vector terms, while the isovector-scalar term is not included into a Lagrangian. Furthermore, the derivative part includes only the isoscalar-scalar contribution:

$$\mathcal{L}^{\text{der}} = -\frac{1}{2}\delta_S(\partial_\nu\bar{\psi}\psi)(\partial^\nu\bar{\psi}\psi). \quad (1.5)$$

Even though such terms could in principle be included in each isospace-space channel, experimental data can in practice constrain only one such term [NVR08]. Inclusion of derivative term in the isoscalar-scalar channel only is consistent with conventional meson-exchange RMF models, where a mass of σ -meson is adjusted to experimental data and free values are used for masses of ω - and ρ -mesons [NVR11]. Finally, the effective Lagrangian includes coupling of protons on electromagnetic field:

$$\mathcal{L}^{\text{EM}} = -e\bar{\psi}A_\mu\gamma^\mu\frac{1-\tau_3}{2}\psi. \quad (1.6)$$

Dynamics of a nuclear system is determined by the principle of least action:

$$S = \int dx^4 \mathcal{L}(x), \quad \delta S = 0, \quad (1.7)$$

which leads to the Euler-Lagrange equation:

$$\frac{\partial \mathcal{L}}{\partial \bar{\psi}} + \frac{\partial \mathcal{L}}{\partial \rho_V} \frac{\partial \rho_V}{\partial \bar{\psi}} - \partial_\mu \frac{\partial \mathcal{L}}{\partial (\partial_\mu \bar{\psi})} = 0. \quad (1.8)$$

Carrying out variation of Lagrangian with respect to the adjoint spinor $\bar{\psi}$ yields the single-nucleon Dirac equation:

$$\left[\gamma_\mu \left(i\partial^\mu - \Sigma_V^\mu - \Sigma_{TV}^\mu - \Sigma_R^\mu \right) - \left(m + \Sigma_S \right) \right] \psi = 0, \quad (1.9)$$

where the isoscalar-scalar nucleon self-energy Σ_S , the isoscalar-vector self-energy Σ_V^μ , and the isovector-vector self-energy Σ_{TV}^μ read:

$$\Sigma_S = \alpha_S(\rho_V)(\bar{\psi}\psi) - \delta_S \Delta(\bar{\psi}\psi), \quad (1.10)$$

$$\Sigma_V^\mu = \alpha_V(\rho_V)(\bar{\psi}\gamma^\mu\psi) + e \frac{1 - \tau_3}{2} A^\mu, \quad (1.11)$$

$$\Sigma_{TV}^\mu = \alpha_{TV}(\rho_V)(\bar{\psi}\vec{\tau}\gamma^\mu\psi). \quad (1.12)$$

In addition, Dirac equations includes contribution from the rearrangement term:

$$\Sigma_R^\mu = \frac{1}{2} \frac{\bar{\psi}\gamma^\mu\psi}{\rho_V} \left[\frac{d\alpha_S}{d\rho_V}(\bar{\psi}\psi)(\bar{\psi}\psi) + \frac{d\alpha_V}{d\rho_V}(\bar{\psi}\gamma_\mu\psi)(\bar{\psi}\gamma^\mu\psi) + \frac{d\alpha_{TV}}{d\rho_V}(\bar{\psi}\vec{\tau}\gamma_\mu\psi)(\bar{\psi}\vec{\tau}\gamma^\mu\psi) \right], \quad (1.13)$$

which arises from variation of density-dependent coupling constants α_S , α_V , and α_{TV} with respect to nucleon field $\bar{\psi}$. For models with density-dependent couplings, inclusion of the rearrangement self-energies is shown to be essential for energy-momentum conservation and thermodynamic consistency [NVFR02, FLW95]. In addition, it is assumed that couplings are functions of vector density, $\rho_V = \sqrt{j_\mu j^\mu}$, where $j^\mu = \bar{\psi}\gamma^\mu\psi$ is the nucleon four-current. Alternative option would have been making the couplings functions of scalar density. Nevertheless, vector density appears as a more natural choice because it is related to a conserved nucleon number, while no such conservation law holds in a case of scalar density. Guided by the microscopic density dependence of the vector and scalar self-energies in nuclear matter, a particular ansatz for the functional form of couplings is introduced [NVR08]:

$$\alpha_i(\rho_V) = a_i + (b_i + c_i x) e^{-d_i x}, \quad (i = S, V, TV), \quad (1.14)$$

where $x = \rho_V/\rho_{\text{sat}}$, $\rho_{\text{sat}} = 0.152 \text{ fm}^{-3}$ denotes nucleon saturation density in symmetric nuclear matter, and twelve free parameters are yet to be determined via fitting procedure.

Dirac equation (1.9) describes dynamics of a nuclear system. On the other hand, the corresponding EDF can be derived by employing the Legendre transformation on a

TABLE 1.1: List of phenomenological parameters of DD-PC1 functional (first row) and their adopted values obtained by fitting to experimental data on infinite nuclear matter and finite nuclei (second row) [NVR08]. See text for details.

| $a_S[\text{fm}^2]$ | $b_S[\text{fm}^2]$ | $c_S[\text{fm}^2]$ | d_S | $a_V[\text{fm}^2]$ | $b_V[\text{fm}^2]$ | d_V | $b_{TV}[\text{fm}^2]$ | d_{TV} | $\delta_S[\text{fm}^4]$ |
|--------------------|--------------------|--------------------|--------|--------------------|--------------------|--------|-----------------------|----------|-------------------------|
| -10.0462 | -9.1504 | -6.4273 | 1.3724 | 5.9195 | 8.8637 | 0.6584 | 1.8360 | 0.6400 | -0.8150 |

Lagrangian density \mathcal{L} . This yields the Hamiltonian density \mathcal{H} :

$$\mathcal{H} = \frac{\partial \mathcal{L}}{\partial(\partial_0 \phi_i)} \partial^0 \phi_i - \mathcal{L}, \quad (1.15)$$

where ϕ_i represents either nucleon or photon field. Hamiltonian density, which corresponds to the 00 component of energy-momentum tensor, is then used to determine the effective Hamiltonian operator H^4 :

$$H = \int d^3 \mathbf{r} \mathcal{H}(\mathbf{r}). \quad (1.16)$$

Within the mean-field approximation, the total correlated many-body state $|\Psi\rangle$ is represented by a simple product state $|\Phi\rangle$. The DD-PC1 energy density functional corresponds to the expectation value of the effective Hamiltonian operator in this product state:

$$E_{\text{DD-PC1}}[\hat{\rho}] \equiv \langle \Phi | H | \Phi \rangle = \int d^3 \mathbf{r} \mathcal{E}(\mathbf{r}), \quad (1.17)$$

where a total energy density:

$$\mathcal{E}(\mathbf{r}) = \mathcal{E}^{\text{kin}}(\mathbf{r}) + \mathcal{E}^{\text{int}}(\mathbf{r}) + \mathcal{E}^{\text{EM}}(\mathbf{r}) \quad (1.18)$$

is composed of the kinetic part $\mathcal{E}^{\text{kin}}(\mathbf{r})$, the interaction part $\mathcal{E}^{\text{int}}(\mathbf{r})$, and the electromagnetic part $\mathcal{E}^{\text{EM}}(\mathbf{r})$:

$$\mathcal{E}^{\text{kin}}(\mathbf{r}) = \sum_{i=1}^N \psi_{\alpha_i}^\dagger (\boldsymbol{\alpha} \cdot \mathbf{p} + \beta m) \psi_{\alpha_i}, \quad (1.19)$$

$$\mathcal{E}^{\text{int}}(\mathbf{r}) = \frac{1}{2} \alpha_S \rho_S^2 + \frac{1}{2} \alpha_V j_\mu j^\mu + \frac{1}{2} \alpha_{TV} \vec{j}_\mu \vec{j}^\mu + \frac{1}{2} \delta_S \rho_S \Delta \rho_S, \quad (1.20)$$

$$\mathcal{E}^{\text{EM}}(\mathbf{r}) = \frac{1}{2} e j_c^\mu A_\mu. \quad (1.21)$$

⁴We call our Hamiltonian operator effective because it explicitly depends on nucleonic density and as such it is different from a genuine density-independent Hamiltonian operator. This distinction lies at the root of some theoretical difficulties that can manifest themselves on a multi-reference level and that will be discussed in the next chapter.

Here, we have introduced a shorthand notation for the scalar density ρ_S , the baryon current $j^\mu = (\rho_V, \mathbf{j})$, the isovector current $\vec{j}^\mu = (\rho_3, \mathbf{j}_3)$, and the electromagnetic current $j_c^\mu = (\rho_c, \mathbf{j}_c)$ in the self-consistent ground state of atomic nucleus:

$$\rho_S(\mathbf{r}) \equiv \langle \Phi | \bar{\psi} \psi | \Phi \rangle = \sum_{i=1}^N \bar{\psi}_{\alpha_i}(\mathbf{r}) \psi_{\alpha_i}(\mathbf{r}), \quad (1.22a)$$

$$j^\mu(\mathbf{r}) \equiv \langle \Phi | \bar{\psi} \gamma^\mu \psi | \Phi \rangle = \sum_{i=1}^N \bar{\psi}_{\alpha_i}(\mathbf{r}) \gamma^\mu \psi_{\alpha_i}(\mathbf{r}), \quad (1.22b)$$

$$\vec{j}^\mu(\mathbf{r}) \equiv \langle \Phi | \bar{\psi} \vec{\tau} \gamma^\mu \psi | \Phi \rangle = \sum_{i=1}^N \bar{\psi}_{\alpha_i}(\mathbf{r}) \vec{\tau} \gamma^\mu \psi_{\alpha_i}(\mathbf{r}), \quad (1.22c)$$

$$j_c^\mu(\mathbf{r}) \equiv \langle \Phi | \bar{\psi} \gamma^\mu \frac{1 - \tau_3}{2} \psi | \Phi \rangle = \sum_{i=1}^N \bar{\psi}_{\alpha_i}(\mathbf{r}) \gamma^\mu \frac{1 - \tau_3}{2} \psi_{\alpha_i}(\mathbf{r}), \quad (1.22d)$$

where sums run over all occupied positive-energy single-nucleon orbitals. Particular structure of $|\Phi\rangle$ will be discussed in Section 1.2. The ground-state energy of a nuclear system (1.17) is determined by a self-consistent solution to the Dirac equation (1.9). Starting from an initial nuclear field (usually something of the Woods-Saxon type), a first set of orbitals $\{\psi_i\}$ can be obtained. These orbitals are then used to calculate densities and currents, (1.22a) - (1.22d), which give rise to refined nuclear fields, (1.10) - (1.13). In the next step, these fields serve as a new source to the Dirac equation. The self-consistent procedure is repeated until a convergence is reached and a ground-state description of atomic nucleus is obtained.

Twelve parameters in various isospace-space channels together with the strength parameter of a derivative term form an initial set of 13 free parameters of the DD-PC1 interaction. Some of them will be discarded prior to the fitting procedure. To start with, a functional form of coupling constant in the isovector-vector channel was determined from results of Dirac-Brueckner calculations of asymmetric nuclear matter [dJL98], and two parameters (a_{TV} and c_{TV}) were therefore set to zero [NVR08]. In addition, parameter c_V was also set to zero in order to reduce a number of parameters. The remaining ten parameters were simultaneously adjusted to infinite and semi-infinite nuclear matter properties, as well as to the binding energies of 64 axially symmetric deformed nuclei in mass regions $A \approx 150 - 180$ and $A \approx 230 - 250$. Details of the fitting procedure can be found in Ref. [NVR08], while in Table 1.1 we list the adopted values of parameters⁵. DD-PC1 functional has been further tested in calculations of ground-state properties of spherical and deformed medium-heavy and heavy nuclei, including binding energies, charge radii, deformation parameters, neutron skin thickness, and excitation energies of giant multipole resonance. The only relevant deviations from data have been found in calculations of binding energies in spherical closed-shell nuclei. This discrepancy can be understood in terms of a relatively low effective nucleon mass that, when a relativistic

⁵It is interesting to mention that, quite recently, concepts from information geometry were used to analyze parameter sensitivity for a nuclear energy density functional, improve the fitting procedure, and eventually further reduce a number of parameters [NV16, NIV17].

zero and total isospin one. On the other hand, when a number of neutrons approaches a number of protons, two types of nucleons occupy similar orbitals near Fermi surface and neutron-proton pairs can be formed in both the $T = 1$ and $T = 0$ channel [FM14]. However, due to the breaking of the underlying signature symmetry, simultaneous inclusion of both types of pairing is notoriously complicated within the EDF framework [BHR03]. Therefore, in this work we adopt a strategy of virtually all EDF models and explicitly treat only the like-particle pairing. Furthermore, even though relativistic pairing interactions in finite nuclei have been formally developed, at the moment there is no empirical evidence for any relativistic effects in nucleon pairing [Ser01]. Therefore, in this work we employ a standard hybrid method by adding the non-relativistic pairing force to the relativistic energy density functional (more details on this method can be found, for example, in a review paper of Ref. [VALR05]). Commonly used tactics in relativistic models is including a pairing force which is based on the Gogny interaction. On the one hand, this choice avoids a problem of cutoff dependence which plagues zero-range implementations of pairing force, such as monopole pairing or density-dependent δ -pairing interactions. On the other hand, a price to pay is the non-locality of pairing field and, consequently, the inherited complexity of numerical implementation. In order to reduce the cost of numerical implementation, a separable form of pairing has been introduced in calculations of both spherical and deformed nuclei [Dug04, TMR09c, TMR09a, TMR09b, NRV⁺10]. Simple separable forces are demonstrated to reproduce pairing properties in spherical and deformed nuclei on almost the same footing as the original Gogny force, while reducing a computational cost significantly. As additional features, they both preserve translational invariance and maintain a finite range.

The separable pairing force that will be used throughout this study is a non-relativistic force separable in momentum space [TMR09a, TMR09b]:

$$\langle k|V_{\text{sep}}^{1S_0}|k'\rangle = -Gp(k)p(k'), \quad (1.23)$$

with a simple Gaussian ansatz $p(k) = e^{-a^2k^2}$ for the momentum-dependent function. Starting from a gap equation in the 1S_0 channel:

$$\Delta(k) = - \int_0^\infty \frac{k'^2 dk'}{2\pi^2} \langle k|V_{\text{sep}}^{1S_0}|k'\rangle \frac{\Delta(k')}{2E(k')}, \quad (1.24)$$

two free parameters of the force, G and a , were adjusted to reproduce in infinite nuclear matter the bell-shape curve of pairing gap as calculated with Gogny force. In this work we adopt a set of parameters that was obtained by fitting to the D1S parameterization of Gogny force, that is, $G = 728 \text{ MeV fm}^3$ and $a = 0.644 \text{ fm}$. Nevertheless, since the original force was adjusted to data on infinite nuclear matter, there is no guarantee that exactly the same strength has to hold for all finite nuclear systems. Therefore, and in accordance with the phenomenological spirit of a model, an additional scaling parameter f has been introduced in practical implementations of separable pairing in finite nuclei that accounts for different pairing properties throughout the nuclide chart (see, e.g., Section II of Ref. [AAR16]). Refined methods to determine nuclear mass-dependence of this factor can be

employed, such as fine tuning it in a comparison between experimental moments of inertia and those obtained in cranked relativistic Hartree-Bogoliubov calculations [AARR14, AAR16]. In this work, however, we choose to simply fix the value of scaling parameter to $f = 0.9$ and use the same pairing force throughout the entire study.

In order to determine matrix elements of the pairing interaction, a separable force of Eq. (1.23) is first transformed from momentum space to coordinate space:

$$V(\mathbf{r}_1, \mathbf{r}_2, \mathbf{r}'_1, \mathbf{r}'_2) = -G\delta(\mathbf{R} - \mathbf{R}')P(r)P(r')\frac{1}{2}(1 - P_\sigma), \quad (1.25)$$

where $\mathbf{R} = \frac{1}{2}(\mathbf{r}_1 + \mathbf{r}_2)$ and $\mathbf{r} = \mathbf{r}_1 - \mathbf{r}_2$ denote the center of mass and relative coordinates of two paired particles, respectively, and $P_\sigma = \sigma_1 \cdot \sigma_2$ is a spin operator. In addition, $P(r)$ corresponds to a Fourier transform of $p(k)$ and reads:

$$P(r) = \frac{1}{(4\pi a^2)^{3/2}} e^{-\frac{r^2+r_1^2}{4a^2}}. \quad (1.26)$$

Obviously, separable pairing force has a finite range in coordinate space. In addition, because of the presence of $\delta(\mathbf{R} - \mathbf{R}')$, it preserves a translational invariance. To proceed further with our calculation, it is necessary to define a relevant single-particle basis in which the pairing force matrix elements will be computed. Prior to that, let us first introduce a framework that provides a unified self-consistent account of both mean-field and pairing correlations.

1.2. Relativistic Hartree-Bogoliubov Model

1.2.1 The Independent Quasiparticle Picture

So far, we have defined and discussed effective interactions in two distinct interaction channels, that is, the density-dependent point-coupling (DD-PC1) functional in particle-hole channel and the separable pairing force in particle-particle channel. In this section, we will introduce a framework which enables us to treat two of those simultaneously and on an equal footing (detailed discussions on this framework can be found in standard textbooks [RS80, BR85] and references cited therein). In order to achieve that, we will first have to give up on the intuitive picture of independent particles (nucleons), that are associated with a set of single-particle operators $\{c_\alpha^\dagger, c_\alpha\}$ and can be generated from a physical vacuum $|0\rangle$ via $|\alpha\rangle = c_\alpha^\dagger |0\rangle$ ⁶. Since pairing correlations scatter pairs of nucleons in time-reversed states around the Fermi surface, single nucleons do not represent convenient degrees of freedom anymore. In place of that, one introduces a concept of independent quasiparticles, that can be thought of as independent particles dressed in correlations generated by pairing interaction. These quasiparticles are associated with a

⁶More details on the second quantization formalism are given in Appendix A.

set of single-quasiparticle operators $\{\beta_\mu^\dagger, \beta_\mu\}$, and a transition between particle and quasiparticle frameworks is given by the unitary Bogoliubov transformation [RS80, BR85]:

$$\beta_\mu = \sum_\alpha \left(U_{\alpha\mu}^* c_\alpha + V_{\alpha\mu}^* c_\alpha^\dagger \right), \quad (1.27)$$

$$\beta_\mu^\dagger = \sum_\alpha \left(U_{\alpha\mu} c_\alpha^\dagger + V_{\alpha\mu} c_\alpha \right), \quad (1.28)$$

where sums run over the entire configuration space. Evidently, quasiparticle operators mix particle creation and annihilation operators. Nevertheless, they still satisfy standard fermionic anticommutation relations:

$$\{\beta_\mu, \beta_\nu\} = 0, \quad \{\beta_\mu^\dagger, \beta_\nu^\dagger\} = 0, \quad \{\beta_\mu, \beta_\nu^\dagger\} = \delta_{\mu\nu}. \quad (1.29)$$

Bogoliubov transformation can be written in a more compact form:

$$\begin{pmatrix} \beta \\ \beta^\dagger \end{pmatrix} = \mathcal{W}^\dagger \begin{pmatrix} c \\ c^\dagger \end{pmatrix}, \quad (1.30)$$

where the unitary transformational matrix \mathcal{W} reads:

$$\mathcal{W} = \begin{pmatrix} U & V^* \\ V^* & U \end{pmatrix}. \quad (1.31)$$

Bogoliubov matrices U and V play a central role within this framework, as they determine properties of independent quasiparticles. However, their form is not completely arbitrary. In fact, as a consequence of anticommutation relations for quasiparticle operators (1.29), it can be shown that Bogoliubov matrices need to satisfy the following expressions:

$$\begin{aligned} U^\dagger U + V^\dagger V &= \mathbf{1}, & UU^\dagger + V^* V^T &= \mathbf{1}, \\ U^T V + V^T U &= 0, & UV^\dagger + V^* U^T &= 0. \end{aligned} \quad (1.32)$$

Within the non-relativistic quasiparticle picture, ground state of the nuclear many-body system $|\Phi\rangle$ is constructed by applying quasiparticle annihilation operators on a true (bare) vacuum state:

$$|\Phi\rangle = \prod_\mu \beta_\mu |0\rangle. \quad (1.33)$$

This, in turn, means that the ground state is now a vacuum with respect to independent quasiparticles:

$$\beta_\mu |\Phi\rangle = 0, \quad \forall \mu. \quad (1.34)$$

State that satisfies these conditions for a corresponding set of quasiparticle operators $\{\beta_\mu^\dagger, \beta_\mu\}$ is called the Hartree-Fock-Bogoliubov (HFB) state. In the next subsection, we will discuss a particular realization of HFB theory, the relativistic Hartree-Bogoliubov (RHB) model.

1.2.2 Relativistic Hartree-Bogoliubov Equation

The HFB framework, as already emphasized several times throughout this manuscript, provides a unified description of ph and pp correlations on a mean-field level. In contrast to more phenomenological approaches such as the Bardeen-Cooper-Schrieffer (BCS) theory, HFB model is applicable across the entire chart of nuclides, for strongly-bound and weakly-bound nuclei alike. We point out that a particular realization of HFB theory which will be used in this work, the relativistic Hartree-Bogoliubov model, bears some differences in comparison to the conventional HFB framework [Val61]. Here, we list some of the most relevant ones:

- Formally speaking, HFB framework is developed within the Hamiltonian-based picture, meaning that a starting point of the conventional HFB calculation is a genuine Hamiltonian operator. On the other hand, starting point of our calculation is a phenomenological EDF of normal and anomalous densities.
- Unlike the situation encountered in the original HFB framework, mean-field and pairing part of our interaction are derived from different sources.
- Fock (exchange) terms are excluded from our calculation, in both the mean-field and pairing channels of interaction.
- Due to a covariant structure of framework, relativistic Bogoliubov matrices U and V will additionally differentiate between large and small components of nucleonic wave function, a feature which is absent from the non-relativistic formulations of the theory.

The RHB model defined in this way has proven to be a highly successful framework for a relativistic description of ground state properties of atomic nuclei [Men16, NVR11]. The RHB state $|\Phi\rangle$ and single-particle operators $\{c_\alpha^\dagger, c_\alpha\}$ can be used to define a Hermitian normal density ρ and a skew-symmetric pairing tensor (anomalous density) κ :

$$\rho_{\alpha\gamma} = \frac{\langle \Phi | c_\gamma^\dagger c_\alpha | \Phi \rangle}{\langle \Phi | \Phi \rangle} = (V^* V^T)_{\alpha\gamma}, \quad (1.35)$$

$$\kappa_{\alpha\gamma} = \frac{\langle \Phi | c_\gamma c_\alpha | \Phi \rangle}{\langle \Phi | \Phi \rangle} = (V^* U^T)_{\alpha\gamma}, \quad (1.36)$$

$$\kappa_{\alpha\gamma}^* = \frac{\langle \Phi | c_\alpha^\dagger c_\gamma^\dagger | \Phi \rangle}{\langle \Phi | \Phi \rangle} = (V U^\dagger)_{\alpha\gamma}. \quad (1.37)$$

Once pairing is included into the model, the EDF does not anymore depend on a normal density only, but it additionally becomes a functional of a pairing tensor:

$$E_{\text{RHB}}[\hat{\rho}, \hat{\kappa}, \hat{\kappa}^*] = E_{\text{RMF}}[\hat{\rho}] + E_{\text{pair}}[\hat{\kappa}, \hat{\kappa}^*]. \quad (1.38)$$

Here, $E_{\text{RMF}}[\hat{\rho}]$ is the usual relativistic mean-field functional, while the pairing functional can be calculated as:

$$E_{\text{pair}}[\hat{\kappa}, \hat{\kappa}^*] = \frac{1}{4} \sum_{\alpha_1 \gamma_1} \sum_{\alpha_2 \gamma_2} \hat{\kappa}_{\alpha_1 \gamma_1}^* \langle \alpha_1 \gamma_1 | V^{pp} | \alpha_2 \gamma_2 \rangle \hat{\kappa}_{\alpha_2 \gamma_2}, \quad (1.39)$$

with $\langle \alpha_1 \gamma_1 | V^{pp} | \alpha_2 \gamma_2 \rangle$ representing matrix elements of a general two-body pairing interaction. In the present work, a mean-field functional corresponds to the DD-PC1 functional as defined in (1.17), while pairing matrix elements are derived from a separable pairing force of (1.25). Normal density $\hat{\rho}$ and anomalous density $\hat{\kappa}$ build together the generalized density matrix $\hat{\mathcal{R}}$:

$$\hat{\mathcal{R}} = \begin{pmatrix} \hat{\rho} & \hat{\kappa} \\ -\hat{\kappa}^* & 1 - \hat{\rho}^* \end{pmatrix}, \quad (1.40)$$

which is idempotent and encodes all of the information about nuclear system that was originally present in the RHB wave function $|\Phi\rangle$. Within the Hamiltonian-based picture of HFB, a Wick theorem with respect to $|\Phi\rangle$ is employed in order to determine energy functional $E[\hat{\rho}, \hat{\kappa}, \hat{\kappa}^*]$ that depends on normal and anomalous density. In the next step, one varies:

$$\delta \left[E[\hat{\rho}, \hat{\kappa}, \hat{\kappa}^*] - \lambda \text{Tr}\{\hat{\rho}\} - \text{Tr}\{\lambda(\hat{\mathcal{R}}^2 - \hat{\mathcal{R}})\} \right] = 0 \quad (1.41)$$

with respect to $\delta\hat{\mathcal{R}}$, which yields HFB equation. Relativistic Hartree-Bogoliubov equation has precisely the same form and it reads:

$$\begin{pmatrix} \hat{h}_D - \lambda & \hat{\Delta} \\ -\hat{\Delta}^* & -\hat{h}_D^* + \lambda \end{pmatrix} \begin{pmatrix} U_k \\ V_k \end{pmatrix} = E_k \begin{pmatrix} U_k \\ V_k \end{pmatrix}. \quad (1.42)$$

The left-hand side of Eq. (1.42) contains two fields. The self-consistent (Hartree-Fock) field \hat{h}_D corresponds to the Dirac Hamiltonian of Eq. (1.9) and it drives the single-particle shell structure of atomic nucleus, while the pairing (Bogoliubov) field $\hat{\Delta}$ is responsible for scattering of paired nucleons around the Fermi surface. The chemical potential λ is determined by the particle number subsidiary condition that the expectation value of particle number operator in nuclear ground state corresponds to the actual number of nucleons. Column vectors of the RHB eigenvalue problem denote quasiparticle wave functions, and E_k are quasiparticle energies. We note that a dimension of the RHB equation is twice as large as a dimension of the corresponding Dirac equation. Therefore, for each eigenvector (U_k, V_k) with positive quasiparticle energy $E_k > 0$ there exists an eigenvector (V_k^*, U_k^*) with negative quasiparticle energy $-E_k$. Due to a fermionic character of the theory, levels E_k and $-E_k$ cannot be occupied simultaneously, that is, one needs to choose either the positive or negative eigenvalue and the corresponding eigenvector. Within the *no sea* approximation, one should in principle choose solutions with positive quasiparticle energies (particles) for states above the Dirac sea, and solutions with negative quasiparticle energies (antiparticles) for states in the Dirac sea [Men16]. Nevertheless, due to a large Dirac gap, contribution of antiparticles to normal and anomalous densities is negligible⁷. Therefore, in this work we employ a common tactics and take into account only contributions from positive energy states. This choice enabled us to reduce a computational time significantly by reducing a dimension of the corresponding equation. On the other hand, a price we were willing to pay was rendering the anomalous density κ antisymmetric only up to an excellent approximation.

Within the RHB framework, quasiparticle wave functions are composed of the large component f and the small component g :

$$U_k = \begin{pmatrix} f_k^{(U)} \\ ig_k^{(U)} \end{pmatrix}, \quad V_k = \begin{pmatrix} f_k^{(V)} \\ ig_k^{(V)} \end{pmatrix}. \quad (1.43)$$

The corresponding equations can be solved either directly in the coordinate space [MR96, MPR97] or, more commonly, by expanding nuclear spinors in a discrete basis of choice, typically harmonic oscillator [GRT90] or Woods-Saxon [ZMR03] basis. In this work, we employ a mixed method that combines the configurational and coordinate space representations [Vau73, NPVR14]. Since axial-symmetry of RHB states is imposed, corresponding equation (1.42) is first solved in the configurational space of the axially symmetric harmonic oscillator. In the next step, obtained wave functions are used to calculate densities and currents in the coordinate space. Eigenfunctions of the axially symmetric harmonic oscillator $\Phi_\alpha(\mathbf{r}, s)$ are characterized by a set of quantum numbers $\{\alpha\} = \{n_z, n_\perp, \Lambda, m_s\}$, where n_z and n_\perp represent a number of quanta (nodes) in the z - and the r_\perp - directions

⁷We have verified computationally that this statement indeed holds in practice.

of cylindrical coordinate system, respectively, while Λ and m_s denote components of the orbital angular momentum and of the spin along the z -axis. Details of the harmonic oscillator basis and its coordinate representation in terms of Hermite and associated Laguerre polynomials are given in Appendix A. Here, we note the explicit expansion of Dirac spinor in terms of basis states $\Phi_\alpha(\mathbf{r}, s)$ and isospin wave function χ_{t_i} :

$$\psi_k^{(i)}(\mathbf{r}, s, t) = \begin{pmatrix} \sum_{\alpha}^{\alpha_{max}} f_{\alpha,k}^{(i)} \Phi_{\alpha}(\mathbf{r}, s) \chi_{t_i}(t) \\ i \sum_{\tilde{\alpha}}^{\tilde{\alpha}_{max}} g_{\tilde{\alpha},k}^{(i)} \Phi_{\tilde{\alpha}}(\mathbf{r}, s) \chi_{t_i}(t) \end{pmatrix}, \quad i = U, V. \quad (1.44)$$

In order to avoid the appearance of spurious states with a very large number of radial nodes close to the Fermi surface, maximal quantum numbers for the expansion of large and small component of Dirac spinor, α_{max} and $\tilde{\alpha}_{max}$, are different [GRT90]. In particular, quantum numbers α and $\tilde{\alpha}$ are determined in such a way that the corresponding major oscillator quantum numbers $N = 2n_{\perp} + n_z + \Lambda$ are not larger than N_{sh} for the expansion of large components and not larger than $N_{sh} + 1$ for the expansion of small components. The $i = V$ component of Dirac spinor (1.44) is used to calculate densities and currents in the coordinate space (1.22a)-(1.22d). On the other hand, pairing tensor $\hat{\kappa}$ is kept in the configurational space and the corresponding matrix elements of pairing field $\hat{\Delta}$ can be calculated as:

$$\hat{\Delta}_{\alpha_1\gamma_1} = \frac{1}{2} \sum_{\alpha_2\gamma_2} \langle \alpha_1\gamma_1 | V^{pp} | \alpha_2\gamma_2 \rangle \hat{\kappa}_{\alpha_2\gamma_2}. \quad (1.45)$$

Here, $\langle \alpha_1\gamma_1 | V^{pp} | \alpha_2\gamma_2 \rangle$ corresponds to a matrix element of the two-body pairing interaction (1.25) in the harmonic oscillator basis that can be computed using the Talmi-Moshinsky techniques for cylindrical coordinates (more details can be found in Ref. [TMR09c] and references cited therein). In practical implementations, only large components of (1.44) are used to build non-relativistic pairing tensor $\hat{\kappa}$ (1.36), while other components of the tensor are safely omitted. By expanding nuclear spinors in a sufficiently large harmonic oscillator basis, self-consistent solution to the RHB equation provides us with an approximate description of a ground state of atomic nucleus. In spite of a fact that it formally corresponds to a symmetry-broken wave packet of various eigenstates with good quantum numbers (such as angular momenta, particle numbers, etc.), the RHB-type state represents a powerful tool for accessing different nuclear ground-state properties, including binding energies, radii, and deformation parameters. Moreover, by imposing constraints on values of different quantities, the RHB framework grants us the license to explore energy landscapes around the self-consistent minima.

1.2.3 Constrained RHB Calculation

The conventional HFB framework, both in its spirit and its basic implementation, is a ground-state theory. This means that, as long as employed without any additional

constraints, the virtue of Ritz variational principle will grant us a state that minimizes a total energy of the system. Nevertheless, by imposing additional constraints on values of various quantities, it is possible to obtain a state that minimizes a total energy of the system under that very constraint. For example, by imposing a constraint on values of nuclear radii it is possible to artificially inflate a nucleus and thereby study the role of saturation in forming of α -clusters [GS13, EKNV14a]. Another possibility is including a constraint on particle-number dispersion in order to study the effect of pairing fluctuations on fission dynamics [ZLN⁺16]. The most common constraints, however, are those imposed on values of electric multipole moments or, equivalently, deformation parameters. Of course, a pool of possible constraints is primarily determined by a choice of symmetries that nuclear system is *a priori* allowed or forbidden to break. In this work, we impose the axial and time-reversal symmetry of RHB states, which means that triaxial shapes and odd systems are out of the reach to start with. On the other hand, we allow our even-even nucleus to deform in both the quadrupole and octupole direction. A choice of the quadrupole degree of freedom is rather obvious, since all nuclei (except for very few doubly-magic isotopes) exhibit deviations from a spherical shape. A choice of the octupole degree of freedom is motivated by a fact that many α -clusterized structures, such as the expected $^{16}\text{O} + \alpha$ configuration in ^{20}Ne isotope, are characterized by precisely the parity-breaking octupole deformation. In practice, we employ the method of quadratic constraint and impose constraints on the quadrupole Q_{20} and octupole Q_{30} moments. This method uses an unrestricted variation of the function:

$$\langle H \rangle + \sum_{\lambda=2,3} C_{\lambda 0} (\langle \hat{Q}_{\lambda 0} \rangle - q_{\lambda 0})^2, \quad (1.46)$$

where $\langle H \rangle$ is total energy, $\langle \hat{Q}_{\lambda 0} \rangle$ denotes expectation value of the mass multipole operators $\hat{Q}_{\lambda \mu} \equiv r^\lambda Y_{\lambda \mu}$, $q_{\lambda 0}$ are the constrained values of multipole operators, and $C_{\lambda 0}$ are corresponding stiffness constants. In general, values of multipole moments $\langle \hat{Q}_{\lambda 0} \rangle$ will coincide with constrained values $q_{\lambda 0}$ only at a stationary point, and a difference will depend on stiffness constant $C_{\lambda 0}$. In particular, smaller values of $C_{\lambda 0}$ will lead to larger deviations of $\langle \hat{Q}_{\lambda 0} \rangle$ from the corresponding $q_{\lambda 0}$, while increasing $C_{\lambda 0}$ often destroys convergence of the self-consistent procedure. This deficiency can be resolved by implementing the augmented Lagrangian method [SSBN10]. Furthermore, we introduce dimensionless deformation parameters β_λ , defined as:

$$\beta_\lambda = \frac{4\pi}{3AR^\lambda} q_{\lambda 0}, \quad R = r_0 A^{1/3}, \quad (1.47)$$

with $r_0 = 1.2$ fm. This kind of constrained calculus enables us to access configurations in the entire plane spanned by a set of deformations $\{q\} = \{\beta_2, \beta_3\}$, and the corresponding RHB states will be denoted as $|\Phi(q)\rangle$. An interesting analysis can be carried out already on this level, particularly in terms of the rigidity/softness of constrained energy surfaces that determine relevance of collective correlations related to symmetry restoration and configuration mixing. In addition, appearance of local minima on energy landscapes may

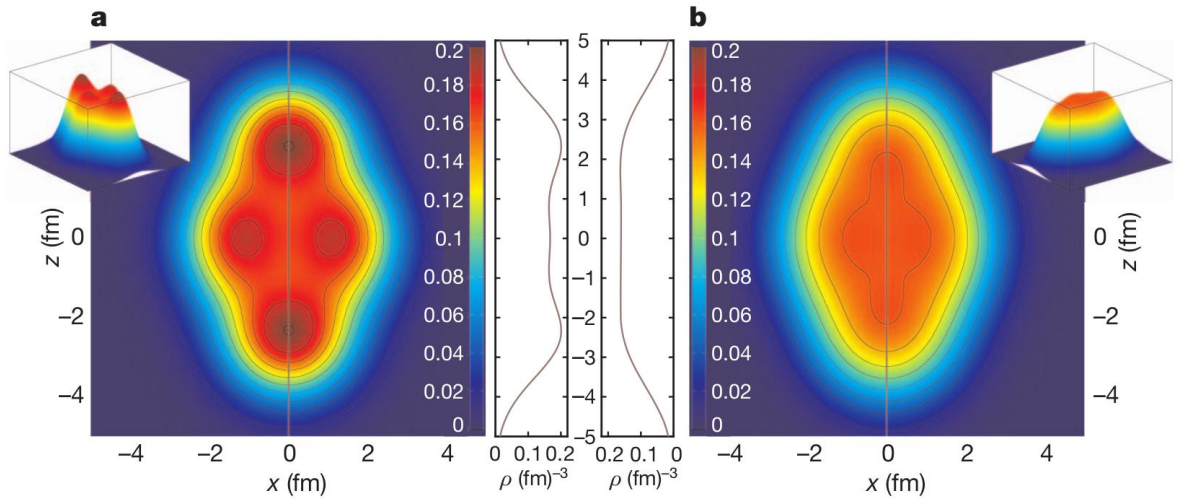


FIGURE 1.2: Self-consistent ground-state densities of ^{20}Ne isotope in the $x-z$ plane of the intrinsic reference frame. Densities calculated with the relativistic DD-ME2 functional (left panel) and the non-relativistic Skyrme SLy4 functional (right panel) are compared. The two inserts on each panel show the corresponding three-dimensional density plots and the density profiles (ρ) along the symmetry axis ($x=0$). Figure taken from Ref. [EKNV12].

offer a qualitative insight into the structure of excited nuclear configurations. Nevertheless, in order to carry out a more quantitative analysis, it would be beneficial to have a framework that treats all of these configurations on an equal footing and determines their relative contributions to a true ground state via variational procedure. A framework which does precisely that exists, and it is known as the MR-EDF. It is essentially a two-step process. In the first step, one restores relevant symmetries that are broken on a mean-field level. For a present study, these include rotational, particle number, and parity symmetry. In the second step, collective state of atomic nucleus is built from symmetry-conserving configurations, and detailed description of nuclear spectroscopy is obtained via variational procedure. The practical extension of RHB framework to a multi-reference level represents the main original contribution of this manuscript and it will be extensively discussed in Chapter 2. Before that, let us just briefly overview some of the recent results on nuclear clustering that have been obtained within the RMF framework.

1.3. Nuclear Clustering within the RMF Framework

Cluster structures in α -conjugate nuclei have been a subject of numerous studies within the mean-field framework [ASPG05, MKS+06, RMUO11, IMIO11, RB11, GS13, Rob14]. The purpose or the capacity of this section is not to give a comprehensive and balanced overview of nuclear clustering from the mean-field perspective, or even from the relativistic mean-field perspective. Rather than that, we will briefly overview some of the recent results that have been obtained by the Bruyères-Orsay-Zagreb collaboration and that elucidate a context of the present work. Let us start with the self-consistent ground-state density distributions of ^{20}Ne isotope [EKNV12] that are plotted in Figure 1.2. Mean-field

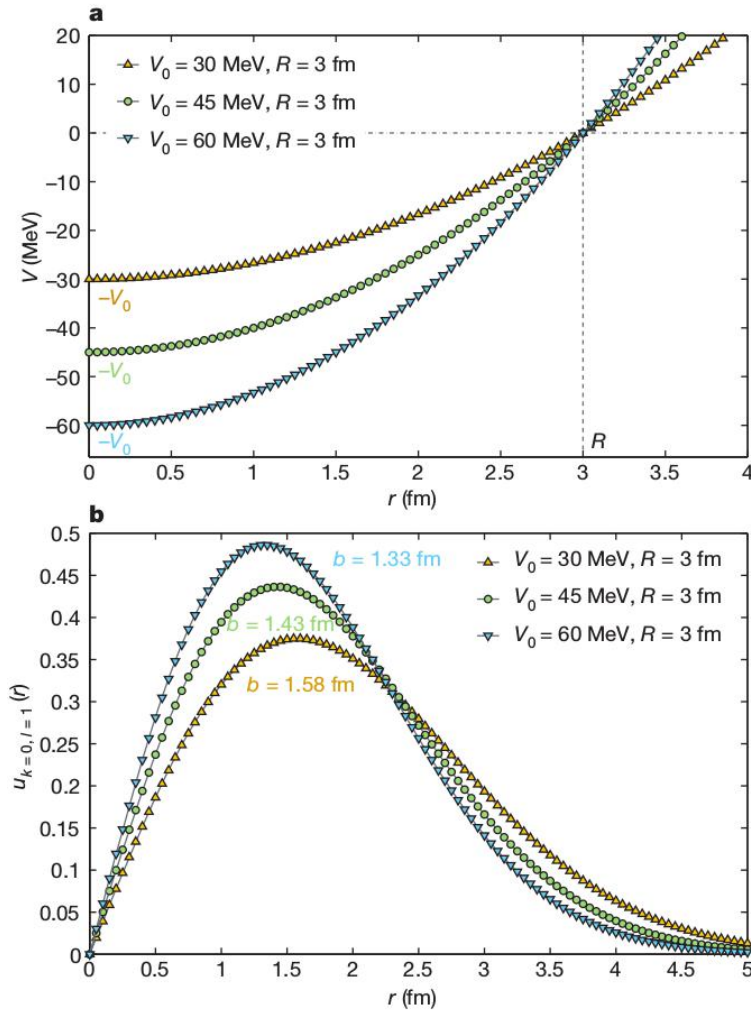


FIGURE 1.3: Harmonic oscillator potentials with different depths. Upper panel: Three potentials ($V_0 = -30, -45, -60$ MeV) with the same radius ($R = 3$ fm) as functions of radial coordinate r . Lower panel: Radial wavefunctions $u_{kl}(r)$ of the corresponding first p -state, where k and l are the radial and the azimuthal quantum number, respectively. Figure taken from Ref. [EKNV12].

calculations were carried out by using representatives of two different classes of functionals: the relativistic meson-exchange DD-ME2 functional [LNVR05] (left panel) and the non-relativistic Skyrme SLy4 functional [CBH⁺98] (right panel). Both functionals reproduce experimental ground-state observables such as binding energies, charge, and matter radii with a typical accuracy of roughly 1%. In addition, they yield very similar values of equilibrium deformation parameters. Nevertheless, the obtained intrinsic densities are manifestly different. As can be seen in Fig. 1.2, density obtained with the non-relativistic functional exhibits smooth behavior typical of Fermi liquids, with an extended surface region in which the density decreases very gradually from the central value of around 0.16 fm^{-3} . The relativistic functional, on the other hand, predicts a much more localized density, with density peaks as large as 0.20 fm^{-3} . Different localization profiles of equilibrium densities can be traced back to the different energy spacing of the corresponding single-nucleon spectra [EKNV12], that are proportional to the intrinsic deformation and

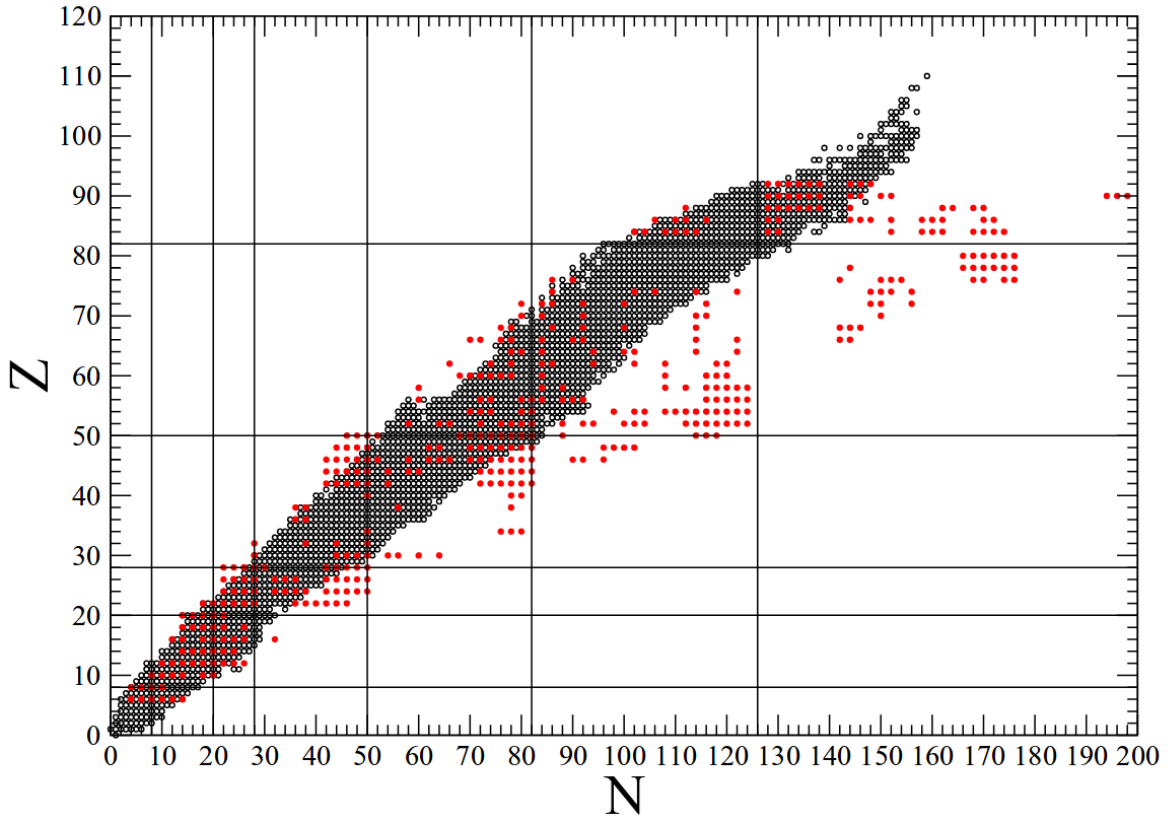


FIGURE 1.4: Microscopic axially symmetric RHB prediction of nuclei that have small radial dispersion of the single-particle states of valence nucleons Δr (red circles), plotted on the background of empirically known nuclides in the $N - Z$ plane. Figure taken from Ref. [EKL18].

to the depth of the underlying single-nucleon potential. Since both functionals predict almost identical equilibrium deformations, differences in densities were linked to differences in the corresponding potentials. As already noted in Ref. [EKNV14b], this situation is rather similar to the one encountered in gaseous systems of ultracold atoms held in three-dimensional optical lattice potentials [GME⁺02]. By gradually increasing the depth of the confining potential, one can observe the transition from a phase in which each atom is spread out over the entire lattice to the insulating phase of localized atoms. Of course, in the self-bound systems like atomic nuclei one cannot simply vary the depth of the single-nucleon potential, but equivalent effect is obtained by performing calculations with different effective interactions. In fact, depth of the DD-ME2 single-neutron (single-proton) potential for ^{20}Ne isotope is -78.6 MeV (-72.8 MeV), and it is pronouncedly deeper than the corresponding depths -69.5 MeV (-64.6 MeV) of the SLy4 functional. Within the relativistic framework, depth of the single-nucleon potential is determined by the two local self-consistent potentials of opposite signs: the attractive scalar potential ($S \approx -400$ MeV) and the repulsive vector potential ($V \approx 320$ MeV). Their sum $V + S$ uniquely determines the confining nuclear potential, while their difference $V - S$ simultaneously governs the splitting between spin-orbit partners in finite nuclei. Consequently, the effective single-nucleon spin-orbit force for finite nuclei manifests itself naturally with the empirical strength within the relativistic framework. On the other hand, the non-relativistic approaches include the spin-orbit potential in a purely phenomenological way,

with the interaction strength that is adjusted to empirical energy spacings between the spin-orbit partners.

The effect of depth of potential on localization of wave functions is schematically depicted in Figure 1.3. In the upper panel, we show three harmonic oscillator potentials with different depths ($V_0 = 30, 45,$ and 60 MeV) but with the same radii $R = 3$ fm. The lower panel shows the radial wavefunctions of the corresponding p -states. It is obvious that a larger depth of the potential leads to a smaller oscillator length and, finally, to a more pronounced localization of the wave function in both the classically allowed and forbidden region. On a more quantitative level, one can introduce the localization parameter α [EKNV13, EKL18]:

$$\alpha_{\text{loc}} \equiv \frac{2\Delta r}{\bar{r}}, \quad (1.48)$$

which corresponds to a ratio between the spatial dispersion of the single-nucleon wave function:

$$\Delta r = \sqrt{\langle r^2 \rangle - \langle r \rangle^2}, \quad (1.49)$$

and the average internucleon distance \bar{r} . For large values of α nucleons are delocalized and nucleus behaves as a quantum liquid. For example, the doubly-magic ^{208}Pb isotope has self-consistent values of localization parameter roughly $\alpha \approx 1.3$, both within the relativistic and non-relativistic framework [EKNV13], and it exhibits a typical quantum-liquid behavior. At the opposite end, when the average internucleon distance exceeds the nucleon spatial dispersion, nucleons localize on nodes of the hypothetical crystal-like structure. The intermediate values of α are marked by a hybrid phase of cluster states which are expected to appear for $\alpha \approx 1$ values. Within the harmonic oscillator approximation, the localization parameter of Eq. (1.50) can be expressed as [EKL18]:

$$\alpha_{\text{HO}} \simeq \frac{\sqrt{\hbar(2n-1)}}{(2mV_0r_0^2)^{1/4}} A^{1/6}, \quad (1.50)$$

where n corresponds to the radial quantum number, V_0 denotes the depth of the potential at $r = 0$, and $r_0 = 1.25$ fm is a constant. This expression nicely elucidates the assertion that the deeper potential favors formation of clusters, as larger V_0 values explicitly yield smaller values of the localization parameter. In addition, dependence of the localization parameter α_{HO} on $A^{1/6}$ shows that cluster states are preferably formed in lighter nuclei, and the transition from coexisting cluster and mean-field states to a Fermi-liquid state should occur for nuclei with $A \approx 20 - 30$ [EKNV13, EKL18], which is in qualitative agreement with the experiment [FHKE+18]. Of course, a more quantitative analysis requires a more microscopic approach. Self-consistent ground-state solutions for a set of self-conjugate nuclei were used to calculate corresponding α values both within the relativistic and non-relativistic framework [EKNV13]. The general conclusion was that the

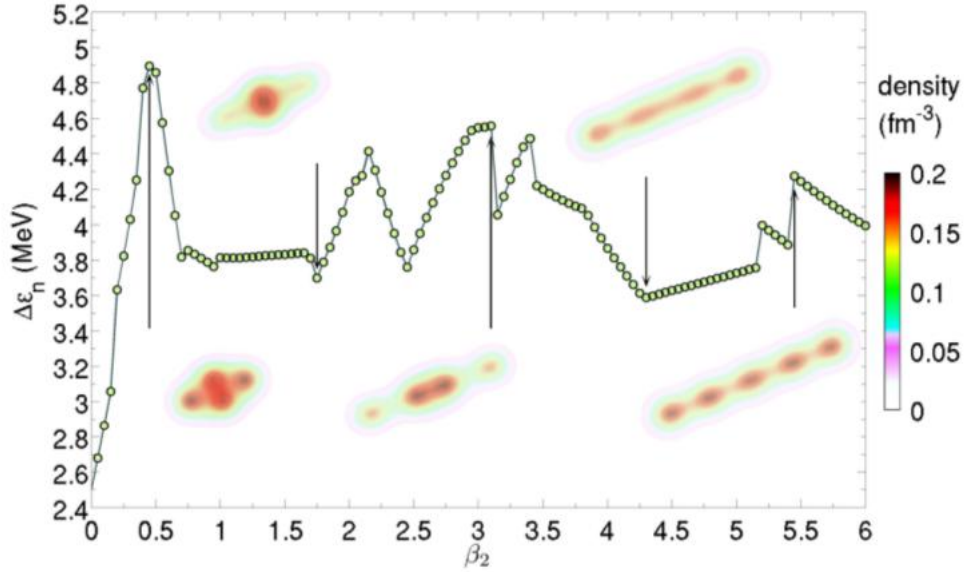


FIGURE 1.5: Mean value of the energy gap between consecutive occupied neutron single-particle levels as a function of axial quadrupole deformation parameter β_2 in ^{20}Ne isotope. The insets display the total nucleonic density at the corresponding deformation. In order to limit the vertical scale, the maximum mean value of the energy gap in the plot does not exceed 5 MeV. Figure taken from Ref. [EKNV14b].

values calculated with DD-ME2 functional are systematically smaller than those obtained using SLy4 functional, thus favoring more pronounced localization of nucleonic densities within the relativistic framework. Very recently, the self-consistent RHB calculations based on the DD-ME2 functional were performed in order to calculate single-nucleon dispersions in axially-symmetric nuclei over the entire nuclide chart [EKL18]. The microscopic values of dispersions Δr have been calculated for all single-particle states. Figure 1.4 shows the chart of nuclides and indicates (in red circles) those nuclei for which both neutron and proton valence states exhibit significantly small dispersions (of the order of 1 fm). In addition to light nuclei, these systematic calculations are able to predict areas of pronounced localization in medium-heavy and heavy nuclei, in agreement with the empirically known α - and cluster-radioactivity.

From a microscopic perspective, small values of dispersions Δr can be understood as reflection of the enhanced isolation or degeneracy of the corresponding single-particle states. As noted in Ref. [AJ94] and further discussed in Ref. [EKNV14b], an isolated level of the single-particle energy spectrum in a deformed self-conjugate nucleus can correspond to an α cluster, due to a simultaneous effect of the time-invariance and isospin symmetries. In such scenarios two protons and two neutrons have very similar wave functions, and localization of these functions facilitates the formation of α clusters [EKNV14b]. This is in agreement with the empirical observation that cluster structures form more easily in lighter nuclei, since heavier nuclei are marked by increasingly more dense single-particle spectra where isolated states are less likely to appear. In order to demonstrate the role of level degeneracy in formation of clusterized structures, in Figure 1.5 we show the mean value of the energy gap between consecutive occupied neutron levels $\Delta\epsilon_n$ as a function of

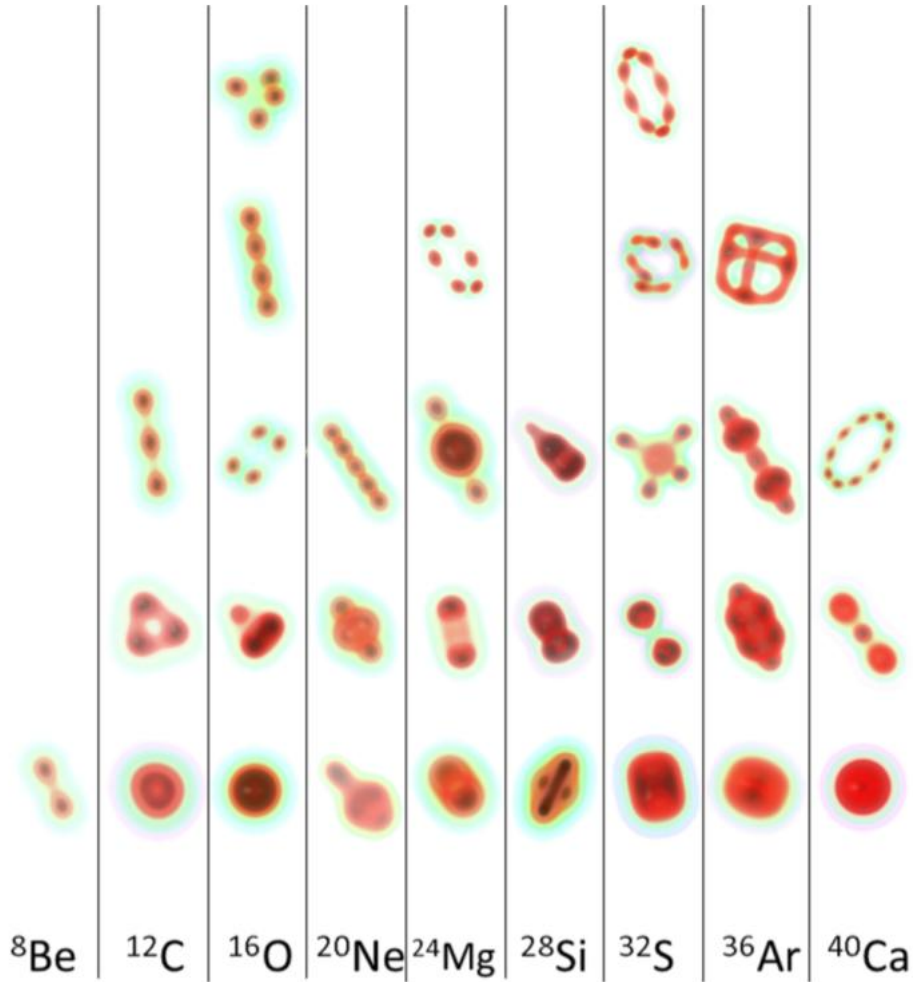


FIGURE 1.6: EDF-based analog of the conventional Ikeda diagram: Positive-parity projected intrinsic densities of various excited configurations in a chosen set of self-conjugate nuclei. For each nucleus the density in the bottom row corresponds to the equilibrium configuration. Other selected densities are displayed in order of increasing excitation energy. Figure taken from Ref. [EKNV14b].

the deformation parameter β_2 in ^{20}Ne isotope. This value is calculated as $\Delta\epsilon_n = \sum_i \Delta\epsilon_i$, where $\Delta\epsilon_i = \epsilon_{i+1} - \epsilon_i$ represents the energy gap between two successive neutron levels. Looking at Fig. 1.5, one can notice a correlation between the increase of energy gaps and formation of clusters in the corresponding intrinsic densities, that are displayed as insets. Even at very large deformations, much more localized linear chain structures are found at β_2 values that correspond to the enhanced energy gaps. In addition, relation between the appearance of clusters in light self-bound systems and the saturation property of internucleon interaction was studied in Ref. [EKNV14a], by inflating the spherical ^{16}O nucleus within the constrained RHB calculation and analyzing the obtained density distributions.

In terms of collective deformations, clusterized structures can appear as local minima on energy hypersurfaces spanned by deformation parameters of different multiplicities (quadrupole, octupole, ...) and different symmetry properties (axial, non-axial,

...). By employing constrained calculations on those hypersurfaces, one can produce the EDF-based analog of conventional Ikeda diagram, which illustrates the coexistence of mean-field and cluster structures that appear close to the corresponding decay threshold [ITH68]. Such calculations were performed in Ref. [EKNV14b] and the resulting diagram is shown in Figure 1.6. In order to generate various cluster structures for a chosen set of self-conjugate nuclei, the RHB calculations based on DD-ME2 functional were allowed to break both the axial and parity symmetry. The obtained positive-parity projected intrinsic densities of different configurations are displayed in Fig. 1.6. The lowest density for each nucleus corresponds to the equilibrium configuration. All of the other densities, save for the ring-like configurations, correspond to local minima on energy hypersurfaces and they appear in the ascending excitation energy order. The lightest isotope, ^8Be , exhibits the 2α structure already in its ground state. The ground state of ^{12}C corresponds to a weakly-oblate density distribution, while triangular arrangements and linear 3α chains appear at higher energies. ^{16}O is shown to display an interesting 4α cluster structure with tetrahedral symmetry in the excited states, and the equilibrium configuration of ^{20}Ne corresponds to the octupole-deformed $^{16}\text{O}+\alpha$ configuration. Nevertheless, a more quantitative description of these states, including the precise excitation energies of each state and transition strengths between them, requires the inclusion of collective correlations related to the restoration of symmetries and configuration mixing. Such extension enables us to answer two crucial questions: (a) can the model reproduce relevant experimental data on studied nuclei, and (b) do the signatures of clusterization survive beyond the simple mean-field picture. How can such an extension be performed - that is the topic of the following chapter.

Restoration of Symmetries and Configuration Mixing

Symmetry, as wide or narrow as you may define its meaning, is one idea by which man through the ages has tried to comprehend and create order, beauty, and perfection.

Hermann Weyl, "Symmetry"

Basic implementation of the nuclear EDF framework is realized in terms of the mean-field approximation. The very notion of mean-field is closely related to the concept of spontaneous breaking of symmetries of nuclear Hamiltonian [DS10, RS80], which enables us to grasp many correlations in a relatively simple manner. However, the resulting many-body state, rather than carrying good quantum numbers, corresponds to a symmetry-broken wave packet of states with good quantum numbers. It is well known that a true spontaneous symmetry breaking can occur only in infinite systems. In finite systems such as atomic nuclei, on the other hand, quantum fluctuations will eventually cause a symmetry-breaking wave packet to relax into one of the eigenstates of nuclear Hamiltonian. Therefore, these wave packets provide us with only an approximate description of nuclear system, and broken symmetries ultimately need to be recovered. Restoration of symmetries is typically carried out by applying techniques rooted in the group theory [Ham62, RS80], and by considering linear combinations of symmetry-breaking states that are rotated in a phase space related to the corresponding symmetry group. In order to account for the magnitude of symmetry breaking as well, a linear combination of different symmetry-restored states is further constructed within the configuration mixing scheme. This step is formally equivalent to the generator coordinate method (GCM) by Hill, Wheeler, and Griffin [HW53, GW57], with multipole deformation moments, pairing degree of freedom, or radii typically playing the role of collective coordinates. These two steps combined comprise the multi-reference EDF (MR-EDF) framework.

Collective MR-EDF models, based on both the non-relativistic and relativistic effective interactions, currently represent state-of-the-art tool for nuclear structure studies (for detailed discussions see reviews in Refs. [BHR03, NVR11, Egi16, RRR18] and references cited therein). Virtually all modern MR-EDFs include the axially symmetric quadrupole deformation as a generating coordinate within the configuration mixing scheme [BFH03, RGER03, NVR06b]. Motivation for this is rather obvious: spherical shapes can account for only a small number of nuclides at magic nucleon numbers, while all the other areas of nuclide chart can only be accessed by allowing for the rotational symmetry to be broken. Simultaneous breaking of rotational and axial symmetry additionally extends the reach of a collective model, and within the past decade MR-EDF calculations based on axial and triaxial quadrupole-deformed shapes have been successfully performed [BH08, RE10]. More recently, studies that use axially symmetric quadrupole and octupole deformations as generating coordinates have been reported as well [BRR16, ZYL⁺16]. On the other hand, configuration-mixing symmetry-restoring calculations that would allow for simultaneous breaking of rotational, axial, and parity symmetry are yet to be performed. Besides breaking and restoring of spatial symmetries, another relevant degree of freedom is provided by pairing correlations, that induce the violation of particle number invariance in nuclear systems. The vast majority of present MR-EDF models takes into account only phase fluctuations of pairing correlations through the restoration of good particle number, while fluctuations in the corresponding magnitude are typically neglected. Nonetheless, these fluctuations can also be accounted for by using the particle number dispersion as a collective degree of freedom in the configuration mixing scheme [VER13, ZLN⁺16]. Finally, very recent extension of the MR-EDF framework included, in addition to the axial and triaxial quadrupole deformations, the cranking frequency as a collective coordinate [EBR16]. Such extension is proposed to cure the well-known deficiency of overly stretched collective spectra that is a byproduct of the standard procedure of rotational symmetry restoration. Overall, the choice of appropriate generating coordinates in configuration mixing calculations is primarily determined by properties of the nucleus under consideration. However, the required computational time grows rapidly with increasing the number of generating coordinates. This fact has so far limited practical implementations of the MR-EDF framework to only two (in majority of cases) or at most three (exceptionally) generating coordinates at a time. In addition to studies of even-even nuclei that are routinely performed, the MR-EDF framework was recently extended to account for odd nuclear systems as well [BABH14, BE16].

In this chapter, we will introduce the MR-EDF framework based on restoration of symmetries of RHB states and the subsequent configuration mixing. In Section 2.1, we will start with some general remarks on breaking and restoring of symmetries in nuclear systems and the underlying formalism rooted in group theory. Rotational symmetry, particle number symmetry, and parity symmetry that are particularly relevant for this work will be discussed in some more detail. Section 2.2 first summarizes basic principles of the configuration mixing scheme based on Hill-Wheeler-Griffin's framework and then proceeds to discuss the specific realization of the framework in terms of mixing of symmetry-restored RHB configurations. Method for deriving and solving the HWG equation, evaluation of corresponding norm overlap and Hamiltonian kernels, as well as the calculation of various observables that can be compared to experiment will all be addressed.

2.1. Restoration of Broken Symmetries

2.1.1 Breaking and Restoring Symmetries

Symmetries are fundamental features of physical systems, classical and quantum ones alike. From the Noether's theorem to the famous Higgs mechanism, they determine properties of the system and manifest themselves in the underlying equations of motion. In simple terms, symmetry is just a name for the operation which leaves the physical system invariant, that is, which transforms it into a state that is completely indistinguishable from the original one. For example, the ground state of an even-even nucleus in its laboratory frame is invariant under spatial rotations: whatever¹ one does with this tiny ball of quantum liquid it will remain exactly the same. Formally, each symmetry is associated with the corresponding operator \hat{X} . System is said to be symmetric under transformation induced by \hat{X} if \hat{X} commutes with Hamiltonian of the system, that is, $[\hat{X}, H] = 0$. For nuclear systems, set of operators $\{\hat{X}\}$ corresponds to the translational, rotational, particle number, parity, parity number, and time-reversal symmetries that are exactly preserved by the nuclear interaction. In addition, isospin invariance is an approximate symmetry in atomic nuclei, since a weak symmetry breaking is induced by the electromagnetic interaction between protons. The true wave function of the system should correspond to the eigenstate of operators $\{\hat{X}\}$ and, consequently, carry good quantum numbers related to each of those symmetries (good linear and angular momenta, number of particles, ...). However, imposing such severe restrictions on our trial wave functions within the variational procedure of SR-EDF would seriously limit the available variational space. For example, if we require our trial wave function of Slater or Bogoliubov type to obey the translational symmetry, the only possible solution would be a pure plane wave function. Not much in nuclear physics can be described with plane waves. Therefore, an alternative approach is usually adopted, where a system is allowed to deform and break symmetries of nuclear Hamiltonian. The breaking of each symmetry is guided by the corresponding order parameter, $\mathbf{g} = |\mathbf{g}|e^{i\varphi_g}$, where $|\mathbf{g}|$ and φ_g denote the magnitude and phase of the order parameter, respectively. The concept of spontaneous symmetry breaking is schematically depicted in Figure 2.1, where we show the energy of the system as a function of magnitude $|\mathbf{g}|$ and phase φ_g of the order parameter. For $|\mathbf{g}| = 0$, a symmetry-conserving state is obtained. By allowing for fluctuations in magnitude of the order parameter, an absolute minimum can be found at configuration $|\mathbf{g}_{\min}| \neq 0$ which does not anymore possess good symmetry of nuclear Hamiltonian. Additionally, the energy of this symmetry-broken state is independent of the phase of the order parameter φ_g . Restoration of symmetries explores the *Mexican hat* potential in the azimuthal direction, by combining states with different phases of the order parameter. This accounts to transition from the *intrinsic* frame of reference, characterized by a deformed nucleus that is not under influence of any restoring force such as rotation, to the *laboratory* frame of reference, where numerous observables of symmetry-conserving state can be calculated.

¹Unless, I guess, you try smashing it against the wall. However, I advise you strongly against doing this and, even if you did it, no one would know how to write down the corresponding operator anyway.

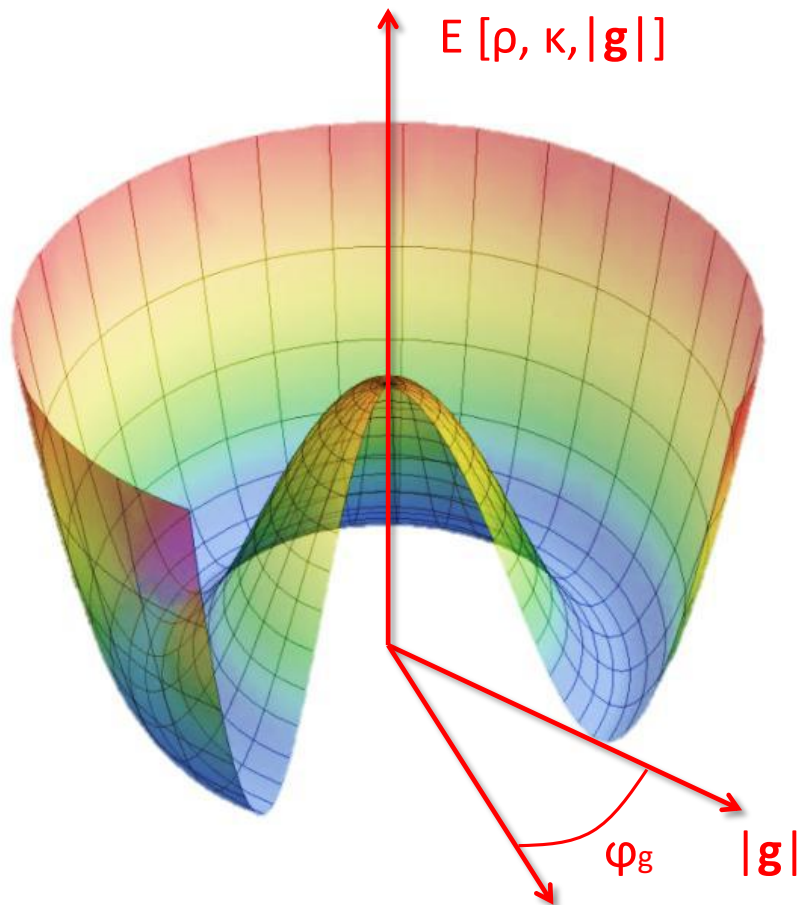


FIGURE 2.1: Schematic representation of the spontaneous symmetry breaking. Energy of the system is shown as a function of magnitude $|\mathbf{g}|$ and phase φ_g of the order parameter \mathbf{g} . See text for discussion.

Configuration mixing, on the other hand, explores the *Mexican hat* potential in the radial direction, by further mixing symmetry-restored states with different magnitudes of the order parameter. Both of these steps introduce additional correlations to the system and, finally, yield a collective symmetry-conserving state which is more strongly bound than a symmetry-broken state we started with in a first place.

Restoration of broken symmetries is based on the underlying group structure of symmetry transformations [Ham62, RS80, Dug14]. Here, we will briefly overview only basic terminology of the group theory formalism that is relevant for the present study. More details on group theory and its applications to physical problems can be found, for example, in a book *Group Theory and its applications to Physical problems* by M. Hamermesh [Ham62]. In addition, a more general discussion on the group theory aspects of MR-EDF calculations can be found in Chapter III of a doctoral thesis by B. Bally [Bal14]. For the purpose of this study, let us consider a continuous and compact Lie group of symmetries

TABLE 2.1: Basic properties of nuclear symmetries that are broken and restored within our calculation: rotational invariance, particle number invariance, and parity invariance. We list the underlying groups, corresponding quantum numbers, parameters of groups, operators that generate transformation, irreducible transformations, as well as their respective dimensions. See text for more details.

| | | | |
|------------------------------|--|---|---|
| symmetry | rotational | particle number | parity |
| broken by | deformation (any multipole) | pairing or finite temperature | deformation (odd multipoles) |
| group \mathcal{G} | $SO(3)$ | $U(1)$ | $I_\pi \equiv \{\hat{\mathbb{I}}, \hat{\mathbb{I}}\}$ |
| quantum number | angular momentum J | particle numbers N and Z | parity π |
| parameters g | α, β, γ | φ_N, φ_Z | - |
| operators \hat{U} | $e^{-i\alpha\hat{J}_z} e^{-i\beta\hat{J}_y} e^{-i\gamma\hat{J}_z}$ | $e^{i\varphi_N\hat{N}} e^{i\varphi_Z\hat{Z}}$ | $\{\hat{\mathbb{I}}, \hat{\mathbb{I}}\}$ |
| irreps $S_{ab}^\lambda(g)$ | $D_{MK}^J(\alpha, \beta, \gamma), J \in \mathbb{N}$ | $e^{i\varphi_{N,Z}m}, m \in \mathbb{Z}$ | $D^p(I), p \in \{-1, 1\}$ |
| irreps dimension d_λ | $2J + 1$ | 1 | 1 |

$\mathcal{G} = \{R(g)\}$. Elements of the symmetry group $R(g)$ commute with the nuclear Hamiltonian, $[R(g), H] = 0$, and they are parameterized by a set of real parameters $\{g\}$ defined over domain $D_{\mathcal{G}}$. Generators of symmetry transformations \hat{U} are unitary operators acting on the Hilbert space that can be built as the exponential maps of the symmetry group elements. Furthermore, one introduces the irreducible representations (irreps) of the symmetry group, $S_{ab}^\lambda(g)$. They are unitary and orthogonal, have dimension d_λ , and are labeled by eigenvalues λ of the corresponding Casimir operator. This enables us to decompose any function $f(g)$ defined over $D_{\mathcal{G}}$ in terms of the irreps of the corresponding group:

$$f(g) = \sum_{\lambda ab} f_{ab}^\lambda S_{ab}^\lambda(g), \quad (2.1)$$

with $\{f_{ab}^\lambda\}$ as expansion coefficients, and $a, b \in \{1, \dots, d_\lambda\}$. Projectors onto good quantum numbers, that are to be applied on symmetry-broken states, can be built by taking linear combination of generating operators \hat{U} multiplied by the corresponding irreps $S_{ab}^\lambda(g)$ and with the appropriate integration (de Haar) measure. In Table 2.1 we summarize basic properties of nuclear symmetries that are broken and restored within our calculation: rotational invariance, particle number invariance, and parity invariance. In the following subsections we will analyze each of them separately.

2.1.2 Rotational Symmetry

Among nuclear symmetries that are broken on a SR-EDF level, rotational symmetry is arguably the most relevant one. Spontaneous breaking of rotational symmetry appears in all nuclei where neither neutron or proton number is magical, and it has as a consequence the undesired property that the obtained state does not carry good quantum number of total angular momentum J . This is at odds with the empirical fact that the energy of an isolated (rotationally invariant) nucleus does not change under rotations. The underlying group $SO(3)$ (or, more broadly, $SU(2)$) is continuous and Lie group of symmetries, with three spatial Euler angles $\Omega \equiv (\alpha, \beta, \gamma)$ playing the role of group parameters. Operator that projects the intrinsic state on a state with good values of angular momentum (AM) reads:

$$\hat{P}_{MK}^J = \frac{2J+1}{16\pi^2} \int_0^{2\pi} d\alpha \int_0^\pi d\beta \sin\beta \int_0^{4\pi} d\gamma D_{MK}^{J*}(\alpha, \beta, \gamma) \hat{R}(\alpha, \beta, \gamma), \quad (2.2)$$

where $D_{MK}^J(\alpha, \beta, \gamma)$ denotes Wigner D -matrix [VMK88], and the rotation operator reads:

$$\hat{R}(\alpha, \beta, \gamma) = e^{-i\alpha\hat{J}_z} e^{-i\beta\hat{J}_y} e^{-i\gamma\hat{J}_z}. \quad (2.3)$$

Wigner D -matrix, an irrep of the $SO(3)$ symmetry group, corresponds to matrix elements of the rotation operator:

$$D_{MK}^J(\alpha, \beta, \gamma) = \langle JM | \hat{R}(\alpha, \beta, \gamma) | JK \rangle \quad (2.4)$$

where $|JM\rangle$ denotes a many-body state that is an eigenstate of the total angular momentum operator squared, \hat{J}^2 , and the z -component of total angular momentum operator, \hat{J}_z , simultaneously. The projection operator can then be decomposed in terms of these symmetry-conserving states:

$$\hat{P}_{MK}^J = \sum_{\alpha} |JM\alpha\rangle \langle JM\alpha|, \quad (2.5)$$

where index α ² additionally encapsulates all of the remaining quantum numbers that are necessary to unambiguously define a state. In addition, projection operator satisfies the following relations:

$$\begin{aligned} \hat{P}_{MK}^J \hat{P}_{M'K'}^{J'} &= \delta_{JJ'} \delta_{M'K} \hat{P}_{MK'}^J, \\ (\hat{P}_{MK}^J)^\dagger &= \hat{P}_{KM}^J. \end{aligned} \quad (2.6)$$

²A few rows above α represented the Euler angle, which may cause some confusion. However, as it will become apparent a few rows below, axial symmetry excludes angles α and γ from the further analysis. Therefore, we reclaim these handy Greek letters to denote other quantities further on in the manuscript.

As can be seen from Eq. (2.2), restoration of a good angular momentum for the most general RHB state $|\Phi(q_i)\rangle$ requires carrying out integrals over three Euler angles. From a computational perspective, this is a rather time-consuming task. However, by assuming axial symmetry of the RHB state:

$$\hat{J}_z |\Phi(q_i)\rangle = 0 \quad \rightarrow \quad e^{i\chi\hat{J}_z} |\Phi(q_i)\rangle = |\Phi(q_i)\rangle, \quad \forall \chi \in \mathbb{R}, \quad (2.7)$$

this task can be simplified considerably, since in that case integrals over Euler angles α and γ can be carried out analytically. Furthermore, the following relation:

$$e^{-i\beta\hat{J}_y} = e^{i\frac{\pi}{2}\hat{J}_z} e^{-i\beta\hat{J}_x} e^{-i\frac{\pi}{2}\hat{J}_z}, \quad (2.8)$$

combined with the axial symmetry property of the RHB state (2.7), can be used to finally write down the rotation operator as:

$$\hat{R}(\beta) = e^{-i\beta\hat{J}_x}, \quad (2.9)$$

which will help us to exploit the self-consistent simplex-x symmetry of intrinsic states and the consequent block structure of the corresponding U and V matrices. More details on eigenstates of the simplex-x operator and the expansion of RHB states in the corresponding basis are given in Appendix A. In practical implementations, we will need to evaluate matrix elements $R_{\alpha\gamma}(\beta)$ of rotation operator in the single-particle basis $\{c_\alpha^\dagger, c_\alpha\}$:

$$\hat{R}(\beta) = \sum_{\alpha\gamma} R_{\alpha\gamma}(\beta) c_\alpha^\dagger c_\gamma, \quad (2.10)$$

where α and γ denote indices of the single-particle basis. Details on calculation of matrix elements $R_{\alpha\gamma}(\beta)$ in the simplex-x basis are also given in Appendix A.

2.1.3 Particle Number Symmetry

Particle number symmetry is broken in all but doubly magic nuclei. As a consequence of introducing pairing correlations to the system through the Bogoliubov transformation, the RHB states are not eigenstates of proton and neutron number operators. Since an isolated atomic nucleus has a well-defined (integer) number of nucleons, the particle number symmetry obviously needs to be restored. The underlying group of symmetries, $U(1)$, is compact, Abelian, and unitary group of degree 1, with gauge angle $\varphi \in [0, 2\pi]$ playing the role of a group parameter. Operators that project the intrinsic state on a state with a good particle number (PN) read:

$$\hat{P}^N = \frac{1}{2\pi} \int_0^{2\pi} d\varphi_N e^{i(\hat{N}-N_0)\varphi_N}, \quad \hat{P}^Z = \frac{1}{2\pi} \int_0^{2\pi} d\varphi_Z e^{i(\hat{Z}-Z_0)\varphi_Z}, \quad (2.11)$$

where N_0 (Z_0) is the desired number of neutrons (protons), while \hat{N} (\hat{Z}) represents the neutron (proton) number operator:

$$\hat{N} = \sum_{\alpha} \hat{c}_{N,\alpha}^{\dagger} \hat{c}_{N,\alpha}, \quad \hat{Z} = \sum_{\alpha} \hat{c}_{Z,\alpha}^{\dagger} \hat{c}_{Z,\alpha}. \quad (2.12)$$

Here, sets of operators $\{\hat{c}_{N,\alpha}^{\dagger}, \hat{c}_{N,\alpha}\}$ ($\{\hat{c}_{Z,\alpha}^{\dagger}, \hat{c}_{Z,\alpha}\}$) correspond to the single-neutron (single-proton) creation and annihilation operators. The irreducible representation of $U(1)$ symmetry group in each isospin channel is one-dimensional, and it corresponds to a matrix element of the operator that rotates the intrinsic state in a gauge space:

$$e^{i\varphi_N N_0} = \langle N_0 | e^{i\varphi_N \hat{N}} | N_0 \rangle, \quad e^{i\varphi_Z Z_0} = \langle Z_0 | e^{i\varphi_Z \hat{Z}} | Z_0 \rangle, \quad (2.13)$$

where $|N_0\rangle$ and $|Z_0\rangle$ denote a many-body state that is an eigenstate of the neutron number and proton number operator, respectively. Projection operators can be decomposed in terms of these states:

$$\hat{P}^N = \sum_{\alpha} |N_0\alpha\rangle \langle N_0\alpha|, \quad \hat{P}^Z = \sum_{\alpha} |Z_0\alpha\rangle \langle Z_0\alpha| \quad (2.14)$$

where index α again encapsulates all of the remaining quantum numbers that are necessary to unambiguously define a state. Furthermore, projection operators satisfy the standard relations:

$$(\hat{P}^{N,Z})^{\dagger} = P^{N,Z}, \quad (P^{N,Z})^2 = P^{N,Z}. \quad (2.15)$$

In practical implementations, integration interval of projection operators (2.11) can be reduced to $[0, \pi]$ using the property of good number parity of the intrinsic state. The resulting integral is further discretized using the Fomenko expansion [Fom70]:

$$\hat{P}^{N_{\tau}} = \frac{1}{N_{\varphi}} \sum_{l=1}^{N_{\varphi}} e^{i\varphi_l(\hat{N}_{\tau}-N_{\tau 0})}, \quad \varphi_l = \frac{\pi}{N_{\varphi}} l, \quad N_{\tau} = N, Z. \quad (2.16)$$

We note that in the present work we employ the projection after variation (PAV) version of symmetry restoration, both for the angular momentum projection (AMP) and for the particle number projection (PNP). Within the PAV framework, the RHB energy is first minimized and the resulting wave function is subsequently projected on good quantum numbers. This approach is different from the variation after projection (VAP) technique,

where one directly minimizes the projected energy in each variational step. Due to a huge computational cost of AM-VAP calculations, the AM-PAV has been a conventional choice in virtually all MR-EDF calculations. The price to pay is the fact that such variational procedure favors $J = 0$ state, while higher angular momenta are increasingly less favored, which stretches the obtained spectra. This anomaly can be accounted for through the inclusion of cranking frequency as a generating coordinate in the configuration mixing calculations [EBR16]. On the other hand, PN-VAP calculations are computationally less demanding than AMP-VAP calculations, and they have been repeatedly performed within the non-relativistic framework [AER01, SDK⁺07]. The simpler PN-PAV framework arguably grasps less pairing correlations and provides inferior description in the weak pairing regime, but it still represents significantly more economical approach from the computational perspective and it will therefore be employed throughout this study.

2.1.4 Parity Symmetry

Breaking of parity symmetry is related to the non-vanishing value of the lowest odd-multipolarity electric moment, that is, the electric octupole moment. Microscopically, octupole collectivity is driven by the existence of pairs of opposite-parity single-particle orbitals near Fermi surface with angular momenta $\Delta l = 3$ that are strongly coupled through octupole interaction [BN96]. Even though signatures of octupole collectivity and the corresponding excitations can be detected and studied over the entire nuclide chart [RB11], strong experimental traces of octupole collectivity have only recently been observed in ^{224}Ra [G⁺13] and ^{144}Ba [B⁺16] isotopes. Among lighter nuclei, the expected α -clustering in parity-doublets of ^{20}Ne [RB11, EKNV14b] makes breaking of parity invariance the necessary ingredient of any theoretical model that aims to comprehensively describe this isotope. From the group theory perspective, the underlying group of symmetries is finite and Abelian, comprising of only two elements: the identity operator $\hat{\mathbb{1}}$ and the parity operator $\hat{\Pi}$. This makes the parity projection by far the easiest one to perform. The operator that projects the intrinsic state on a state with good parity reads:

$$\hat{P}_\pi = \frac{1}{2}(\hat{\mathbb{1}} + \pi\hat{\Pi}), \quad (2.17)$$

where the quantum number of parity can take only two values, $\pi = \pm 1$. In practical implementations, restoration of good parity quantum number of the RHB state $|\Phi(q)\rangle$, $\{q\} = \{\beta_2, \beta_3\}$, can be performed following two different prescriptions. The first option is to calculate the operator (2.17) in a single-particle basis of choice (typically the harmonic oscillator basis) and directly apply it on a symmetry-broken state $|\Phi(\beta_2, \beta_3)\rangle$. That way, one avoids having to carry out separate minimization procedure for RHB states with negative values of octupole deformation parameter, $|\Phi(\beta_2, -|\beta_3|)\rangle$. The alternative option is to calculate RHB states with both positive and negative β_3 values, and then use the virtue of configuration mixing in order to restore good parity of collective states without ever explicitly applying the projection operator. The equivalence of the two approaches

can be demonstrated rather easily. First, we take into account that the parity operator $\hat{\Pi}$ flips the sign of β_3 value of the RHB state:

$$\hat{\Pi} |\Phi(\beta_2, \beta_3)\rangle = |\Phi(\beta_2, -\beta_3)\rangle. \quad (2.18)$$

Then by simply applying the projection operator (2.17) on the RHB state with a positive β_3 value:

$$|\Psi^\pi\rangle = \hat{P}_\pi |\Phi(\beta_2, |\beta_3|)\rangle = \frac{1}{2} (|\Phi(\beta_2, |\beta_3|)\rangle + \pi |\Phi(\beta_2, -|\beta_3|)\rangle), \quad (2.19)$$

one obtains the parity-conserving state, with either positive ($\pi = +1$) or negative ($\pi = -1$) parity. The state $|\Psi^\pi\rangle$ obviously corresponds to a linear combination of two RHB states with positive and negative β_3 values, which proves the asserted equivalence. In this work, we will adopt the latter prescription and restore the parity symmetry by using the reflection-symmetric basis, that is, by ensuring that for each $|\Phi(\beta_2, |\beta_3|)\rangle$ state the basis always contains the corresponding $|\Phi(\beta_2, -|\beta_3|)\rangle$ state as well.

2.1.5 Translational Symmetry

Finally, localization of nuclear mean-field causes breaking of the translational invariance in all atomic nuclei. However, the exact projection on good values of linear momentum is notoriously numerically expensive [MFH84], particularly when combined with restorations of other symmetries such as the rotational symmetry. Consequently, restoration of translational symmetry is usually accounted for in an approximate manner. One of the most common center-of-mass corrections corresponds to adding the expectation value:

$$E_{\text{c.m.}} = -\frac{\langle \hat{\mathbf{P}}_{\text{c.m.}}^2 \rangle}{2mA} \quad (2.20)$$

to the total energy, where $\hat{\mathbf{P}}_{\text{c.m.}}$ is the total momentum of a nucleus with A nucleons. Validity of this approximation increases with the increase of nucleon number A , and it finally vanishes for infinite nuclear systems. The expression (2.20) can be further simplified by evaluating it analytically within the harmonic oscillator approximation [BRRM00]:

$$E_{\text{c.m.}}^{\text{HO}} = -\frac{3}{4} 41A^{-1/3} \text{ MeV}. \quad (2.21)$$

The correction of Eq. (2.21) will be used in the present study. This expression is constant for each nucleus, that is, it does not depend on the many-body wave function. Therefore, it will not affect the variational equations and it can be added *a posteriori* to the energy of the symmetry-restored collective state. More details on the restoration of translational symmetry can be found in Refs. [BRRM00, BHR03] and references cited therein.

2.2. Configuration Mixing Scheme

2.2.1 Basic Principles of the Hill-Wheeler-Griffin's Method

The generator coordinate method (GCM) theory by Hill, Wheeler, and Griffin [HW53, GW57] is one of the most widely used methods for describing large amplitude collective motion of fermionic systems [RS80]. It is a variational method within which a collective state of quantum system is constructed as a linear combination of many different product wave functions. In particular, the GCM ansatz for a collective state of quantum system reads [RS80, Won70, Lat74]:

$$|\Psi_\alpha\rangle = \int d\theta f_\alpha(\theta) |\Phi(\theta)\rangle, \quad (2.22)$$

where $|\Phi(\theta)\rangle$ denotes generating intrinsic functions, conveniently chosen for a problem under consideration, while $f_\alpha(\theta)$ are weight functions yet to be determined through the variational procedure. Both generating functions and weight functions depend on $\{\theta\}$, a set of parameters called generating coordinates. Generating coordinates can in principle be complex [Lat74] and, therefore, integral in (2.22) should run over all corresponding real and imaginary parts. Finally, label α encapsulates all the relevant quantum numbers of a collective state. Energy of the collective state (2.22), whose dynamics is governed by a Hamiltonian operator \hat{H} , is a functional of weight functions:

$$E_\alpha[f_\alpha] = \frac{\int d\theta \int d\theta' f_\alpha^*(\theta) \mathcal{H}(\theta, \theta') f_\alpha(\theta')}{\int d\theta \int d\theta' f_\alpha^*(\theta) \mathcal{N}(\theta, \theta') f_\alpha(\theta')}, \quad (2.23)$$

where two Hermitian objects have been introduced, namely the Hamiltonian kernel:

$$\mathcal{H}(\theta, \theta') = \langle \Phi(\theta) | \hat{H} | \Phi(\theta') \rangle, \quad (2.24)$$

and the norm overlap kernel:

$$\mathcal{N}(\theta, \theta') = \langle \Phi(\theta) | \Phi(\theta') \rangle. \quad (2.25)$$

Weight functions $f_\alpha(\theta)$ can be determined by applying the variational principle onto the energy functional (2.23) of a collective state:

$$\frac{\delta}{\delta f_\alpha^*(\theta)} E_\alpha[f_\alpha] = 0. \quad (2.26)$$

The corresponding domain of variation is usually kept rather flexible, with the sole requirement being that - whatever weight functions turn out to be - they ultimately yield normalizable collective states (2.22). Variational principle leads to the Hill-Wheeler-Griffin (HWG) equation:

$$\int d\theta' \left[\mathcal{H}(\theta, \theta') - E_\alpha \mathcal{N}(\theta, \theta') \right] f_\alpha(\theta') = 0. \quad (2.27)$$

Formally, the HWG equation has a form of Fredholm integral equation of the first kind and, together with the collective state normalizability condition, it represents a generalized eigenvalue problem. Solving the HWG equation provides one with the excited energies E_α of a quantum system, as well as with the corresponding weight functions $f_\alpha(\theta)$ that can be used to calculate various observables. Literature on general aspects of GCM framework is rather abundant [RS80, Won70, Lat74, Lat76]. In the following subsections, however, we will focus on basic constituents of the particular realization of the framework that is used in the present study.

2.2.2 Mixing of Symmetry-Restored Configurations

Within our study, a set of generating functions $\{|\Phi(\theta)\rangle\}$ is given by a set of product states that are obtained by solving the RHB equations and additionally projected onto good values of angular momenta, particle numbers, and parity. Furthermore, generating coordinates $\{\theta\}$ correspond to the axially symmetric quadrupole (β_2) and octupole (β_3) deformation parameters, and will be denoted as $q_i \equiv (\beta_{2i}, \beta_{3i})$ further on. The collective symmetry-conserving state can therefore be written as:

$$|\Psi_\alpha^{JM;NZ;\pi}\rangle = \sum_{i \geq 0} \sum_K f_\alpha^{JK;NZ;\pi}(q_i) \hat{P}_{MK}^J \hat{P}^N \hat{P}^Z \hat{P}^\pi |\Phi(q_i)\rangle, \quad (2.28)$$

where a sum in index i runs over a set of RHB states with non-negative values of β_3 parameter. Operator that projects on good values of angular momentum \hat{P}_{MK}^J is defined in Eq. (2.2). As already discussed in Section 2.1.2, the axial symmetry of RHB states (2.7) enables us to perform integrals over two out of three Euler angles analytically. This reduces the computational cost significantly but, in turn, restricts the angular momentum projection to $K = 0$ components only. Furthermore, operators that project on good values of particle numbers \hat{P}^N and \hat{P}^Z are defined in Eq. (2.11). In practical implementations, they are substituted by the corresponding Fomenko expansions of Eq. (2.16). Finally, technique of projecting on good values of parity has been discussed in Section 2.1.4. Since the good parity of collective states is recovered by ensuring that the RHB basis is reflection-symmetric, the corresponding operator \hat{P}^π will not be explicitly written further on. Rather than that, we extend the sum over index i of Eq. (2.28) by additionally including states with negative values of β_3 parameter, and let the described virtue of

reflection-symmetric RHB basis do the projecting job for us. The discretized version of HWG equation within the MR-EDF framework reads:

$$\sum_j \left[\mathcal{H}^{J;NZ;\pi}(q_i, q_j) - E_\alpha^{J;NZ;\pi} \mathcal{N}^{J;NZ;\pi}(q_i, q_j) \right] f_\alpha^{J;NZ;\pi}(q_j) = 0. \quad (2.29)$$

Here, the Hamiltonian kernel $\mathcal{H}^{J;NZ;\pi}(q_i, q_j)$ and the norm overlap kernel $\mathcal{N}^{J;NZ;\pi}(q_i, q_j)$ are defined as:

$$\begin{aligned} \mathcal{O}^{J;NZ;\pi}(q_i, q_j) &= \frac{2J+1}{2} \delta_{M0} \delta_{K0} \int_0^\pi d\beta \sin \beta d_{00}^{J*}(\beta) \frac{1}{N_\varphi^2} \sum_{l_N=1}^{N_\varphi} \sum_{l_Z=1}^{N_\varphi} e^{-i\varphi_{l_N} N_0} e^{-i\varphi_{l_Z} Z_0} \\ &\times \langle \Phi(q_i) | \hat{O} e^{-i\beta \hat{J}_x} e^{i\varphi_{l_N} \hat{N}} e^{i\varphi_{l_Z} \hat{Z}} | \Phi(q_j) \rangle, \end{aligned} \quad (2.30)$$

where $d_{00}^{J*}(\beta)$ denotes Wigner- d matrix [VMK88], and operator \hat{O} corresponds to the identity operator and to the Hamiltonian operator for the norm overlap kernel and the Hamiltonian kernel, respectively. Details on calculation of these kernels will be discussed in Section 2.2.4.

The HWG equation in a form of Eq. (2.29) represents a generalized eigenvalue problem. Consequently, the weight functions $f_\alpha^{J;NZ;\pi}(q_i)$ do not form an orthogonal set and cannot be interpreted as collective wave functions for variable q_i . Therefore, the first step in solving the HWG equation is introducing an another set of functions:

$$g_\alpha^{J;NZ;\pi}(q_i) = \sum_j (\mathcal{N}^{J;NZ;\pi})^{1/2}(q_i, q_j) f_\alpha^{J;NZ;\pi}(q_j), \quad (2.31)$$

that are indeed orthogonal and play the role of collective wave functions. After exchanging weight functions for the collective wave functions, the HWG equation assumes a form of the ordinary eigenvalue problem:

$$\sum_j \tilde{\mathcal{H}}^{J;NZ;\pi}(q_i, q_j) g_\alpha^{J;NZ;\pi}(q_j) = E_\alpha^{J;NZ;\pi} g_\alpha^{J;NZ;\pi}(q_i), \quad (2.32)$$

with the modified Hamiltonian kernel:

$$\tilde{\mathcal{H}}^{J;NZ;\pi}(q_i, q_j) = \sum_{k,l} (\mathcal{N}^{J;NZ;\pi})^{-1/2}(q_i, q_k) \mathcal{H}^{J;NZ;\pi}(q_k, q_l) (\mathcal{N}^{J;NZ;\pi})^{-1/2}(q_l, q_j). \quad (2.33)$$

The eigenvalue problem for the norm overlap kernel reads:

$$\sum_j \mathcal{N}^{J;NZ;\pi}(q_i, q_j) u_k^{J;NZ;\pi}(q_j) = n_k^{J;NZ;\pi} u_k^{J;NZ;\pi}(q_i), \quad (2.34)$$

where $u_k^{J;NZ;\pi}(q_i)$ and $n_k^{J;NZ;\pi}$ are the corresponding eigenvectors and eigenvalues, respectively. Inversion of the norm overlap kernel in Eq. (2.33) is formally possible only if the kernel matrix does not have any zero eigenvalues. In practical implementations, one encounters norm eigenvectors with very small eigenvalues, that are a direct consequence of the fact that the original set of generating functions is not linearly independent. These states need to be removed from the basis, while the remaining states are used to build the collective Hamiltonian:

$$\mathcal{H}_{kl,c}^{J;NZ;\pi} = \frac{1}{\sqrt{n_k^{J;NZ;\pi}}} \frac{1}{\sqrt{n_l^{J;NZ;\pi}}} \sum_{i,j} u_k^{J;NZ;\pi}(q_i) \tilde{\mathcal{H}}^{J;NZ;\pi}(q_i, q_j) u_l^{J;NZ;\pi}(q_j), \quad (2.35)$$

which can be easily diagonalized using the standard diagonalization techniques:

$$\sum_l \mathcal{H}_{kl,c}^{J;NZ;\pi} g_{l,\alpha}^{J;NZ;\pi} = E_\alpha^{J;NZ;\pi} g_{k,\alpha}^{J;NZ;\pi}. \quad (2.36)$$

Diagonalization takes place in the collective space spanned by the natural basis states:

$$|k\rangle = \frac{1}{\sqrt{n_k^{J;NZ;\pi}}} \sum_i u_k^{J;NZ;\pi}(q_i) \hat{P}_{00}^J \hat{P}^N \hat{P}^Z |\Phi(q_i)\rangle, \quad (2.37)$$

whose dimension is equal to or smaller than the dimension of the original HWG problem. Solving the Eq. (2.36) for each value of angular momentum J and parity π separately³ determines both the energy of the ground state and energies of the excited states. We note that only states with natural spin-parity, that is, states which satisfy the rule $(-1)^J = \pi$ are accessible with the present model. The collective wave functions $g_\alpha^{J;NZ;\pi}(q_i)$ and the weight functions $f_\alpha^{J;NZ;\pi}(q_i)$ are finally calculated from the eigenfunctions of the norm overlap as:

$$g_\alpha^{J;NZ;\pi}(q_i) = \sum_k g_{k,\alpha}^{J;NZ;\pi} u_k^{J;NZ;\pi}(q_i), \quad (2.38)$$

$$f_\alpha^{J;NZ;\pi}(q_i) = \sum_k \frac{g_{k,\alpha}^{J;NZ;\pi}}{\sqrt{n_k^{J;NZ;\pi}}} u_k^{J;NZ;\pi}(q_i). \quad (2.39)$$

³In principle, one could additionally project on each value of number of neutrons and protons, (N, Z) . However, we only project on values (N_0, Z_0) that correspond to a real nucleus under consideration.

2.2.3 Structural Properties of Collective States

Collective wave functions of Eq. (2.38) do not represent a physical observable. However, amplitudes of the collective wave functions squared $|g_\alpha^{J;NZ;\pi}(q_i)|^2$ manifest the degree of shape fluctuations in both the quadrupole and octupole directions, and as such they provide an insight into the structure of collective states in the intrinsic frame. On a more quantitative level, one can calculate average values of quadrupole and octupole deformation parameters in the collective state:

$$\langle \beta_2 \rangle_\alpha^{J;NZ;\pi} = \sum_i |g_\alpha^{J;NZ;\pi}(q_i)|^2 \beta_{2i}, \quad (2.40)$$

$$\langle |\beta_3| \rangle_\alpha^{J;NZ;\pi} = \sum_i |g_\alpha^{J;NZ;\pi}(q_i)|^2 |\beta_{3i}|, \quad (2.41)$$

where in the octupole direction we have taken an absolute value of deformation parameter because $\langle \beta_3 \rangle$ vanishes identically for all states with good parity. These quantities provide a good indication about the dominant mean-field configurations in a collective state. In addition, they enable us to characterize the intrinsic density of a collective state by calculating corresponding RHB densities constrained to the $\langle \beta_2 \rangle_\alpha^{J;NZ;\pi}$ and $\langle |\beta_3| \rangle_\alpha^{J;NZ;\pi}$ values. Furthermore, weight functions and collective wave functions can be used to calculate values of various observables, both in a collective state and between two different collective states. The most common examples are electric spectroscopic quadrupole moments and electric multipole transition strengths, that have been routinely calculated within the MR-EDF framework for decades [RS80, RGER02, Fru07]. Electric spectroscopic quadrupole moment of the collective state α with total spin-parity J^π can be computed as:

$$Q_2^{\text{spec}}(J_\alpha^\pi) = e \sqrt{\frac{16\pi}{5}} \begin{pmatrix} J & 2 & J \\ J & 0 & -J \end{pmatrix} \sum_{q_i q_f} f_\alpha^{J;NZ;\pi^*}(q_f) \langle J q_f || \hat{Q}_2 || J q_i \rangle f_\alpha^{J;NZ;\pi}(q_i). \quad (2.42)$$

The reduced electric transition strength of multipolarity λ between an initial collective state α_i of total spin-parity $J_i^{\pi_i}$ and a final collective state α_f of total spin-parity $J_f^{\pi_f}$ can be computed as:

$$B(E\lambda; J_{\alpha_i}^{\pi_i} \rightarrow J_{\alpha_f}^{\pi_f}) = \frac{e^2}{2J_i + 1} \left| \sum_{q_i q_f} f_{\alpha_f}^{J_f;NZ;\pi_f^*}(q_f) \langle J_f q_f || \hat{Q}_\lambda || J_i q_i \rangle f_{\alpha_i}^{J_i;NZ;\pi_i}(q_i) \right|^2. \quad (2.43)$$

Quantity $\langle J_f q_f || \hat{Q}_\lambda || J_i q_i \rangle$ in Eqs. (2.42) and (2.43) corresponds to the reduced matrix element of the electric multipole operator $\hat{Q}_{\lambda\mu}$. More practical details on calculation of Q_2^{spec} and $B(E\lambda)$ can be found in Appendix B.1. Here, we note that all the quantities are

calculated in full configurational space. Therefore, there is no need to introduce effective charges and e always denotes the bare value of the proton charge.

Recently, the MR-EDF framework has been extended by including calculation of transition densities between low-lying excited states [YBH15]. This extension enables us to determine form factors for electron scattering off nuclei, that represent a very useful tool in studies of nuclear density distributions [Wal04, Won98, YBH15]. The longitudinal form factor for an angular momentum transfer L can be computed as the Fourier-Bessel transform of the reduced transition density $\rho_{J_i\alpha_i,L}^{J_f\alpha_f}(r)$ from an initial state α_i of total spin-parity $J_i^{\pi_i}$ to a final state α_f of total spin-parity $J_f^{\pi_f}$:

$$F_L(q) = \frac{\sqrt{4\pi}}{Z} \int_0^\infty dr r^2 \rho_{J_i\alpha_i,L}^{J_f\alpha_f}(r) j_L(qr), \quad (2.44)$$

where q denotes momentum transfer and $j_L(qr)$ is the spherical Bessel function of the first kind. The reduced transition density corresponds to the radial part of the 3D transition density and it can be calculated as:

$$\rho_{J_i\alpha_i,L}^{J_f\alpha_f}(r) = (-1)^{J_f-J_i} \frac{2J_f+1}{2J_i+1} \sum_K \langle J_f 0 L K | J_i K \rangle \int d\hat{\mathbf{r}} \rho_{\alpha_f\alpha_i}^{J_f J_i K 0}(\mathbf{r}) Y_{LK}^*(\hat{\mathbf{r}}), \quad (2.45)$$

where $Y_{LK}^*(\hat{\mathbf{r}})$ are spherical harmonics and $\rho_{\alpha_f\alpha_i}^{J_f J_i K 0}(\mathbf{r})$ denotes the pseudo GCM density as defined in [YBH15]. The pseudo GCM density does not represent an observable, but it can be used to calculate nuclear densities in the laboratory frame:

$$\rho_\alpha^{\text{lab}}(\mathbf{r}) = \sum_\lambda Y_{\lambda 0}(\hat{\mathbf{r}}) \langle J 0 \lambda 0 | J 0 \rangle \sum_K \langle J 0 \lambda K | J K \rangle \int d\hat{\mathbf{r}}' \rho_{\alpha\alpha}^{J J K 0}(r, \hat{\mathbf{r}}') Y_{\lambda K}^*(\hat{\mathbf{r}}'). \quad (2.46)$$

More details on calculation of pseudo GCM densities and general aspects of implementing the electron-nucleus scattering formalism to the present model can be found in Appendix B.2.

2.2.4 Evaluation of Norm Overlap and Hamiltonian Kernels

Evaluation of the Hamiltonian kernel (2.24) and the norm overlap kernel (2.25) lies at the very heart of the MR-EDF method. The simplest way of handling the norm overlaps is approximating them with Gaussian functions [RS80]. This assumption is based on an observation that the overlap $\mathcal{N}(\theta, \theta')$ is rapidly decreasing function of distance $|\theta - \theta'|$, that is, that the overlap between $|\Phi(\theta)\rangle$ and $|\Phi(\theta')\rangle$ does not vanish only when θ and θ' are relatively close to each other. Within the Gaussian overlap approximation (GOA), the norm overlap therefore reads:

$$\mathcal{N}(\theta, \theta') = e^{-\frac{1}{2}\gamma(\chi)(\theta-\theta')^2}, \quad (2.47)$$

with the width $\gamma(\chi)$ typically being a function of the center of mass coordinate $\chi = \frac{1}{2}(\theta + \theta')$. If one additionally assumes that a ratio between the Hamiltonian kernel and the norm overlap kernel is a smooth function of generating coordinates, it is possible to locally expand kernels up to the second order in $\theta - \theta'$ variable. In this way, the HWG equation transforms into the second-order differential (Schrödinger) equation, and the GCM framework is replaced by the well-known collective Hamiltonian model [RS80, PR09]. On the other hand, if one decides to remain exact, the overlap between two RHB states can be calculated using the conventional Onishi formula [OY66, RS80]:

$$\mathcal{N}(\theta, \theta') = \langle \Phi(\theta) | \Phi(\theta') \rangle = [\det (U^\dagger(\theta')U(\theta) + V^\dagger(\theta')V(\theta))]^{1/2}, \quad (2.48)$$

where $U(\theta)$ and $V(\theta)$ are Bogoliubov wave functions introduced in Chapter 1. The fact that the Onishi formula yields the sign ambiguity in a case when intrinsic states do not preserve any discrete symmetries has haunted nuclear community for decades. Various techniques to bypass this deficiency have therefore been proposed, including the method of analytical continuation [HHR82] and the Neergård's method [NW83]. More recently, an elegant Pfaffian formula based on Grassman algebra that completely resolves the sign ambiguity has been developed by L. Robledo [Rob09, BR12]. In this work, we will use the conventional framework of Onishi in order to calculate norm overlaps between the RHB states. Due to the discrete simplex-x and time-reversal symmetries of the intrinsic states, the matrix under determinant [see Eq. (2.48)] will exhibit a block structure with identical blocks, which can be exploited to unambiguously fix the corresponding sign. In particular, overlap between the RHB state $|\Phi(q_i)\rangle$ and the RHB state $|\Phi(q_j)\rangle$ that has been rotated by a rotational angle β and a gauge angle φ in any of the two isospin channels reads:

$$\begin{aligned} \mathcal{N}(q_i, q_j, \beta, \varphi) &= \langle \Phi(q_i) | e^{-i\beta \hat{J}_x} e^{i\varphi \hat{N}} | \Phi(q_j) \rangle \\ &= [e^{-i\beta \text{Tr}[J_x] + \varphi \text{Tr}[1]} \det N_g(q_i, q_j, \beta, \varphi)]^{\frac{1}{2}}, \end{aligned} \quad (2.49)$$

where we have introduced:

$$N_g(q_i, q_j, \beta, \varphi) = e^{-i\varphi} U^T(q_i) R^*(\beta) U^*(q_j) + e^{i\varphi} V^T(q_i) R(\beta) V^*(q_j), \quad (2.50)$$

and $R(\beta)$ corresponds the matrix of rotation operator in the simplex-x basis, details of which are given in Appendix A.

Furthermore, the MR-EDF framework can be thought of as an extension of the SR-EDF framework, where a basic functional $\mathcal{E}_{\text{SR-EDF}}[\hat{\rho}, \hat{\kappa}, \hat{\kappa}^*]$ of intrinsic densities (1.36) has been replaced by a more general functional $\mathcal{E}_{\text{MR-EDF}}[\hat{\rho}^{10}, \hat{\kappa}^{10}, \hat{\kappa}^{10*}]$ of transition densities between different RHB states. In other words, the ground state expectation value of the

effective nuclear Hamiltonian operator [cf. Eqs. (1.17) and (1.38)] has been replaced by a generalized Hamiltonian kernel of two different RHB states, possibly rotated in both the coordinate and gauge space. Since the starting point of our calculation is a density-dependent effective interaction rather than a genuine Hamiltonian operator, a meaningful prescription for determining Hamiltonian kernel has to be chosen. This prescription needs to fulfill four basic requirements [Rob07, Rob10]:

1. The obtained energies have to be scalar.
2. The obtained energies have to be real.
3. All expressions should reduce to the corresponding mean-field expressions for diagonal elements of the Hamiltonian kernel, $\mathcal{H}(\theta, \theta)$.
4. Small-amplitude approximation to the exact GCM framework should correspond to the conventional version of random phase approximation (RPA).

It turns out that, among different prescriptions that are available on the market⁴, it is only the mixed density prescription that satisfies all of the listed conditions [RGER02]. Motivated by the generalized Wick theorem⁵, mixed-density prescription for AMP and PNP calculations reads:

$$\rho_{\alpha\gamma}^{10} = \frac{\langle \Phi(q_i) | c_\gamma^\dagger c_\alpha e^{-i\beta \hat{J}_x} e^{i\varphi \hat{N}} | \Phi(q_j) \rangle}{\langle \Phi(q_i) | e^{-i\beta \hat{J}_x} e^{i\varphi \hat{N}} | \Phi(q_j) \rangle} = (e^{i\varphi} R(\beta) V^*(q_j) N_g^{-1} V^T(q_i))_{\alpha\gamma}, \quad (2.51)$$

$$\kappa_{\alpha\gamma}^{10} = \frac{\langle \Phi(q_i) | c_\gamma c_\alpha e^{-i\beta \hat{J}_x} e^{i\varphi \hat{N}} | \Phi(q_j) \rangle}{\langle \Phi(q_i) | e^{-i\beta \hat{J}_x} e^{i\varphi \hat{N}} | \Phi(q_j) \rangle} = (e^{i\varphi} R(\beta) V^*(q_j) N_g^{-1} U^T(q_i))_{\alpha\gamma}, \quad (2.52)$$

$$\kappa_{\alpha\gamma}^{01*} = \frac{\langle \Phi(q_i) | c_\alpha^\dagger c_\gamma^\dagger e^{-i\beta \hat{J}_x} e^{i\varphi \hat{N}} | \Phi(q_j) \rangle}{\langle \Phi(q_i) | e^{-i\beta \hat{J}_x} e^{i\varphi \hat{N}} | \Phi(q_j) \rangle} = -(e^{-i\varphi} R^*(\beta) U^*(q_j) N_g^{-1} V^T(q_i))_{\alpha\gamma}. \quad (2.53)$$

The nondiagonal elements of the MR-EDF kernel are therefore computed by replacing intrinsic densities in all the SR-EDF density-dependent terms (including the density-dependent coupling constants) with transition densities obtained from Eqs. (2.51) - (2.53).

Finally, let us briefly comment on the fact that the Hamiltonian kernel employed in our study does not correspond to the expectation value of a genuine Hamiltonian operator. This is a common property of virtually all EDF models, non-relativistic and relativistic alike, and it occurs for (at least) one of the three reasons:

⁴Another possible choice is the so-called projected density prescription, which maintains a pleasant property of preserving symmetries of nuclear Hamiltonian. However, while this prescription works well in a case of particle number symmetry, it was shown to yield catastrophic results when employed in calculations that restore spatial symmetries [Rob10]. Nonetheless, a hybrid method of using projected density in PNP calculation and mixed density in AMP calculation can be employed in order to avoid problems related to raising (generally complex) mixed densities to the non-integer powers [RRR18].

⁵We say that the generalized Wick theorem provides a motivation rather than a formal foundation, since its applicability extends only to theories based on a genuine Hamiltonian operator. This is obviously not the case for a vast majority of MR-EDF models.

1. The effective interaction is density-dependent.
In order to correct for too large incompressibility and properly describe the nuclear surface properties, virtually all modern EDF parameterizations include at least one density-dependent term. Most notably, the most successful covariant realizations of the EDF framework are explicitly built as density-dependent models.
2. Vertices used in ph and pp channel are different and possibly not antisymmetric.
This is particularly the case for Skyrme EDFs, where different vertices were introduced in order to account for too small or even repulsive pairing matrix elements derived from the original interaction [SBB⁺13], and for relativistic EDFs, where a non-relativistic pairing force is typically added to the functional [VALR05]. On the other hand, Gogny EDFs are characterized by using the same antisymmetrized vertices everywhere. Nevertheless, it has been argued that their density-dependence still makes it impossible for the phenomenological functional to be mapped on a functional that is a strict expectation value of a many-body Hamiltonian [BDL09].
3. The exchange terms of the interaction are either approximated or omitted.
The exact treatment of all exchange terms can increase the required computational time by an order of magnitude. These terms are therefore often either approximated by simpler expressions (such as the Slater approximation to the Coulomb exchange potential) or completely omitted (in case of which their physical effect is accounted for through the adjustment of phenomenological coupling constants).

The undesired consequence of these approximations is breaking of the exchange symmetry (Pauli principle), that produces spurious self-interaction and self-pairing contributions to the nuclear EDF [AER01, DSNR07, DBB⁺09, LDB09, BDL09]. These non-physical contributions were demonstrated to manifest themselves through divergences and/or finite steps when considering the symmetry-restored energies as functions of collective coordinates. In particular, while situation in AMP calculations appears to be less severe [Egi16], the PNP calculations for very large values of discretization points N_φ were shown to exhibit finite steps and discontinuities whenever a single-particle level crosses the Fermi energy [BDL09]. One should note that this theoretical drawback is related only to the employed energy functional, and not to the product states in question. Therefore, even though they may be affected indirectly, all observables that are calculated as expectation values of the corresponding genuine operators do not contain any explicit spurious contributions. Research towards spuriousity-free MR-EDF calculations is still in its infancy and it is currently moving in two separate directions: one of them is development of the regularization schemes for the existing functionals [LDB09, BDL09] and the other one is development of the pseudo-potential-based-EDF parameterizations that are *a priori* free of spuriousities [SBB⁺13]. In the meantime, one should stay aware of the existing theoretical drawbacks and, if possible, try to estimate their influence on predictions of the respective model.

Part II

Microscopic Description of Clustering in Light Nuclei

A Computational Interlude

What can be asserted without evidence can be dismissed without evidence.

Christopher Hitchens' razor

In the preceding chapters we have introduced and described a collective nuclear model based on the restoration of symmetries of intrinsic states and the subsequent configuration mixing. In the following chapters, this framework will be employed in a study of clustering phenomena in neon and carbon isotopes. However, before discussing physical aspects of the study, let us first address some of the issues related to the computational implementation of the model. In particular, we will address the question of convergence of results with respect to various discretization parameters, both on the SR-EDF and on the MR-EDF level. To begin with, computational aspects of the mean-field calculations will be discussed. The RHB calculations were performed by using the quadrupole-deformed axially-symmetric version of the DIRHB package [NPVR14] as a starting point, and by further extending it in order to additionally include the axially-symmetric octupole degree of freedom. Since the number of required configurations is relatively low (as compared to, for example, nuclear fission calculations), it is the least time-consuming part of our calculation. In the next step, the restoration of good angular momentum, particle number, and parity of RHB states were built upon the mean-field code. This step represents the most time-consuming part of the calculation. The symmetry-restored configurations were then mixed in order to build the symmetry-conserving collective states and study their spectroscopic properties. In the second part of this chapter, we will examine convergence of the obtained projected energies with respect to the number of integration points in the β -Euler angle and the φ -gauge angle. The need for this is (at least) two-fold. First, as in any other discretized calculation, it is necessary to verify that the particular choice of mesh provides a satisfactory convergence of calculated quantities. The second reason is to demonstrate the influence of the theoretical drawback related to the fact that the

employed functional does not correspond to the expectation value of a genuine Hamiltonian operator (for more details see Section 2.2.4 and references cited therein). Finally, we will discuss the influence of linear dependence (overcompleteness) of the original set of RHB basis functions on the output of the model. These linear dependencies are routinely removed by reducing the size of a natural basis [see Eq. (2.37)] and by verifying that the obtained spectra is stable with respect to the number of remaining natural basis states. For the sake of brevity, the entire analysis of this chapter will be based only on a case of ^{20}Ne isotope, that we conveniently choose as a representative for a class of light nuclei.

3.1. Convergence of Mean-Field Calculation

Starting point of our calculation is the axially-symmetric quadrupole-deformed version of the DIRHB package, which computes the ground-state properties of even-even nuclei using the framework of relativistic self-consistent mean-field models [NPVR14]. This code was first extended by including the axially-symmetric octupole degree of freedom, which enabled us to perform self-consistent calculations in the entire $\beta_2 - \beta_3$ plane. The RHB equations were solved in the configurational space of axially-symmetric harmonic oscillator, by expanding the large and the small component of nuclear spinors in bases of the corresponding eigenfunctions. As already emphasized in Chapter 1, the appearance of spurious states is avoided by choosing quantum numbers $|\alpha\rangle = |n_z n_\perp \Lambda m_s\rangle$ in such a way that their combination does not exceed the maximal major quantum number $N_{sh} = 2n_\perp + |\Lambda| + n_z$ for the large component of nuclear spinor and the maximal major quantum number $N_{sh} + 1$ for the small component of nuclear spinor. Of course, the convergence of results with respect to the size of basis N_{sh} has to be verified. Therefore, in the left panel of Figure 3.1 we plot the differences of calculated RHB binding energies $\Delta E_{\text{RHB}}^{N_{sh}} = E_{\text{RHB}}^{N_{sh}} - E_{\text{RHB}}^{N_{sh}+2}$ of ^{20}Ne isotope for different numbers of oscillator shells $N_{sh} = 6, 8, 10$ in the $(\beta_2, \beta_3 > 0)$ plane¹. Dashed contours connect points with the same $\Delta E_{\text{RHB}}^{N_{sh}}$ values and they are separated by 1 MeV. The constrained RHB equations were solved on a two-dimensional mesh, by imposing constraints on the axially-symmetric quadrupole and octupole moments and implementing the augmented Lagrangian method [SSBN10]. The resulting mesh covers a wide range of deformations in both the quadrupole and octupole degree of freedom: $\beta_2 \in [-0.6, 1.5]$ and $\beta_3 \in [-2.0, 2.0]$. The step size on the oblate and on the prolate side were taken to be $\Delta\beta_2 = 0.15$ and $\Delta\beta_2 = 0.3$, respectively, while the step size in the octupole direction equals $\Delta\beta_3 = 0.2$. After solving the RHB equation, all of the configurations with energy more than 20 MeV above the equilibrium were removed from the basis. Of course, the exclusion of such high-energy states does not influence the predictive power of our model which ultimately aims to describe the low-lying structure of atomic nuclei. The remaining states, which will be included in the subsequent symmetry restoration and configuration mixing, are denoted with red circles in the left panel of Fig. 3.1. By inspecting the Fig. 3.1, one can verify that a satisfactory convergence for all the states is obtained for $N_{sh} = 10$ oscillator shells. In particular, a

¹The $(\beta_2, \beta_3 < 0)$ plane is equivalent to the $(\beta_2, \beta_3 > 0)$ plane, that is, one can be obtained by mirroring the other one around the $\beta_3 = 0$ axis.

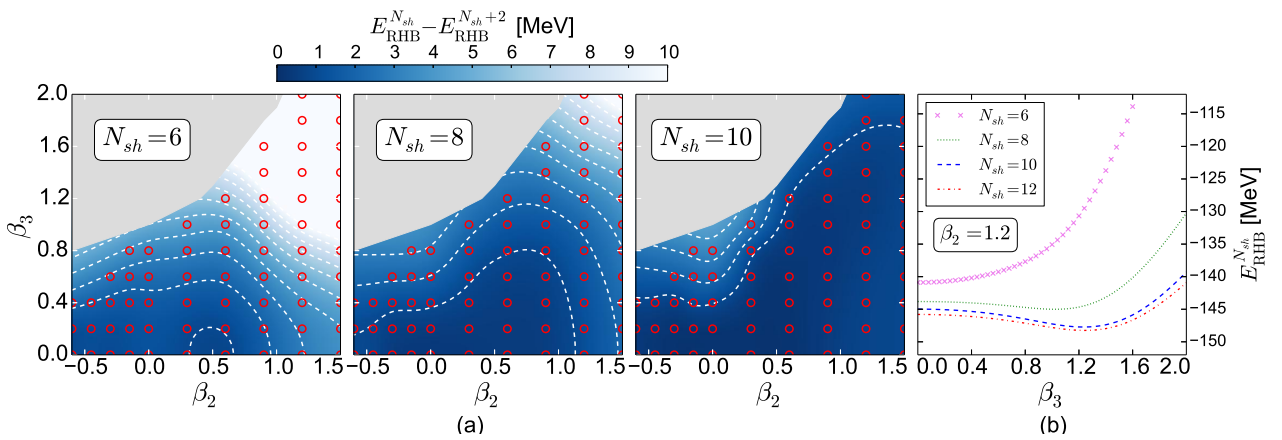


FIGURE 3.1: Left panel (a): differences of calculated RHB binding energies $\Delta E_{\text{RHB}}^{N_{sh}} = E_{\text{RHB}}^{N_{sh}} - E_{\text{RHB}}^{N_{sh}+2}$ of ^{20}Ne isotope for different numbers of oscillator shells N_{sh} in the $(\beta_2, \beta_3 > 0)$ plane. Dashed contours are separated by 1 MeV. Red points denote calculated configurations that are at most 20 MeV above the equilibrium configuration. Right panel (b): RHB binding energies of $(\beta_2 = 1.2, \beta_3 > 0)$ configurations for different numbers of oscillator shells N_{sh} .

shift to 12 oscillator shells brings less than 1 MeV of binding for a large majority of chosen states. Only a small minority of states, predominantly at larger β_3 deformations and on the oblate side of $\beta_2 - \beta_3$ plane, have converged with $\Delta E_{\text{RHB}}^{N_{sh}=10} > 1$ MeV. However, as it will be demonstrated in the following chapter, this part of the $\beta_2 - \beta_3$ plane will not play any relevant role in the description of nuclear collective dynamics. In fact, it is well established that the absolute value of binding energy does not significantly affect the collective nuclear motion, as long as the shape of the energy landscape is preserved [RGER02]. In order to demonstrate this point, in the right panel of Fig. 3.1 we show the calculated RHB binding energies of $(\beta_2 = 1.2, \beta_3 > 0)$ configurations for different numbers of oscillator shells N_{sh} . While the $N_{sh} = 6$ and $N_{sh} = 8$ values are obviously not sufficient to obtain a proper convergence, especially for larger β_3 deformations, the $N_{sh} = 10$ and $N_{sh} = 12$ curves indeed exhibit almost identical shape. Similar conclusions can be drawn if one inspects the corresponding plots for other considered isotopes. Therefore, a value of $N_{sh} = 10$ oscillator shells is adopted in solving RHB equations for all the further calculations. The resulting wave functions are first obtained in the configurational space of harmonic oscillator, and they are subsequently used to calculate densities in the same configurational space. These densities are then transformed to the cylindrical coordinate space (r_{\perp}, z, ϕ) , where they are employed to compute various terms of the energy density functional. Discretization in the z - and r_{\perp} - directions have been carried out following the Gauss-Hermite and Gauss-Laguerre quadrature methods, respectively, and the corresponding number of points equal $N_{GH} = 16$ and $N_{GL} = 14$, respectively. Computational time required to compute one RHB configuration will depend on its distance from the absolute minimum. For configurations with reasonable binding energies (that is, at most 20 MeV above the absolute minimum) and $N_{sh} = 10$ oscillator shells, depending on the machine, the required computational time will typically range between ten and thirty seconds. Of course, increasing the size of a single-particle basis will significantly increase the required computational time, both for the SR-EDF and for the MR-EDF calculation.

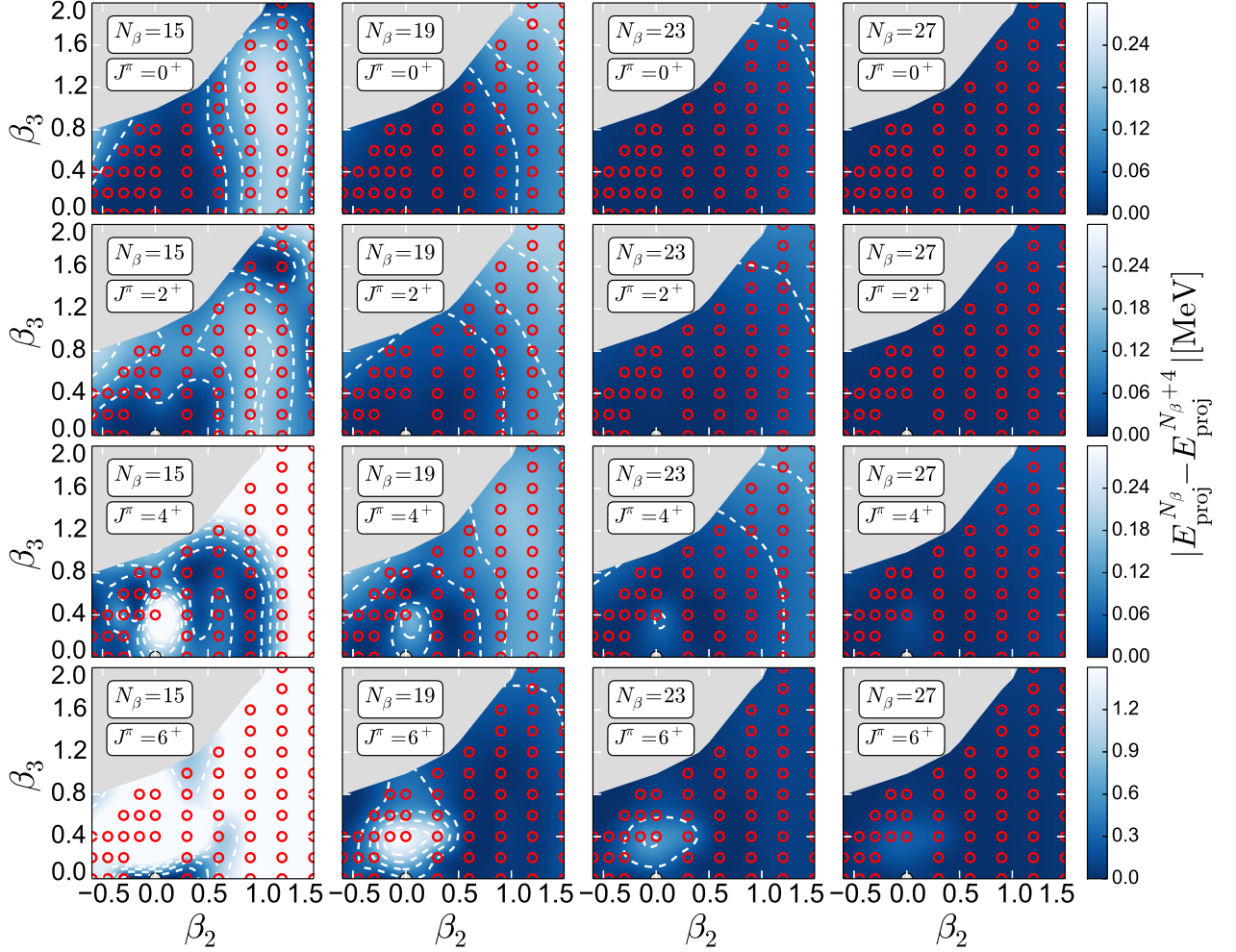


FIGURE 3.2: Absolute energy differences $\Delta E_{\text{proj}}^{N_\beta} = |E_{\text{proj}}^{N_\beta} - E_{\text{proj}}^{N_\beta+4}|$ of states projected on even-positive spin-parities for different numbers of β -Euler angle mesh points N_β . Separation of dashed lines on all panels corresponds to the separation of neighboring ticks on their respective colorbars, that is, to 0.06, 0.06, 0.06, 0.3 MeV for $J^\pi = 0^+, 2^+, 4^+, 6^+$, respectively. Red circles denote configurations that are included in the symmetry restoration and configuration mixing calculation. Results are shown for ^{20}Ne isotope. See text for more details.

3.2. Convergence of Symmetry-Restoring Calculation

3.2.1 Convergence of Projected Energies

Restoration of broken symmetries of the RHB states and the subsequent configuration mixing represent the most numerically-involved part of our calculation. The reason for this is rather obvious: while the SR-EDF is a functional of (normal and anomalous) density matrices, the MR-EDF can be seen as a more general functional of all the transition density matrices. This means that, starting from $N^{\text{SR-EDF}}$ states in the RHB basis, all of the relevant symmetry-restored quantities have to be calculated for $N^{\text{MR-EDF}} = N^{\text{SR-EDF}}(N^{\text{SR-EDF}} + 1)/2$ configurations. Formally, these quantities represent

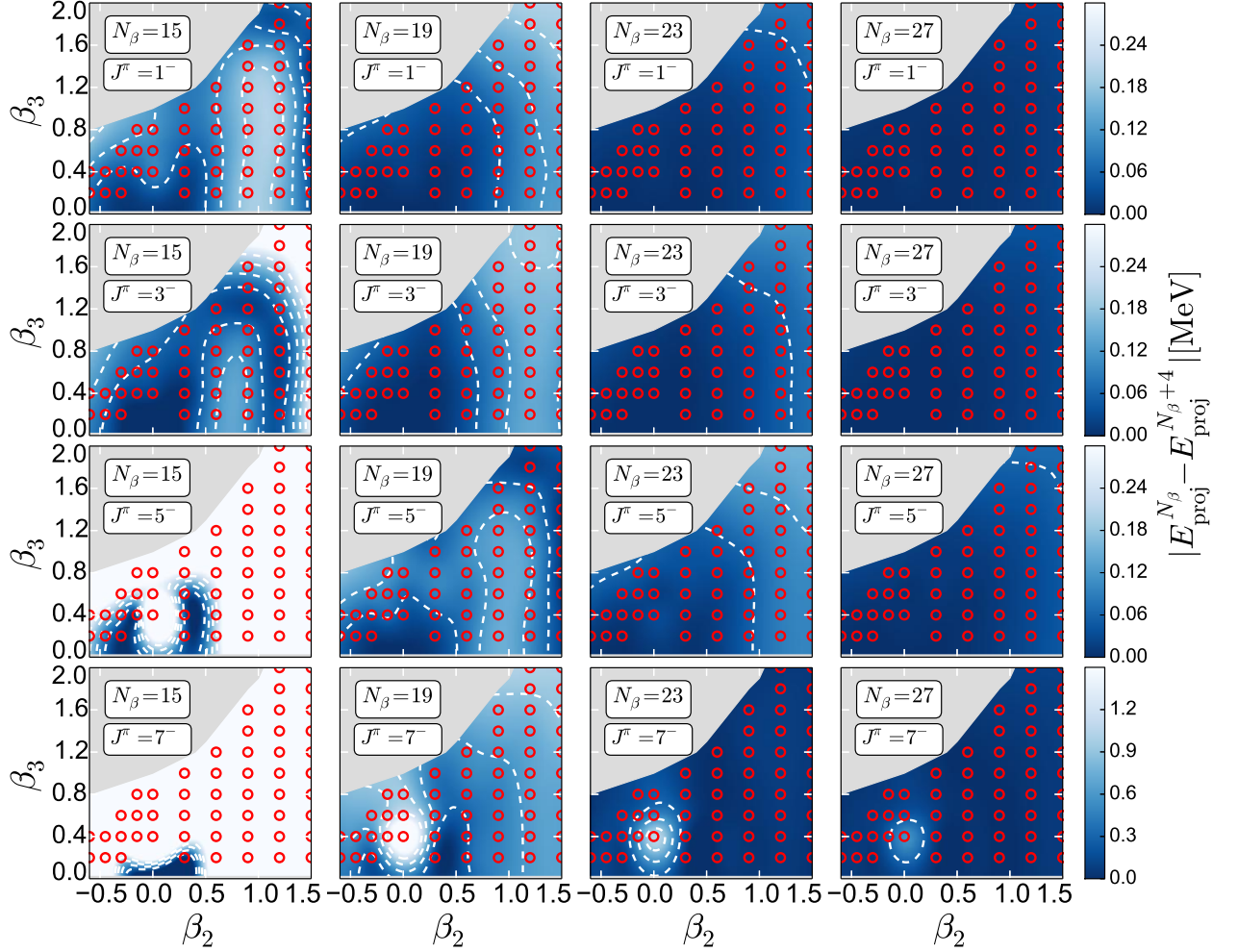


FIGURE 3.3: Absolute energy differences $\Delta E_{\text{proj}}^{N_\beta} = |E_{\text{proj}}^{N_\beta} - E_{\text{proj}}^{N_\beta+4}|$ of states projected onto odd-negative spin-parities for different numbers of β -Euler angle mesh points N_β . Separation of dashed lines on all panels corresponds to the separation of neighboring ticks on their respective colorbars, that is, to 0.06, 0.06, 0.06, 0.3 MeV for $J^\pi = 1^-, 3^-, 5^-, 7^-$, respectively. Red circles denote configurations that are included in the symmetry restoration and configuration mixing calculation. Results are shown for ^{20}Ne isotope. See text for more details.

the non-diagonal matrix elements of the corresponding operators between a non-rotated RHB state and a RHB state that is rotated both by Euler angles (α, β, γ) in the coordinate space and by gauge angles (φ_N, φ_Z) in the gauge spaces of two isospin channels. By applying the projection operator and integrating over all the rotational and gauge angles, a symmetry-restored quantity is obtained.

Starting from the AMP case, the axial symmetry of RHB states enables us to carry out integrals over Euler angles α and γ analytically, which significantly reduces the computational cost. Consequently, we are left with integral in the β -Euler angle that needs to be computed numerically. In order to analyze the convergence of calculated energies with the number of mesh points in β -direction N_β , in Figure 3.2 we plot the absolute energy differences $\Delta E_{\text{proj}}^{N_\beta} = |E_{\text{proj}}^{N_\beta} - E_{\text{proj}}^{N_\beta+4}|$ of states projected onto even-positive spin-parities $J^\pi = 0^+, 2^+, 4^+, 6^+$ for different numbers of mesh points $N_\beta = 15, 19, 23, 27$. The corresponding $\Delta E_{\text{proj}}^{N_\beta}$ values projected onto odd-negative spin-parities $J^\pi = 1^-, 3^-, 5^-, 7^-$

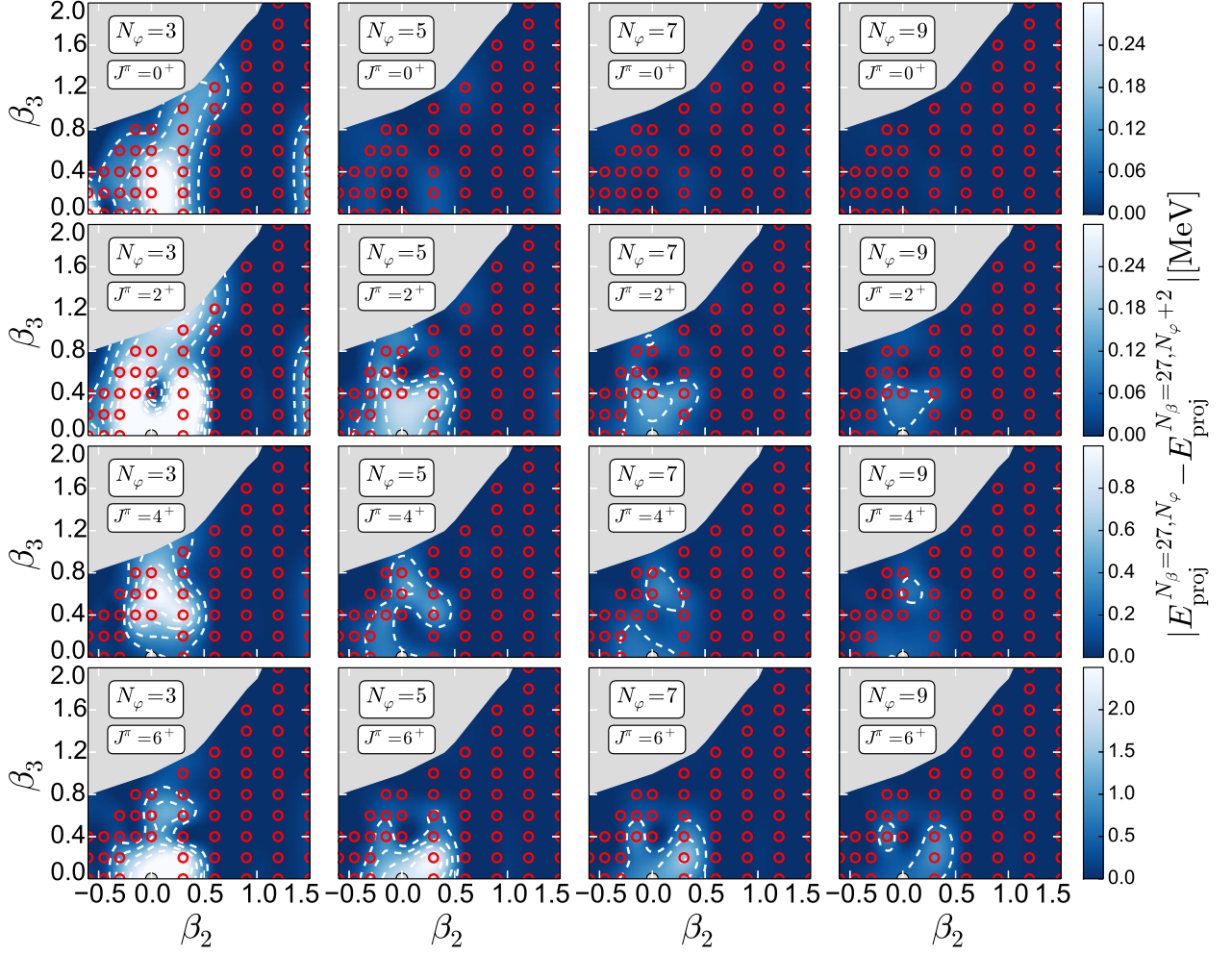


FIGURE 3.4: Absolute energy differences $\Delta E_{\text{proj}}^{N_{\beta}=27, N_{\varphi}} = |E_{\text{proj}}^{N_{\beta}=27, N_{\varphi}} - E_{\text{proj}}^{N_{\beta}=27, N_{\varphi}+2}|$ of states projected onto even-positive spin-parities $J^{\pi} = 0^{+}, 2^{+}, 4^{+}, 6^{+}$ and particle numbers $N_N, N_Z = 10$ for different numbers of gauge-angle mesh points $N_{\varphi_N} = N_{\varphi_Z} \equiv N_{\varphi}$. Separation of dashed lines on all panels corresponds to the separation of neighboring ticks on their respective colorbars, that is, to 0.06, 0.06, 0.2, 0.5 MeV for $J^{\pi} = 0^{+}, 2^{+}, 4^{+}, 2^{+}$, respectively. Red circles denote configurations that are included in the symmetry restoration and configuration mixing scheme. Results are shown for ^{20}Ne isotope. See text for more details.

are shown in Figure 3.3. As before, red circles denote configurations that are included in the symmetry restoration and configuration mixing calculation. Note that the angular momentum projection for the spherical ($\beta_2 = 0, \beta_3 = 0$) configuration is well defined only for $J^{\pi} = 0^{+}$ and it is therefore omitted from all the other plots. Similarly, parity projection for reflection-symmetric ($\beta_3 = 0$) configurations is well defined only for positive parity, hence these configurations are omitted from Fig. 3.3. In addition, several other configurations close to the spherical point are characterized by very small values of the projected norm overlap kernel and their angular-momentum projected energies cannot be determined accurately. These states will not play any relevant role in the configuration mixing calculations and they can be safely omitted. Starting from angular momenta $0 \leq J \leq 3$, a reasonable convergence is obtained already for $N_{\beta} = 19$. In particular, a

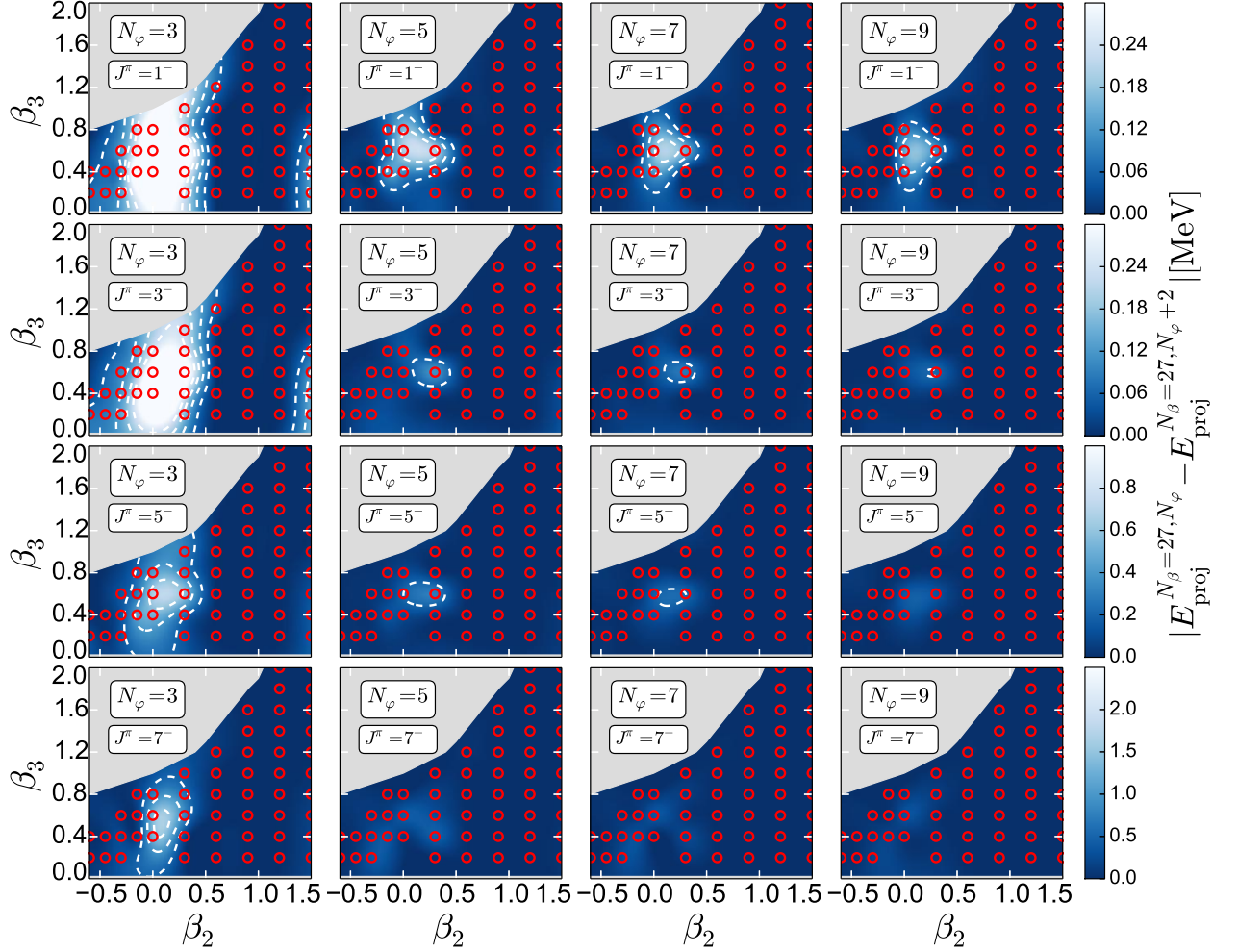


FIGURE 3.5: Absolute energy differences $\Delta E_{\text{proj}}^{N_{\beta}=27, N_{\varphi}} = |E_{\text{proj}}^{N_{\beta}=27, N_{\varphi}} - E_{\text{proj}}^{N_{\beta}=27, N_{\varphi}+2}|$ of states projected onto odd-negative spin-parities $J^{\pi} = 1^{-}, 3^{-}, 5^{-}, 7^{-}$ and particle numbers $N_N, N_Z = 10$ for different numbers of gauge-angle mesh points $N_{\varphi_N} = N_{\varphi_Z} \equiv N_{\varphi}$. Separation of dashed lines on all panels corresponds to the separation of neighboring ticks on their respective colorbars, that is, to 0.06, 0.06, 0.2, 0.5 MeV for $J^{\pi} = 1^{-}, 3^{-}, 5^{-}, 7^{-}$, respectively. Red circles denote configurations that are included in the symmetry restoration and configuration mixing scheme. Results are shown for ^{20}Ne isotope. See text for more details.

shift to $N_{\beta} = 23$ brings less than 0.2 MeV of binding for all the considered states. However, the increase of angular momenta is accompanied by weakening of this convergence, since a higher order of the corresponding associated Legendre polynomials in numerical evaluation of projection integrals requires the inclusion of more mesh points. Therefore, in order to ensure a satisfactory convergence for a wide range of angular momenta, a value of $N_{\beta} = 27$ is adopted in all the further calculations. This choice means that, when compared to values obtained for $N_{\beta} = 31$, energies of states with angular momenta $0 \leq J \leq 5$ have converged within $\Delta E_{\text{proj}}^{N_{\beta}=27} = 0.06$ MeV, while all of the states with angular momentum $J = 6^{+}$ and all but one state with angular momentum $J = 7^{-}$ have converged within $\Delta E_{\text{proj}}^{N_{\beta}=27} = 0.3$ MeV. Similar conclusions can be drawn when inspecting results for other considered isotopes. In the next step, a number of mesh points in β -Euler angle is fixed at $N_{\beta} = 27$ and restoration of good neutron and proton numbers is added

to the states with good angular momenta. In Figure 3.4 we plot the absolute energy differences $\Delta E_{\text{proj}}^{N_\beta=27, N_\varphi} = |E_{\text{proj}}^{N_\beta=27, N_\varphi} - E_{\text{proj}}^{N_\beta=27, N_\varphi+2}|$ of states projected onto even-positive spin-parities $J^\pi = 0^+, 2^+, 4^+, 6^+$ and particle numbers $N_N, N_Z = 10$ for different numbers of gauge-angle mesh points $N_{\varphi_N}, N_{\varphi_Z} = 3, 5, 7, 9$. The corresponding $\Delta E_{\text{proj}}^{N_\beta=27, N_\varphi}$ values projected onto odd-negative spin-parities $J^\pi = 1^-, 3^-, 5^-, 7^-$ are shown in Figure 3.5. Starting from the $J = 0^+$ angular momentum, satisfactory convergence is obtained already for $N_\varphi = 5$ mesh points. However, as in the case of the AMP only, convergence of the simultaneous AMP and PNP is worsened as the angular momentum is increased. Therefore, in order to ensure a satisfactory convergence, a value of $N_\varphi = 9$ is adopted in all the further calculations.

3.2.2 Some Convergence Issues

As previously discussed in Section 2.2.4, a theoretical drawback of all the standard EDFs, non-relativistic and relativistic alike, is the fact that the Hamiltonian kernel which they employ does not correspond to the expectation value of a genuine Hamiltonian operator. The unpleasant consequences of this drawback, the appearance of divergences, finite steps, and/or discontinuities when plotting projected energies as functions of generating coordinate, have been reported on multiple places [AER01, DSNR07, BDL09]. Even though these anomalies follow directly from the formal properties of the framework, they are often not manifested explicitly in practical implementations of the model. The reason for this is (at least) two-fold: (a) Anomalies are expected to appear only at certain deformations, that is, only for configurations that contain a single-particle level very close to the Fermi surface. Therefore, a choice of mesh in generating coordinates that is not dense enough may completely conceal the anomalies. (b) Anomalies are expected to be unveiled only for very fine discretization meshes of projection integrals. Therefore, discretization parameters that are typically sufficient to obtain a reasonable convergence may not unveil the underlying anomalies. In order to demonstrate quantitatively the concrete effect of this discussion on predictions of our model, in the upper panel of Figure 3.6 we plot the convergence patterns of energies projected onto angular momentum $J^\pi = 2^+$ for all the states in the RHB basis (this is, of course, equivalent to plotting projected energy as a function of two generating coordinates). Blue lines denote the case when only AMP is performed: the dash-dotted line corresponds to difference in projected energies obtained for $N_\beta = 27$ and $N_\beta = 71$, while the dotted line corresponds to difference in projected energies obtained with $N_\beta = 27$ and $N_\beta = 171$. Therefore, in addition to calculation performed with the value of discretization parameter that was already demonstrated to yield satisfactory convergence ($N_\beta = 27$), we performed calculations with two significantly (and unreasonably) larger values of discretization parameter. Nevertheless, the convergence of energies of angular-momentum-projected states appears to persist almost perfectly on the entire $\beta_2 - \beta_3$ plane, save for a barely noticeable dip at around $N_{\text{state}}(\beta_2, \beta_3) = 50$. In the next step, value of AMP discretization parameter was fixed to $N_\beta = 27$ and PNP was performed with three different values of discretization parameter N_φ . The corresponding differences in energies are denoted with red lines: the dash-dotted line corresponds to

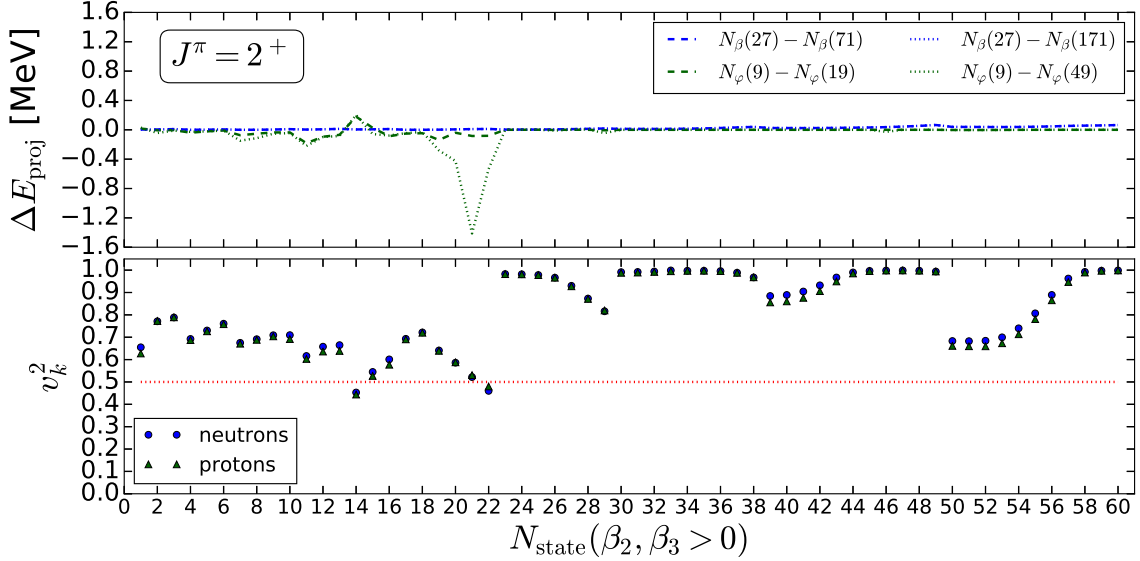


FIGURE 3.6: Upper panel (a): Convergence pattern of energies projected onto angular momentum $J^\pi = 2^+$ for states $N_{\text{state}}(\beta_2, \beta_3 > 0)$ in the RHB basis. Blue lines denote the case when only AMP is performed: the dash-dotted line corresponds to difference in energies obtained for $N_\beta = 27$ and $N_\beta = 71$, while the dotted line corresponds to difference in energies obtained with $N_\beta = 27$ and $N_\beta = 171$. Red lines denote the case when both AMP ($N_\beta = 27$) and PNP are performed: the dash-dotted line corresponds to difference in energies obtained for $N_\varphi = 9$ and $N_\varphi = 19$, while the dotted line corresponds to difference in energies obtained with $N_\varphi = 9$ and $N_\varphi = 49$. Lower panel (b): Occupation probabilities of single-neutron (circles) and single-proton (triangles) levels of $N_{\text{state}}(\beta_2, \beta_3 > 0)$ states that are closest to the Fermi surface ($v_k^2 = 0.5$). Results are shown for ^{20}Ne isotope. See text for more details.

difference in projected energies obtained with $N_\varphi = 9$ and $N_\varphi = 19$, while the dotted line corresponds to difference in projected energies obtained with $N_\varphi = 9$ and $N_\varphi = 49$. Once again, in addition to calculation performed with the value of discretization parameter that was already demonstrated to yield satisfactory convergence ($N_\varphi = 9$), we performed calculations with two significantly (and unreasonably) larger values of discretization parameter. This time, however, we encounter a disturbance in the convergence pattern. In particular, for $N_\varphi = 19$ small deviations can be seen in the region $6 \leq N_{\text{state}}(\beta_2, \beta_3) \leq 24$ that peak at about $\Delta E_{\text{proj}} \approx 0.2$ MeV for the 14th basis state. To put it into perspective, let us repeat that a satisfactory convergence of the RHB calculation was proclaimed for states with $\Delta E_{\text{RHB}}^{N_{\text{sh}}=10} \leq 1$ MeV. By further increasing the discretization parameter to $N_\varphi = 49$, the maximum of deviation switches to 21st basis state and it equals roughly $\Delta E_{\text{proj}} \approx 1.5$ MeV. As discussed earlier in the manuscript and extensively in the literature [AER01, DBB⁺09, BDL09], the origin of these anomalies can be traced back to properties of the underlying single-particle spectra. In order to examine this claim in more details, in the lower panel of Fig. 3.6 we plot the occupation probabilities of single-neutron and single-proton levels of basis states that are closest to the Fermi surface ($v_k^2 = 0.5$). Comparing the two panels, it soon becomes apparent that the ΔE_{proj} maxima for both red lines from the upper panel (that is, the 14th and the 21st basis state) indeed correspond to cases in the lower panel when single-particle states are located very close to the Fermi surface. Equivalent analyses could be carried out for states with higher values of angular

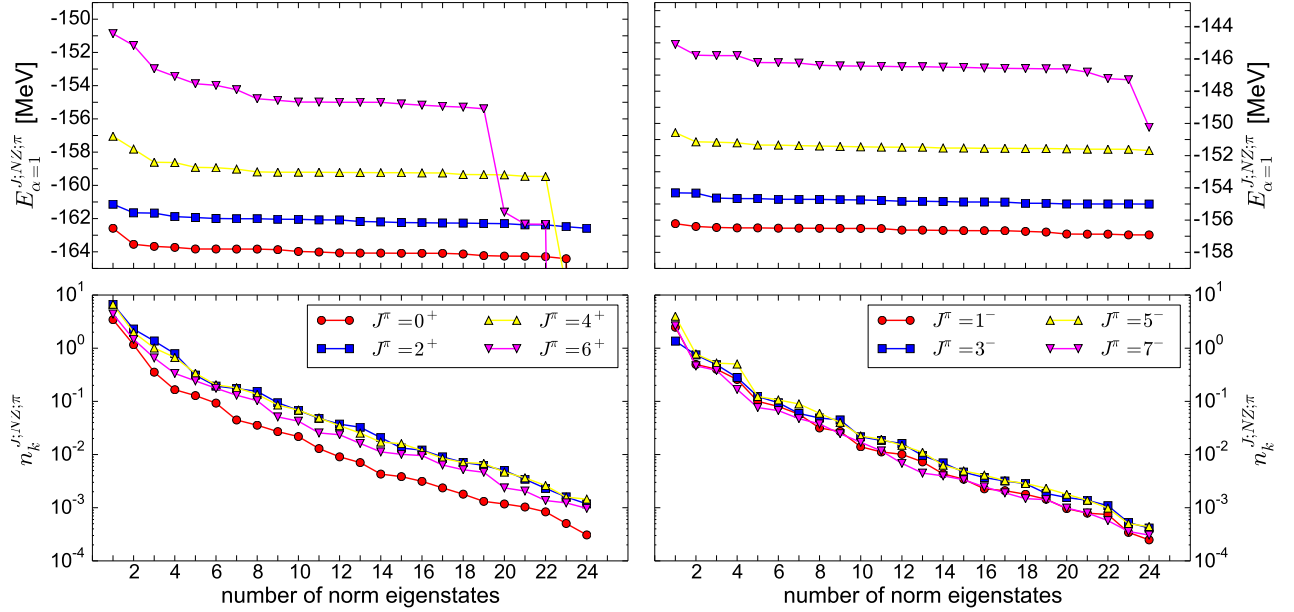


FIGURE 3.7: Upper panel: Excitation energies of collective positive-parity (left) and negative-parity (right) collective states in ^{20}Ne isotope as a function of the number of considered norm overlap eigenstates. Eigenstates are labeled in the decreasing order of eigenvalues. Lower panel: Eigenvalues of the norm overlap for positive-parity (left) and negative-parity (right) collective states. See text for more details.

momenta J^π and for projections with larger values of discretization parameter N_φ . Both of these changes are likely to lead to further disturbances of the convergence pattern: the former one because higher J^π states have weaker convergence to start with, and the latter one because larger proportion of the existing pole is likely to be caught by the projection integral. However, completely spurious-free calculations at the level of implementation as advanced as the present one are still exceptionally scarce within the non-relativistic framework [BABH14], and they are yet to be performed within the relativistic framework. In the meantime, we reiterate that this simple analysis did not reveal any notable issues concerning AMP calculations, while combined AMP and PNP convergence is yet rather stable for a reasonable range of discretization parameters.

3.3. Configuration Mixing and Linear Dependencies

Final step of the calculation corresponds to mixing of symmetry-restored RHB configurations. The obtained HWG equation is solved by diagonalizing the collective Hamiltonian [see Eq. (2.35)] in the basis of natural states [see Eq. (2.37)]. Already a short inspection of these two equations reveals a potential issue. Namely, if the norm overlap eigenvalues $n_k^{J;NZ;\pi}$ become too small they may cause numerical instabilities when defining the natural basis and, consequently, when diagonalizing the collective Hamiltonian. In practice, small values of $n_k^{J;NZ;\pi}$ stem from linear dependencies of the initial set of

RHB wave functions $|\Phi(q_i)\rangle$. For this reason, there is no practical gain in including RHB states that are too close to each other in the space of generating coordinates, since such choice will only introduce additional linear dependencies to the model. Equivalently, by choosing the mesh with reasonable $\Delta\beta_2$ and $\Delta\beta_3$ steps one can minimize the influence of linear dependencies. Nevertheless, they will always persist to a certain level, and they need to be accounted for. Typically, this is done by inspecting the obtained energies of collective states as functions of the number of included natural basis states. The so-called *plateau* condition then asserts that, after norm overlap eigenstates with smallest eigenvalues are discarded, these energies should remain rather constant for a wide range of states [BDF⁺90]. Therefore, in the upper panel of Figure 3.7 we plot the excitation energies of collective positive-parity states (left) and negative-parity states (right) in ²⁰Ne isotope as functions of the number of considered norm overlap eigenstates. We note that eigenstates with eigenvalues $n_k^{J;NZ;\pi} < 10^{-4}$ were *a priori* removed from the basis. The remaining states are labeled in the decreasing order of eigenvalues, that is, the first state is the one with the largest eigenvalue. The corresponding eigenvalues are additionally plotted in the lower panel of Fig. 3.7. Inspecting the upper panel of Fig. 3.7, one notices that energies of the lowest-lying positive-parity states $J^\pi = 0^+, 2^+$ and negative-parity states $J^\pi = 1^-, 3^-, 5^-$ remain stable for the entire range of norm eigenstates. On the other hand, for $J^\pi = 4^+, 6^+$ and $J^\pi = 7^-$ one first introduces a cutoff in the natural basis and then adopts the *plateau* values. Equivalent analysis has been carried out for other nuclei under consideration and the corresponding *plateau* values have been adopted.

3.4. Concluding Remarks

To summarize, in this chapter we have discussed computational aspects of our study that serve as a practical precondition for the successful implementation of the model in the following chapters. In particular, we have demonstrated that the chosen size of the axially-symmetric harmonic oscillator basis ($N_{sh} = 10$) ensures a satisfactory convergence of the RHB calculation. Furthermore, we have analyzed in more detail practical issues related to the restoration of symmetries of the intrinsic states. Values of discretization parameters $N_\beta = 27$ (for AMP) and $N_\varphi = 9$ (for PNP) were shown to provide a satisfactory convergence of projected energies for angular momenta $0 \leq J \leq 7$ and for a wide range of deformations in both the quadrupole and octupole degree of freedom. In addition, we have briefly discussed the impact of different approximations related to the form of the effective interaction on predictions of the present model. Our simple analysis did not reveal any notable issues concerning the AMP calculations, while convergence of the combined AMP and PNP calculations is rather stable for a reasonable range of discretization parameters. Finally, we have addressed the impact of linear dependencies of the initial set of basis functions on final predictions of the collective model. In order to satisfy the *plateau* condition, these linear dependencies are accounted for by inspecting the obtained collective energies as functions of the size of natural basis and removing the states related to very small norm eigenvalues. We are now ready to focus on physical aspects of the study, which will be thoroughly discussed in the following two chapters.

Quadrupole-Octupole Collectivity and Clusters in Neon Isotopes

Poets say science takes away from the beauty of the stars - mere globs of gas atoms. Nothing is "mere". I too can see the stars on a desert night, and feel them. But do I see less or more?

Richard Feynman, "The Feynman Lectures on Physics, Vol. I"

The molecule-like structure of the self-conjugate ^{20}Ne nucleus was first theorized by the pioneers of nuclear cluster physics already more than 50 years ago [HI68, ITH68]. The two low-lying bands of this isotope, the positive-parity $K^\pi = 0^+$ band built upon the ground state and the negative-parity $K^\pi = 0^-$ band built upon the first $J^\pi = 1^-$ state, are believed to form the inversion doublets and exhibit the equivalent $^{16}\text{O} + \alpha$ structure [HI68, FHKE+18]. The appearance of clusterized configurations already in the nuclear ground state is rather exceptional phenomenon in terms of the conventional Ikeda diagrams [ITH68] which predict the formation of cluster structures as excited states close to the corresponding α -decay threshold. This almost unique feature of the ^{20}Ne ground state has attracted significant theoretical attention in the past. Various approaches have been employed in order to study its low-energy structure, including the angular-momentum-projected Hartree-Fock model [OYN04], the resonating group method [MKF75], the 5α generator coordinate method [NYH+75], the antisymmetrized molecular dynamics model [KEH95, Kim04, TKH04], and the generalized Tohsaki-Horiuchi-Schuck-Röpke wave function model [ZRX+12]. In addition, reflection-asymmetric equilibrium densities were predicted within the parity-restored SR-EDF framework, based on both the Gogny [RB11] and relativistic [EKNV14b] interactions. Another interesting feature of this isotope is the suggested dissolution of reflection-asymmetric structures at high angular momenta states by decreasing the equilibrium distance between the two clusters, ^{16}O and α . This is, of course, unexpected because centrifugal effects should in principle elongate the nucleus. Recently, a beyond mean-field study of reflection-asymmetric molecular structures and, in

particular, of the antistretching mechanism in ^{20}Ne was performed within the relativistic MR-EDF framework based on the covariant PC-PK1 functional and the BCS approximation [ZYL⁺16]. It has been pointed out that a special deformation-dependent moment of inertia, governed by the underlying shell structure, could be in part responsible for the rotation-induced dissolution of cluster structures in the negative-parity states.

Furthermore, in addition to clusters in self-conjugate nuclei, the neutron-rich isotopes are interesting in the context of excess neutrons playing the role of molecular bonding between clusterized structures. One such example is the chain of even-even neon isotopes that can be described as an $\alpha + ^{16}\text{O} + xn$ system. The structure of the lightest isotope with such a structure, ^{22}Ne , was previously analyzed with the AMD model [Kim07], and both the molecular orbital bands and the $\alpha + ^{18}\text{O}$ molecular bands has been predicted. Quadrupole collectivity of heavy neon isotopes close to the neutron drip-line was previously studied within the EDF framework based on Gogny interaction [RGER03]. Particularly interesting is the case of ^{24}Ne isotope, where a strong shape-coexisting nature of the ground state was predicted [RGER03]. The neutron-rich neon isotopes have also drawn some attention in the context of nuclear magicity. In particular, a reduction of the $N = 20$ spherical shell gap has been experimentally observed in ^{30}Ne isotope, while a new neutron shell gap was predicted to be formed in ^{26}Ne isotope [SP08].

All things considered, neon isotopic chain, with the formation and dissolution of the low-lying cluster structures, with the appearance of shape-coexistence phenomenon, and with the erosion of old and emergence of new magic numbers, represents a truly rich playground for theoretical considerations. In Ref. [MEK⁺18a] we have studied the structure of even-even neon isotopes within the relativistic MR-EDF framework. Starting from a self-consistent RHB calculation of axially-symmetric and reflection-asymmetric deformation energy surfaces, the collective angular-momentum and parity-conserving states were built using projection and configuration mixing techniques. In the present work, we are further extending that framework by including the projection of intrinsic states onto good neutron and proton numbers. Following the strategy of Ref. [MEK⁺18a], the fully symmetry-restoring framework is employed in a systematic study of quadrupole-octupole collectivity and cluster structures in neon isotopes. The content and the form of the chapter will therefore largely rely on the analysis carried out in Ref. [MEK⁺18a]. In Section 4.1, we will study the ground-state properties of neon isotopic chain, including binding energies, charge radii, and two-neutron separation energies. Furthermore, we will demonstrate the effect of symmetry restoration and configuration mixing on a structure of the ground state and analyze the obtained wave functions in some more detail. In Section 4.2, we will study the low-lying systematics of the neon isotopic chain, including potential energy surfaces projected onto various angular momenta, excitation energies of the low-lying collective states, as well as the transition strengths between them. Detailed spectroscopy of $^{22,24}\text{Ne}$ and $^{32,34}\text{Ne}$ isotopes will additionally be analyzed. Finally, in Section 4.3 we will focus more attention on the particularly interesting case of the self-conjugate ^{20}Ne isotope. The obtained spectroscopic properties will be thoroughly compared to the available experimental data and to the predictions of other theoretical models. In addition, cluster components of collective states in the intrinsic frame will be analyzed.

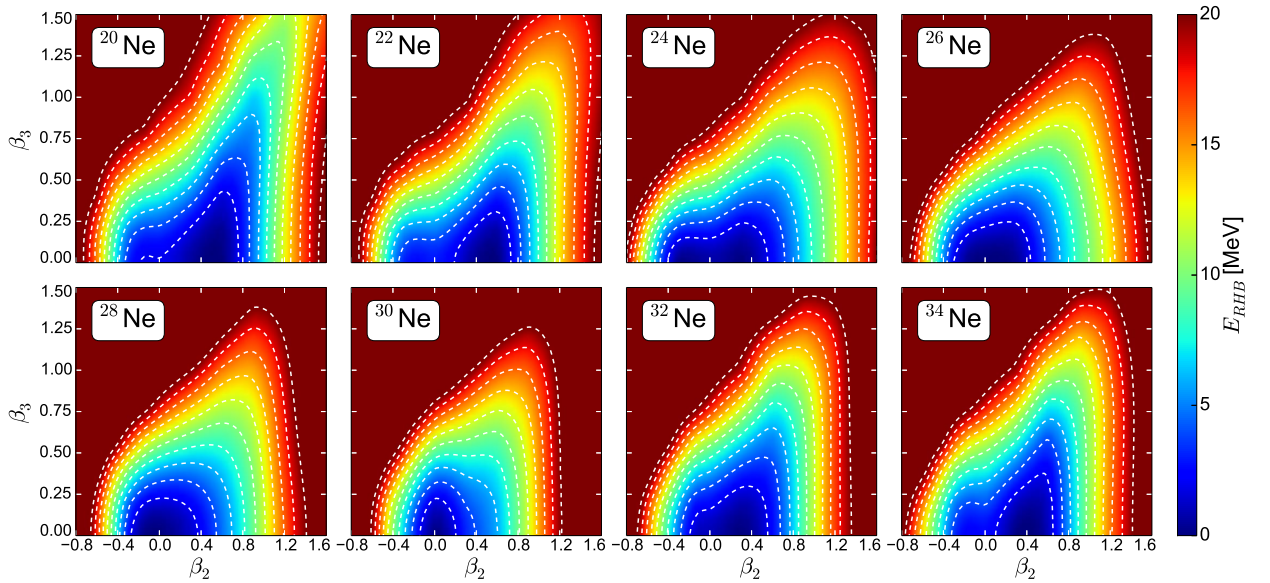


FIGURE 4.1: Self-consistent RHB binding energies of even-even $^{20-34}\text{Ne}$ isotopes, in the $\beta_2 - \beta_3$ plane. For each nucleus, energies are normalized with respect to the energy of the corresponding absolute minimum. Dashed contours are separated by 2 MeV.

4.1. Ground-State Properties of Neon Isotopes

4.1.1 The Mean-Field Analysis

Our analysis of the ground-state properties of even-even neon isotopes starts with the self-consistent RHB calculation. The RHB equations were solved in the configurational space of axially-symmetric harmonic oscillator, by expanding the large and the small component of nuclear spinors in the corresponding bases with $N_{sh} = 10$ and $N_{sh} = 11$, respectively. These calculations cover a wide range of deformations in both the quadrupole and octupole direction, $\beta_2 \in [-0.6, 1.5]$ and $\beta_3 \in [-2.0, 2.0]$, with steps in the oblate, prolate, and octupole direction being $\Delta\beta_2 = 0.15$, $\Delta\beta_2 = 0.3$, and $\Delta\beta_3 = 0.2$, respectively. The obtained binding energies for the entire isotopic chain are shown in Figure 4.1. For each isotope, energies have been normalized with respect to the energy of the corresponding absolute minimum. These minima are found at reflection-symmetric ($\beta_3 = 0$) configurations along the entire isotopic chain, and the corresponding quadrupole deformation parameters, binding energies, and charge radii are listed in Table 4.1. Two of the lightest isotopes considered, ^{20}Ne and ^{22}Ne , are prolate-deformed nuclei with equilibrium quadrupole deformations $\beta_2 \approx 0.5$. By adding two more neutrons, a nearly-degenerate oblate-deformed minimum at $\beta_2 = -0.27$ and prolate-deformed minimum at $\beta_2 = 0.29$ are developed in ^{24}Ne . Further addition of neutrons leads to development of nearly-spherical minima in ^{26}Ne and ^{28}Ne isotopes, and a spherical equilibrium in ^{30}Ne isotope due to the $N = 20$ neutron shell closure. Moving further away from the magic number, the neutron-rich isotopes ^{32}Ne and ^{34}Ne display prolate minima with deformations $\beta_2 = 0.31$

TABLE 4.1: Self-consistent RHB values of the axial quadrupole deformation parameters β_2 in ground states of $^{20-34}\text{Ne}$ isotopes. Axial octupole deformation parameters β_3 vanish in ground states of all isotopes. In addition, equilibrium binding energies (second row) and charge radii (fourth row) are given. The corresponding relative errors with respect to the experimental data, $R_{\text{err}}^{\text{calc.-exp.}} = (E_{\text{B}}^{\text{calc.}} - E_{\text{B}}^{\text{exp.}})/|E_{\text{B}}^{\text{exp.}}|$, on binding energies [WAK+17] and charge radii [AM13], are given in the third and the fifth row, respectively.

| | ^{20}Ne | ^{22}Ne | ^{24}Ne | ^{26}Ne | ^{28}Ne | ^{30}Ne | ^{32}Ne | ^{34}Ne |
|--|------------------|------------------|------------------|------------------|------------------|------------------|------------------|------------------|
| β_2 | 0.51 | 0.50 | -0.25 | -0.04 | -0.05 | 0.00 | 0.31 | 0.43 |
| E_{B} [MeV] | -157.89 | -177.24 | -191.03 | -202.95 | -211.48 | -218.68 | -218.95 | -220.23 |
| $R_{\text{err}}^{\text{calc.-exp.}}$ [%] | 1.6 | 0.3 | 0.4 | -0.6 | -2.2 | -3.6 | -2.6 | -3.0 |
| R_{ch} [fm] | 3.00 | 2.99 | 2.94 | 2.93 | 2.98 | 3.02 | 3.09 | 3.14 |
| $R_{\text{err}}^{\text{calc.-exp.}}$ [%] | -0.2 | 1.3 | 1.4 | 0.2 | 0.5 | - | - | - |

and $\beta_2 = 0.43$, respectively.

Calculated binding energies of equilibrium configurations are listed in the second row of Tab. 4.1 and the corresponding relative errors in comparison with the experimental data [WAK+17], $R_{\text{err}}^{\text{calc.-exp.}} = (E_{\text{B}}^{\text{calc.}} - E_{\text{B}}^{\text{exp.}})/|E_{\text{B}}^{\text{exp.}}|$, are listed in the third row. Overall agreement for lighter isotopes is quite good, while our calculation tends to overestimate binding energy of neutron-rich isotopes. Similar behavior was already observed in the relativistic HFB calculations based on the DD-ME2 functional [EKAV11]. In addition, the large-scale calculations based on the Gogny D1S force reported a systematic drift towards theoretical overbinding in neutron-rich isotopes [HG07]. This anomaly was linked to the imprecise treatment of energy dependence in the neutron matter during fitting procedure and it was fixed in later parameterizations [CGH08, GHGP09]. We note that the DD-PC1 functional was fitted exclusively to data on finite nuclei and that the overbinding of closed-shell systems due to a relatively low effective nucleon mass was noticed already in the very first application [NVR08]. Therefore, it is expected that the largest deviation in Tab. 4.1 is found in the spherical ^{30}Ne isotope. Moreover, the ground-state quadrupole deformation of ^{30}Ne is, in fact, experimentally well-established [SP08] and this overbinding can, at least partially, be attributed to the fact that the obtained spherical state includes the abnormally large amount of pairing correlations. These correlations increase the total binding energy of a nucleus and would normally be absent from the well-deformed state. Generally, it is well known that the choice of the pairing force has a significant impact on the topology of potential energy surfaces. In particular, larger pairing strength drives energy surfaces towards spherical shapes [AAR16], which has a direct and important influence on heights of fission barriers and spontaneous fission half-lives in heavy and superheavy nuclei [KALR10, RGR14]. In this context, one should note that the parameters of pairing force used in this study were originally adjusted to reproduce the pairing gap at the Fermi surface in symmetric nuclear matter as calculated with the Gogny D1S force [TMR09a]. Therefore, there is no guarantee that the same parameters will be optimal for calculations in finite nuclei over the entire nuclide chart. In practice, one could fine tune the pairing strength in order to better reproduce experimental binding

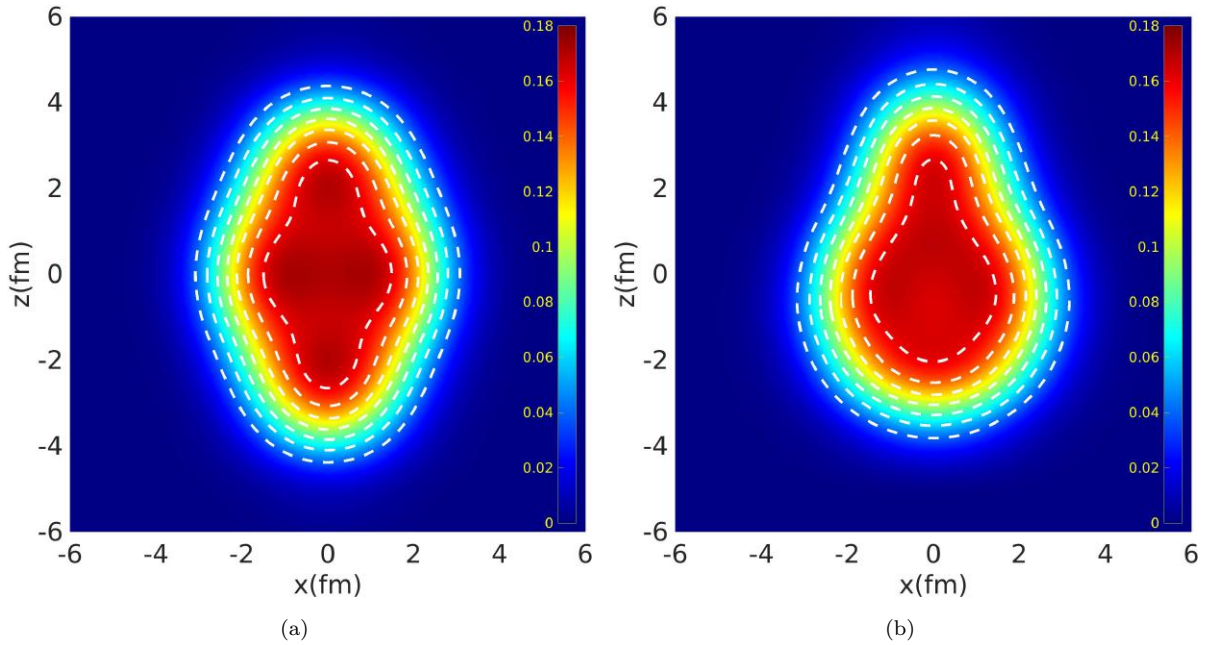


FIGURE 4.2: Nucleon densities (in fm^{-3}) of ^{20}Ne in the $x - z$ plane of the intrinsic frame of reference. Left panel (a): Density corresponding to the absolute minimum $(\beta_2, \beta_3) = (0.51, 0.0)$ of the self-consistent RHB energy surface [see Fig. 4.1]. Right panel (b): Density corresponding to the absolute minimum $(\beta_2, \beta_3) = (0.45, 0.40)$ of the symmetry-restored $J^\pi = 0^+$ energy surface [see Fig. 4.3].

energies or available empirical pairing gaps in finite nuclei. However, for the sake of staying true to the principle of globality, we choose to stick to the exactly same parameters of the pairing interaction over the entire isotopic chain.

Calculated charge radii of equilibrium configuration are given in the fourth row of Table 4.1. They compare rather favorably with the experimental data [AM13], as well as with the relativistic HFB calculations based on the DD-ME2 functional [EKAV11]. The ^{20}Ne ground state is associated with a large quadrupole deformation, which gives rise to the intrinsically-deformed charge distribution and, consequently, large charge radius. On the other hand, the smallest charge radius is found in ^{24}Ne isotope, due to the $d_{5/2}$ subshell closure. Further addition of neutrons leads to the enhancement of charge radii in heavier isotopes. However, the charge radius of ^{20}Ne is first exceeded only in ^{30}Ne , an isotope with twice as large number of neutrons. The large quadrupole deformation of the ^{20}Ne ground state is mirrored in its deformed intrinsic density distribution, which is plotted in the left panel of Figure 4.2.

4.1.2 The Effect of Collective Correlations

The mean-field approach is characterized by breaking of various symmetries that eventually need to be recovered. Restoration of angular momentum, particle number, and

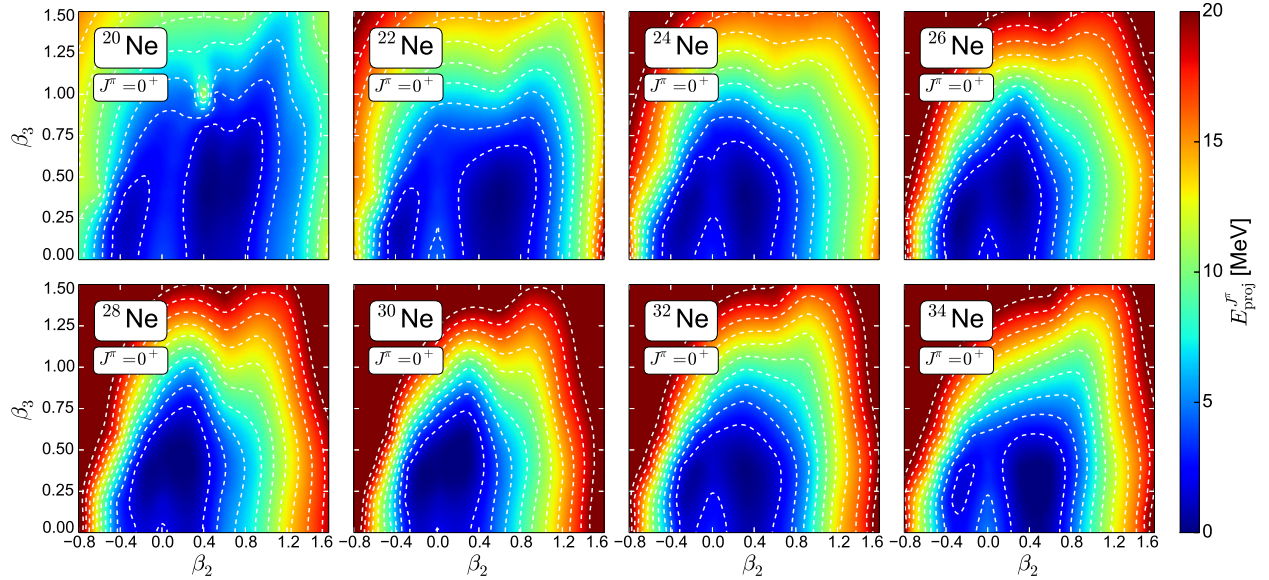


FIGURE 4.3: Angular momentum-, particle number-, and parity-projected energy surfaces of even-even $^{20-34}\text{Ne}$ isotopes, for spin and parity $J^\pi = 0^+$ in the $\beta_2 - \beta_3$ plane. For each nucleus, energies are normalized with respect to the binding energy of the corresponding absolute minimum. Dashed contours are separated by 2 MeV.

parity symmetry were simultaneously performed within our study, using the tools described in previous chapters. Discretization parameters of the corresponding integrals, that is $N_\beta = 27$ for AMP and $N_\varphi = 9$ for PNP, were verified to ensure satisfactory convergence for all values of angular momenta $0 \leq J \leq 7$ and a broad range of quadrupole and octupole deformations [for more details, see Chapter 3]. In order to demonstrate the influence of symmetry restoration on topology of the ground-state potential energy surfaces, in Figure 4.3 we show the angular-momentum, particle-number, and parity-projected potential energy surfaces of ground states ($J^\pi = 0^+$) of $^{20-34}\text{Ne}$ isotopes in $\beta_2 - \beta_3$ plane. A prominent feature in Fig. 4.3 is the fact that parity projection shifts the position of all the minima towards reflection-asymmetric ($\beta_3 \neq 0$) configurations. Angular momentum and particle number projections additionally modify the topography of mean-field energy maps by lowering deformed configurations, thereby forming local oblate-deformed minima for all isotopes. In particular, an absolute minimum for the ^{20}Ne isotope is found at the octupole-deformed ($\beta_2 = 0.45, \beta_3 = 0.4$) configuration. The characteristic pear-like density distribution which corresponds to the equivalent (β_2, β_3) configuration in the intrinsic frame¹ is plotted in the right panel of Fig. 4.2.

However, the obtained energy surfaces are rather soft in both the β_2 and β_3 directions, indicating that configuration mixing calculations will play a crucial role for a quantitative description of the structure of neon isotopes. Solving the corresponding HWG equation gives us an access to the correlated ground states, as well as to the structure of the excited states. Here, one should recall that parameters of the effective interaction [NVR08] have

¹Of course, density distribution of the symmetry-restored $J^\pi = 0^+$ state in the laboratory frame for any (β_2, β_3) combination would be spherically symmetric.

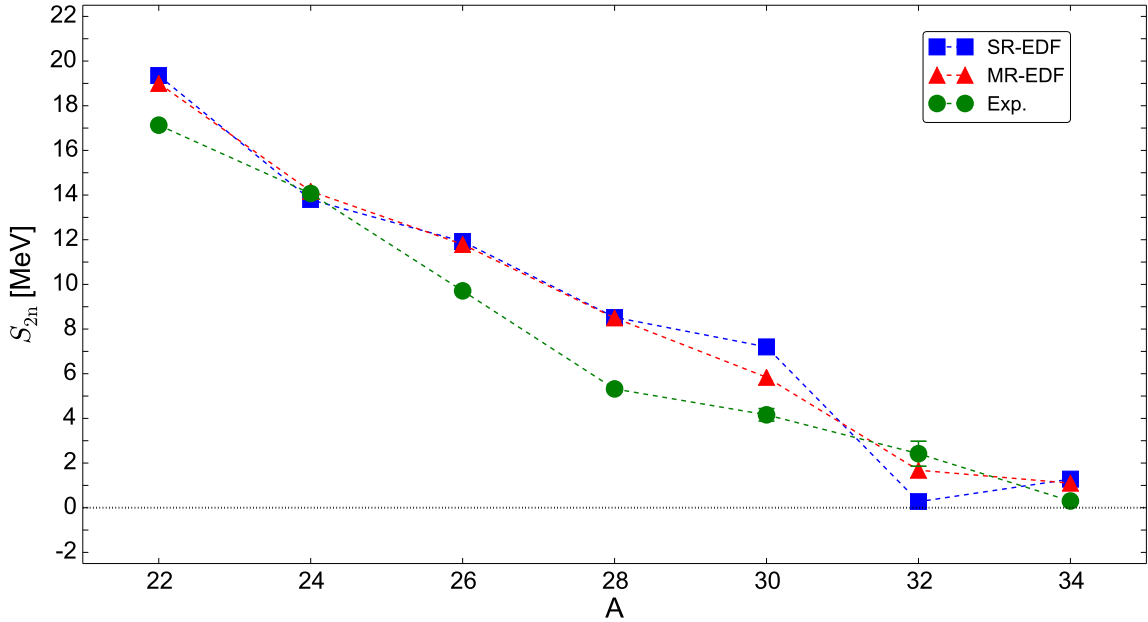


FIGURE 4.4: Two-neutron separation energies of $^{22-34}\text{Ne}$ isotopes. The SR-EDF values obtained on a mean-field level (squares), and MR-EDF values obtained after configuration mixing of symmetry-restored configurations (triangles), are compared to the available experimental data [WAK⁺17].

been fitted to experimental data on binding energies of deformed nuclei on a mean-field level. This means that some of the correlations related to the restoration of rotational symmetry have already been implicitly included in the functional and the subsequent restoration of symmetries and configuration mixing may represent double counting of those correlations². Therefore, the absolute values of binding energies obtained after configuration mixing should not be directly compared to the experimental data. Nevertheless, the differences between binding energies in each nucleus, which give rise to the excitation spectra, as well as differences between the ground-state binding energies in different isotopes, which give rise to the neutron separation energies, do have physical meaning. Therefore, in order to analyze the predicted stability of neon isotopes against the two-neutron emission, in Figure 4.4 we display the two-neutron separation energies $S_{2n} = E_{0^+}(A-2, Z) - E_{0^+}(A, Z)$ for even-even $^{22-34}\text{Ne}$ isotopes. The MR-EDF values obtained after mixing of symmetry-restored configurations are compared with the available experimental data [WAK⁺17] and, to quantify correlation effects, with the SR-EDF results obtained on the RHB level. The SR-EDF results for the two-neutron separation energies, that is, the differences between binding energies of the corresponding equilibrium minima, generally overestimate the experimental values, except for ^{32}Ne . It appears

²One could account for this double counting by adjusting the functional to the pseudodata, obtained by subtracting correlation effects from experimental masses. Alternatively, parameters of the functional could be fitted directly on a beyond mean-field level, as was, for example, done for the Gogny D1M effective interaction [GHGP09].

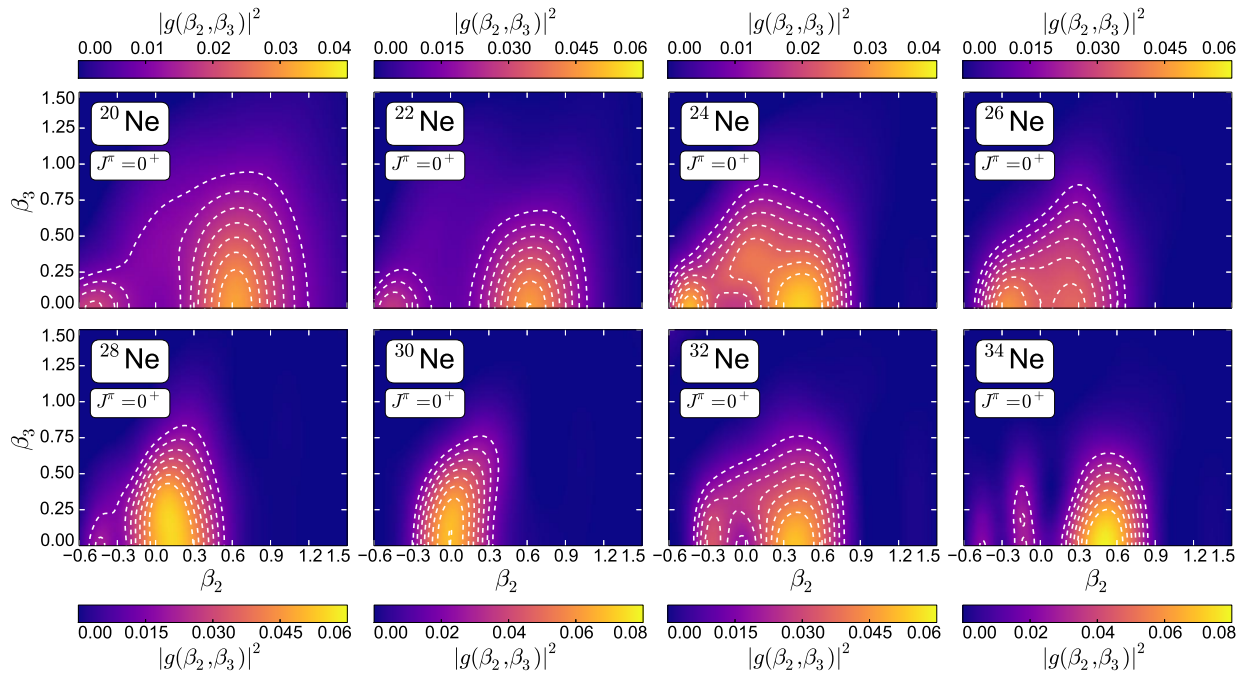


FIGURE 4.5: Amplitudes of collective wave functions squared $|g(\beta_2, \beta_3)|^2$ of the ground states of $^{20-34}\text{Ne}$ isotopes. Dashed contours in the $\beta_2 - \beta_3$ plane successively denote a 10% decrease starting from the largest value of the amplitude.

that for $A < 30$ configuration mixing does not produce a significant impact on the calculated two-neutron separation energies. Closer to the dripline, however, one notices that the inclusion of collective correlations through symmetry restoration and configuration mixing starts to play much more important role, shifting calculated values closer to the experimental ones. In addition, we have verified that ^{34}Ne is indeed the last stable neon isotope, since both the two-neutron and the four-neutron separation energies for ^{36}Ne are calculated to be negative. A similar improvement of the predicted two-neutron separation energies for neon isotopes was also obtained in the angular-momentum-projected configuration mixing study based on the Gogny D1S interaction [RGER03]. However, the calculated S_{2n} value for ^{34}Ne reported therein was slightly negative, that is, this isotope was predicted to be unstable against the two-neutron emission.

Even though the ground-state spectroscopic quadrupole moments vanish identically in even-even nuclei, it is instructive to calculate expectation values of quadrupole deformation parameters in correlated ground states. These values can be obtained by averaging the deformation parameter β_2 over the entire $\beta_2 - \beta_3$ plane, with the wave functions of each collective state J_α^π playing the role of corresponding weights [see Eq. (2.40)]. In Figure 4.5 we display the amplitudes squared of the ground-state collective wave functions for $^{20-34}\text{Ne}$. As noted before, this quantity is not an observable, but still it provides a useful insight into the structure of correlated ground states. In contrast to the mean-field RHB equilibrium minimum which corresponds to a single configuration in the (β_2, β_3) plane, the amplitude of the ground state collective wave function manifests the degree of shape fluctuations in both quadrupole and octupole directions. In the left panel of Figure 4.6 we plot the MR-EDF average β_2 deformation values for $^{20-34}\text{Ne}$ isotopes in

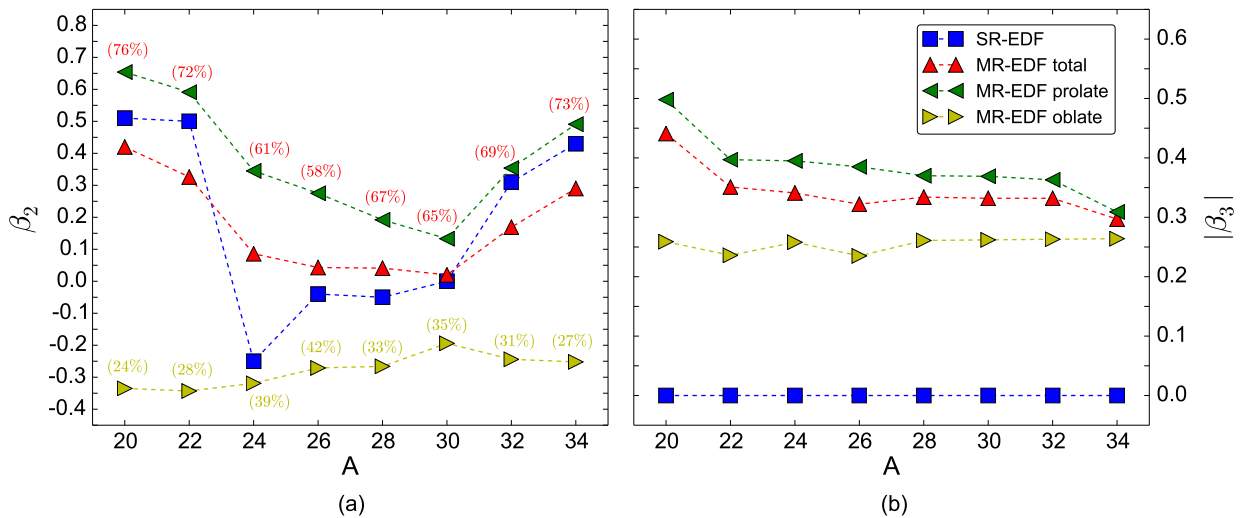


FIGURE 4.6: Deformation parameters β_2 (left panel (a)) and $|\beta_3|$ (right panel (b)) of $^{20-34}\text{Ne}$ isotopes that correspond to self-consistent minima on the SR-EDF level, in comparison with the MR-EDF values of the corresponding correlated ground states. The deformations obtained by averaging over only prolate (triangle left) and only oblate (triangle right) configurations, as well as their respective contributions to the total collective wave function, are also shown.

comparison to deformations that correspond to the self-consistent minima on the SR-EDF level. Since the contributions of oblate configurations to the total collective wave functions are larger than 20% over the entire isotopic chain, we additionally display the β_2 deformations obtained by averaging over only prolate (left triangle) and only oblate (right triangle) configurations. In parentheses, we include the respective contributions to the total collective wave function from both prolate and oblate configurations. One notices that oblate configurations give a significant contribution for all isotopes, and this contribution is more pronounced in $^{24-32}\text{Ne}$. The nucleus ^{24}Ne , which exhibits nearly degenerate oblate and prolate minima on the mean-field level, preserves this structure even after symmetry restoration and configuration mixing. In particular, dominant component of the correlated ground state is prolate-deformed and peaks at $\beta_2 \approx 0.35$, but nearly 40% of the collective wave function spreads over the oblate side and peaks at $\beta_2 \approx 0.3$. A similar behavior is also found in the ^{26}Ne isotope. The semimagic nucleus ^{30}Ne is found to be very weakly prolate-deformed, in contrast to the large ground-state quadrupole deformation deduced from the experiment [SP08]. By removing two neutrons, the nearly spherical structure of the ground state appears to be preserved in ^{28}Ne . The addition of two neutrons, however, leads to the formation of a barrier at the spherical configuration of ^{32}Ne . The resulting collective wave function resembles the shape-coexisting structure, even though the prolate component is significantly more pronounced. In the right panel of Fig. 4.6 we plot the corresponding values of the octupole deformation parameter. Since $\langle\beta_3\rangle$ vanishes identically for all collective states with good parity, we plot instead the average values of the corresponding modulus [see Eq. (2.41)]. The $\langle|\beta_3|\rangle$ values quantify

the role of octupole degree of freedom in the analyzed ground states. Obviously, octupole collectivity is very pronounced in ^{20}Ne isotope, while it is somewhat weaker and approximately constant over the rest of the isotopic chain, with average values varying between $\langle|\beta_3|\rangle = 0.30$ and $\langle|\beta_3|\rangle = 0.35$.

4.2. Excited-State Properties of Neon Isotopes

4.2.1 Systematics of the Low-Lying States

In addition to the ground-state properties that were discussed in the previous section, the MR-EDF framework enables us to access properties of excited states of atomic nuclei. Our analysis of the excited states of neon isotopes starts with the inspection of symmetry-restored potential energy surfaces. In Figures 4.7 and 4.8 we show the angular-momentum, particle-number, and parity-projected potential energy surfaces of the positive-parity states $J^\pi = 2^+, 4^+$ of $^{20-34}\text{Ne}$ isotopes in $\beta_2 - \beta_3$ plane. Note that the angular momentum projection for the spherical configuration is well defined only for $J^\pi = 0^+$ and it is therefore omitted from these plots. The $J^\pi = 2^+$ surfaces still preserve to a significant extent the oblate-deformed components that were present in the ground-state potential energy surfaces of Fig. 4.3. In particular, absolute (even though shallow) minima in both the ^{24}Ne and ^{28}Ne isotope are found at oblate-deformed configurations. By further rotating a nucleus, prolate-deformed minima are stabilized on $J^\pi = 4^+$ surfaces for all isotopes. Furthermore, in Figures 4.9 and 4.10 we show the angular-momentum, particle-number, and parity-projected potential energy surfaces of the negative-parity states $J^\pi = 1^-, 3^-$ of $^{20-34}\text{Ne}$ isotopes in $\beta_2 - \beta_3$ plane. Note that parity projection for reflection-symmetric ($\beta_3 = 0$) configurations is well defined only for positive parity, hence these configurations are omitted in Figs. 4.9 and 4.10. The negative-parity-projected surfaces are rather soft in the octupole direction. The absolute minima are located on the prolate side of the $\beta_2 - \beta_3$ plane and they are separated by at least 4 MeV from the corresponding $J^\pi = 0^+$ absolute minima. Common feature of

TABLE 4.2: Calculated ground-state band spectroscopic quadrupole moments for $J^\pi = 2^+, 4^+, 6^+$ in the even-even $^{20-34}\text{Ne}$ isotopes. Additionally, in the last row we list the number of configurations that were taken into account within the configuration mixing scheme.

| | ^{20}Ne | ^{22}Ne | ^{24}Ne | ^{26}Ne | ^{28}Ne | ^{30}Ne | ^{32}Ne | ^{34}Ne |
|---|------------------|------------------|------------------|------------------|------------------|------------------|------------------|------------------|
| $Q_2^{\text{spec}}(2_1^+) [\text{efm}^2]$ | -15.00 | -14.01 | -4.71 | -8.26 | -4.36 | -13.84 | -12.26 | -14.80 |
| $Q_2^{\text{spec}}(4_1^+) [\text{efm}^2]$ | -19.89 | -18.27 | -9.02 | -14.50 | -14.79 | -20.17 | -16.81 | -19.50 |
| $Q_2^{\text{spec}}(6_1^+) [\text{efm}^2]$ | -20.47 | -21.11 | -11.70 | -17.78 | -22.74 | -23.28 | -17.48 | -21.33 |
| $N^{\text{SR-EDF}}$ | 118 | 112 | 111 | 115 | 118 | 113 | 115 | 115 |

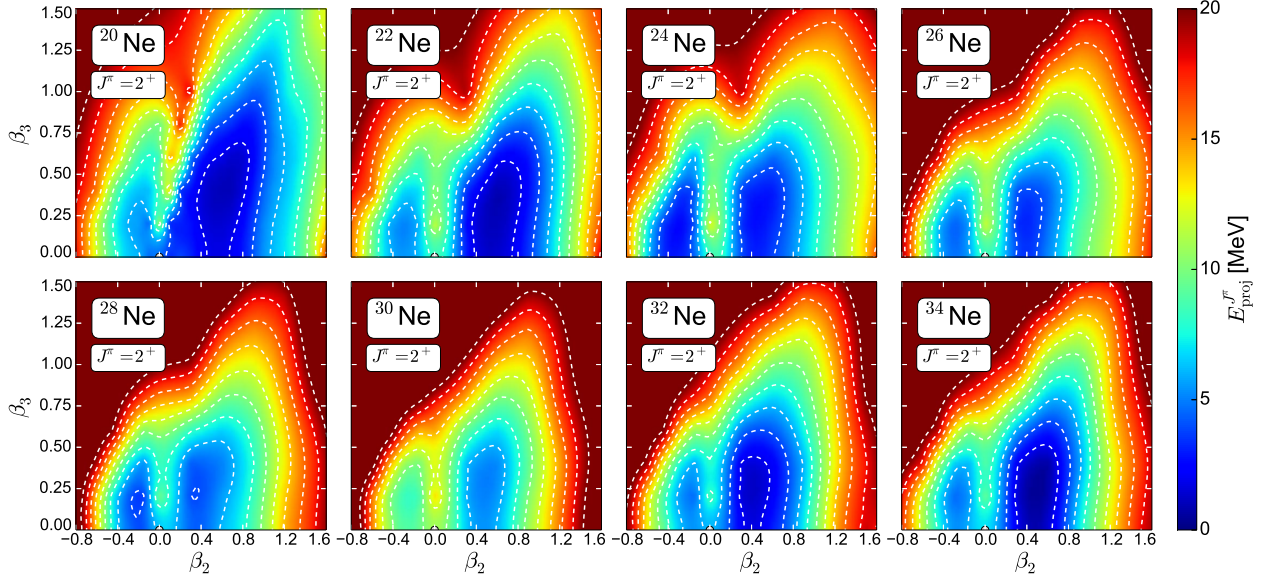


FIGURE 4.7: Angular momentum-, particle number-, and parity-projected energy surfaces of even-even $^{20-34}\text{Ne}$ isotopes, for spin and parity $J^\pi = 2^+$ in the $\beta_2 - \beta_3$ plane. For each nucleus, energies are normalized with respect to the binding energy of the corresponding $J^\pi = 0^+$ absolute minimum. Dashed contours are separated by 2 MeV.

all projected energy maps is that restoration of symmetries significantly modifies the initial topology of each map, indicating that configuration mixing calculations will play a crucial role for a quantitative description of the structure of neon isotopes. In Table 4.2 we therefore list the number of configurations $N^{\text{SR-EDF}}$ that were taken into account for each isotope within the configuration mixing scheme. As explained earlier, a set of RHB states was initially generated on a discretized mesh in the $\beta_2 - \beta_3$ plane. Configurations

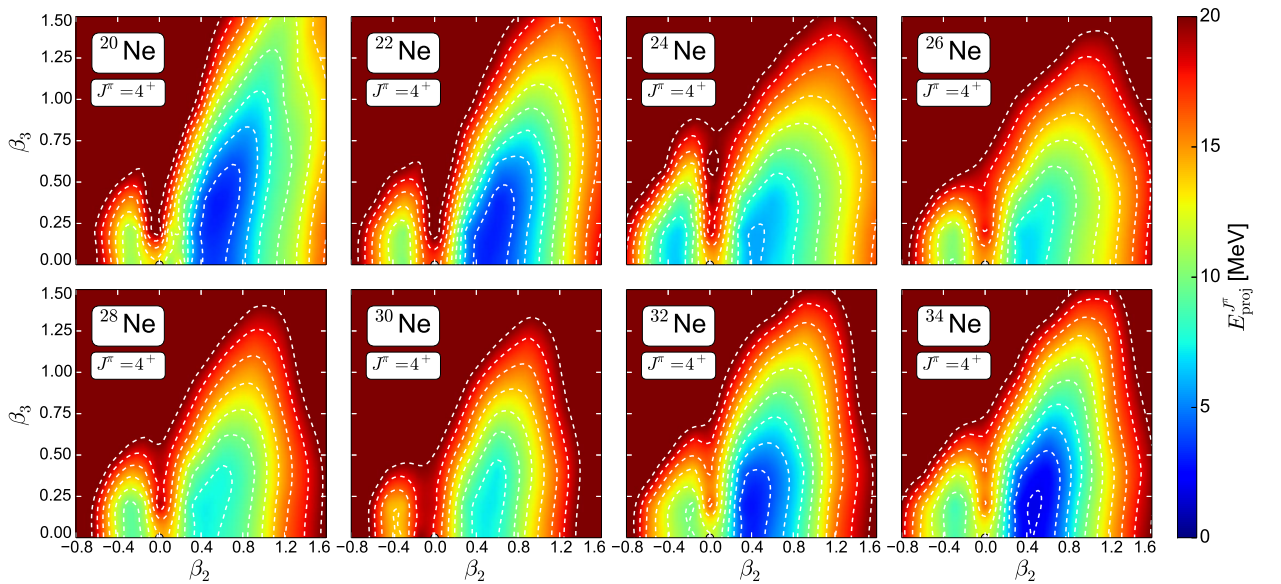


FIGURE 4.8: Same as in the caption to Figure 4.7, but for spin and parity $J^\pi = 4^+$.

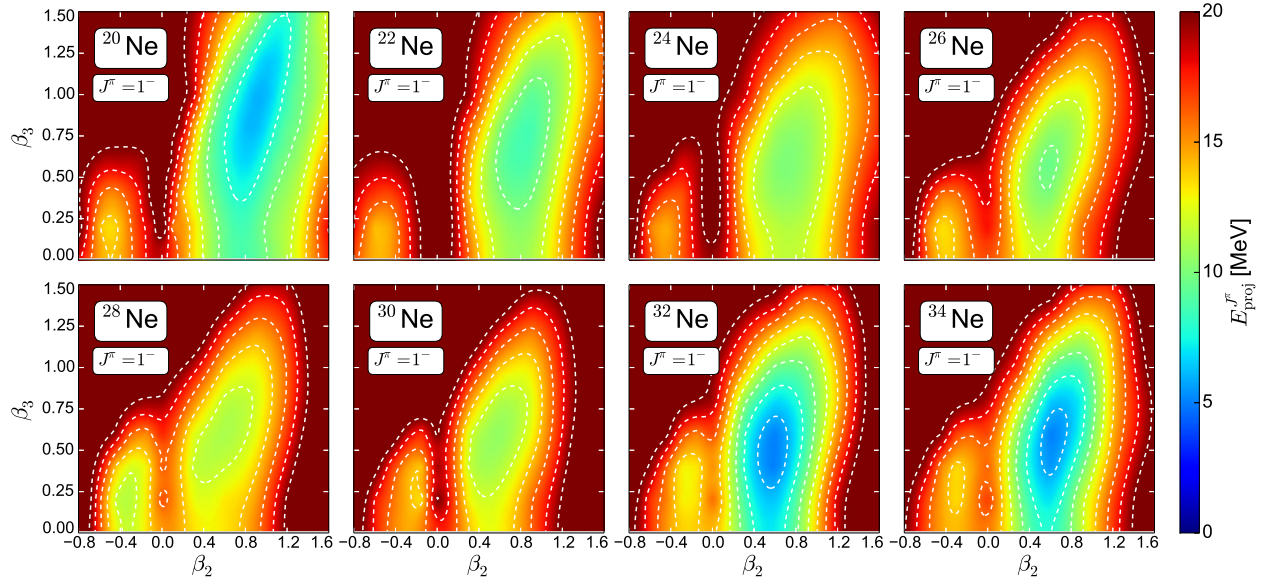


FIGURE 4.9: Angular momentum-, particle number-, and parity-projected energy surfaces of even-even $^{20-34}\text{Ne}$ isotopes, for spin and parity $J^\pi = 1^-$ in the $\beta_2 - \beta_3$ plane. For each nucleus, energies are normalized with respect to the binding energy of the corresponding $J^\pi = 0^+$ absolute minimum. Dashed contours are separated by 2 MeV.

with binding energies that are much higher than energy of the equilibrium configuration (roughly 20 MeV and above) are eliminated from the basis. In this way, one keeps the number of configurations that are being mixed between 110 and 120. Of course, the exclusion of such high-energy states does not influence the predictive power of a model that ultimately aims to describe the low-lying nuclear structure. The remaining states are projected onto good quantum numbers and further mixed within the GCM framework.

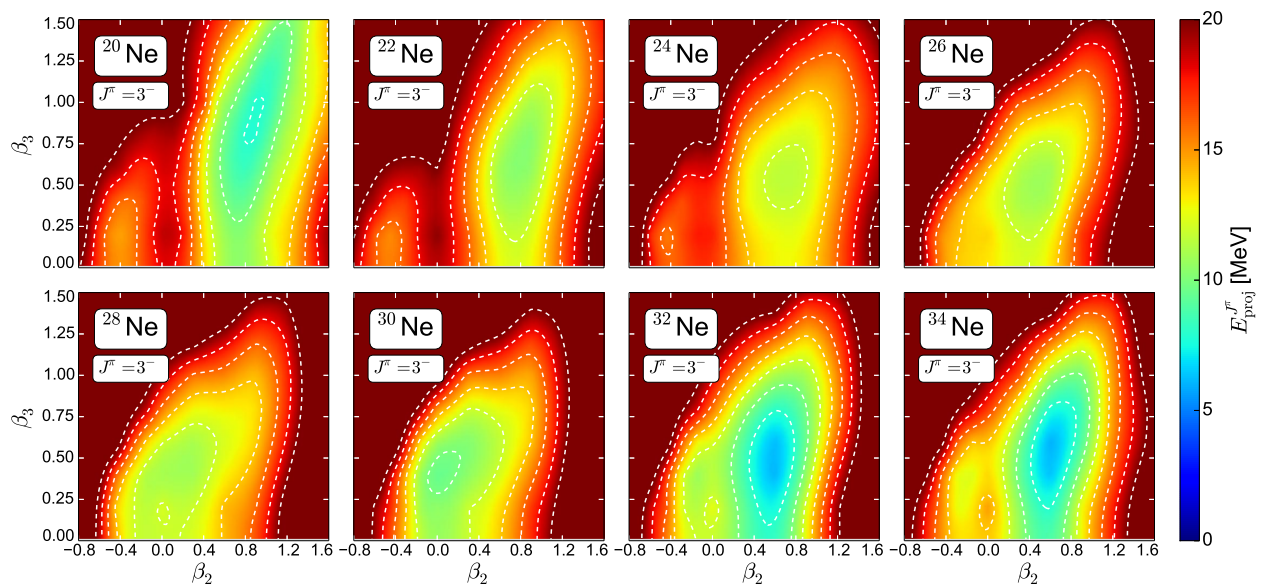


FIGURE 4.10: Same as in the caption to Figure 4.9, but for spin and parity $J^\pi = 3^-$.

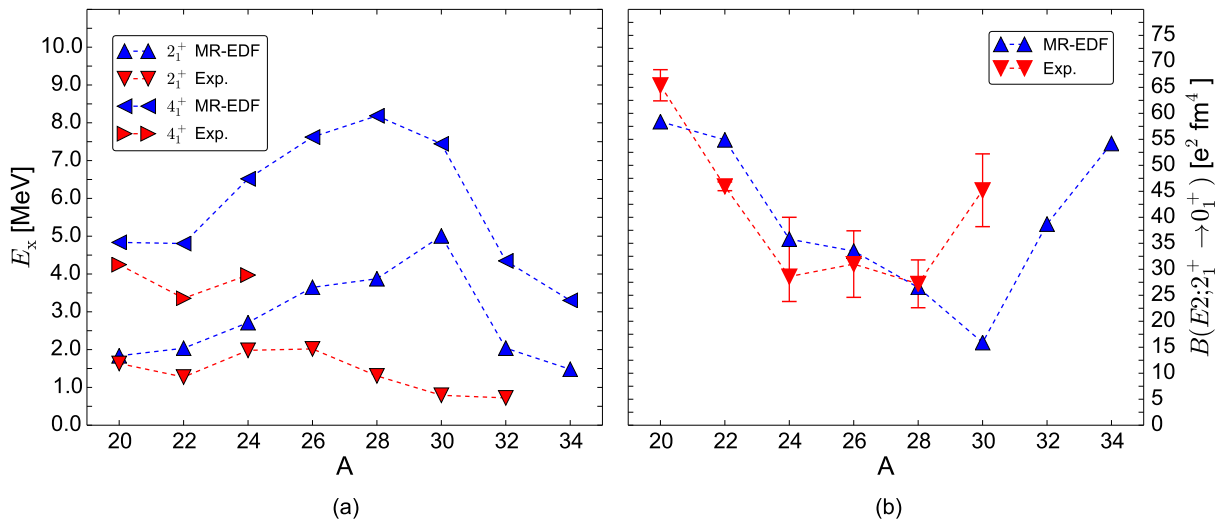


FIGURE 4.11: Calculated excitation energies of the 2_1^+ and 4_1^+ states [left panel (a)] and the transition strengths $B(E2; 2_1^+ \rightarrow 0_1^+)$ [right panel (b)] in even-even $^{20-34}\text{Ne}$ isotopes, compared with the available experimental data [NNDC, PSSH16].

The obtained excitation energies of the 2_1^+ and 4_1^+ states in $^{20-34}\text{Ne}$ isotopes are plotted in the left panel of Fig. 4.11 and compared to the available experimental data. Predictions of our model for lighter isotopes $^{20-24}\text{Ne}$ are in rather good agreement with data. However, when approaching the $N = 20$ neutron shell the theoretical results begin to diverge from experiment, and this is especially pronounced in the ^{30}Ne isotope. This discrepancy originates from the fact that the DD-PC1 functional predicts the $N = 20$ neutron shell closure even for the very neutron-rich isotopes. On the other hand, the breakdown of the $N = 20$ neutron magic number is experimentally a well-established phenomenon [SP08], leading to the large quadrupole deformation in the ground state of ^{30}Ne isotope. We note that a similar issue occurred in a previous study of ^{32}Mg based on the relativistic functional PC-F1 [NVR06a], as well as in some calculations based on non-relativistic EDFs, e.g., the SLy4 effective interaction [HBC⁺00]. In addition, the present study is restricted to axial shapes, whereas in some of the heavier isotopes additional degrees of freedom, such as triaxial, could play an important role.

The calculated electric transition rates from these 2_1^+ states to the corresponding ground states are displayed in the right panel of Fig. 4.11 and compared with the available data. Theoretical results reproduce the experimental values rather well over the entire isotopic chain. The only exception is ^{30}Ne isotope where, because of the predicted $N = 20$ neutron shell closure, we obtain the $B(E2; 2_1^+ \rightarrow 0_1^+)$ value that is much smaller than the corresponding experimental value. Furthermore, in Table 4.2 we list the calculated ground-state band spectroscopic quadrupole moments for neon isotopic chain. In comparison to the previously reported values that were calculated without the particle number projection [MEK⁺18a], the newly-obtained values of $Q_2^{\text{spec}}(2_1^+)$ are systematically reduced in all isotopes. This phenomenon can be understood as a consequence of the fact

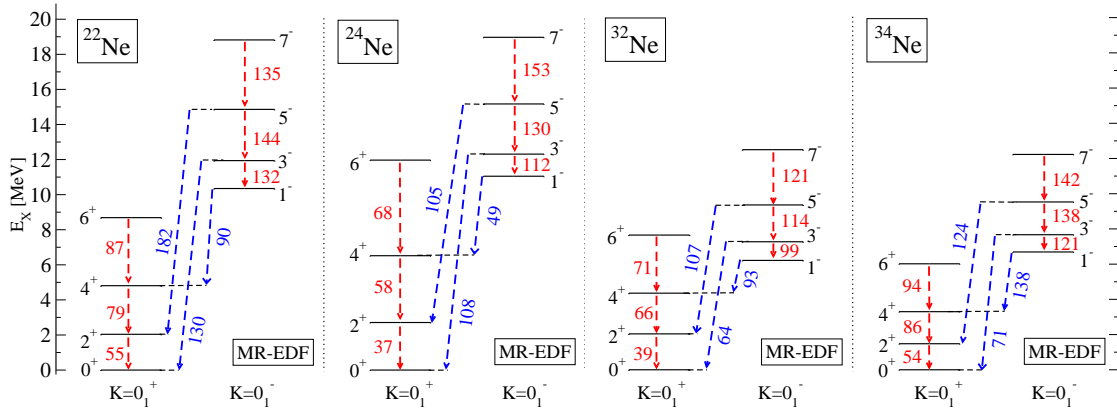


FIGURE 4.12: Calculated low-energy spectra of $^{22,24}\text{Ne}$ (left panel) and $^{32,34}\text{Ne}$ (right panel). The E2 reduced transition strengths within the bands (red color, in $e^2\text{fm}^4$) and E3 transition strengths between the bands (blue color, in $e^2\text{fm}^6$) are also shown.

that PNP additionally lowers energies of the oblate-deformed configurations, thereby increasing their relative contribution to the 2_1^+ collective wave functions and, consequently, reducing the corresponding spectroscopic quadrupole moments. When compared to the available experimental data³ for ^{20}Ne , namely $Q_2^{\text{spec}}(2_1^+)_{B(E2)} = 16.5 \pm 0.5 \text{ efm}^2$ [PBSH16] and $Q_2^{\text{spec}}(2_1^+)_{RE} = 23 \pm 3 \text{ efm}^2$ [Sto05], this accounts to reduction from -16.61 efm^2 [MEK+18a] to -15.00 efm^2 , therefore somewhat underestimating the former experimental value⁴. Empirical value for ^{22}Ne , $Q_2^{\text{spec}}(2_1^+)_{RE} = 19 \pm 4 \text{ efm}^2$ [Sto05], is underestimated by a similar amount. The 2_1^+ states in $^{24-28}\text{Ne}$ isotopes still preserve a significant contribution from oblate-deformed configurations, yielding somewhat smaller absolute values for the spectroscopic quadrupole moments. Increasing angular momentum stabilizes the prolate-deformed shapes and this is consistent with larger absolute values for the spectroscopic quadrupole moments of the 4_1^+ and 6_1^+ states. Notable exception is ^{24}Ne isotope where oblate configurations remain relevant even at high angular momenta, making its $Q_2^{\text{spec}}(6_1^+)$ value pronouncedly lower than in other isotopes.

4.2.2 Structure of the Neutron-Rich Isotopes

To conclude this section, let us study in a bit more detail the spectroscopic properties of a chosen set of neutron-rich isotopes. In the left panel of Figure 4.12 we display the detailed excitation spectra for ^{22}Ne and ^{24}Ne isotopes. The E2 transition strengths within

³Two of the most common ways of empirically estimating the nuclear spectroscopic quadrupole moment are (i) extracting $Q_2^{\text{spec}}(J^\pi)_{B(E2)}$ from measured electric transition strengths and (ii) determining $Q_2^{\text{spec}}(J^\pi)_{RE}$ using the so-called reorientation effect [BGR56]. The fact that the ratio of these two quantities for 2_1^+ state in ^{20}Ne equals to roughly 1.4 is still not completely understood.

⁴In other words, the model that includes PNP (and is thereby formally superior to the model without PNP) actually worsens predictions as compared to the experiment. Peculiar as it may seem, it reminds me of a comment made by an experienced colleague at one of the workshops I attended. While discussing a similar issue, he remarked: *Just because it agrees with the experiment it doesn't mean it is correct.* I find this statement more profound now than the first time I heard it.

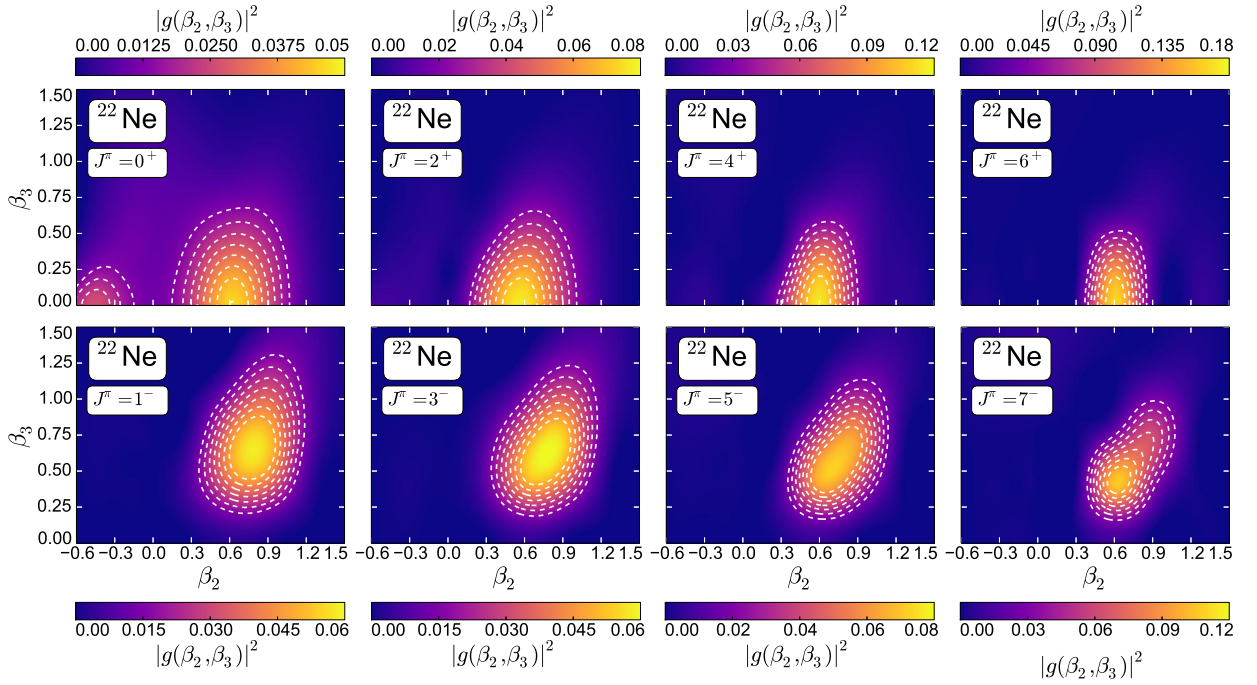


FIGURE 4.13: Amplitudes of collective wave functions squared $|g(\beta_2, \beta_3)|^2$ of the low-energy levels in ^{22}Ne . Dashed contours in the $\beta_2 - \beta_3$ plane successively denote a 10% decrease starting from the largest value of the amplitude.

the bands and E3 transition strengths between the bands are also shown. When compared to the ground-state band of ^{22}Ne , adding just two more neutrons significantly stretches the ground-state band of ^{24}Ne . Such pronounced differences in band structures should be reflected in the corresponding collective wave functions, whose amplitudes squared are given

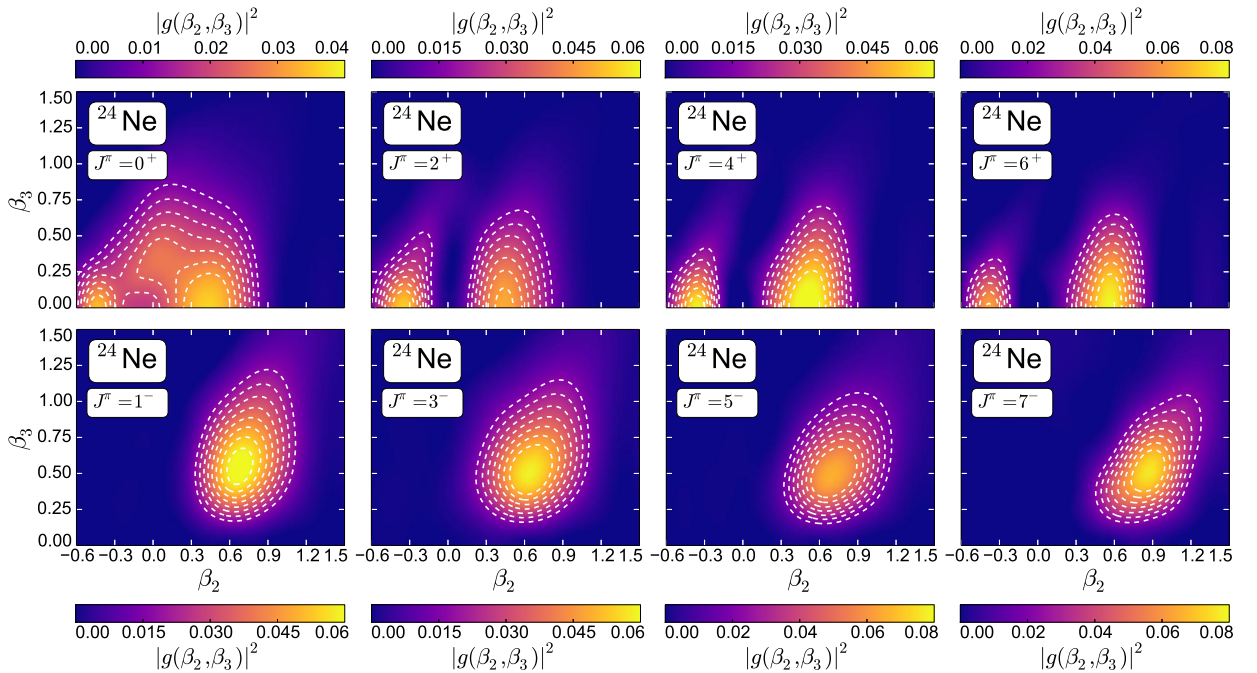
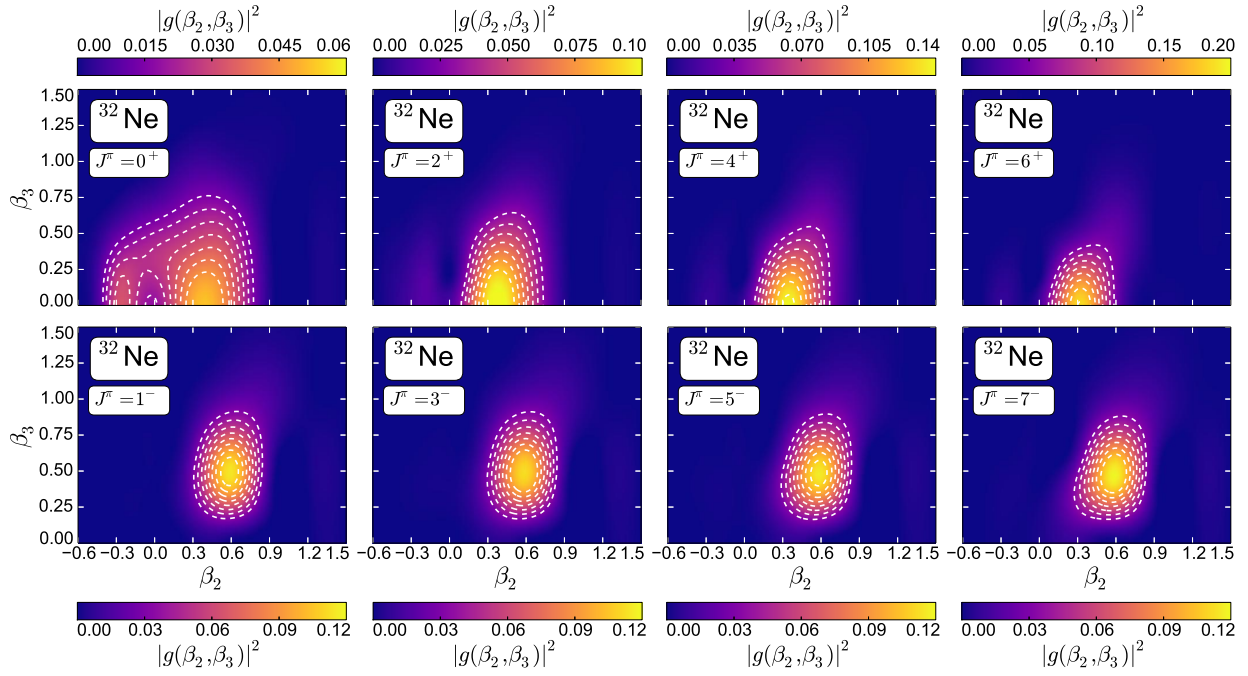
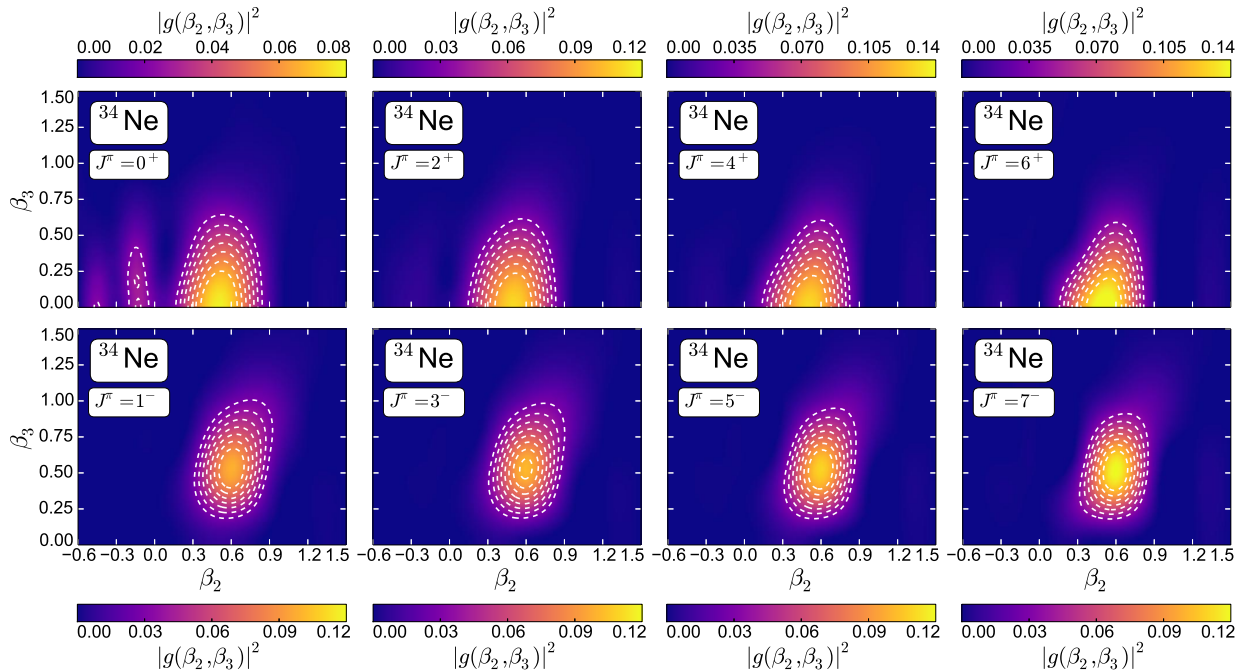


FIGURE 4.14: Same as in the caption to Figure 4.13, but for ^{24}Ne isotope.


 FIGURE 4.15: Same as in the caption to Figure 4.13, but for ^{32}Ne isotope.

in the upper rows of Figures 4.13 and 4.14. While, as discussed before, the ground state of both isotopes contains significant contributions from oblate configurations, the ^{22}Ne isotope becomes pronouncedly prolate-deformed at higher angular momenta. This is in contrast with the situation encountered in ^{24}Ne isotope, where even the wave function of the high-energy 6_1^+ state contains almost 40% of oblate-deformed admixtures. Differences in the structure of collective states are, in addition to the spectroscopic quadrupole moments


 FIGURE 4.16: Same as in the caption to Figure 4.13, but for ^{34}Ne isotope.

[see Table 4.2], also mirrored in differences of the corresponding transition strengths. In particular, the obtained $E2$ transition strengths within the ground-state band of ^{24}Ne are significantly reduced as compared to those in ^{22}Ne isotope. On the other hand, energies of the negative-parity bands remain rather similar in both isotopes. The corresponding amplitudes of the collective wave functions squared, which are given in the lower rows of Figs. 4.13 and 4.14, are spread over large β_3 values on a prolate side of the $\beta_2 - \beta_3$ plane. The increase of angular momentum enhances the average β_2 deformation of negative-parity states in ^{24}Ne , leading to the gradual increase of the corresponding intraband transition strengths. This trend is reversed in ^{22}Ne isotope. There, the average β_2 actually reduces with the increase of angular momentum, which explains the suppression of the $7_1^- \rightarrow 5_1^-$ transition strength as compared to the $5_1^- \rightarrow 3_1^-$ transition. Even though at this place we do not engage in an elaborate discussion on the structure of other excited bands, they are in practice also accessible with our model. Let us only mention that the calculated energies of 0_2^+ and 2_2^+ states in ^{24}Ne isotope (6.76 MeV and 5.83 MeV, respectively) are significantly lower than energies of the corresponding states in ^{22}Ne isotope (9.33 MeV and 9.96 MeV, respectively), thus pointing towards the presence of strong shape coexistence in ^{24}Ne . Moreover, in agreement with the experimental data, the calculated 2_2^+ state is found below both the 0_2^+ and the 4_1^+ state in this isotope.

In the right panel of Figure 4.12 we display the detailed excitation spectra for two of the most neutron-abundant neon isotopes, ^{32}Ne and ^{34}Ne . The corresponding amplitudes of collective wave functions squared are given in Figures 4.15 and 4.16. Both isotopes are predicted to be stable against two-neutron emission and, moreover, the calculated two-neutron separation energies are found to be in a very good agreement with the experimental data [see Fig. 4.4]. The ground-state band spectrum of ^{32}Ne is similar to that of lighter ^{22}Ne isotope, but the calculated $B(E2; 2_1^+ \rightarrow 0_1^+)$ transition is rather small and closer to that of the shape-coexisting ^{24}Ne . The ground-state band spectrum of ^{34}Ne , which is built on the prolate-deformed 0_1^+ state, is significantly compressed. In particular, energies of the 2_1^+ and 4_1^+ states are found to be the lowest over the entire isotopic chain, while the calculated $B(E2; 2_1^+ \rightarrow 0_1^+)$ transition is rather large and comparable to the one in ^{22}Ne isotope. On the other hand, the negative-parity spectra of $^{32,34}\text{Ne}$ isotopes are rather similar and the corresponding bandheads are found at relatively low energies, indicating pronounced collectivity.

4.3. Structure of the Self-Conjugate ^{20}Ne Isotope

4.3.1 Spectroscopy of Collective States

The ^{20}Ne isotope represents a very interesting example of a nucleus that exhibits admixtures of cluster configurations already in the ground state. Previous studies based on both the non-relativistic [RB11] and relativistic [EKNV14b] EDF framework have shown that the reflection-asymmetric $^{16}\text{O}+\alpha$ structure appears already on the SR-EDF level. However, in order to obtain a quantitative description of the corresponding low-energy

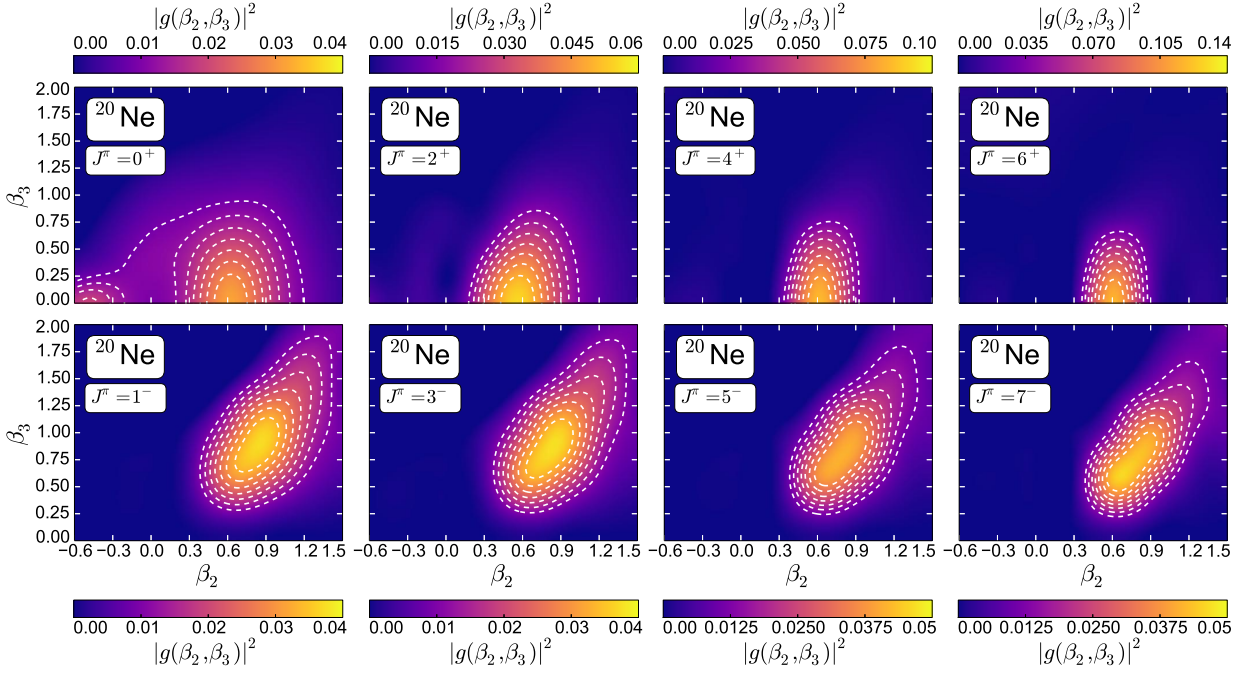


FIGURE 4.18: Amplitudes of collective wave functions squared $|g(\beta_2, \beta_3)|^2$ of the low-energy levels of ^{20}Ne . Dashed contours in the $\beta_2 - \beta_3$ plane successively denote a 10% decrease starting from the largest value of the amplitude.

In particular, the obtained excitation spectra for the two referent theoretical models are somewhat compressed in comparison to the experiment, while the present calculation yields spectrum that is slightly stretched as compared to the experiment. The two MR-EDF models slightly underestimate the moment of inertia for the negative-parity band, that is, the energy levels in the negative-parity band are a bit spread out compared to the experimental values. The best agreement with data for the transition strengths within the ground-state band is obtained with the AMD model. As compared to the experimental values, the present calculation predicts a marginally smaller $B(E2; 2_1^+ \rightarrow 0_1^+)$ value and somewhat overestimates $B(E2; 4_1^+ \rightarrow 2_1^+)$ and $B(E2; 6_1^+ \rightarrow 4_1^+)$ values. We note that the overall trend and, in particular, $B(E2; 4_1^+ \rightarrow 2_1^+)$ and $B(E2; 6_1^+ \rightarrow 4_1^+)$ values are rather similar to the PC-PK1 calculation with the *optimal configuration* set. Main differences in predictions of the two MR-EDF models could probably be attributed to the different selection of basis states used in the configuration mixing calculation. In the upper row of Figure 4.18 we plot the amplitudes of collective wave functions squared for the ground-state band states in the (β_2, β_3) plane. One notices that, while the collective wave function for 0_1^+ displays a significant contribution from oblate configurations ($\approx 25\%$), the wave functions of states with higher angular momenta are increasingly more concentrated on the prolate side of the plane. Completely omitting oblate configurations from the basis space (*full configuration* set in the PC-PK1 calculation) can only yield a prolate-deformed ground state, hence overestimating the $B(E2; 2_1^+ \rightarrow 0_1^+)$ value. The inclusion of just one oblate configuration (*optimal configuration* set in the PC-PK1 calculation) will shift this value closer to both the experimental data and to the prediction of our model.

The E2 transition strengths for the $K^\pi = 0^-$ band obtained in the present study

agree well with the AMD calculation, particularly for the $3_1^- \rightarrow 1_1^-$ and $5_1^- \rightarrow 3_1^-$ transitions. One also notices a very good agreement between the predicted and experimental $B(E2; 3_1^- \rightarrow 1_1^-)$ value. On the other hand, the transition strengths obtained in the PC-PK1 calculation based on the *full configuration* set differ considerably from the other two models and the experiment. This problem can apparently be solved by using the *optimal configuration* set, even though in this case the inclusion of oblate configuration in configuration mixing cannot be a viable explanation, since reported negative-parity states should not contain any oblate contributions. In the lower row of Fig. 4.18 we plot the calculated amplitudes of collective wave functions squared for the negative-parity band. These can be directly compared with the right column in Ref. [ZYL⁺16], where the same amplitudes were calculated using the PC-PK1 interaction with the *full configuration* set. We notice that the present calculation predicts for all wave functions to be concentrated at roughly similar deformations, ($\beta_2 \approx 0.9, \beta_3 \approx 1.0$). On the other hand, the PC-PK1 study predicts a broader distribution of the corresponding wave functions, with the peak position shifting towards smaller values of β_2 with increasing angular momentum. Finally, our predictions for the E3 transition strengths between the $K^\pi = 0^-$ and $K^\pi = 0^+$ bands are in fair agreement with the results obtained in Ref. [ZYL⁺16] using both basis sets, except maybe for the $B(E3; 1_1^- \rightarrow 4_1^+)$ transition that is significantly smaller within our model.

4.3.2 Cluster Structures in Collective States

Restoration of symmetries and the accompanying transition to the laboratory frame of reference can smear out information on clustering that were present in the intrinsic frame. The most obvious example is the collective 0^+ state which, regardless of its properties in the intrinsic frame, necessarily exhibits the spherically-symmetric density in the laboratory frame. Therefore, intrinsic densities represent a more convenient and informative choice when studying clusterized structures in the collective states. In the present work, intrinsic densities for each collective state are generated by performing RHB calculations constrained to the corresponding correlated (β_2, β_3) values. The correlated values of deformation parameters (β_2, β_3) are obtained by averaging over the prolate-deformed and oblate-deformed configurations separately, and using the collective wave functions of each state as the corresponding weights [see Eqs. (2.40) and (2.41)]. In order to illustrate the evolution of cluster structures in the collective states of ^{20}Ne , in Figure 4.19 we display the characteristic intrinsic nucleon densities of the ground-state band and the $K^\pi = 0^-$ band. For each state, the corresponding prolate and/or oblate deformation parameters (β_2, β_3) , as well as the respective contribution of prolate or oblate configurations to the total collective wave function, are given. Only in the ground state there is a significant ($> 10\%$) contribution of oblate configurations, while for all other ground-band states the intrinsic structure is dominated by prolate configurations. The major contribution to the ^{20}Ne ground state still comes from the reflection-asymmetric prolate-deformed $^{16}\text{O}+\alpha$ configuration, accounting for about 3/4 of its collective wave function. Nevertheless, it also contains nearly 25% admixture of the oblate-deformed

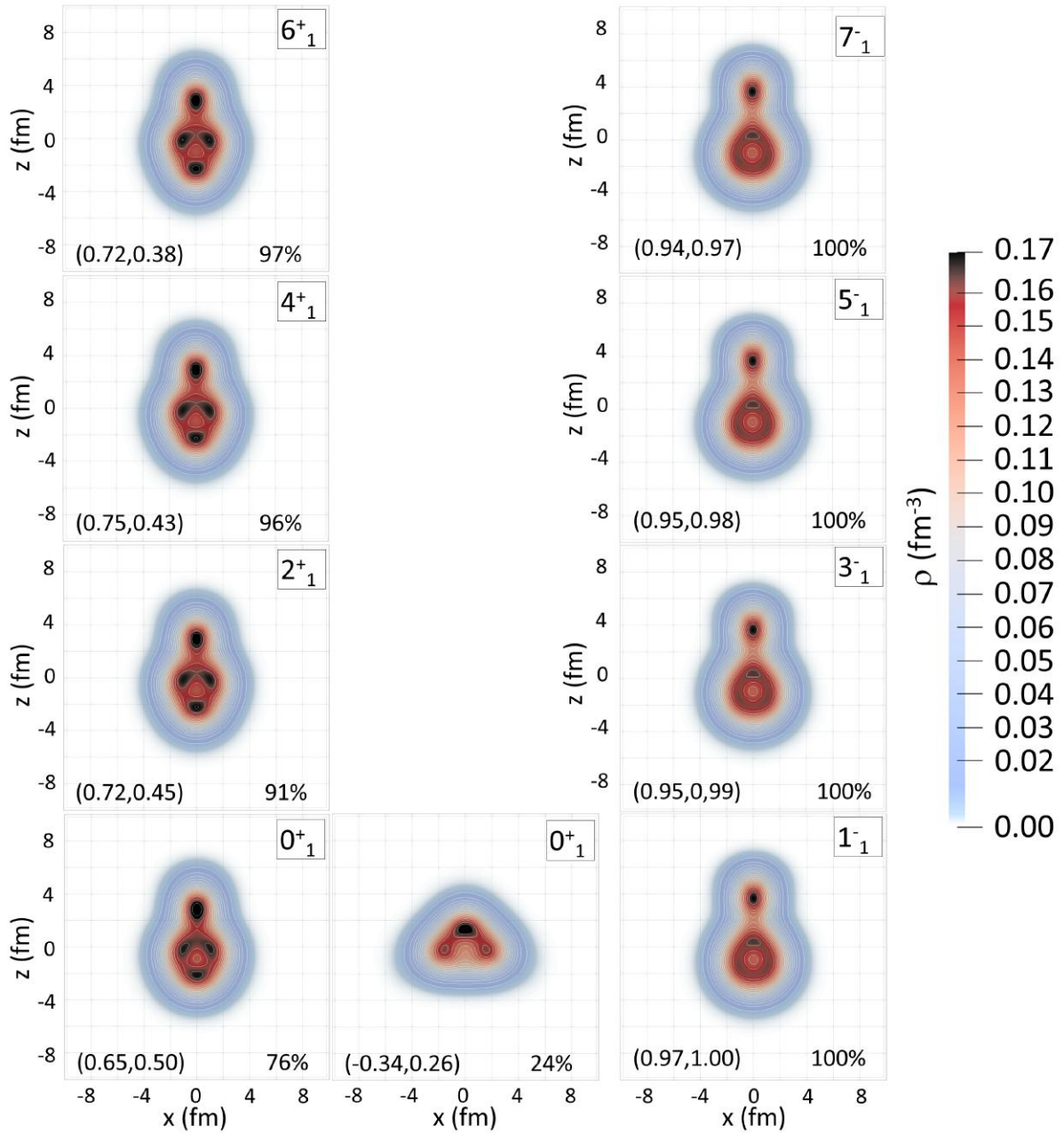


FIGURE 4.19: Characteristic intrinsic nucleon densities of collective states of the ground-state band and the $K^\pi = 0^-$ band in ^{20}Ne . The corresponding average deformation parameters (β_2, β_3) , as well as the respective contributions of prolate and/or oblate configurations, are given. See text for more details.

configurations with a characteristic intrinsic density resembling the $2\alpha + ^{12}\text{C}$ structure⁵. The predicted transitional character of ^{20}Ne ground state between mean-field and cluster-like structures is in agreement with AMD analyses [Kim04]. It is remarkable that, starting from a basis of almost 120 mean-field states, the MR-EDF calculation brings out the two

⁵Of course, the inclusion of a true $2\alpha + ^{12}\text{C}$ configuration would require breaking of axial symmetry, which is obviously out of the scope of the present study.

main components of the collective state which are used as *a priori* basis states in custom built cluster models [TKH04]. The transitional nature of the ground state is usually invoked to explain the relatively high excitation energy of its parity-doublet 1_1^- state, which is predicted to exhibit a pronounced $^{16}\text{O}+\alpha$ structure by both the present study and AMD calculation. Increasing angular momentum leads to a very gradual dissipation of the $^{16}\text{O}+\alpha$ structure in the $K^\pi = 0^-$ band. This process was reported to occur with much faster rate in the AMD calculation [Kim04], as well as in the MR-EDF calculation based on PC-PK1+BCS framework [ZYL⁺16]. In our study, however, dissipational process in the $K^\pi = 0^-$ band seems to be compensated to a large extent by the centrifugal effects that tend to elongate the nucleus. On the other hand, increasing angular momentum in the ground-state band leads to the increase of average β_2 deformation and to the decrease of average β_3 deformation. As a result of this process, a weak α - ^{12}C - α -like structure appears to develop in the $J^\pi = 6^+$ collective state of ^{20}Ne .

4.4. Concluding Remarks

In this chapter we have performed the fully symmetry-restoring study of quadrupole-octupole collectivity and cluster structures in eight even-even neon isotopes. Between 111 and 118 axially-symmetric and reflection-asymmetric RHB states were first projected onto good values of angular momenta, particle number, and parity, and then mixed within the MR-EDF framework. This approach enabled a consistent, parameter-free calculation of excitation spectra and electric transition strengths, both for the ground-state band and for the excited $K^\pi = 0^\pm$ bands. The obtained results were compared to the available experimental data, as well as to the predictions of other theoretical models.

The ground-state experimental values of binding energies and charge radii were reproduced reasonably well already on the SR-EDF level. By including collective correlations related to the restoration of broken symmetries and configuration mixing, we have demonstrated the stability of considered isotopes with respect to neutron emissions. Additionally, the inclusion of collective correlations has revealed a rather complex structure of the correlated ground states. In particular, octupole degree of freedom was demonstrated to play a rather relevant role and symmetry-projected minima of all isotopes were found at the reflection-asymmetric configurations. Furthermore, significant admixtures of oblate configurations ($> 20\%$ of the corresponding collective wave functions) were found over the entire isotopic chain. Most notably, both mean-field and symmetry-projected energy surfaces of the ^{24}Ne ground state were found to display the co-existing prolate and oblate minima, while as much as 40% of the corresponding wave function was shown to spread on an oblate side of the $\beta_2 - \beta_3$ plane.

The energies of 2_1^+ and 4_1^+ states, as well as the $B(E2; 2_1^+ \rightarrow 0_1^+)$ transition strengths, were shown to be in reasonable agreement with data over the entire isotopic chain. The agreement is particularly good in lighter isotopes, $^{20,22,24}\text{Ne}$, while the obtained sphericity of ^{30}Ne is not supported by the recent experimental data. This can be understood as a consequence of the fact that global effective interactions cannot always account for the particular properties determined by shell evolution in each mass region. In this case, the

erosion of the $N = 20$ shell closure in very neutron-rich nuclei is simply not reproduced by the DD-PC1 functional. Nevertheless, it was shown that the further addition of neutrons leads to development of a strong prolate deformation in the most neutron-abundant neon isotope, ^{34}Ne . This nucleus exhibits a pronouncedly compressed ground-state band as compared to other isotopes, with the lowest excitation energies of 2_1^+ and 4_1^+ states over the entire isotopic chain. Additionally, signatures of the ground-state shape-coexistence were demonstrated to survive in the excited states of ^{24}Ne isotope. In particular, its 6_1^+ still contains almost 40% contribution from the oblate configurations, while 0_2^+ and 2_2^+ states in this isotope are found at much lower energies than the corresponding states in ^{22}Ne isotope.

Finally, we have paid special attention to the case of the self-conjugate ^{20}Ne isotope. The obtained spectroscopic properties were thoroughly compared to the experimental data, as well as to the predictions of two other theoretical models. In particular, our calculation was shown to exhibit a level of accuracy that is comparable to the one obtained using more specific models, such as the antisymmetrized molecular dynamics. The ground state of ^{20}Ne was demonstrated to have predominantly $^{16}\text{O}+\alpha$ structure, while about 25% of its collective wave function corresponds to the oblate-deformed $2\alpha+^{12}\text{C}$ -like structure. The increase of angular momentum leads to the predominance of prolate shapes and a gradual dissolution of the $^{16}\text{O}+\alpha$ structure. In the negative-parity band this dissolution occurs at much slower rate than reported in previous studies, while in the positive-parity band it leads towards development of the $\alpha-^{12}\text{C}-\alpha$ -like structure in $J^\pi = 6^+$ state.

Cluster Structures in ^{12}C Isotope

Nothing in life is to be feared, it is only to be understood.

Now is the time to understand more, so that we may fear less.

Marie Curie, as quoted in "Our Precarious Habitat" by M. A. Benarde

Formation of clusters, transitional states between quantum liquid and solid phases of finite systems, is a common feature in light atomic nuclei [Bec10, Bec12, Bec14, HIK12, FHKE⁺18]. Particularly favorable conditions for the appearance of cluster structures are found in light self-conjugate nuclei, where various exotic configurations are thought to be formed. Probably one of the most striking examples is the self-conjugate ^{12}C isotope, where axial oblate, triangular, linear 3α , and bent arm configurations are all predicted to exist in the low-lying structure [KE07, NF04, CFN⁺07, THSR01, Fun15, FSF⁺13]. The ground state of ^{12}C lies about 7.3 MeV below the α -decay threshold. Therefore, cluster structures are expected to be significantly suppressed in the lowest 0^+ state, as it exhibits a more compact intrinsic density distribution. The $K^\pi = 0_1^+$ rotational band built upon the ground state consists of the 2_1^+ state at 4.4 MeV and the 4_1^+ state at 14.1 MeV. Very recently, new reorientation-effect measurements in the 2_1^+ state have confirmed its pronounced oblate deformation through the relatively large and positive value of the corresponding spectroscopic quadrupole moment [R⁺18]. Furthermore, the 0_2^+ state at 7.65 MeV, the famous Hoyle state, is arguably one of the most studied collective nuclear states overall [FF14, THSR17], largely due to the fact that it plays a major role in the stellar nucleosynthesis of ^{12}C through the so-called triple- α process. In particular, the presence of the Hoyle state resonantly boosts the capture process of an α -particle on ^8Be by more than 10 million times, thereby making a decisive impact on the abundance of ^{12}C isotope in the universe and, consequently, the appearance of organic life on Earth. Remarkable results on the structure of the Hoyle state have recently been simultaneously reported by two independent groups of researchers [D⁺17, SKW⁺17], strongly indicating that the Hoyle state predominantly decays through an intermediate emission of an α -particle. In

parallel with experimental advances, various theoretical approaches have been employed to study rich variety of shapes in ^{12}C , including the antisymmetrized molecular dynamics model [KE07], the fermionic molecular dynamics model [NF04, CFN+07], the THSR wave function model [THSR01, Fun15], the configuration mixing Skyrme calculations with Gaussian wave packets [FSF+13], and the cranked RMF theory [RZZ+18]. Both AMD and FMD calculations predict for the Hoyle state to be dominated by a weakly-interacting assembly of $^8\text{Be}+\alpha$ configurations [KE07, CFN+07], while the THSR model describes Hoyle state in terms of an actual condensate of α -particles [THSR01]. Furthermore, 3α linear chain structures were predicted to exist in higher 0^+ states of ^{12}C [KE07, CFN+07], even though the stability of these configurations against bending still remains an open question [RZZ+18]. A detailed review on recent experimental and theoretical advances in studies of cluster structures in light nuclei and, particularly, in the ^{12}C isotope can be found in Ref. [FHKE+18]. Additionally, structure of the Hoyle state has been a subject of multiple dedicated review papers (see, for example, Refs. [FF14] and [THSR17]).

In this chapter, we will employ the previously described MR-EDF model in a study of collective spectroscopy and cluster structures in ^{12}C isotope [MEK+18b]. A wide range of quadrupole- and octupole-deformed axially-symmetric RHB states are projected onto good values of angular momenta, particle numbers, and parity, and further mixed in order to build the symmetry-conserving positive-parity collective states. In Section 5.1.1 we analyze the potential energy surface of ^{12}C , both on the mean-field and symmetry-conserving level. Furthermore, in Sec 5.1.2 we present the spectroscopic results for ^{12}C in comparison to the available data and to predictions of other theoretical models. The structure of the collective states in the intrinsic frame is discussed in Sec. 5.1.3, while in Sec. 5.1.4 we present the results for both the elastic and inelastic form factors for electron- ^{12}C scattering.

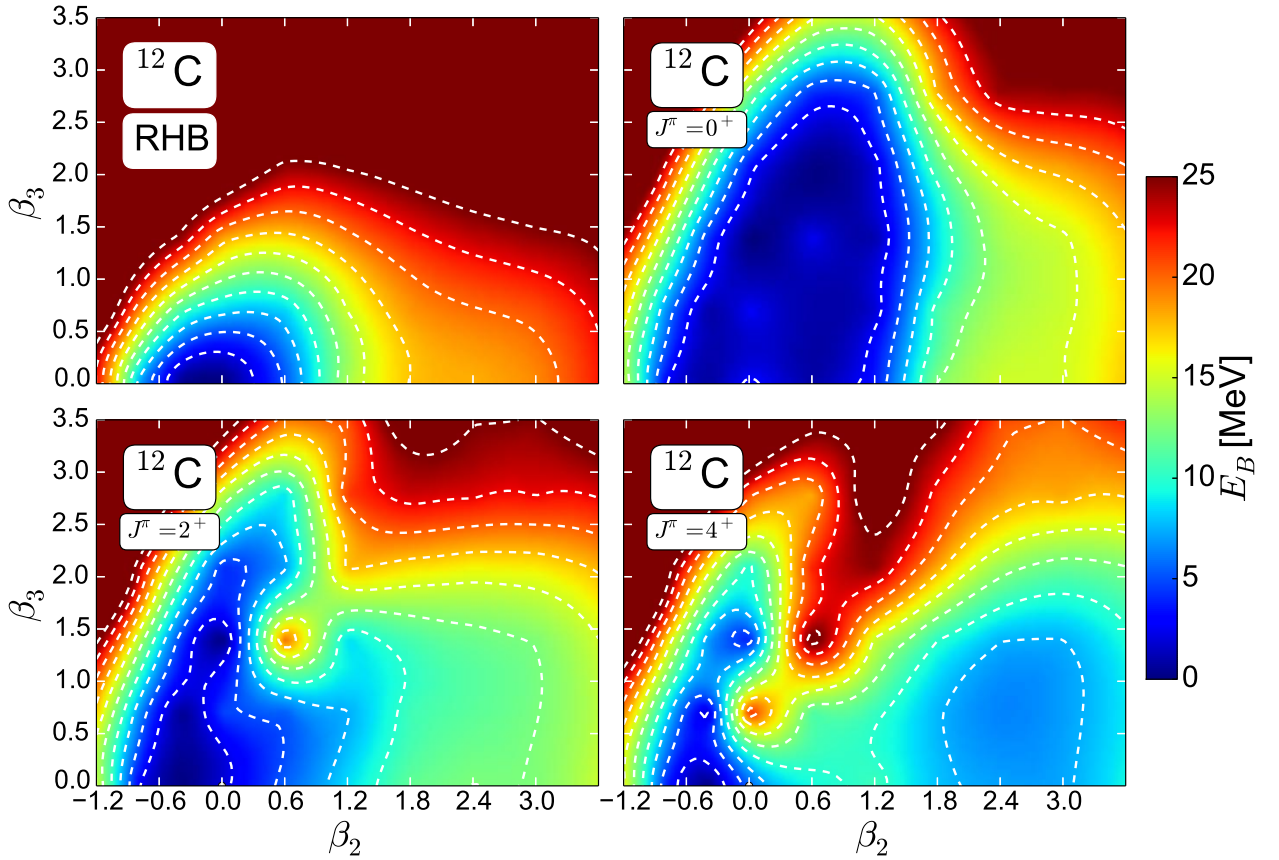


FIGURE 5.1: Potential energy surfaces of ^{12}C isotope in the $\beta_2 - \beta_3$ plane. In addition to the self-consistent RHB binding energies (the upper left panel), we display the angular momentum-, particle number-, and parity-projected energy surfaces for spin-parities $J^\pi = 0^+, 2^+, 4^+$. For each surface, energies are normalized with respect to the energy of the corresponding absolute minimum. Dashed contours are separated by 2.5 MeV.

5.1. Structure of the ^{12}C Isotope

5.1.1 Potential Energy Maps

We begin our analysis with the self-consistent RHB calculation, performed by expanding nuclear spinors in the configuration space of axially-symmetric harmonic oscillator with $N_{sh} = 10$ major oscillator shells for the large and $N_{sh} = 11$ for the small component of spinor. This calculation covers a wide range of deformations in both the quadrupole and octupole direction, $\beta_2 \in [-1.2, 3.6]$ and $\beta_3 \in [-3.5, 3.5]$, with steps in the oblate, prolate, and octupole direction being $\Delta\beta_2 = 0.4$, $\Delta\beta_2 = 0.6$, and $\Delta\beta_3 = 0.7$, respectively. The calculated potential energy surfaces are shown in the upper left panel of Figure 5.1. Although the absolute minimum of the RHB energy surface is found for the spherical ($\beta_2 = 0, \beta_3 = 0$) configuration, we note that the surface is rather soft for the following range of deformations: $\beta_2 \approx [-0.6, 0.6]$ and $|\beta_3| \approx [0.0, 0.5]$. In order to demonstrate the influence of symmetry restoration on the topology of the RHB surface, other panels

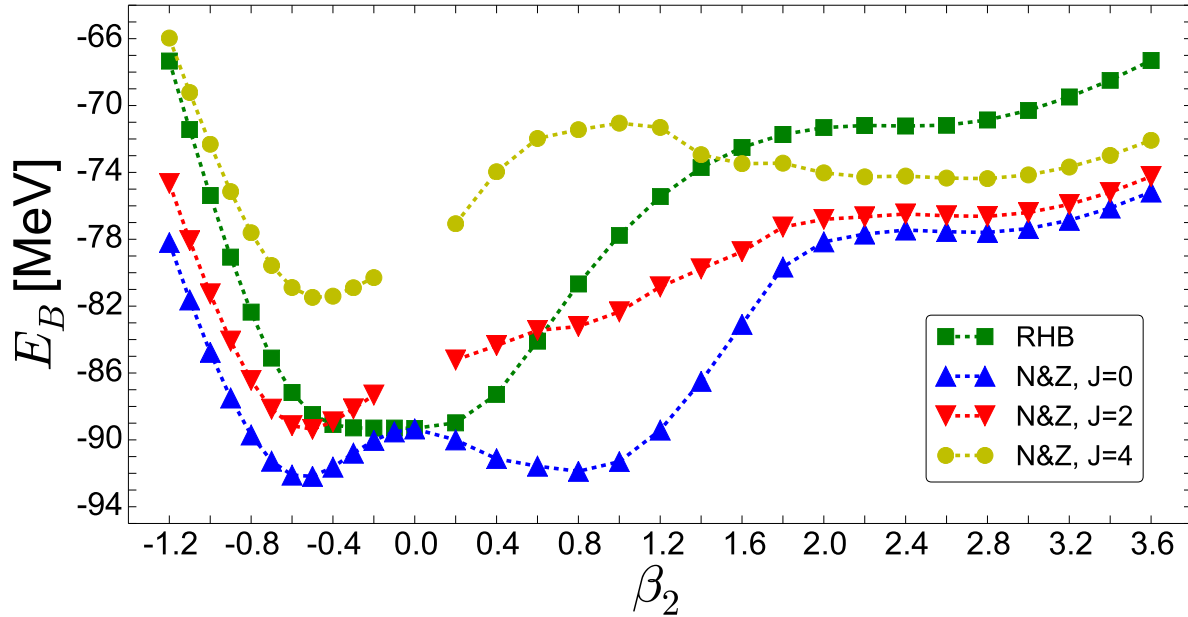


FIGURE 5.2: Potential energy curves of ^{12}C isotope as functions of axial quadrupole deformation β_2 for parity-conserving ($\beta_3 = 0$) configurations. In addition to the self-consistent RHB binding energies (squares), we display angular momentum- and particle number-projected curves for spin-parities $J^\pi = 0^+, 2^+, 4^+$.

of Fig. 5.1 show the corresponding angular momentum-, particle number-, and parity-projected energy surfaces for spin-parity values $J^\pi = 0^+, 2^+, 4^+$. Already a glance at the $J^\pi = 0^+$ energy surface unveils a dramatic impact of performing the symmetry restoration. In particular, the $J^\pi = 0^+$ energy surface appears significantly softer for a wide range of deformations in comparison to the RHB energy surface. For higher values of angular momentum, the minimum at the oblate side becomes much more pronounced, while intermediate prolate deformations become increasingly less energetically favored. This trend is even more apparent in Figure 5.2, where we make a cut along the parity-conserving ($\beta_3 = 0$) line of Fig. 5.1 and show the potential energy curves as functions of axial quadrupole deformation β_2 . As noted before, the RHB potential energy curve is very flat around the spherical minimum, both in the prolate and oblate direction. The only indication of possible clusterized structures is found at very large prolate deformations, where a shoulder in binding energy curve is formed. On the other hand, energy curve of the symmetry-restored $J^\pi = 0^+$ state exhibits two nearly-degenerate minima: the absolute oblate minimum at $\beta_2 \approx -0.5$ and the prolate minimum at $\beta_2 \approx 0.8$. We note that the binding energy of the symmetry-restored oblate minimum from Fig. 5.2 is very close to the experimental binding energy $E_B^{\text{exp}} = -92.16$ MeV. This is consistent with the fact that the collective 0_1^+ state is expected to correspond to the band-head of an oblate-deformed rotational band. Furthermore, shoulder at large quadrupole deformations is preserved by projections for the $J^\pi = 0^+$ curve and it is additionally lowered by about 5 MeV. The $J^\pi = 2^+$ projected curve preserves both the oblate minimum and the shoulder at large quadrupole deformations, while the former $J^\pi = 0^+$ local minimum

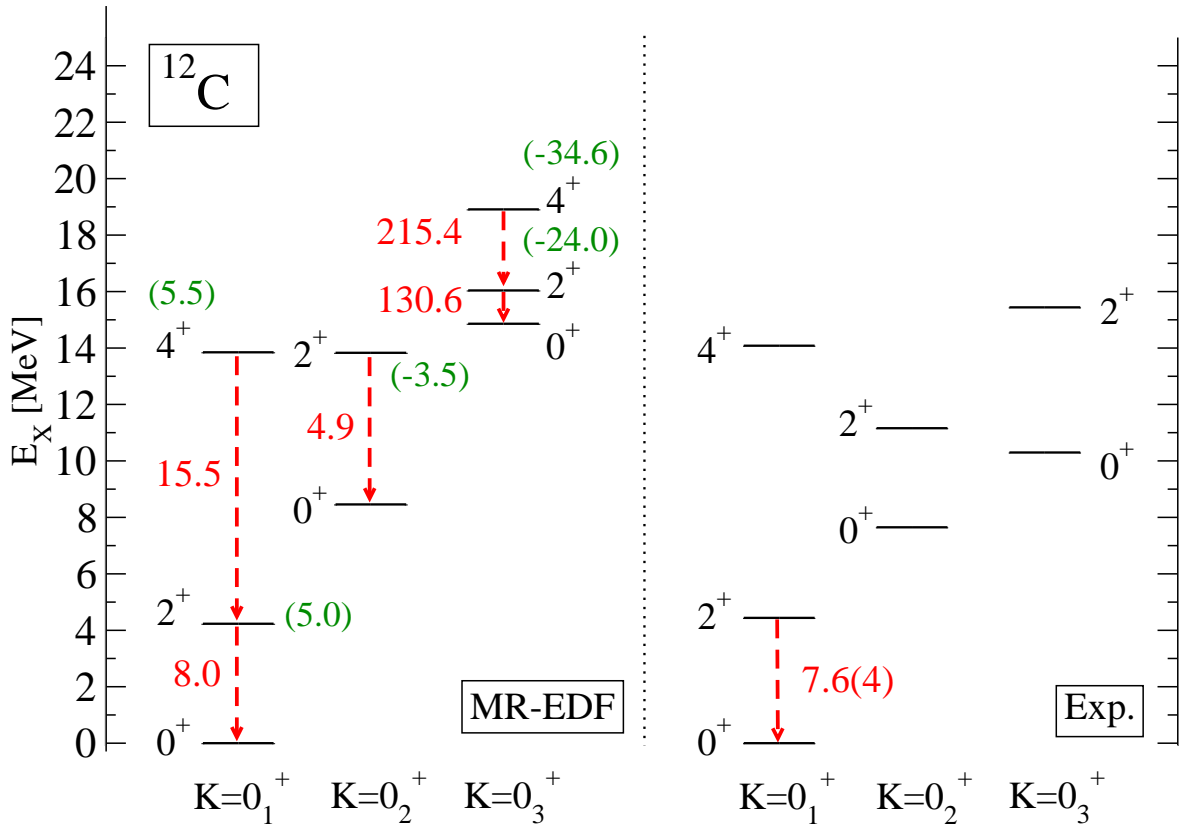


FIGURE 5.3: Calculated low-energy spectrum of ^{12}C compared with the available experimental data [NNDC, AS90]. Calculated intraband $B(E2)$ transition strengths (red color, in $e^2\text{fm}^4$) and spectroscopic quadrupole moments (green color, in efm^2) are also shown. See text for more details.

at intermediate quadrupole deformation transforms into a shoulder. Finally, a barrier is raised at intermediate prolate deformations for the $J^\pi = 4^+$ state. The present analysis demonstrates that the symmetry-restored energy maps encapsulate the vast richness of shapes in ^{12}C and that interesting phenomena can be observed already on this level of calculation. Nevertheless, it is only the configuration mixing procedure, which includes the collective correlations related to both the quadrupole and octupole shape fluctuations, that can ultimately provide us with a quantitative description of ^{12}C spectroscopy.

5.1.2 Spectroscopy of Collective States

In the next step, 72 symmetry-restored configurations were mixed in order to build collective states of ^{12}C with good quantum numbers. The RHB configurations with binding energies that are much higher than energy of the equilibrium configuration (roughly 30 MeV and above) have been eliminated from the basis, without altering the predictive power of the model. In Figure 5.3 we display the calculated low-lying spectrum in comparison to the available experimental data [NNDC, AS90]¹. Calculated intraband

¹Reported spin-parity assignments for states 0_1^+ , 2_1^+ , 4_1^+ , and 0_2^+ are definite, while assignments for other states are still tentative to a certain degree.

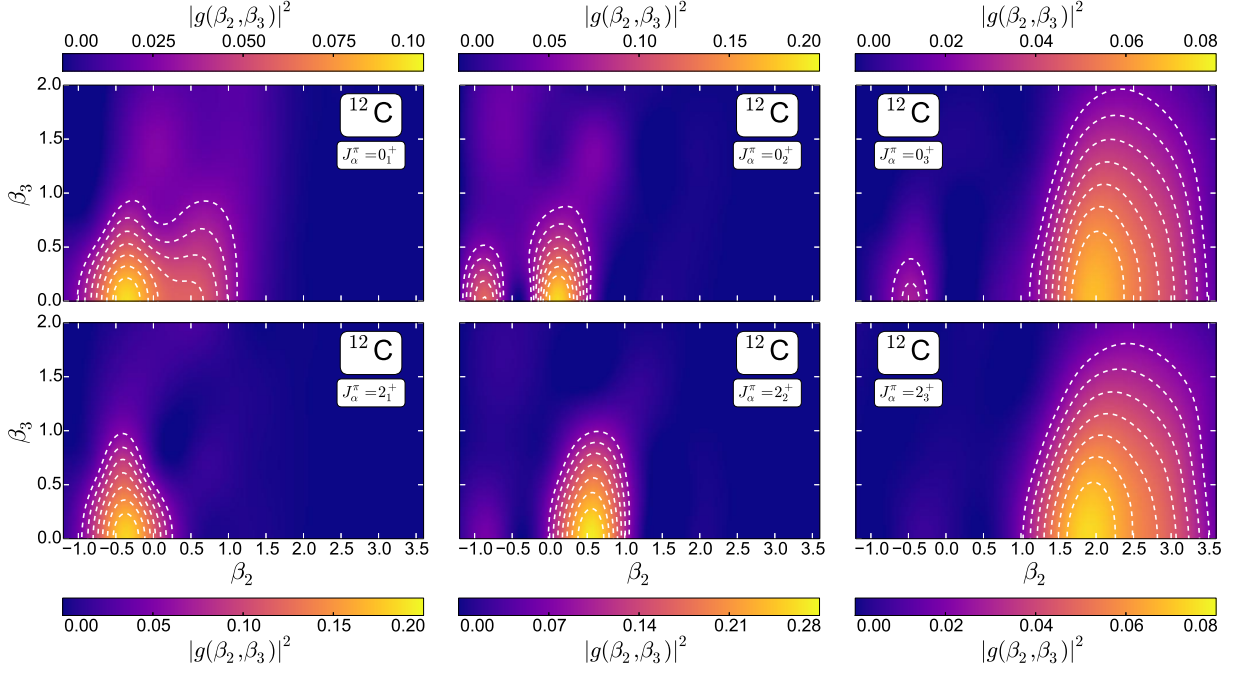


FIGURE 5.4: Amplitudes of collective wave functions squared $|g(\beta_2, \beta_3)|^2$ of the low-energy levels in ^{12}C . Dashed contours in the $\beta_2 - \beta_3$ plane successively denote a 10% decrease starting from the largest value of the amplitude.

$B(E2)$ transition strengths and spectroscopic quadrupole moments of collective states are also shown. The calculated excitation energies of 2_1^+ (4.3 MeV) and 4_1^+ (13.9 MeV) states are only slightly lower than the corresponding experimental values. In addition, their ratio $E(4_1^+)/E(2_1^+) = 3.23$ is in very good agreement with the experimental value of 3.17, strongly indicating a rotational character of the ground-state band. Furthermore, calculated $E2$ transition strength from the 2_1^+ state to the ground state, $B(E2; 2_1^+ \rightarrow 0_1^+) = 8.0 e^2\text{fm}^4$, is in very good agreement with the experimental value. We also note that the calculated spectroscopic quadrupole moment of 2_1^+ state, $Q_{\text{spec}}(2_1^+) = 5.0 e\text{fm}^2$, is within the error bar margin of the very recently obtained experimental value, $Q_{\text{spec}}^{\text{exp}}(2_1^+) = 7.1 \pm 2.5 e\text{fm}^2$ [R⁺18]. It is therefore interesting to mention that, in this specific instance, the global EDF model provides the level of agreement with the experimental data that is comparable to the one provided by the state-of-the-art *ab initio* model reported therein [R⁺18]. Finally, calculated $B(E2; 4_1^+ \rightarrow 2_1^+) = 15.5 e^2\text{fm}^4$ value is in excellent agreement with the AMD prediction $B(E2; 4_1^+ \rightarrow 2_1^+) = 16 e^2\text{fm}^4$ [KE07]. Measurements of this quantity are yet to be performed and they would definitely confirm the rotational character of the ground-state band. On the other hand, the second 4^+ state within our calculation is characterized by a pronouncedly enhanced value of quadrupole deformation parameter, a feature that is shared by the 0_3^+ and 2_3^+ collective states. In addition, it exhibits a very strong $E2$ transition strength to the 2_3^+ state. Therefore, it is assigned to the $K^\pi = 0_3^+$ band and denoted as 4_3^+ further on. Both very large $E2$ intraband transitions and the value of ratio $(E(4_3^+) - E(0_3^+))/(E(2_3^+) - E(0_3^+)) = 3.45$ strongly indicate the rotational character of this band. Additionally, huge spectroscopic quadrupole moments of 4_3^+ and 2_3^+ states support the interpretation of this band as the 3α linear

chain. Calculated value of $B(E2; 2_3^+ \rightarrow 0_3^+) = 130.6 e^2\text{fm}^4$ is somewhat larger than the one reported in Ref. [KE07], but still of the same order of magnitude. Furthermore, the 0_2^+ (Hoyle) state in our study is found at excitation energy that is less than 1 MeV above the experimental value. However, calculated $E2$ transition strength from the corresponding 2_2^+ state is about an order of magnitude smaller than the one obtained in AMD [KE07] and THSR [Fun15] calculations. Even though there are currently no available experimental values that would settle this disagreement, it is likely that our calculation actually underestimates the true value. The reason for this is at least two-fold. Firstly, AMD and THSR models consistently predict for the dominant contribution to the Hoyle state intrinsic density to stem from triaxial configurations. As noted before, these configurations are not included in the present study and an extended study that includes triaxial shapes would be required in order to draw some fairer comparisons. In addition, the asymptotic behavior of three weakly-interacting α particles is notoriously complicated to describe within the harmonic oscillator basis [NGV⁺07, Nef12]. Therefore, it remains an open question whether the self-consistent models based on harmonic oscillator expansions, even once the triaxial shapes have been included, will be able to encompass all the details of the Hoyle state density profile. Nevertheless, we note that the calculated transition strength from the 2_1^+ state to the Hoyle state, $B(E2; 2_1^+ \rightarrow 0_2^+) = 1.7 e^2\text{fm}^4$ compares quite favorably to the experimental value $2.6 \pm 0.4 e^2\text{fm}^4$ and to the AMD ($5.1 e^2\text{fm}^4$) predictions [KE07]. In addition, even the transition strength from the 2_2^+ state to the ground state, $B(E2; 2_2^+ \rightarrow 0_1^+) = 1.3 e^2\text{fm}^4$, is of at least comparable quality as THSR prediction ($2.0 - 2.5 e^2\text{fm}^4$) [Fun15] when compared to the experimental value ($0.73 \pm 0.13 e^2\text{fm}^4$).

5.1.3 Structure of Collective States in the Intrinsic Frame

In Figure 5.4 we show amplitudes of collective wave functions squared $|g(\beta_2, \beta_3)|^2$ of the low-energy levels in ^{12}C . Even though they are not observables, these wave functions provide us with a measure of quadrupole and octupole shape fluctuations in collective states. Moreover, they can be used to calculate averaged values of deformation parameters (β_2, β_3) for each collective state. These values are subsequently used to represent the density distributions of the collective states in the intrinsic frame of reference [see Sec. 4.3.2]. Intrinsic density distributions for the three lowest 0^+ and 2^+ states in ^{12}C isotope are displayed in Figure 5.5. For each state, the corresponding prolate and/or oblate deformation parameters (β_2, β_3) , as well as the respective contribution of prolate or oblate configurations to the total collective wave function, are given. Only 0_1^+ and 0_2^+ states exhibit significant contributions from both the prolate and oblate configurations, while other states display predominance of either prolate or oblate shapes. In particular, situation in the 0_1^+ state is rather similar to the one encountered in the symmetry-restored $J^\pi = 0^+$ potential energy curve of Fig. 5.2, where prolate-deformed local minimum coexists with the oblate-deformed absolute minimum. In fact, maximum of the 0_1^+ collective wave function is also found at the oblate-deformed $(\beta_2, \beta_3) = (-0.4, 0.0)$ configuration. However, $|g(\beta_2, \beta_3)|^2$ has non-negligible contributions from configurations in a rather wide range of

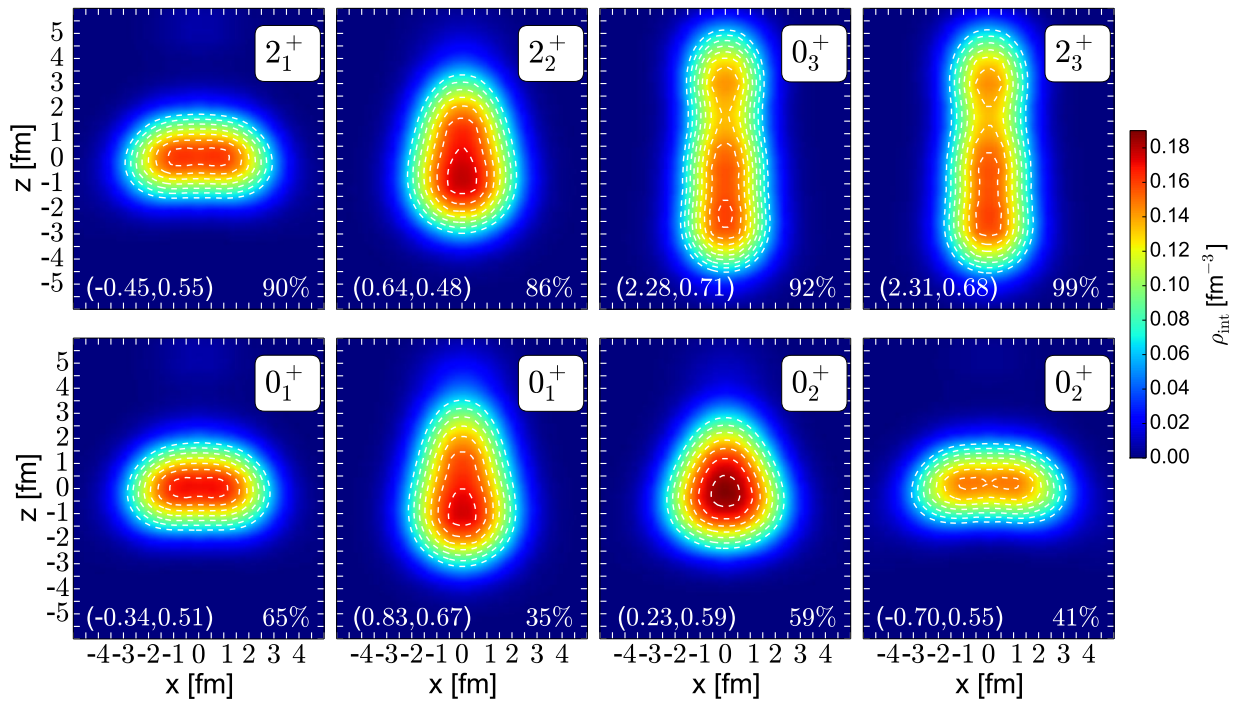


FIGURE 5.5: Characteristic intrinsic nucleon densities of the first three 0^+ and 2^+ collective states in ^{12}C . The corresponding average deformation parameters (β_2, β_3) , as well as the respective contributions of prolate and/or oblate configurations, are given. The lower panel displays states that exhibit significant both prolate and oblate contributions, while the upper panel displays states that are predominantly characterized by either prolate or oblate configuration. See text for more details.

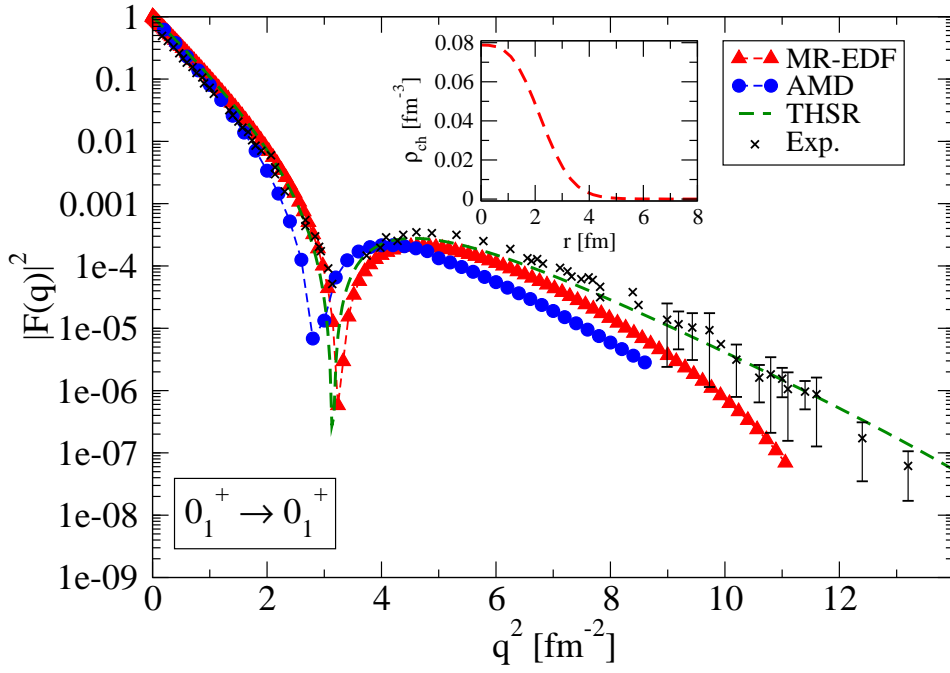
deformations, roughly $\beta_2 \in [-1.2, 1.2]$ and $|\beta_3| \in [0.0, 1.4]$. Averaging over all these configurations incorporates significant contributions from prolate configurations that balance the influence of oblate maximum and would ultimately yield the nearly-spherical density distribution. This clearly does not reflect the actual physical picture of the ^{12}C ground state. Therefore, we follow the prescription of Section 4.3.2 and calculate the correlated (β_2, β_3) values by averaging over the prolate-deformed and oblate-deformed configurations separately, using the collective wave functions as the corresponding weights [see Eqs. (2.40) and (2.41)]. The two plots in the lower left panel of Fig. 5.5 display the obtained densities, as well as the respective contributions of prolate and oblate configurations to the total collective wave function². These densities reflect the complex structure of the ^{12}C ground state, where the maximum of $|g(\beta_2, \beta_3)|^2$ is found at an oblate configuration while tail of the wave function spreads deeply into the prolate side of the $\beta_2 - \beta_3$ plane. On the other hand, collective wave function of the 2_1^+ state is predominantly spread over the $(\beta_2 < 0, \beta_3)$ configurations and the obtained density distribution is oblate-deformed. This can be understood as a consequence of the sway towards oblate shapes in the $J^\pi = 2^+$ energy maps of Figs. 5.1 and 5.2, and it is in agreement with the

²We note that some authors compute the characteristic density of a collective state by using configuration that corresponds to the collective wave function maximum [see, for example, Ref. [ZYL+16]]. With this choice, intrinsic density of 0_1^+ state in the present would exhibit the oblate-deformed reflection-symmetric shape. Nevertheless, for the sake of consistency, we follow the prescription of Chapter 4 and adopt the averaged (β_2, β_3) values as representative deformation parameters.

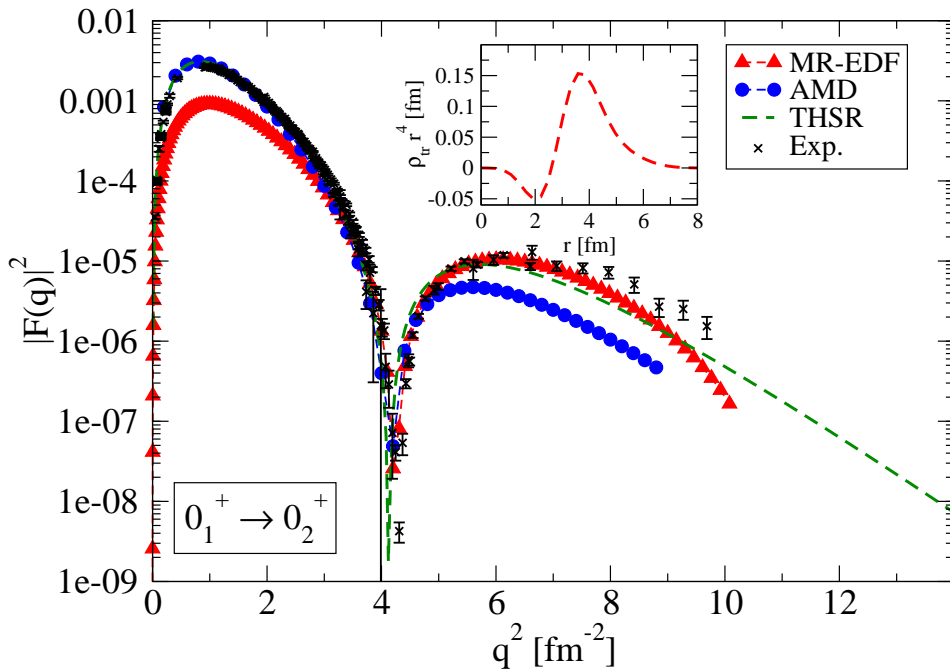
relatively large and positive spectroscopic quadrupole moment of the 2_1^+ state. Moreover, intrinsic nucleon density of the 4_1^+ state is characterized by the $(\beta_2, \beta_3) = (-0.50, 0.58)$ configuration, clearly pointing towards oblate nature of the ground-state band. Furthermore, collective wave function of the 0_2^+ state exhibits two maxima: one at the small prolate deformations and the other one at larger oblate deformations. The corresponding density distributions are obtained equivalently to the 0_1^+ case and they are displayed in the lower right panel of Fig. 5.5. Of course, in order to obtain the expected triangular distribution of the Hoyle state one needs to break the axial symmetry, which is out of the scope of the present work. Finally, the $K^\pi = 0_3^+$ band originates from the shoulder at large β_2 values in Figs. 5.1 and 5.2. In the intrinsic frame of reference, a large quadrupole deformation translates into a pronounced linear structure of 0_3^+ and 2_3^+ collective states, as seen in the upper right panel of Fig. 5.5. The homogeneous alignment of 3α particles would be described by a reflection-symmetric configuration in the intrinsic frame, that is, the corresponding octupole deformation parameter would be negligible. Even though the maxima of 0_3^+ and 2_3^+ wave functions are indeed found at $\beta_3 = 0$ configurations [see Fig. 5.4], fluctuations in octupole direction are rather pronounced in both states. Consequently, the reflection-asymmetric $^8\text{Be}+\alpha$ -like structure is formed in the intrinsic frame. Formation of linear chain structures in ^{12}C isotope has been previously predicted by some theoretical calculations [KE07, NF04], even though they are yet to be confirmed experimentally. Another interesting feature of 3α linear chains is their alleged susceptibility to bending, which would eventually lead to the formation of bent arm structures [KE07, NF04, RZZ⁺18]. However, besides breaking reflection symmetry, such structures additionally break the axial symmetry and they are therefore not included in the present study.

5.1.4 Electron Scattering Form Factors

Additional insight into the structure of collective states is provided by the form factors of the electron-nucleus scattering. Formalism for calculating these quantities within the MR-EDF framework was introduced only recently [YBH15] and details related to our implementation are available in Appendix B.2. In this subsection, we will calculate form factors for electron scattering from ^{12}C for $0_1^+ \rightarrow 0_1^+$ (elastic) and $0_1^+ \rightarrow 0_2^+$ (inelastic) transitions. The basic ingredients of the calculation are collective wave functions, displayed in Fig. 5.4. As noted before, both for the 0_1^+ and for the 0_2^+ state these wave functions are concentrated in the $-1.2 \leq \beta_2 \leq 1.2$ and $0 \leq |\beta_3| \leq 1.4$ part of the $\beta_2 - \beta_3$ plane. Therefore, in order to reduce the computational cost and without neglecting any physical content, only configurations within that range are included in the subsequent calculation of form factor. In the upper panel of Figure 5.6 we show the calculated form factors $|F_0(q)|^2$ for elastic $0_1^+ \rightarrow 0_1^+$ scattering in comparison with the available experimental data. In addition, the inset shows the corresponding charge density, calculated as $\rho_{\text{ch}}(r) = \rho_{01,0}^{01}(r)/\sqrt{4\pi}$, where $\rho_{01,0}^{01}(r)$ is the diagonal element of the reduced transition density that enters the calculation of form factor [see Eq. (2.44)]. Our results for the form factor are compared with predictions of two other theoretical models, namely,



(a)



(b)

FIGURE 5.6: Form factors of electron scattering from ^{12}C for $0_1^+ \rightarrow 0_1^+$ (upper panel) and $0_1^+ \rightarrow 0_2^+$ (lower panel) transitions. Results obtained within our model are compared to the available experimental data for the elastic [SM70, NTH71, SS68] and inelastic [CFN⁺10] form factors, as well as to predictions of AMD [KE07] and THSR [FTH⁺06] models. In addition, insets show the corresponding charge density (upper panel) and the transition charge density (lower panel). See text for more details.

the antisymmetrized molecular dynamics model and the Tohsaki-Horiuchi-Schuck-Röpke wave function model. The AMD calculations [KE07] treat single nucleons as relevant degrees of freedom, describing them in terms of Gaussian wave packets. On the other hand, THSR framework is explicitly built as the α -cluster model, that is, the relevant degrees of freedom are α -particles in Bose-condensed state [FTH⁺06]. In the low momentum-transfer region ($q^2 < 2 \text{ fm}^2$) all models yield similar predictions for the elastic form factor. However, for larger values of the momentum transfer the difference between the three curves becomes visible. In particular, the first zero of $|F_0(q)|^2$ is found at roughly $q^2 \approx 3 \text{ fm}^2$ both in our and in the THSR calculation, while the AMD calculation predicts this zero at somewhat smaller value of the momentum transfer. Details of the elastic form factors can be traced back to the properties of the corresponding charge distribution [FV82, FVR86]. The shift of the position of the first zero towards smaller values of q^2 , in particular, can be attributed to the larger spatial extension of the charge density. Furthermore, the amplitude of the first $|F_0(q)|^2$ maximum is related to the surface thickness of the charge distribution. Larger values of surface thickness yield smaller values of the first maximum, and vice versa. We note that the experimental position and amplitude of the first $|F_0(q)|^2$ maximum are reproduced rather nicely by all models. At very large values of q^2 the THSR model provides the best agreement with the experiment, while our calculation underestimates experimental values. Similar behavior has been observed in Ref. [YBH15] for the case of ^{24}Mg and in Ref. [FSF⁺13] for the case of ^{12}C , where it was argued that the spreading of collective wave function over many deformations generates too large smoothing of the one-body density and thus decreases weights of the large-momentum components of the transition density. Finally, due to its short lifetime, elastic scattering experiments for the Hoyle state have not yet been performed. Therefore, its structure is usually probed via the inelastic scattering experiments from the ground state. In the lower panel of Fig. 5.6 we display the calculated form factors for $0_1^+ \rightarrow 0_2^+$ scattering in comparison with the available experimental data and predictions of the AMD and THSR models. Our calculations reproduce nicely the position of the first maximum, even though the corresponding amplitude is underestimated in comparison to both the experiment and two theoretical models. On the other hand, position of the first zero is reproduced well by all three models. In addition, our model displays good agreement with the experiment up to rather large q^2 values. The inset in the lower panel of Fig. 5.6 displays the corresponding transition charge density, $\rho_{\text{tr}}(r) = \rho_{01,0}^{02}(r)/\sqrt{4\pi}$, where $\rho_{01,0}^{02}(r)$ is the non-diagonal element of the reduced transition density that enters the calculation of form factor [see Eq. (2.44)]. Our prediction for $\rho_{\text{tr}}(r)r^4$ can be directly compared to the experimental transition charge density corresponding to the form factor of Fig. 5.6 [CFN⁺10], as well as to the predictions of the FMD model and the α -cluster model that are plotted in Fig. 3 of Ref. [CFN⁺10]. While the position of the minimum of $\rho_{\text{tr}}(r)r^4$ is very similar for all four curves considered, our calculation predicts somewhat smaller amplitude in comparison to both the experiment and other models. Furthermore, FMD and α -cluster model overestimate the experimental maximum value of the $\rho_{\text{tr}}(r)r^4$ curve, located at $r \approx 4 \text{ fm}$. Our calculation, on the other hand, notably underestimates it. This difference is then naturally reflected in the underestimated value of form factor in comparison to the experiment, particularly at low values of momentum transfer. The inclusion of triaxial degree of freedom, that undeniably plays an important role in the 0_2^+

state, would likely modify the calculated transition charge density and, consequently, the corresponding form factor. Whether such an upgrade to the model will actually bring the expected shift towards experimental values³ remains to be examined in the future.

5.2. Concluding Remarks

In this chapter, we have performed the fully symmetry-conserving study of the low-lying spectroscopy and cluster structures in ^{12}C isotope. Axially-symmetric and reflection-asymmetric RHB states were first projected onto good values of angular momenta, particle number, and parity, and then mixed within the MR-EDF framework. Starting from an effective interaction that was fitted to data on heavy nuclei and a formalism that does not *a priori* assume any clusterized structures, the employed framework enabled a consistent, parameter-free calculation of collective excitation spectra and the corresponding electric transition strengths in the very light ^{12}C isotope.

In particular, we have focused our attention on the structure of the three lowest $K^\pi = 0^+$ bands. Overall, empirical properties of the ground-state band have been accurately reproduced. Collective 2_1^+ and 4_1^+ states are found at energies that are only marginally lower than the experimental values, and the corresponding ratio $E(4_1^+)/E(2_1^+)$ strongly indicates the rotational character of the *yrast* band. Moreover, calculated $E2$ transition strength from the 2_1^+ state to the ground state is within the experimental error bar margin, while positive spectroscopic quadrupole moments confirm oblate deformation of the $K^\pi = 0_1^+$ band. The present model does not include triaxial shapes and it therefore does not reproduce the $B(E2; 2_2^+ \rightarrow 0_2^+)$ strength within the Hoyle band as calculated with the AMD and the THSR theoretical models. Nevertheless, the obtained 0_2^+ state is located less than 1 MeV above its measured position, and the calculated $B(E2; 2_1^+ \rightarrow 0_2^+)$ strength is in rather good agreement with the experiment. Furthermore, the excited band built upon the 0_3^+ state was demonstrated to have a strong rotational character with rather large spectroscopic quadrupole moments and intraband $E2$ transition strengths. In the intrinsic frame, this band exhibits the pronounced linear chain structure that corresponds to the $^8\text{Be}+\alpha$ configuration. Finally, both elastic and inelastic form factors show good agreement with the experimental data for a rather wide range of momentum transfers. In this particular aspect, the present global model exhibits a predictive power which can compete with that of the most successful models for cluster studies.

³Remember the morals of footnote 4 on p. 84.

Conclusion and Outlook

Three passions, simple but overwhelmingly strong, have governed my life: the longing for love, the search for knowledge, and unbearable pity for the suffering of mankind. These passions, like great winds, have blown me hither and thither, in a wayward course, over a great ocean of anguish, reaching to the very verge of despair. (...) This has been my life. I have found it worth living, and would gladly live it again if the chance were offered me.

Bertrand Russell, Prologue to Autobiography

The framework of energy density functionals currently provides the most complete and accurate description of ground-state and excited-state properties of atomic nuclei over the entire nuclide chart. EDF-based models, especially when extended to include the restoration of broken symmetries and subsequent configuration mixing, represent state-of-the-art tool for studies of various structure phenomena, from light nuclear systems to superheavy nuclei and from the valley of β -stability to the particle drip-lines. Some of the advantages of using manifestly covariant functionals involve the natural inclusion of the spin-orbit potential, the unique parameterization of nucleon currents, as well as the explanation of empirical pseudospin symmetry in terms of relativistic mean-fields. Recently, it was also demonstrated that relativistic EDFs, when compared to their non-relativistic counterparts, predict significantly more localized density distributions in light nuclei. This property of covariant framework was linked to the larger depth of the underlying single-nucleon potential, which corresponds to a sum of the large attractive scalar and repulsive vector Lorentz fields. In practical terms, this feature makes relativistic EDF models a particularly convenient framework for studies of formation of clusters, that can be considered as a transitional phenomenon between quantum liquid and solid phases in atomic nuclei.

In this thesis, we have developed the fully symmetry-conserving collective model for nuclear structure studies based on the relativistic EDF framework. Starting point of our calculation was the RHB model, which provides a unified description of particle-hole and particle-particle correlations on a mean-field level. In the ph channel we have used the point-coupling DD-PC1 functional, while a pairing force separable in momentum space was employed in the pp channel. Both axial and time-reversal symmetry of the intrinsic states were imposed, while they were allowed to break the rotational, particle number, and parity symmetry. This kind of analysis enabled an access to nuclear configurations

in the entire plane spanned by the axially-symmetric quadrupole and octupole deformations, providing a basic description of nuclear ground-states in terms of the symmetry-breaking wave functions. In the next step, the restoration of angular momentum, particle number, and parity of intrinsic states were all simultaneously performed. The symmetry-restored configurations were further mixed within the MR-EDF framework in order to build collective nuclear states with good quantum numbers. Solving the corresponding HWG equation yielded the excitation spectra and collective wave functions that could then be used to calculate various observables, such as spectroscopic quadrupole moments and electromagnetic multipole transition strengths. Finally, the recently-developed BMF techniques for studies of correlated densities and electron scattering form factors were implemented to the model. Ultimately, we have developed the state-of-the-art collective model for nuclear structure studies that can, together with the eventual extensions, be applied in analyses of various phenomena over the entire nuclide chart. In this work, the model was employed in a study of clustering phenomena in neon and carbon isotopes. Starting from an effective interaction that was fitted to data on medium-heavy and heavy nuclei and a formalism that does not *a priori* assume any clusterized structures, the employed framework enabled a consistent, parameter-free calculation of collective excitation spectra and the corresponding electric transition strengths in light and very light nuclear systems.

As a first application of the model, we have carried out a comprehensive study of quadrupole-octupole collectivity and cluster structures in neon isotopes. The ground-state experimental values of binding energies and charge radii were reproduced reasonably well already on the SR-EDF level. On the MR-EDF level, correlated ground states were demonstrated to exhibit a rather complex structure, with significant contributions from both the prolate- and oblate-deformed configurations. The corresponding two-neutron separation energies showed good agreement with the experimental data, and ^{34}Ne is confirmed to be the last stable even-even isotope of neon. Furthermore, good agreement with the experimental low-lying excitation energies and transition strengths was obtained over the entire isotopic chain. Signatures of the shape-coexistence were detected in ^{24}Ne isotope, while the drip-line ^{34}Ne nucleus was found to exhibit a prolate-deformed structure with significantly compressed collective spectrum. Calculated spectrum for the self-conjugate ^{20}Ne isotope was shown to exhibit a level of accuracy that is comparable to the one obtained using some more specific models, such as the AMD theory. It was demonstrated that the obtained lowest positive- and negative-parity doublet bands are dominated by the $^{16}\text{O}+\alpha$ structure in the intrinsic frame. The ground state of ^{20}Ne contains significant contribution from oblate-deformed configurations, while the increase of angular momentum leads towards predominance of prolate shapes and development of the α - ^{12}C - α -like structure in the $J^\pi = 6^+$ state. In the negative-parity band this dissolution occurs at much slower rate than reported in some previous studies and a pronounced $^{16}\text{O}+\alpha$ structure persists even up to $J^\pi = 7^-$ in the present calculation.

Furthermore, the symmetry-restoring framework was employed in a study of the low-lying positive-parity spectroscopy and cluster structures in ^{12}C isotope. Empirical properties of the ground-state band have been accurately reproduced, including the excitation

energies and spectroscopic quadrupole moments of the excited states, as well as the intraband quadrupole transition strengths. The excited band built on 0_3^+ state was demonstrated to have a strong rotational character and exhibit the pronounced linear chain structure in the intrinsic frame. Even though the present model does not include triaxial shapes and therefore does not reproduce intrinsic density profile of the Hoyle state as calculated with some dedicated cluster models, the obtained 0_2^+ state is located less than 1 MeV above its measured position. In addition, both elastic and inelastic form factors show good agreement with the experimental data for a rather wide range of momentum transfers. In this particular aspect, the present global model exhibits a predictive power which can compete with that of the most successful models for cluster studies.

The upcoming advancements in computational capabilities will most likely render configuration-mixing calculations with three or even more generating coordinates computationally feasible in the near future. Consequently, the simultaneous inclusion of triaxial, octupole, and eventually tetrahedral intrinsic shapes will enable global MR-EDF models to simultaneously probe the vast richness of cluster structures (for example, triangular and pear-shaped configurations) that arguably coexist in the low-lying states of light nuclei. From a more microscopic perspective, the single-particle content of the nuclear wave function, which is routinely accessed on the SR-EDF level, is typically overlooked on the MR-EDF level. In fact, the extraction of single-particle occupancies from correlated collective states has been only recently addressed [RPN16]. Further development and implementation of such methods will enable us to access the single-particle content of the correlated collective states and thereby possibly reveal some interesting implications for the formation of clusters. Finally, the intrinsic densities used in this work provide a rather qualitative measure of the degree of clustering and the employment of some more rigorous localization measures [RMUO11] may provide an additional insight into the underlying causes for the spatial localization of nucleons. The global symmetry-conserving MR-EDF models such as the one developed in this manuscript, especially when extended to include the listed and possible other upgrades, present one of the most promising theoretical tools for studies of the coexistence of the quantum-liquid and cluster states in atomic nuclei.

The Single-Particle Bases

RHB equations in this study are solved in the configuration space of axially symmetric harmonic oscillator, as previously discussed in Chapter 1. Within the framework of second quantization, single-particle states that span this space are generated from a bare vacuum state $|0\rangle$ by applying a corresponding set of single-particle creation and annihilation operators, $\{c_\alpha^\dagger, c_\alpha\}$. In all practical implementations, however, a specific representation of these states needs to be chosen. In this appendix, we will first briefly overview the most important facts about the second quantization formalism. Then, we will proceed to define the coordinate space representation of eigenstates of the axially symmetric harmonic oscillator potential, that are extensively used throughout the study. Furthermore, we will demonstrate how this basis can be used to define a basis of eigenfunctions of the simplex-x operator. These eigenfunctions will be a basis of choice for our considerations in Chapter 2. Furthermore, we will derive necessary expressions for the expansion of large and small components of Bogoliubov wave function in the simplex-x basis. Finally, we will derive matrix elements of rotation operator in the simplex-x basis.

A.1. A Brief Note on Second Quantization

Term *second quantization* is somewhat misleading, since it implies the additional quantizing of quantum physics formalism. In contrast to what the name may imply, the second quantization should simply be thought of as an alternative formulation of the (already quantized) framework which turns out to be specially convenient when juggling various algebraic manipulations in solving the nuclear many-body problem. A rather comprehensive overview of second quantization formalism is, for example, given in Chapter 1 of the classic textbook by J.-P. Blaizot and G. Ripka [BR85]. At this place, we will only set up the stage for a theory to play on, and briefly review the most important formulas that are typically used massively between what is presented as a starting expression and what is given as a final result. To start with, we define the playground of our theory to

be the Fock space \mathcal{F} , which corresponds to a direct sum of Hilbert spaces associated with different particle numbers:

$$\mathcal{F} = \mathcal{H}_0 \oplus \mathcal{H}_1 \cdots \oplus \mathcal{H}_N \oplus \dots, \quad (\text{A.1})$$

where a Hilbert space \mathcal{H}_N provides the totally antisymmetric N -body basis of reference \mathcal{B}_N . In particular, the \mathcal{H}_0 space contains only a bare vacuum $|0\rangle$ state. Transformation to the 1-body space \mathcal{H}_1 is dictated by a set of particle creation and annihilation operators $\{c_\alpha^\dagger, c_\alpha\}$:

$$c_\alpha^\dagger |0\rangle = |\alpha\rangle, \quad c_\alpha |\alpha\rangle = |0\rangle, \quad (\text{A.2})$$

where the Pauli principle for fermions implies:

$$c_\alpha^\dagger |\alpha\rangle = 0, \quad c_\alpha |0\rangle = 0. \quad (\text{A.3})$$

Furthermore, these operators can be used to transform a system from the \mathcal{H}_N space to the \mathcal{H}_{N-1} space:

$$c_\mu |\nu\alpha\beta\dots\rangle = \begin{cases} |\alpha\beta\dots\rangle & \text{if } \mu = \nu, \\ 0 & \text{if } \mu \neq \nu, \end{cases} \quad (\text{A.4})$$

as well as to transform a system from the \mathcal{H}_N space to the \mathcal{H}_{N+1} space:

$$c_\mu^\dagger |\alpha\beta\dots\nu\dots\rangle = \begin{cases} |\mu\alpha\beta\dots\nu\dots\rangle & \text{if } \mu \neq \nu, \\ 0 & \text{if } \mu = \nu. \end{cases} \quad (\text{A.5})$$

In general the N -body basis $\mathcal{B}_N = \{|1 : \alpha; 2 : \beta; \dots\rangle\}$ ¹ will satisfy a property of orthonormality:

$$\langle 1 : \alpha; 2 : \beta \dots | 1 : \alpha'; 2 : \beta' \dots \rangle = \delta_{\alpha\alpha'} \delta_{\beta\beta'} \dots \quad (\text{A.6})$$

Particle creation and annihilation operators are related by Hermitian conjugation and satisfy standard fermionic anticommutation relations:

$$\{c_\alpha, c_\beta^\dagger\} = c_\alpha c_\beta^\dagger + c_\beta^\dagger c_\alpha = \delta_{\alpha\beta}, \quad (\text{A.7a})$$

$$\{c_\alpha, c_\beta\} = \{c_\alpha^\dagger, c_\beta^\dagger\} = 0. \quad (\text{A.7b})$$

¹In the coordinate representation, \mathcal{B}_N will typically correspond to the Slater determinants basis.

Within the second quantization formalism, the one-body operator \hat{A} can be written as:

$$\hat{A} = \sum_{\alpha\beta} A_{\alpha\beta} c_{\alpha}^{\dagger} c_{\beta}, \quad (\text{A.8})$$

while the two-body operator \hat{B} can be written as:

$$\hat{B} = \frac{1}{2} \sum_{\alpha\beta\gamma\delta} B_{\alpha\beta\gamma\delta} c_{\alpha}^{\dagger} c_{\beta}^{\dagger} c_{\delta} c_{\gamma}, \quad (\text{A.9})$$

where coefficients $A_{\alpha\beta}$ and $B_{\alpha\beta\gamma\delta}$ correspond to matrix elements of operators \hat{A} and \hat{B} in \mathcal{B}_1 and \mathcal{B}_2 bases, respectively. We note that a unitary transformation between the single-particle basis defined here and the single-quasiparticle basis of Bogoliubov framework is given by Eq. (1.32). More information on interesting properties of this transformation can be read, for example, in Appendix E of the Ring-Schuck textbook [RS80].

A.2. Coordinate Representation of the Harmonic Oscillator Basis

Eigenfunctions of the axially symmetric harmonic oscillator $|\alpha\rangle$ live in a one-body \mathcal{H}_1 space, and they are composed of the coordinate space part and the spin part:

$$|\alpha\rangle \equiv |\alpha\rangle_{\text{space}} \cdot |\alpha\rangle_{\text{spin}} = |n_z n_{\perp} \Lambda m_s\rangle. \quad (\text{A.10})$$

State $|\alpha\rangle$ is characterized by a set of quantum numbers $\{\alpha\} = \{n_z, n_{\perp}, \Lambda, m_s\}$, where n_z and n_{\perp} represent number of quanta (nodes) in the z - and the r_{\perp} - directions, respectively, while Λ and m_s denote components of the orbital angular momentum and of the spin along the z - axis. Spatial part of the total function corresponds to eigenfunctions of the harmonic oscillator potential [GRT90]:

$$V_{\text{osc}}(z, r_{\perp}) = \frac{1}{2} M \omega_z^2 z^2 + \frac{1}{2} M \omega_{\perp}^2 r_{\perp}^2. \quad (\text{A.11})$$

Taking into account conservation of nuclear volume under deformation, the perpendicular oscillator frequency $\hbar\omega_{\perp}$ and the axial oscillator frequency $\hbar\omega_z$ can be written in terms of the spherical oscillator frequency $\hbar\omega_0$ and the deformation parameter β_0 :

$$\begin{aligned} \hbar\omega_{\perp} &= \hbar\omega_0 e^{\frac{1}{2}\sqrt{5/4\pi}\beta_0}, \\ \hbar\omega_z &= \hbar\omega_0 e^{-\sqrt{5/4\pi}\beta_0}. \end{aligned} \quad (\text{A.12})$$

The corresponding oscillator length parameters are $b_{\perp} = \sqrt{\hbar/M\omega_{\perp}}$ and $b_z = \sqrt{\hbar/M\omega_z}$, where the equality $b_{\perp}b_z = b_0^3$ holds due to a volume conservation. Therefore, constants $\hbar\omega_0$ and β_0 uniquely define our potential and, consequently, our basis². In the coordinate representation, spatial part $|\alpha\rangle_{\text{space}}$ of the total eigenfunction (A.10) can be explicitly written as:

$$\Phi_{n_z, n_{\perp}, \Lambda}(z, r_{\perp}, \phi) = \phi_{n_z}(z)\phi_{n_{\perp}}^{\Lambda}(r_{\perp})\frac{1}{\sqrt{2\pi}}e^{i\Lambda\phi}. \quad (\text{A.13})$$

Here, eigenfunctions in the z -direction read:

$$\phi_{n_z}(z) = \frac{N_{n_z}}{\sqrt{b_z}}H_{n_z}(\xi)e^{-\xi^2/2}, \quad \xi = z/b_z, \quad (\text{A.14})$$

with the normalization constant:

$$N_{n_z} = \frac{1}{\sqrt{\sqrt{\pi}2^{n_z}n_z!}}, \quad (\text{A.15})$$

and the Hermite polynomials $H_{n_z}(\xi)$ defined in Ref. [AS65]. The orthogonality relation for Hermite polynomials

$$\int_{-\infty}^{\infty} dx H_m(x)H_n(x)e^{-x^2} = \sqrt{\pi}2^n n! \delta_{mn} \quad (\text{A.16})$$

implies the orthogonality relation for eigenfunctions in the z -direction:

$$\int_{-\infty}^{\infty} dz \phi_{n_z}(z)\phi_{n'_z}(z) = \delta_{n_z n'_z}. \quad (\text{A.17})$$

In addition, properties of Hermite polynomials [AS65] can be used to show that the eigenfunctions in the z -direction satisfy useful relations:

$$\begin{aligned} \partial_z \phi_{n_z}(z) &= \frac{1}{\sqrt{2}b_z} \left[-\sqrt{n_z+1}\phi_{n_z+1}(z) + \sqrt{n_z}\phi_{n_z-1}(z) \right], \\ z\phi_{n_z}(z) &= \frac{b_z}{2} \left[\sqrt{n_z+1}\phi_{n_z+1}(z) + \sqrt{n_z}\phi_{n_z-1}(z) \right]. \end{aligned} \quad (\text{A.18})$$

Eigenfunctions in the r_{\perp} -direction read:

²In practical implementations, values of $\hbar\omega_0$ and β_0 should be chosen optimally in order to achieve fast convergence. Of course, calculated value of any physical observable has to be independent of the particular choice of basis parameters.

$$\phi_{n_{\perp}}^{\Lambda}(r_{\perp}) = \frac{N_{n_{\perp}}^{\Lambda}}{b_{\perp}} \sqrt{2} \eta^{\Lambda/2} L_{n_{\perp}}^{\Lambda}(\eta) e^{-\eta/2}, \quad \eta = r_{\perp}^2/b_{\perp}^2, \quad (\text{A.19})$$

with the normalization constant:

$$N_{n_{\perp}}^{\Lambda} = \sqrt{\frac{n_{\perp}!}{(n_{\perp} + \Lambda)!}}, \quad (\text{A.20})$$

and the associated Laguerre polynomials $L_{n_{\perp}}^{\Lambda}(\eta)$ defined in Ref. [AS65]. The orthogonality relation for associated Laguerre polynomials

$$\int_0^{\infty} dx x^{\alpha} e^{-x} L_n^{(\alpha)}(x) L_m^{(\alpha)}(x) = \frac{\Gamma(n + \alpha + 1)}{n!} \delta_{mn} \quad (\text{A.21})$$

implies the orthogonality relation for eigenfunctions in the r_{\perp} -direction:

$$\int_0^{\infty} dr_{\perp} \phi_{n_{\perp}}^{\Lambda}(r_{\perp}) \phi_{n'_{\perp}}^{\Lambda}(r_{\perp}) r_{\perp} = \delta_{n_{\perp} n'_{\perp}}. \quad (\text{A.22})$$

In addition, orthogonality of eigenfunctions in the ϕ -direction can be demonstrated trivially:

$$\int_0^{2\pi} d\phi \frac{1}{\sqrt{2\pi}} e^{-i\Lambda'\phi} \frac{1}{\sqrt{2\pi}} e^{i\Lambda\phi} = \delta_{\Lambda\Lambda'}. \quad (\text{A.23})$$

The spin part $|\alpha\rangle_{\text{spin}}$ of total eigenfunction (A.10) is an eigenvector of the z -component of the total spin operator:

$$\hat{S}_z |s; m_s\rangle = \hbar m_s |s; m_s\rangle. \quad (\text{A.24})$$

For $s = \frac{1}{2}$ fermions such as nucleons, possible projections of total spin on the symmetry axis are $m_s = +\frac{1}{2}$ (corresponding state is denoted as $|\uparrow\rangle$) and $m_s = -\frac{1}{2}$ (corresponding state is denoted as $|\downarrow\rangle$). Finally, total eigenfunction of the axially symmetric harmonic oscillator reads:

$$\Phi_{\alpha}(\mathbf{r}, s) = \Phi_{n_z, n_{\perp}, \Lambda}(z, r_{\perp}, \phi) \times \chi_{m_s}(s). \quad (\text{A.25})$$

These functions are used to expand large and the small components of nuclear spinor of Eq. (1.44). Furthermore, even though a state $|\alpha\rangle$ does not carry a good quantum number of total angular momentum J , its projection j_z on a symmetry axis still represents a good quantum number. The corresponding eigenvalue reads:

$$\Omega = \Lambda + m_s. \quad (\text{A.26})$$

Finally, eigenfunction of the Kramers-degenerated time-reversed state $|\bar{\alpha}\rangle$ with $\Omega_{\bar{\alpha}} = -\Omega_{\alpha}$ reads:

$$\begin{aligned} \Phi_{\bar{\alpha}}(r_{\perp}, z, \phi, s) &= \hat{T}\Phi_{\alpha}(r_{\perp}, z, \phi, s) \\ &= \phi_{n_z}(z)\phi_{n_{\perp}}^{\Lambda}(r_{\perp})\frac{1}{\sqrt{2\pi}}e^{-i\Lambda\phi}(-1)^{1/2-m_s}\chi_{-m_s}(s). \end{aligned} \quad (\text{A.27})$$

A.3. The Simplex-X Basis

The simplex-x operator $\hat{\Pi}_x$ is defined as a product of the parity operator $\hat{\Pi}$ and the operator of rotation by 180° around the x -axis:

$$\hat{\Pi}_x = \hat{\Pi}e^{-i\pi\hat{J}_x} = \hat{\Pi}e^{-i\pi\hat{L}_x}e^{-i\pi\hat{S}_x}. \quad (\text{A.28})$$

The product of the parity and the $e^{-i\pi\hat{L}_x}$ operators corresponds to the transformation in Cartesian coordinates $(x, y, z) \rightarrow (-x, y, z)$, and to the transformation in cylindrical coordinates $(z, r_{\perp}, \phi) \rightarrow (z, r_{\perp}, \pi - \phi)$. In addition, the spin part of the operator can be rewritten as:

$$e^{-i\pi\hat{S}_x} = e^{-i\frac{\pi}{2}\hat{\sigma}_x} = \sum_{n=0}^{\infty} \frac{1}{n!} \left(-i\frac{\pi}{2}\right)^n \sigma_x^n, \quad (\text{A.29})$$

where σ_x denotes the x -component of Pauli matrices:

$$\sigma_x = \begin{pmatrix} 0 & 1 \\ 1 & 0 \end{pmatrix}, \quad \sigma_y = \begin{pmatrix} 0 & -i \\ i & 0 \end{pmatrix}, \quad \sigma_z = \begin{pmatrix} 1 & 0 \\ 0 & -1 \end{pmatrix}, \quad (\text{A.30})$$

that are Hermitian, unitary, and possess the property of involutory:

$$\sigma_x^2 = \sigma_y^2 = \sigma_z^2 = \begin{pmatrix} 1 & 0 \\ 0 & 1 \end{pmatrix} = \mathbb{1}. \quad (\text{A.31})$$

Separating the total sum into even and odd parts, using the property of involutory of Pauli matrices, and recognizing the Taylor series expansion for cosine and sine functions, the expression (A.29) can be rewritten as:

$$\begin{aligned}
e^{-i\pi\hat{S}_x} &= \sum_{k=0}^{\infty} \frac{1}{(2k)!} (-i\frac{\pi}{2})^{2k} \sigma_x^{2k} + \sum_{k=0}^{\infty} \frac{1}{(2k+1)!} (-i\frac{\pi}{2})^{2k+1} \sigma_x^{2k+1} \\
&= \sum_{k=0}^{\infty} \frac{(-1)^k}{(2k)!} (\frac{\pi}{2})^{2k} \mathbb{1} - i\sigma_x \sum_{k=0}^{\infty} \frac{(-1)^k}{(2k+1)!} (\frac{\pi}{2})^{2k+1} \\
&= \cos \frac{\pi}{2} \mathbb{1} - i\sigma_x \sin \frac{\pi}{2} \\
&= -i\sigma_x.
\end{aligned} \tag{A.32}$$

It therefore follows that applying the simplex-x operator of Eq. (A.28) on the harmonic oscillator eigenstate of (A.10) yields:

$$\hat{\Pi}_x |n_z n_{\perp} \Lambda m_s\rangle = -i(-1)^{\Lambda} |n_z n_{\perp} - \Lambda - m_s\rangle. \tag{A.33}$$

This enables us to construct states that are eigenstates of the simplex-x operator:

$$\hat{\Pi}_x |n_z n_{\perp} \Lambda; +i\rangle = (+i) |n_z n_{\perp} \Lambda; +i\rangle, \tag{A.34a}$$

$$\hat{\Pi}_x |n_z n_{\perp} \Lambda; -i\rangle = (-i) |n_z n_{\perp} \Lambda; -i\rangle. \tag{A.34b}$$

where quantum number Λ can take both positive and negative values. The coordinate space representations of states (A.34a) and (A.34b) in terms of eigenfunctions of the axially symmetric harmonic oscillator reads:

$$\Phi_{[n_z n_{\perp} \Lambda; +i]}(\mathbf{r}) = \frac{1}{\sqrt{2}} [\Phi_{[n_z n_{\perp} \Lambda \uparrow]}(\mathbf{r}) - (-1)^{\Lambda} \Phi_{[n_z n_{\perp} - \Lambda \downarrow]}(\mathbf{r})], \tag{A.35a}$$

$$\Phi_{[n_z n_{\perp} \Lambda; -i]}(\mathbf{r}) = \frac{(-1)^{\Lambda}}{\sqrt{2}} [\Phi_{[n_z n_{\perp} \Lambda \uparrow]}(\mathbf{r}) + (-1)^{\Lambda} \Phi_{[n_z n_{\perp} - \Lambda \downarrow]}(\mathbf{r})]. \tag{A.35b}$$

In addition, using Eq. (A.27), it can be demonstrated that the time-reversal operator \hat{T} transforms the $|s = +i\rangle$ state into the $|s = -i\rangle$ state:

$$\hat{T} \Phi_{[n_z n_{\perp} \Lambda; +i]}(\mathbf{r}) = \Phi_{[n_z n_{\perp} \Lambda; -i]}(\mathbf{r}), \tag{A.36}$$

and the $|s = -i\rangle$ state into the $-|s = +i\rangle$ state:

$$\hat{T} \Phi_{[n_z n_{\perp} \Lambda; -i]}(\mathbf{r}) = -\Phi_{[n_z n_{\perp} \Lambda; +i]}(\mathbf{r}), \tag{A.37}$$

where $\hat{T}^2 = -1$, and states $|s = +i\rangle$ and $|s = -i\rangle$ are orthogonal and Kramers degenerated.

A.4. Bogoliubov States in the Simplex-X Basis

Solutions to the RHB equations are axially symmetric, that is, each state belongs to a certain $\Omega = \Lambda + m_s$ block. Components of the $U_k(\mathbf{r})$ and $V_k(\mathbf{r})$ wave functions [c.f. Eq. (1.43)] can therefore be expanded in terms of the harmonic oscillator eigenfunctions in the following manner:

$$U_k^\Omega(\mathbf{r}) = \sum_{n_z n_\perp} \left(U_{k[n_z n_\perp \uparrow]}^\Omega \Phi_{[n_z n_\perp \Lambda = \Omega - \frac{1}{2} \uparrow]}(\mathbf{r}) + U_{k[n_z n_\perp \downarrow]}^\Omega \Phi_{[n_z n_\perp \Lambda = \Omega + \frac{1}{2} \downarrow]}(\mathbf{r}) \right), \quad (\text{A.38a})$$

$$V_k^\Omega(\mathbf{r}) = \sum_{n_z n_\perp} \left(V_{k[n_z n_\perp \uparrow]}^\Omega \Phi_{[n_z n_\perp \Lambda = -\Omega + \frac{1}{2} \downarrow]}(\mathbf{r}) - V_{k[n_z n_\perp \downarrow]}^\Omega \Phi_{[n_z n_\perp \Lambda = -\Omega - \frac{1}{2} \uparrow]}(\mathbf{r}) \right). \quad (\text{A.38b})$$

Assuming that the expansion coefficients $U_{k[n_z n_\perp m_s]}^\Omega$ and $V_{k[n_z n_\perp m_s]}^\Omega$ are real, we can obtain the time-reversed states as:

$$\hat{T}U_k^\Omega(\mathbf{r}) = \sum_{n_z n_\perp} \left(U_{k[n_z n_\perp \uparrow]}^\Omega \Phi_{[n_z n_\perp \Lambda = -\Omega + \frac{1}{2} \downarrow]}(\mathbf{r}) - U_{k[n_z n_\perp \downarrow]}^\Omega \Phi_{[n_z n_\perp \Lambda = -\Omega - \frac{1}{2} \uparrow]}(\mathbf{r}) \right), \quad (\text{A.39a})$$

$$\hat{T}V_k^\Omega(\mathbf{r}) = \sum_{n_z n_\perp} \left(-V_{k[n_z n_\perp \uparrow]}^\Omega \Phi_{[n_z n_\perp \Lambda = \Omega - \frac{1}{2} \uparrow]}(\mathbf{r}) - V_{k[n_z n_\perp \downarrow]}^\Omega \Phi_{[n_z n_\perp \Lambda = \Omega + \frac{1}{2} \downarrow]}(\mathbf{r}) \right). \quad (\text{A.39b})$$

In order to expand these states in the simplex-x basis, we first invert the relations (A.35a) and (A.35b):

$$\Phi_{[n_z n_\perp \Lambda \uparrow]}(\mathbf{r}) = \frac{1}{\sqrt{2}} \left[\Phi_{[n_z n_\perp \Lambda; +i]}(\mathbf{r}) + (-1)^\Lambda \Phi_{[n_z n_\perp \Lambda; -i]}(\mathbf{r}) \right], \quad (\text{A.40a})$$

$$\Phi_{[n_z n_\perp -\Lambda \downarrow]}(\mathbf{r}) = \frac{1}{\sqrt{2}} \left[-(-1)^\Lambda \Phi_{[n_z n_\perp \Lambda; +i]}(\mathbf{r}) + \Phi_{[n_z n_\perp \Lambda; -i]}(\mathbf{r}) \right]. \quad (\text{A.40b})$$

These expressions are then plugged into the Eqs. (A.38a) and (A.38b):

$$\begin{aligned}
U_k^\Omega(\mathbf{r}) &= \sum_{n_z n_\perp} \frac{1}{\sqrt{2}} U_{k[n_z n_\perp \uparrow]}^\Omega \Phi_{[n_z n_\perp \Lambda = \Omega - \frac{1}{2}; +i]}(\mathbf{r}) \\
&+ \sum_{n_z n_\perp} \frac{1}{\sqrt{2}} (-1)^{\Omega - \frac{1}{2}} U_{k[n_z n_\perp \downarrow]}^\Omega \Phi_{[n_z n_\perp \Lambda = -\Omega - \frac{1}{2}; +i]}(\mathbf{r}) \\
&+ \sum_{n_z n_\perp} \frac{1}{\sqrt{2}} (-1)^{\Omega - \frac{1}{2}} U_{k[n_z n_\perp \uparrow]}^\Omega \Phi_{[n_z n_\perp \Lambda = \Omega - \frac{1}{2}; -i]}(\mathbf{r}) \\
&+ \sum_{n_z n_\perp} \frac{1}{\sqrt{2}} U_{k[n_z n_\perp \downarrow]}^\Omega \Phi_{[n_z n_\perp \Lambda = -\Omega - \frac{1}{2}; -i]}(\mathbf{r}),
\end{aligned} \tag{A.41}$$

$$\begin{aligned}
V_k^\Omega(\mathbf{r}) &= \sum_{n_z n_\perp} \frac{1}{\sqrt{2}} (-1)^{\Omega + \frac{1}{2}} V_{k[n_z n_\perp \uparrow]}^\Omega \Phi_{[n_z n_\perp \Lambda = \Omega - \frac{1}{2}; +i]}(\mathbf{r}) \\
&+ \sum_{n_z n_\perp} \frac{(-1)}{\sqrt{2}} V_{k[n_z n_\perp \downarrow]}^\Omega \Phi_{[n_z n_\perp \Lambda = -\Omega - \frac{1}{2}; +i]}(\mathbf{r}) \\
&+ \sum_{n_z n_\perp} \frac{1}{\sqrt{2}} V_{k[n_z n_\perp \uparrow]}^\Omega \Phi_{[n_z n_\perp \Lambda = \Omega - \frac{1}{2}; -i]}(\mathbf{r}) \\
&+ \sum_{n_z n_\perp} \frac{1}{\sqrt{2}} (-1)^{\Omega - \frac{1}{2}} V_{k[n_z n_\perp \downarrow]}^\Omega \Phi_{[n_z n_\perp \Lambda = -\Omega - \frac{1}{2}; -i]}(\mathbf{r}),
\end{aligned} \tag{A.42}$$

as well as into the Eqs. (A.39a) and (A.39b):

$$\begin{aligned}
\hat{T}U_k^\Omega(\mathbf{r}) &= \sum_{n_z n_\perp} \frac{1}{\sqrt{2}} (-1)^{\Omega + \frac{1}{2}} U_{k[n_z n_\perp \uparrow]}^\Omega \Phi_{[n_z n_\perp \Lambda = \Omega - \frac{1}{2}; +i]}(\mathbf{r}) \\
&+ \sum_{n_z n_\perp} \frac{(-1)}{\sqrt{2}} U_{k[n_z n_\perp \downarrow]}^\Omega \Phi_{[n_z n_\perp \Lambda = -\Omega - \frac{1}{2}; +i]}(\mathbf{r}) \\
&+ \sum_{n_z n_\perp} \frac{1}{\sqrt{2}} U_{k[n_z n_\perp \uparrow]}^\Omega \Phi_{[n_z n_\perp \Lambda = \Omega - \frac{1}{2}; -i]}(\mathbf{r}) \\
&+ \sum_{n_z n_\perp} \frac{1}{\sqrt{2}} (-1)^{\Omega - \frac{1}{2}} U_{k[n_z n_\perp \downarrow]}^\Omega \Phi_{[n_z n_\perp \Lambda = -\Omega - \frac{1}{2}; -i]}(\mathbf{r}),
\end{aligned} \tag{A.43}$$

$$\begin{aligned}
\hat{T}V_k^\Omega(\mathbf{r}) &= \sum_{n_z n_\perp} \frac{(-1)}{\sqrt{2}} V_{k[n_z n_\perp \uparrow]}^\Omega \Phi_{[n_z n_\perp \Lambda = \Omega - \frac{1}{2}; +i]}(\mathbf{r}) \\
&+ \sum_{n_z n_\perp} \frac{1}{\sqrt{2}} (-1)^{\Omega + \frac{1}{2}} V_{k[n_z n_\perp \downarrow]}^\Omega \Phi_{[n_z n_\perp \Lambda = -\Omega - \frac{1}{2}; +i]}(\mathbf{r}) \\
&+ \sum_{n_z n_\perp} \frac{1}{\sqrt{2}} (-1)^{\Omega + \frac{1}{2}} V_{k[n_z n_\perp \uparrow]}^\Omega \Phi_{[n_z n_\perp \Lambda = \Omega - \frac{1}{2}; -i]}(\mathbf{r}) \\
&+ \sum_{n_z n_\perp} \frac{(-1)}{\sqrt{2}} V_{k[n_z n_\perp \downarrow]}^\Omega \Phi_{[n_z n_\perp \Lambda = -\Omega - \frac{1}{2}; -i]}(\mathbf{r}).
\end{aligned} \tag{A.44}$$

Since pairs of states $\{U_k^\Omega(\mathbf{r}), \hat{T}U_k^\Omega(\mathbf{r})\}$ and $\{V_k^\Omega(\mathbf{r}), \hat{T}V_k^\Omega(\mathbf{r})\}$ are Kramers degenerated, any

linear combination also corresponds to the ground-state solution of the RHB equations. We will use this property in order to generate states which are both solutions to the RHB equations and eigenstates of the $\hat{\Pi}_x$ operator. In particular, linear combination

$$\begin{aligned} \frac{1}{\sqrt{2}} \left\{ U_k^\Omega(\mathbf{r}) - (-1)^{\Omega-\frac{1}{2}} \hat{T} U_k^\Omega(\mathbf{r}) \right\} &= \sum_{n_z n_\perp} U_{k[n_z n_\perp \Lambda \geq 0]}^{\Omega, s=+i} \Phi_{[n_z n_\perp \Lambda = \Omega - \frac{1}{2}; +i]}(\mathbf{r}) \\ &+ \sum_{n_z n_\perp} U_{k[n_z n_\perp \Lambda < 0]}^{\Omega, s=+i} \Phi_{[n_z n_\perp \Lambda = -\Omega - \frac{1}{2}; +i]}(\mathbf{r}) \end{aligned} \quad (\text{A.45})$$

is an eigenstate with $s = +i$ and coefficients:

$$U_{k[n_z n_\perp \Lambda \geq 0]}^{\Omega, s=+i} = U_{k[n_z n_\perp \uparrow]}^\Omega, \quad U_{k[n_z n_\perp \Lambda < 0]}^{\Omega, s=+i} = -(-1)^\Lambda U_{k[n_z n_\perp \downarrow]}^\Omega, \quad (\text{A.46})$$

while the linear combination

$$\begin{aligned} \frac{1}{\sqrt{2}} \left\{ U_k^\Omega(\mathbf{r}) + (-1)^{\Omega-\frac{1}{2}} \hat{T} U_k^\Omega(\mathbf{r}) \right\} &= \sum_{n_z n_\perp} U_{k[n_z n_\perp \Lambda \geq 0]}^{\Omega, s=-i} \Phi_{[n_z n_\perp \Lambda = \Omega - \frac{1}{2}; -i]}(\mathbf{r}) \\ &+ \sum_{n_z n_\perp} U_{k[n_z n_\perp \Lambda < 0]}^{\Omega, s=-i} \Phi_{[n_z n_\perp \Lambda = -\Omega - \frac{1}{2}; -i]}(\mathbf{r}) \end{aligned} \quad (\text{A.47})$$

is an eigenstate with $s = -i$ and coefficients:

$$U_{k[n_z n_\perp \Lambda \geq 0]}^{\Omega, s=-i} = (-1)^\Lambda U_{k[n_z n_\perp \uparrow]}^\Omega, \quad U_{k[n_z n_\perp \Lambda < 0]}^{\Omega, s=-i} = U_{k[n_z n_\perp \downarrow]}^\Omega. \quad (\text{A.48})$$

On the other hand, linear combination:

$$\begin{aligned} \frac{1}{\sqrt{2}} \left\{ V_k^\Omega(\mathbf{r}) - (-1)^{\Omega-\frac{1}{2}} \hat{T} V_k^\Omega(\mathbf{r}) \right\} &= \sum_{n_z n_\perp} V_{k[n_z n_\perp \Lambda \geq 0]}^{\Omega, s=-i} \Phi_{[n_z n_\perp \Lambda = \Omega - \frac{1}{2}; -i]}(\mathbf{r}) \\ &+ \sum_{n_z n_\perp} V_{k[n_z n_\perp \Lambda < 0]}^{\Omega, s=-i} \Phi_{[n_z n_\perp \Lambda = -\Omega - \frac{1}{2}; -i]}(\mathbf{r}) \end{aligned} \quad (\text{A.49})$$

is an eigenstate with $s = -i$ and coefficients:

$$V_{k[n_z n_\perp \Lambda \geq 0]}^{\Omega, s=-i} = V_{k[n_z n_\perp \uparrow]}^\Omega, \quad V_{k[n_z n_\perp \Lambda < 0]}^{\Omega, s=-i} = -(-1)^\Lambda V_{k[n_z n_\perp \downarrow]}^\Omega, \quad (\text{A.50})$$

while the linear combination:

$$\begin{aligned} \frac{1}{\sqrt{2}} \left\{ V_k^\Omega(\mathbf{r}) + (-1)^{\Omega-\frac{1}{2}} \hat{T} V_k^\Omega(\mathbf{r}) \right\} &= \sum_{n_z n_\perp} V_{k[n_z n_\perp \Lambda \geq 0]}^{\Omega, s=+i} \Phi_{[n_z n_\perp \Lambda = \Omega - \frac{1}{2}; +i]}(\mathbf{r}) \\ &+ \sum_{n_z n_\perp} V_{k[n_z n_\perp \Lambda < 0]}^{\Omega, s=+i} \Phi_{[n_z n_\perp \Lambda = -\Omega - \frac{1}{2}; +i]}(\mathbf{r}) \end{aligned} \quad (\text{A.51})$$

is an eigenstate with $s = +i$ and coefficients:

$$V_{k[n_z n_\perp \Lambda \geq 0]}^{\Omega, s=+i} = -(-1)^\Lambda V_{k[n_z n_\perp \uparrow]}^\Omega, \quad V_{k[n_z n_\perp \Lambda < 0]}^{\Omega, s=+i} = -V_{k[n_z n_\perp \downarrow]}^\Omega. \quad (\text{A.52})$$

In fact, by taking a linear combination for the RHB state of Eq. (1.44):

$$\begin{aligned} \frac{1}{\sqrt{2}} \left\{ \psi_k^{\Omega, i}(\mathbf{r}) \mp (-1)^{\Omega-\frac{1}{2}} \hat{T} \psi_k^{\Omega, i}(\mathbf{r}, s) \right\} &= \frac{1}{\sqrt{2}} \left\{ \begin{pmatrix} f_k^{\Omega, i}(\mathbf{r}) \\ i g_k^{\Omega, i}(\mathbf{r}) \end{pmatrix} \mp (-1)^{\Omega-\frac{1}{2}} \begin{pmatrix} \hat{T} f_k^{\Omega, i}(\mathbf{r}) \\ -i \hat{T} g_k^{\Omega, i}(\mathbf{r}) \end{pmatrix} \right\} \\ &= \frac{1}{\sqrt{2}} \left\{ \begin{pmatrix} f_k^{\Omega, i}(\mathbf{r}) \mp (-1)^{\Omega-\frac{1}{2}} \hat{T} f_k^{\Omega, i}(\mathbf{r}) \\ i g_k^{\Omega, i}(\mathbf{r}) \pm i (-1)^{\Omega-\frac{1}{2}} \hat{T} g_k^{\Omega, i}(\mathbf{r}) \end{pmatrix} \right\}, \end{aligned} \quad (\text{A.53})$$

where $i = U, V$, we can see that in each block the large and the small component of the total wave function should be expanded in the bases of the opposite simplex-x eigenvalues. We note that the first block is defined as the one where the linear combination of the left-hand-side of the Eq. (A.53) corresponds to the difference of terms, while the second block is defined as the one where the linear combination corresponds to the sum of terms. To sum up, the expansion coefficients corresponding to the first block are:

$$\begin{aligned} f_{k[n_z n_\perp \Lambda \geq 0]}^{\Omega, U, s=+i} &= f_{k[n_z n_\perp \uparrow]}^{\Omega, U}, & f_{k[n_z n_\perp \Lambda < 0]}^{\Omega, U, s=+i} &= -(-1)^\Lambda f_{k[n_z n_\perp \downarrow]}^{\Omega, U}, \\ g_{k[n_z n_\perp \Lambda \geq 0]}^{\Omega, U, s=-i} &= (-1)^\Lambda g_{k[n_z n_\perp \uparrow]}^{\Omega, U}, & g_{k[n_z n_\perp \Lambda < 0]}^{\Omega, U, s=-i} &= g_{k[n_z n_\perp \downarrow]}^{\Omega, U}, \\ f_{k[n_z n_\perp \Lambda \geq 0]}^{\Omega, V, s=-i} &= f_{k[n_z n_\perp \uparrow]}^{\Omega, V}, & f_{k[n_z n_\perp \Lambda < 0]}^{\Omega, V, s=-i} &= -(-1)^\Lambda f_{k[n_z n_\perp \downarrow]}^{\Omega, V}, \\ g_{k[n_z n_\perp \Lambda \geq 0]}^{\Omega, V, s=+i} &= -(-1)^\Lambda g_{k[n_z n_\perp \uparrow]}^{\Omega, V}, & g_{k[n_z n_\perp \Lambda < 0]}^{\Omega, V, s=+i} &= -g_{k[n_z n_\perp \downarrow]}^{\Omega, V}. \end{aligned} \quad (\text{A.54})$$

The expansion coefficients corresponding to the second block are:

$$\begin{aligned} f_{k[n_z n_\perp \Lambda \geq 0]}^{\Omega, U, s=-i} &= (-1)^\Lambda f_{k[n_z n_\perp \uparrow]}^{\Omega, U}, & f_{k[n_z n_\perp \Lambda < 0]}^{\Omega, U, s=-i} &= f_{k[n_z n_\perp \downarrow]}^{\Omega, U}, \\ g_{k[n_z n_\perp \Lambda \geq 0]}^{\Omega, U, s=+i} &= g_{k[n_z n_\perp \uparrow]}^{\Omega, U}, & g_{k[n_z n_\perp \Lambda < 0]}^{\Omega, U, s=+i} &= -(-1)^\Lambda g_{k[n_z n_\perp \downarrow]}^{\Omega, U}, \\ f_{k[n_z n_\perp \Lambda \geq 0]}^{\Omega, V, s=+i} &= -(-1)^\Lambda f_{k[n_z n_\perp \uparrow]}^{\Omega, V}, & f_{k[n_z n_\perp \Lambda < 0]}^{\Omega, V, s=+i} &= -f_{k[n_z n_\perp \downarrow]}^{\Omega, V}, \\ g_{k[n_z n_\perp \Lambda \geq 0]}^{\Omega, V, s=-i} &= g_{k[n_z n_\perp \uparrow]}^{\Omega, V}, & g_{k[n_z n_\perp \Lambda < 0]}^{\Omega, V, s=-i} &= -(-1)^\Lambda g_{k[n_z n_\perp \downarrow]}^{\Omega, V}. \end{aligned} \quad (\text{A.55})$$

A.5. Rotation Operator in the Simplex-X Basis

In order to rotate the RHB wave functions of Eq. (1.44), whose expansion coefficients in the simplex-x basis are given by Eqs. (A.54) and (A.55), it is necessary to calculate matrix elements of the $\hat{R}(\beta)$ operator in the simplex-x basis. This will be done in three steps. First, we will calculate matrix elements of the \hat{J}_x operator in the harmonic oscillator basis. Then, these elements will be used to calculate matrix elements of the \hat{J}_x operator in the simplex-x basis. Finally, we will use properties of the matrix eigen decomposition to calculate matrix elements of the $\hat{R}(\beta)$ operator in the simplex-x basis.

Matrix elements of \hat{J}_x in the harmonic oscillator basis

Total angular momentum operator \hat{J}_x can be decomposed into contributions from the orbital angular momentum operator \hat{L}_x and from the spin operator \hat{S}_x , $\hat{J}_x = \hat{L}_x + \hat{S}_x$. The Cartesian-space representation of the orbital angular momentum operator reads:

$$\hat{L}_x = -i\hbar(y\partial_z - z\partial_y). \quad (\text{A.56})$$

Making use of the transformation relations between the Cartesian (x, y, z) and cylindrical (z, r_\perp, ϕ) coordinate systems, the orbital angular momentum operator can be rewritten in terms of the cylindrical coordinates:

$$\hat{L}_x = -\frac{\hbar}{2}r_\perp(e^{i\phi} - e^{-i\phi})\partial_z + \frac{i\hbar}{2}\frac{z}{r_\perp}(e^{i\phi} + e^{-i\phi})\partial_\phi + \frac{\hbar}{2}z(e^{i\phi} - e^{-i\phi})\partial_{r_\perp}. \quad (\text{A.57})$$

Matrix elements of the orbital angular momentum operator in the axially-symmetric harmonic oscillator basis of Eq. (A.25) then read:

$$\begin{aligned} \langle n_z n_\perp \Lambda m_s | \hat{L}_x | n'_z n'_\perp \Lambda' m'_s \rangle &= \delta_{m_s m'_s} \frac{\hbar}{2} \times \\ &\left\{ -\frac{1}{2\pi} \int_{-\infty}^{\infty} dz \phi_{n_z}(z) \partial_z \phi_{n'_z}(z) \int_0^{\infty} dr_\perp r_\perp^2 \phi_{n_\perp|\Lambda|}(r_\perp) \phi_{n'_\perp|\Lambda'|}(r_\perp) \int_0^{2\pi} d\phi e^{i(\Lambda' - \Lambda)\phi} (e^{i\phi} - e^{-i\phi}) \right. \\ &+ \frac{i}{2\pi} \int_{-\infty}^{\infty} dz z \phi_{n_z}(z) \phi_{n'_z}(z) \int_0^{\infty} dr_\perp \phi_{n_\perp|\Lambda|}(r_\perp) \phi_{n'_\perp|\Lambda'|}(r_\perp) \int_0^{2\pi} d\phi (i\Lambda') e^{i(\Lambda' - \Lambda)\phi} (e^{i\phi} + e^{-i\phi}) \\ &\left. + \frac{1}{2\pi} \int_{-\infty}^{\infty} dz z \phi_{n_z}(z) \phi_{n'_z}(z) \int_0^{\infty} dr_\perp r_\perp \phi_{n_\perp|\Lambda|}(r_\perp) \partial_{r_\perp} \phi_{n'_\perp|\Lambda'|}(r_\perp) \int_0^{2\pi} d\phi e^{i(\Lambda' - \Lambda)\phi} (e^{i\phi} - e^{-i\phi}) \right\}, \end{aligned} \quad (\text{A.58})$$

where Kronecker $\delta_{m_s m'_s}$ stems from the fact that the spin space is invariant under action of the orbital angular momentum operator. Here, integrals in the ϕ -direction can be carried out analytically in a trivial manner. Furthermore, by using properties of Hermite polynomials from Eq. (A.18), integrals in the z -direction can also be carried out analytically. Therefore, the final expression for matrix elements of the orbital angular momentum in the harmonic oscillator basis reads:

$$\begin{aligned} \langle n_z n_\perp \Lambda m_s | \hat{L}_x | n'_z n'_\perp \Lambda' m'_s \rangle &= \delta_{m_s m'_s} \frac{\hbar}{2} \times \\ &\left\{ -(\delta_{\Lambda, \Lambda'+1} - \delta_{\Lambda, \Lambda'-1}) \left(-\sqrt{\frac{n'_z+1}{2}} \delta_{n_z, n'_z+1} + \sqrt{\frac{n'_z}{2}} \delta_{n_z, n'_z-1} \right) \frac{1}{b_z} \int_0^\infty dr_\perp r_\perp^2 \phi_{n_\perp|\Lambda|}(r_\perp) \phi_{n'_\perp|\Lambda'}(r_\perp) \right. \\ &- \Lambda' (\delta_{\Lambda, \Lambda'+1} + \delta_{\Lambda, \Lambda'-1}) \left(\sqrt{\frac{n'_z+1}{2}} \delta_{n_z, n'_z+1} + \sqrt{\frac{n'_z}{2}} \delta_{n_z, n'_z-1} \right) b_z \int_0^\infty dr_\perp \phi_{n_\perp|\Lambda|}(r_\perp) \phi_{n'_\perp|\Lambda'}(r_\perp) \\ &\left. + (\delta_{\Lambda, \Lambda'+1} - \delta_{\Lambda, \Lambda'-1}) \left(-\sqrt{\frac{n'_z+1}{2}} \delta_{n_z, n'_z+1} + \sqrt{\frac{n'_z}{2}} \delta_{n_z, n'_z-1} \right) \frac{1}{b_z} \int_0^\infty dr_\perp r_\perp \phi_{n_\perp|\Lambda|}(r_\perp) \partial_{r_\perp} \phi_{n'_\perp|\Lambda'}(r_\perp) \right\}. \end{aligned} \quad (\text{A.59})$$

The remaining integrals in r_\perp -direction are calculated numerically. For the spin part, using the fact that $\hat{\mathbf{S}} = \frac{\hbar}{2} \hat{\sigma}$ as well as properties of Pauli matrices from Eq. (1.30), it is straightforward to calculate the corresponding matrix elements in the harmonic oscillator basis:

$$\langle n_z n_\perp \Lambda m_s | \hat{S}_x | n'_z n'_\perp \Lambda' m'_s \rangle = \frac{\hbar}{2} \delta_{m_s, -m'_s} \times \delta_{n_z n'_z} \delta_{n_\perp n'_\perp} \delta_{\Lambda \Lambda'}. \quad (\text{A.60})$$

Finally, the expression for matrix elements of the total angular momentum operator in the harmonic oscillator basis reads:

$$\langle n_z n_\perp \Lambda m_s | \hat{J}_x | n'_z n'_\perp \Lambda' m'_s \rangle = \langle n_z n_\perp \Lambda m_s | \hat{L}_x | n'_z n'_\perp \Lambda' m'_s \rangle + \frac{\hbar}{2} \delta_{m_s, -m'_s} \times \delta_{n_z n'_z} \delta_{n_\perp n'_\perp} \delta_{\Lambda \Lambda'}. \quad (\text{A.61})$$

Matrix elements of \hat{J}_x in the simplex-x basis

Matrix elements of the \hat{J}_x operator between the $|s = +i\rangle$ eigenstates are straightforwardly written down as:

$$\begin{aligned}
\langle n_z n_\perp \Lambda; +i | \hat{J}_x | n'_z n'_\perp \Lambda'; +i \rangle &= \frac{1}{2} \langle n_z n_\perp \Lambda \uparrow | \hat{L}_x | n'_z n'_\perp \Lambda' \uparrow \rangle \\
&+ \frac{1}{2} (-1)^{\Lambda+\Lambda'} \langle n_z n_\perp - \Lambda \downarrow | \hat{L}_x | n'_z n'_\perp - \Lambda' \downarrow \rangle \\
&- \frac{1}{2} (-1)^{\Lambda'} \langle n_z n_\perp \Lambda \uparrow | \hat{S}_x | n'_z n'_\perp - \Lambda' \downarrow \rangle \\
&- \frac{1}{2} (-1)^\Lambda \langle n_z n_\perp - \Lambda \downarrow | \hat{S}_x | n'_z n'_\perp \Lambda' \uparrow \rangle,
\end{aligned}$$

where we have made use of the fact that the \hat{L}_x operator couples only states with the equal spins, while the \hat{S}_x operator couples only states with the opposite spins. Using properties of Eq. (A.59), it is possible to demonstrate that the first two terms on the right hand side of the upper expression are actually equal. Furthermore, using properties of the spin operator from the Eq. (A.60), we can derive the final expression for the matrix element of \hat{J}_x operator between two $|s = +i\rangle$ eigenstates:

$$\langle n_z n_\perp \Lambda; +i | \hat{J}_x | n'_z n'_\perp \Lambda'; +i \rangle = \langle n_z n_\perp \Lambda | \hat{L}_x | n'_z n'_\perp \Lambda' \rangle - \frac{\hbar}{2} (-1)^\Lambda \delta_{n_z n'_z} \delta_{n_\perp n'_\perp} \delta_{\Lambda - \Lambda'}. \quad (\text{A.62})$$

Carrying out the equivalent calculation with the $|s = -i\rangle$ eigenstate yields:

$$\langle n_z n_\perp \Lambda; -i | \hat{J}_x | n'_z n'_\perp \Lambda'; -i \rangle = -\langle n_z n_\perp \Lambda | \hat{L}_x | n'_z n'_\perp \Lambda' \rangle + \frac{\hbar}{2} (-1)^\Lambda \delta_{n_z n'_z} \delta_{n_\perp n'_\perp} \delta_{\Lambda - \Lambda'}. \quad (\text{A.63})$$

Finally, off-diagonal matrix elements vanish identically:

$$\langle n_z n_\perp \Lambda; +i | \hat{J}_x | n'_z n'_\perp \Lambda'; -i \rangle = \langle n_z n_\perp \Lambda; -i | \hat{J}_x | n'_z n'_\perp \Lambda'; +i \rangle = 0. \quad (\text{A.64})$$

Matrix elements of rotation operator in the simplex-x basis

In order to calculate matrix elements of rotation operator in the simplex-x basis, we invoke the spectral theorem [RS72]. This theorem grants that, given any $n \times n$ symmetric and Hermitian matrix A , there exists an $n \times n$ unitary matrix P , and a diagonal matrix D such that:

$$A = P D P^{-1}, \quad (\text{A.65})$$

where columns of the matrix $P = (\vec{p}_1, \vec{p}_2, \dots, \vec{p}_n)$ correspond to eigenvectors of the matrix A , while the diagonal entries of the matrix D equal to the corresponding eigenvalues.

Furthemore, matrix e^A can be expressed as:

$$e^A = \sum_{m=0}^{\infty} \frac{A^m}{m!} = \sum_{m=0}^{\infty} \frac{PD^mP^{-1}}{m!} = P \sum_{m=0}^{\infty} \frac{D^m}{m!} P^{-1} = Pe^D P^{-1}, \quad (\text{A.66})$$

where the last equality holds because D is diagonal matrix. Finally, if A is a symmetric matrix, it can be shown that from Eq. (A.66) follows $P^{-1} = P^T$. Consequently, the spectral theorem yields an expression:

$$e^A = Pe^D P^T. \quad (\text{A.67})$$

This expression can be used to calculate matrix elements of the rotation operator $e^{-i\beta\hat{J}_x}$ in the simplex-x basis. We proceed as follows:

1. We calculate matrix elements of the $-i\beta\hat{J}_x$ operator in the simplex-x basis, following the Eqs. (A.62) - (A.64). The obtained matrix corresponds to the matrix A from spectral theorem.
2. We diagonalize the $-i\beta\hat{J}_x$ matrix in order to determine the corresponding eigenvector matrix P and the eigenvalue matrix D .
3. We use the fact that the matrix D is diagonal in order to calculate the matrix e^D .
4. We use the relation (A.67) to determine the matrix elements of the $e^{-i\beta\hat{J}_x}$ operator in the simplex-x basis.

Calculation of Electric Observables

Solution to the HWG equation provides us with the collective energy spectra and collective wave functions, as previously discussed in Chapter 2. These wave functions are further used to determine various observables in nuclear collective states that can be compared to experimental data. In this Appendix, we will overview some of the expressions that are relevant for computation of different electric observables. The appendix is divided in two parts. In the first part, we will discuss calculation of electric spectroscopic quadrupole moments and electric multipole transition strengths, quantities that have been routinely computed in MR-EDF calculations for decades. The second part contains an overview of the recently-developed framework for calculation of transition densities between low-lying collective states. This framework enables us to calculate elastic and inelastic form factors for electron scattering off nuclei, as well as the nuclear laboratory-frame densities.

B.1. Spectroscopic Moments and Transition Strengths

The electric spectroscopic quadrupole moment of the collective state α with total spin-parity J^π can be computed as:

$$Q_2^{\text{spec}}(J_\alpha^\pi) = e\sqrt{\frac{16\pi}{5}} \begin{pmatrix} J & 2 & J \\ J & 0 & -J \end{pmatrix} \sum_{q_i q_f} f_\alpha^{J;NZ;\pi^*}(q_f) \langle Jq_f || \hat{Q}_2 || Jq_i \rangle f_\alpha^{J;NZ;\pi}(q_i). \quad (\text{B.1})$$

Equivalently, the reduced electric transition strength of multipolarity λ between an initial collective state α_i of total spin-parity $J_i^{\pi_i}$ and a final collective state α_f of total spin-parity $J_f^{\pi_f}$ can be computed as:

$$B(E\lambda; J_{\alpha_i}^{\pi_i} \rightarrow J_{\alpha_f}^{\pi_f}) = \frac{e^2}{2J_i + 1} \left| \sum_{q_i q_f} f_{\alpha_f}^{J_f; NZ; \pi_f^*}(q_f) \langle J_f q_f || \hat{Q}_\lambda || J_i q_i \rangle f_{\alpha_i}^{J_i; NZ; \pi_i}(q_i) \right|^2. \quad (\text{B.2})$$

In these expressions, $f_{\alpha}^{J; NZ; \pi^*}(q_j)$ correspond to weight functions [see Eq. (2.39)] obtained by solving the HWG equation, $\langle J_f q_f || \hat{Q}_\lambda || J_i q_i \rangle$ is the reduced matrix element of the electric multipole operator $\hat{Q}_{\lambda\mu}$, and sums run over a set of RHB states that have been taken into account in the configuration mixing scheme. The spherical coordinate space representation of the electric multipole operator $\hat{Q}_{\lambda\mu}$ reads:

$$Q_{\lambda\mu}(r, \theta, \phi) = r^\lambda (-1)^\mu \sqrt{\frac{2\lambda + 1}{4\pi} \frac{(\lambda - \mu)!}{(\lambda + \mu)!}} P_{\lambda\mu}(\cos \theta) e^{i\mu\phi}, \quad (\text{B.3})$$

where $P_{\lambda\mu}(\cos \theta)$ denotes associated Legendre polynomials [AS65]. If we assume the axial symmetry and the simplex-x symmetry of the intrinsic states [Fru07], and if we further take into account properties of the projection operators discussed in Chapter 2, the reduced matrix element of electric multipole operator can be written as:

$$\begin{aligned} \langle J_f q_f || \hat{Q}_\lambda || J_i q_i \rangle &= \frac{(2J_i + 1)(2J_f + 1)}{2} (-1)^{J_i - \lambda} \int_0^\pi d\beta \sin \beta \frac{1}{N_\varphi^2} \sum_{l_N=1}^{N_\varphi} \sum_{l_Z=1}^{N_\varphi} e^{-i\varphi_{l_N} N_0} e^{-i\varphi_{l_Z} Z_0} \\ &\times \sum_{\mu'=-\lambda}^{\lambda} i^{\mu'} \begin{pmatrix} J_i & \lambda & J_f \\ -\mu' & \mu' & 0 \end{pmatrix} d_{-\mu'0}^{J_i^*}(\beta) \mathcal{Q}_{\lambda\mu'}(q_i, q_f, \beta, \varphi_{n_N}, \varphi_{n_Z}), \end{aligned} \quad (\text{B.4})$$

where the quantity

$$\mathcal{Q}_{\lambda\mu'}(q_i, q_f, \beta, \varphi_{n_N}, \varphi_{n_Z}) = \langle \Phi(q_f) | \hat{Q}_{\lambda\mu'} e^{-i\beta \hat{J}_x} e^{i\varphi_{l_N} \hat{N}} e^{i\varphi_{l_Z} \hat{Z}} | \Phi(q_i) \rangle \quad (\text{B.5})$$

depends explicitly on the RHB states involved, q_i and q_f , as well as on the rotational and gauge angles β , φ_{n_N} , and φ_{n_Z} . Therefore, for the sake of notational compactness, it is useful to introduce a shorthand notation $\{x\} \equiv \{q_i, q_f, \beta, \varphi_{n_N}, \varphi_{n_Z}\}$. The upper equation can then be rewritten as:

$$\mathcal{Q}_{\lambda\mu'}(\{x\}) = \int d\mathbf{r} Q_{\lambda\mu'}(\mathbf{r}) \rho_p(\mathbf{r}, \{x\}), \quad (\text{B.6})$$

where $Q_{\lambda\mu'}(\mathbf{r})$ is defined in Eq. (B.3) and $\rho_p(\mathbf{r}, \{x\})$ denotes density of protons in the coordinate space:

$$\rho_p(\mathbf{r}, \{x\}) = \sum_m \rho_p^m(r_\perp, z, \{x\}) \begin{Bmatrix} \cos(m\phi) \\ \sin(m\phi) \end{Bmatrix}. \quad (\text{B.7})$$

Here, the upper row corresponds to even values of m , while the lower row corresponds to odd values of m . Explicitly, we have:

$$\begin{aligned} \mathcal{Q}_{\lambda\mu'}(\{x\}) &= (-1)^{\mu'} \sqrt{\frac{2\lambda+1}{4\pi} \frac{(\lambda-\mu')!}{(\lambda+\mu')!}} \int_{-\infty}^{\infty} dz \int_0^{\infty} dr_\perp r_\perp \int_0^{2\pi} d\phi \\ &\times (r_\perp^2 + z^2)^{\frac{\lambda}{2}} P_{\lambda\mu'}\left(\frac{z}{r_\perp}\right) e^{i\mu'\phi} \sum_m \rho_p^m(r_\perp, z, \{x\}) \begin{Bmatrix} \cos(m\phi) \\ \sin(m\phi) \end{Bmatrix}. \end{aligned} \quad (\text{B.8})$$

Integral in the ϕ -direction can be carried out analytically, and we finally obtain:

$$\begin{aligned} \mathcal{Q}_{\lambda\mu'}(\{x\}) &= (-1)^{\mu'} \sqrt{\frac{2\lambda+1}{4\pi} \frac{(\lambda-\mu')!}{(\lambda+\mu')!}} \sum_m \int_{-\infty}^{\infty} dz \int_0^{\infty} dr_\perp r_\perp \\ &\times (r_\perp^2 + z^2)^{\frac{\lambda}{2}} P_{\lambda\mu'}\left(\frac{z}{r_\perp}\right) \rho_p^m(r_\perp, z, \{x\}) \begin{Bmatrix} \pi(\delta_{\mu-m} + \delta_{\mu m}) \\ \frac{\pi}{i}(\delta_{\mu-m} - \delta_{\mu m}) \end{Bmatrix}. \end{aligned} \quad (\text{B.9})$$

The remaining spatial integrals in the z - and r_\perp - directions are carried out numerically, using the Gauss-Hermite and Gauss-Laguerre integration methods, respectively. Furthermore, by inspecting how the sum terms in Eq. (B.4) behave under the exchange $\mu' \rightarrow -\mu'$, it is possible to demonstrate that terms with the same $|\mu'|$ contribute equally to the total sum. Therefore, the final expression for the reduced matrix elements can be written in a compact form:

$$\begin{aligned} \langle J_f q_f || \hat{Q}_\lambda || J_i q_i \rangle &= \\ \mathcal{M}_{J_i, J_f, \lambda} \begin{pmatrix} J_i & \lambda & J_f \\ 0 & 0 & 0 \end{pmatrix} \int_0^\pi d\beta \sin \beta d_{00}^{J_i*} \frac{1}{N_\varphi^2} \sum_{l_N=1}^{N_\varphi} \sum_{l_Z=1}^{N_\varphi} e^{-i\varphi_{l_N} N_0} e^{-i\varphi_{l_Z} Z_0} \mathcal{Q}_{\lambda 0}(\{x\}) \\ + \mathcal{M}_{J_i, J_f, \lambda} \sum_{\mu' > 0} 2i^{\mu'} \begin{pmatrix} J_i & \lambda & J_f \\ -\mu' & \mu' & 0 \end{pmatrix} \int_0^\pi d\beta \sin \beta d_{-\mu' 0}^{J_i*} \frac{1}{N_\varphi^2} \sum_{l_N=1}^{N_\varphi} \sum_{l_Z=1}^{N_\varphi} e^{-i\varphi_{l_N} N_0} e^{-i\varphi_{l_Z} Z_0} \mathcal{Q}_{\lambda\mu'}(\{x\}), \end{aligned} \quad (\text{B.10})$$

where $\mathcal{Q}_{\lambda\mu'}(\{x\})$ is defined in Eq. (B.9) and the angular-momentum-dependent prefactor $\mathcal{M}_{J_i, J_f, \lambda}$ reads:

$$\mathcal{M}_{J_i, J_f, \lambda} = \frac{(2J_i + 1)(2J_f + 1)}{2} (-1)^{J_i + \lambda}. \quad (\text{B.11})$$

It is worth noting that the reduced matrix element will always be a real quantity, since the imaginary unit i in odd- μ' terms of Eq (B.10) and the imaginary unit for odd- μ' terms of Eq. (B.9) will systematically cancel out. Finally, we note that discussed quantities are calculated in full configurational space. Consequently, there is no need to introduce effective charges and e always denotes the bare value of the proton charge.

B.2. Electron-Nucleus Scattering Form Factors

Electron scattering off nuclei represents a very convenient tool to study density distributions in atomic nuclei [Wal04, Won98, YBH15]. Some of the major advantages of using electrons as nuclear structure probes include their point-like nature, the fact that they are easily accelerated in experiments, and an extenuating property that they interact almost exclusively through the well-known electromagnetic interaction. The evergrowing experimental capabilities will soon make this kind of analysis accessible even for the short-lived neutron-rich nuclei. Relatively recently, the MR-EDF framework was extended by J. M. Yao and collaborators by including the calculation of transition densities between the low-lying collective states and the corresponding form factors [YBH15]. In this section, we will discuss details of implementing this formalism to our model. Even though the general framework allows for the additional breaking of axial symmetry, the present study is restricted to axially-symmetric shapes and we will therefore discuss only the specific case when axial symmetry of intrinsic states is preserved. We will start by presenting the formalism for calculation of transition densities and electron scattering form factors. Then, we will lay out the most important relations for determination of nuclear densities in the laboratory frame.

Transition Densities and Form Factors

Starting point of the analysis, which is carried out within the plane-wave Born approximation, is the determination of differential cross section for electron scattering from a spinless nucleus:

$$\frac{d\sigma}{d\Omega} = \frac{d\sigma_M}{d\Omega} \sum_{L \geq 0} |F_L(q)|^2, \quad (\text{B.12})$$

where the Mott cross section $\frac{d\sigma_M}{d\Omega}$ describes scattering from a point-like nucleus of charge Z , while the sum of form factors $F_L(q)$ accounts for the actual finite size and internal structure of a nucleus. The longitudinal Coulomb form factor for angular momentum transfer L can be calculated as the Fourier-Bessel transform of the reduced transition density $\rho_{J_i \alpha_i, L}^{J_f \alpha_f}(r)$ from an initial state α_i of total spin-parity $J_i^{\pi_i}$ to a final state α_f of total spin-parity $J_f^{\pi_f}$ [YBH15]:

$$F_L(q) = \frac{\sqrt{4\pi}}{Z} \int_0^\infty dr r^2 \rho_{J_i \alpha_i, L}^{J_f \alpha_f}(r) j_L(qr). \quad (\text{B.13})$$

where $j_L(qr)$ denotes the spherical Bessel function of the first kind and the normalization coefficient $\frac{\sqrt{4\pi}}{Z}$ has been introduced so that the elastic form factor equals to unity at momentum transfer $q = 0$. The reduced transition density corresponds to the radial part of the 3D transition density and it can be calculated as [YBH15]:

$$\begin{aligned} \rho_{J_i \alpha_i, L}^{J_f \alpha_f}(r) &= (-1)^{J_i - J_f} \frac{2J_f + 1}{2J_i + 1} \sum_{K=-L}^L \langle J_f 0 L K | J_i K \rangle \\ &\times \int_0^{2\pi} d\phi \int_0^\pi d\theta \sin \theta \rho_{\alpha_f \alpha_i}^{J_f J_i K 0}(r, \theta, \phi) Y_{LK}^*(\theta, \phi). \end{aligned} \quad (\text{B.14})$$

Here, $Y_{LK}^*(\theta, \phi)$ denotes spherical harmonics:

$$Y_{LK}^*(\theta, \phi) = (-1)^K \sqrt{\frac{(2L+1)(L-K)!}{4\pi(L+K)!}} P_{LK}(\cos \theta) e^{-iK\phi}, \quad (\text{B.15})$$

where $P_{LK}(\cos \theta)$ corresponds to associated Legendre polynomials [AS65]. Furthermore, Clebsch-Gordan coefficients can generally be expressed in terms of $3j$ -symbols:

$$\langle j_1 m_1 j_2 m_2 | J M \rangle = (-1)^{j_1 - j_2 + M} \sqrt{2J+1} \begin{pmatrix} j_1 & j_2 & J \\ m_1 & m_2 & -M \end{pmatrix}. \quad (\text{B.16})$$

Finally, $\rho_{\alpha_f \alpha_i}^{J_f J_i K 0}(r, \theta, \phi)$ denotes the pseudo GCM density, a quantity which is not an observable but it encapsulates all the information related to the solution of HWG equation. It can be computed using the weight functions of collective states [see Eq. (2.39)]:

$$\rho_{\alpha_f \alpha_i}^{J_f J_i K 0}(r, \theta, \phi) = \sum_{q_f q_i} f_{\alpha_f}^{J_f; N Z; \pi_f^*}(q_f) f_{\alpha_i}^{J_i; N Z; \pi_i^*}(q_i) \rho_{q_f q_i}^{J_i K 0}(r, \theta, \phi), \quad (\text{B.17})$$

where the transition density kernel reads [YBH15]:

$$\rho_{q_f q_i}^{J_i K 0}(r, \theta, \phi) = \frac{2J_i + 1}{2} \int_0^\pi d\beta \sin \beta d_{K0}^{J_i}(\beta) \langle \Phi(q_f) | \hat{\rho}(r, \theta, \phi) e^{-i\beta \hat{J}_y} \hat{P}^N \hat{P}^Z | \Phi(q_i) \rangle. \quad (\text{B.18})$$

The transition density kernel in our case can be reexpressed as:

$$\begin{aligned} \rho_{q_f q_i}^{J_i K 0}(r, \theta, \phi) &= \frac{2J_i + 1}{2} \int_0^\pi d\beta \sin \beta d_{K 0}^{J_i}(\beta) \frac{1}{N_\varphi^2} \sum_{l_N=1}^{N_\varphi} \sum_{l_Z=1}^{N_\varphi} e^{-i\varphi_{l_N} N_0} e^{-i\varphi_{l_Z} Z_0} \\ &\times \sum_m \rho_p^m(r, \theta, \{x\}) i^{\tilde{m}} \cos(m\phi), \end{aligned} \quad (\text{B.19})$$

where tilde on index m denotes:

$$\tilde{m} = m - \frac{1 - (-1)^m}{2}, \quad (\text{B.20})$$

and it yields coefficient i^m for even values of m and coefficient i^{m-1} for odd values of m . Furthermore, $\rho_p^m(r, \theta, \{x\})$ is the standard mixed density of protons as calculated in Chapter 2 and Appendix B.1, with the introduced shorthand notation $\{x\} \equiv \{q_i, q_f, \beta, \varphi_{n_N}, \varphi_{n_Z}\}$. The only notable difference is that, rather than being a function of cylindrical coordinates (r_\perp, z) like before [see Eq. (B.7)], proton density is now a function of spherical coordinates (r, θ) . In order to carry out transformation between the two coordinate systems, the original implementation of the framework first calculates the transition density kernel on an equidistant Cartesian mesh and then interpolates it to the mesh points in spherical coordinates by using the Lagrange-mesh interpolation [YBH15]. However, since densities within our model are first obtained in the configurational space of harmonic oscillator, calculation of the corresponding density in spherical coordinates is straightforward and there is no need to employ any interpolation procedures. The pseudo GCM density can then compactly be written down as:

$$\rho_{\alpha_f \alpha_i}^{J_f J_i K 0}(r, \theta, \phi) = \sum_m \left[\rho_{\alpha_f \alpha_i}^{J_f J_i K 0}(r, \theta) \right]^m i^{\tilde{m}} \cos(m\phi), \quad (\text{B.21})$$

with:

$$\begin{aligned} \left[\rho_{\alpha_f \alpha_i}^{J_f J_i K 0}(r, \theta) \right]^m &= \sum_{q_f q_i} f_{\alpha_f}^{J_f; N Z; \pi_f^*}(q_f) f_{\alpha_i}^{J_i; N Z; \pi_i^*}(q_i) \\ &\times \frac{2J_i + 1}{2} \int_0^\pi d\beta \sin \beta d_{K 0}^{J_i}(\beta) \frac{1}{N_\varphi^2} \sum_{l_N=1}^{N_\varphi} \sum_{l_Z=1}^{N_\varphi} e^{-i\varphi_{l_N} N_0} e^{-i\varphi_{l_Z} Z_0} \rho_p^m(r, \theta, \{x\}). \end{aligned} \quad (\text{B.22})$$

Now, combining Eqs. (B.14) - (B.16) with the Eq. (B.21), the reduced transition density becomes:

$$\begin{aligned} \rho_{J_i\alpha_i,L}^{J_f\alpha_f}(r) &= (-1)^{J_i-L} \frac{2J_f+1}{\sqrt{2J_i+1}} \sum_{K=-L}^L \begin{pmatrix} J_f & L & J_i \\ 0 & K & -K \end{pmatrix} \sqrt{\frac{(2L+1)(L-K)!}{4\pi(L+K)!}} \\ &\times \int_0^{2\pi} d\phi \int_0^\pi d\theta \sin\theta \sum_m \left[\rho_{\alpha_f\alpha_i}^{J_fJ_iK0}(r,\theta) \right]^m i^{\tilde{m}} \cos(m\phi) P_{LK}(\cos\theta) e^{-iK\phi}. \end{aligned} \quad (\text{B.23})$$

In the upper equation, integral in the ϕ -direction can be carried out analytically. This will limit the sum over index m to $m = \pm K$ values only. Additionally, by inspecting how each factor in the sum over K behaves under the exchange $K \rightarrow -K$, one can verify that terms with the same $|K|$ contribute equally to the total sum. Therefore, the final expression for the reduced transition density reads:

$$\begin{aligned} \rho_{J_i\alpha_i,L}^{J_f\alpha_f}(r) &= (-1)^{J_i-L} \frac{2J_f+1}{\sqrt{2J_i+1}} \sum_{K=0}^L \frac{4\pi}{1+\delta_{K0}} \begin{pmatrix} J_f & L & J_i \\ 0 & K & -K \end{pmatrix} \sqrt{\frac{(2L+1)(L-K)!}{4\pi(L+K)!}} \\ &\times i^{\tilde{K}} \int_0^\pi d\theta \sin\theta P_{LK}(\cos\theta) \left[\rho_{\alpha_f\alpha_i}^{J_fJ_iK0}(r,\theta) \right]^K, \end{aligned} \quad (\text{B.24})$$

with tilde transformation of summation index defined in Eq. (B.20). Plugging this expression back to the relation for form factors (B.13) enables us to calculate both elastic and inelastic form factors for electron scattering off nuclei. Nevertheless, a correction for the spurious center-of-mass motion related to the breaking of translational invariance should additionally be introduced. In the present work, this is achieved by folding the calculated form factor with the simple correction obtained in the harmonic oscillator approximation [YBH15]:

$$F_{\text{c.m.}}(q) = e^{q^2 b^2 / (4A)}, \quad (\text{B.25})$$

where $b = \sqrt{\hbar/m\omega_0}$ is the oscillator length parameter, m is the nucleon bare mass and frequency ω_0 is determined from $\hbar\omega_0 = 41A^{-1/3}$ MeV. Finally, let us mention that the multipole transition matrix elements can be calculated directly from the reduced transition density:

$$M_{J_i\alpha_i,L}^{J_f\alpha_f} = \int_0^\infty dr r^{L+2} \rho_{J_i\alpha_i,L}^{J_f\alpha_f}(r). \quad (\text{B.26})$$

The reduced electric transition strength then simply reads:

$$B(EL; J_{\alpha_i}^{\pi_i} \rightarrow J_{\alpha_f}^{\pi_f}) = |M_{J_i\alpha_i,L}^{J_f\alpha_f}|^2. \quad (\text{B.27})$$

Comparing electric transition strengths obtained in two different manners, that is with Eq. (B.2) and Eq. (B.27), provides a useful cross-check for the consistency of our calculation.

Laboratory Frame Densities

The laboratory frame density of the collective state α with spin-parity J^π reads [YBH15]:

$$\begin{aligned} \rho_\alpha^{J^\pi}(r, \theta, \phi) &= \sum_\lambda Y_{\lambda 0}(\theta, \phi) \langle J 0 \lambda 0 | J 0 \rangle \sum_{K=-\lambda}^\lambda \langle J 0 \lambda K | J K \rangle \\ &\times \int_0^{2\pi} d\phi' \int_0^\pi d\theta' \sin \theta' \rho_{\alpha\alpha}^{JJK^0}(r, \theta', \phi') Y_{\lambda K}^*(\theta', \phi'). \end{aligned} \quad (\text{B.28})$$

Using relations (B.15), (B.16), and (B.21), the laboratory density can be rewritten as:

$$\begin{aligned} \rho_\alpha^{J^\pi}(r, \theta, \phi) &= (2J+1) \sum_\lambda \frac{(2\lambda+1)}{4\pi} P_{\lambda 0}(\cos \theta) \begin{pmatrix} J & \lambda & J \\ 0 & 0 & 0 \end{pmatrix} \\ &\times \sum_m i^{\tilde{m}} \sum_{K=-\lambda}^\lambda \begin{pmatrix} J & \lambda & J \\ 0 & K & -K \end{pmatrix} \sqrt{\frac{(\lambda-K)!}{(\lambda+K)!}} \\ &\times \int_0^{2\pi} d\phi' \int_0^\pi d\theta' \sin \theta' \left[\rho_{\alpha\alpha}^{JJK^0}(r, \theta') \right]^m P_{\lambda K}(\cos \theta') \cos(m\phi') e^{-iK\phi'}. \end{aligned} \quad (\text{B.29})$$

Playing the same game as before, that is, carrying out analytically integral in the ϕ' -direction and making use of the symmetry property of the sum over index K , the final expression for the laboratory density reads:

$$\begin{aligned} \rho_\alpha^{J^\pi}(r, \theta, \phi) &= (2J+1) \sum_\lambda \frac{(2\lambda+1)}{4\pi} P_{\lambda 0}(\cos \theta) \begin{pmatrix} J & \lambda & J \\ 0 & 0 & 0 \end{pmatrix} \\ &\times \sum_{K=0}^\lambda i^{\tilde{K}} \frac{4\pi}{1+\delta_{K0}} \begin{pmatrix} J & \lambda & J \\ 0 & K & -K \end{pmatrix} \sqrt{\frac{(\lambda-K)!}{(\lambda+K)!}} \\ &\times \int_0^\pi d\theta' \sin \theta' P_{\lambda K}(\cos \theta') \left[\rho_{\alpha\alpha}^{JJK^0}(r, \theta') \right]^K. \end{aligned} \quad (\text{B.30})$$

with tilde transformation of summation index defined in Eq. (B.20).

Résumé en Français

C.1. Introduction

L'agrégation est un phénomène courant se manifestant à différentes échelles, du monde quantique (molécules, atomes, noyaux) jusqu'aux objets astrophysiques (étoiles, galaxies). En particulier, l'agrégation dans les noyaux atomiques peut être considérée comme un phénomène de transition entre les états dits de liquide quantique (phase de nucléons délocalisés) et de cristal nucléaire. Les signatures de ce phénomène incluent l'émergence de déformations exotiques (formes triangulaires et tétraédriques, chaînes linéaires,...) dans les noyaux $N = Z$ [FHKE⁺18], la formation de structures moléculaires dans les isotopes riches en neutrons (la distribution de nucléons selon plusieurs agrégats s'en retrouve stabilisée par des liaisons covalentes assurées par les neutrons de valence), de même que la radioactivité *cluster* [RJ84, WR11]. Parmi les différentes théories microscopiques permettant d'étudier l'agrégation nucléaire [KEKO12, NF04, THSR01, FHKE⁺18], les approches de type fonctionnelle de la densité pour l'énergie (EDF) en fournissent la description la plus satisfaisante. En effet, les approches EDF ne présupposent aucune structure localisée. De même, leur ingrédient fondamental - l'interaction inter-nucléonique effective - est fixée une fois pour toute au moment de l'ajustement des paramètres du modèle (sur des noyaux lourds en général): aucun réajustement ad hoc n'est réalisé lors de l'application de la méthode EDF aux noyaux légers sujets au phénomène d'agrégation. D'autre part, de récentes études ont souligné l'émergence naturelle de structures localisées lorsque les noyaux sont traités comme des systèmes relativistes dans le cadre des approches relativistes, favorisant ainsi la formation d'agrégats [EKNV12].

Dans cette thèse, nous avons déployé l'approche EDF à son état de l'art pour l'étude de la structure nucléaire. Des calculs Hartree-Bogoliubov relativistes (RHB) contraints à des déformations axiales de modes quadripolaire (Q_{20}) et octupolaire (Q_{30}) fournissent dans un premier temps les ingrédients fondamentaux de l'approche, c'est-à-dire les états RHB minimisant l'énergie du système contraint aux coordonnées collectives (Q_{20}, Q_{30}).

Dans une deuxième étape, ces derniers sont projetés sur de bonnes valeurs de moment angulaire, de parité et de nombre de particules afin de collecter des corrélations nucléoniques supplémentaires provenant des fluctuations quantiques importante de la phase des paramètres d'ordre associés à la brisure de la symétrie sphérique et de la conservation du nombre de nucléons. Enfin ces états projetés sont mélangés à l'aide de la méthode de la coordonnée génératrice (GCM) afin de tenir compte des corrélations nucléoniques associées aux oscillations du champ moyen. Cette dernière approche permet de calculer, de manière cohérente et indépendante de tout paramètre libre, des spectres d'excitations collectives ainsi que les taux de transitions électromagnétiques correspondants sur l'ensemble de la carte des nucléides. La section C.2 introduit ces outils théoriques de façon plus détaillée. Ceux-ci ont ensuite été utilisés dans le but d'étudier l'agrégation nucléaire dans les noyaux légers. Plus précisément, dans la section C.3, nous présentons les résultats principaux de l'étude de la collectivité quadrupolaire-octupolaire et des structures des agrégats dans les isotopes du néon. Dans la section C.4, les résultats principaux de l'étude des structures des agrégats dans l'isotope ^{12}C sont présentés. Enfin, un court résumé de ce travail de thèse et des perspectives associées sont donnés dans la section C.5.

C.2. La Fonctionnelle de la Densité pour l'Énergie

L'approche EDF [BHR03, NVR11, RRR18] fournit actuellement la description la plus complète et la plus précise des états fondamentaux et excités des noyaux atomiques sur l'ensemble de la carte des nucléides. Parmi les approches microscopiques traitant le problème à N corps nucléaire, elle offre un compromis optimal entre la précision globale et la faisabilité du calcul numérique. L'approche EDF peut être scindée en deux niveaux d'implémentation. La réalisation *single-reference* EDF (SR-EDF), parfois appelée champ moyen auto-cohérent (SCMF), représente le noyau à l'aide d'un état produit de (quasi-) nucléons. Les fonctionnelles modernes sont typiquement caractérisées par environ dix à douze paramètres libres, ajustés à l'équation d'état de la matière nucléaire et aux propriétés des noyaux finis. Les corrélations d'appariement, qui jouent un rôle important dans les noyaux à couches ouvertes, peuvent également être prises en compte soit à travers l'approximation Bardeen-Cooper-Schrieffer (BCS), soit dans le cadre de la théorie Hartree-Fock-Bogoliubov (HFB). L'approche SR-EDF peut ensuite être appliquée à l'étude des propriétés de l'état fondamental des noyaux atomiques, telles les énergies de liaison, les rayons de charge et les formes à l'équilibre. Toutefois, dans l'optique d'obtenir les propriétés spectroscopiques des systèmes nucléaires, il est nécessaire d'étendre l'approche de champ moyen en tenant compte des corrélations collectives qui sont induites par des restaurations de symétries et des oscillations du champ moyen. C'est ce que réalise le second niveau d'implémentation des approches EDF, appelé *multi-reference* EDF (MR-EDF) ou encore méthode au-delà du champ moyen (BMF).

Dans ce travail, les calculs RHB sont réalisés en utilisant la fonctionnelle covariante DD-PC1 [NVR11] dans le canal particule-trou et une force d'appariement séparable [Dug04, TMR09a] dans le canal particule-particule. Les équations correspondantes sont

résolues numériquement en développant les spineurs nucléaires dans une base d'oscillateur harmonique à symétrie axiale. Les noyaux considérés peuvent donc adopter une forme prolata (forme d'un cigare) et oblate (forme d'une soucoupe volante), de même que la forme octupolaire (forme d'une poire) qui n'est pas invariante sous la transformation de parité. Ce type d'analyse donne accès à toutes les configurations possibles repérées par les coordonnées collectives (Q_{20}, Q_{30}). Dans l'étape suivante, nous restaurons les symétries les plus pertinentes qui sont brisées au niveau du champ moyen. En particulier, la symétrie rotationnelle, la symétrie du nombre de particule et la symétrie de parité sont toutes simultanément restaurées. De plus, une simple correction du centre de masse qui prend en compte les violations de la symétrie de translation est incluse dans le modèle [BHR03]. Les états de symétries restaurées sont ensuite utilisés comme une base pour l'étape de mélange de configurations, introduite dans le formalisme de la GCM par Hill, Wheeler et Griffin [HW53, GW57, RS80]. Résoudre l'équation de Hill-Wheeler-Griffin correspondante aboutit aux spectres d'excitation et aux fonctions d'onde collectives qui peuvent être utilisées pour calculer différentes observables, telles que les moments quadripolaires spectroscopiques et les taux de transition électromagnétiques multipolaires. Ces quantités peuvent ensuite servir à tester la performance de notre modèle par comparaison avec l'expérience, de même qu'avec les prédictions d'autres modèles théoriques. De plus, nous avons implémenté dans notre modèle les ingrédients nécessaires aux études de diffusions élastique et inélastique d'électrons par des noyaux [YBH15]. A partir des fonctions d'onde collectives des états nucléaires étiquetés par de bons nombres quantiques, nous sommes donc capables de calculer des densités dans le référentiel du laboratoire et des densités de transition entre les états de basse énergie, de même que les facteurs de forme de diffusions élastique et inélastique. Pour première application, ce modèle à l'état de l'art a été employé dans une étude microscopique du phénomène d'agrégation dans les noyaux atomiques légers. En particulier, les structures des agrégats dans les isotopes du néon et dans l'isotope ^{12}C ont été étudiées.

C.3. Structures en Agrégats dans les Isotopes de Néon

La chaîne isotopique du néon, avec la formation et la dissolution des structures en agrégats de basse énergie, l'émergence de coexistences de formes, l'érosion et l'ouverture de nombres magiques, constituent un champ d'application particulièrement riche d'un point de vue théorique [RGER03, Kim04, ZRX⁺12, ZYL⁺16]. Dans cette thèse, nous avons étudié la collectivité quadripolaire-octupolaire et les structures en agrégats dans huit isotopes pair-pair du néon [MEK⁺18a]. Entre 111 et 118 états RHB présentant une symétrie axiale et une asymétrie miroir ont été tout d'abord projetés sur de bonnes valeurs de moments angulaires, de nombre de particules et de parité, puis mélangés dans le cadre de la réalisation MR-EDF. Cette implémentation permet un calcul cohérent et indépendant de tout paramètre libre des spectres d'excitation et des taux de transitions électriques, à la fois pour la bande associée à l'état fondamental et celle associée aux états excités $K^\pi = 0^\pm$. Les résultats obtenus ont été comparés aux données expérimentales existantes ainsi qu'aux prédictions d'autres modèles théoriques.

Les observables dans l'état fondamental de ces isotopes (typiquement l'énergie de liaison et le rayon de charge) sont déjà reproduites de manière satisfaisante à l'étape SR-EDF. En incluant des corrélations collectives liées aux restaurations de symétries brisées et aux oscillations du champ moyen, nous avons démontré la stabilité des isotopes considérés par rapport aux émissions de neutrons et abouti sur une structure complexe pour les divers états de ces isotopes. En particulier, il a été montré que le degré de liberté octupolaire joue un rôle pertinent : tous les isotopes étudiés adoptent une configuration octupolaire dans leur état corrélé de plus basse énergie. Par ailleurs, un mélange conséquent de configurations oblates ($> 20\%$ pour les fonctions d'onde collectives correspondantes) a été trouvé dans l'ensemble de la chaîne isotopique. De manière plus notable, il s'avère que le champ moyen et les surfaces d'énergie de l'état fondamental de l'isotope ^{24}Ne résultants de projections au niveau MR-EDF possèdent des minima coexistants associés à des déformations prolates et oblates, alors que, d'après l'étude réalisée, 40% de la fonction d'onde correspondante est répartie du côté oblate du plan $\beta_2 - \beta_3$.

Les valeurs calculées des énergies des états 2_1^+ et 4_1^+ , de même que les taux de transition $B(E2; 2_1^+ \rightarrow 0_1^+)$, sont raisonnablement en accord avec les données associées à l'ensemble de la chaîne isotopique. Cet accord est particulièrement bon pour les isotopes les plus légers, $^{20,22,24}\text{Ne}$, alors que la sphéricité obtenue pour l'isotope ^{30}Ne ne concorde pas avec les récentes données expérimentales. Cela provient du fait que les interactions effectives globales ne peuvent pas toujours tenir compte des propriétés particulières déterminées par l'évolution de couches dans chaque région de masse. Dans ce cas, la disparition de la fermeture de couches à $N = 20$ dans les noyaux très riches en neutrons n'est simplement pas reproduite par la fonctionnelle DD-PC1. Toutefois, il a été montré qu'un ajout supplémentaire de neutrons mène à un développement d'une forte déformation prolates dans l'isotope du néon le plus riche en neutrons, le ^{34}Ne . Ce noyau manifeste une bande associée à l'état fondamental particulièrement compressée comparé à d'autres isotopes, avec les énergies d'excitation des états 2_1^+ et 4_1^+ les plus basses sur l'ensemble de la chaîne isotopique. De plus, nous avons montré que les signatures de la coexistence de formes de l'état fondamental survit dans les états excités de l'isotope ^{24}Ne . En particulier, ses états 6_1^+ contiennent toujours une contribution de presque 40% de la configuration prolates, alors que les états 0_2^+ et 2_2^+ dans cet isotope ont été obtenus à des énergies bien plus basses que les états correspondants dans l'isotope ^{22}Ne .

Finalement, nous avons prêté spécialement attention au cas de l'isotope auto-conjugué ^{20}Ne . Les propriétés spectroscopiques obtenues ont été minutieusement comparées aux données expérimentales, de même que les prédictions de deux autres modèles. En particulier, il a été montré que notre calcul possède un niveau de précision comparable à ceux réalisés avec d'autres modèles plus spécifiques, tels que la dynamique moléculaire antisymétrisée. Nous avons prouvé que l'état fondamental de l'isotope ^{20}Ne manifeste une structure $^{16}\text{O} + \alpha$ de façon prédominante, alors qu'environ 25% de sa fonction d'onde collective correspond à une structure $2\alpha + ^{12}\text{C}$ de déformation oblate. L'augmentation du moment angulaire mène à la prédominance de forme prolates et une dissolution progressive de la structure $^{16}\text{O} + \alpha$. Dans la bande de parité négative, cette dissolution se produit à un taux bien plus lent que celui trouvé dans les études précédentes, alors que cela mène dans la bande de parité positive à un développement de la structure $\alpha - ^{12}\text{C} - \alpha$ dans l'état $J^\pi = 6^+$.

C.4. Structures en Agrégats dans le ^{12}C

L'isotope ^{12}C fait sans doute partie des noyaux les plus étudiés, avec une structure 3α linéaire, triangulaire, axiale, oblate et une configuration en bras pliés, chacune de ses dernières propriétés ayant été prédites comme étant des structures de basses énergies [KE07, NF04, CFN+07, THSR01, Fun15, FSF+13]. En plus des riches variétés de structure en agrégats qu'il manifeste, cet isotope est particulièrement pertinent pour son rôle crucial dans l'apparition et la conservation de la vie organique sur Terre. Dans cette thèse, nous avons réalisé l'étude théorique de la spectroscopie de basse énergie et des structures en agrégats dans l'isotope ^{12}C [MEK+18b]. Des états RHB possédant une symétrie axiale et une asymétrie miroir ont été tout d'abord projetés sur de bonnes valeurs de moments angulaires, de nombre de particules et de parité, puis mélangés dans le cadre du processus MR-EDF. En débutant par une interaction effective qui a été ajustée à des données provenant de noyaux lourds et un formalisme qui ne présuppose pas de structure en agrégats, la méthode utilisée a permis de calculer, de façon cohérente et indépendante de tout paramètre libre, des spectres d'excitation collectives et de taux de transitions électriques dans les isotopes ^{12}C très légers.

En particulier, nous nous sommes concentrés sur la structure des trois bandes $K^\pi = 0^+$ les plus basses en énergie. Globalement, les propriétés empiriques de la bande associée à l'état fondamental ont été reproduites de façon précise. Les états collectifs 2_1^+ et 4_1^+ ont été obtenus à des énergies qui sont, seulement de manière anecdotique, plus basses que les valeurs expérimentales, et les rapports $E(4_1^+)/E(2_1^+)$ correspondants indiquent fortement le caractère rotationnel de la bande *yrast*. De plus, les taux de transition $E2$ calculés à partir de l'état 2_1^+ jusqu'à l'état fondamental se situent dans les barres d'erreur expérimentales, alors que les moments quadrupolaires spectroscopiques positifs confirment la déformation oblate de la bande $K^\pi = 0_1^+$. Le présent modèle n'inclut pas de formes triaxiales et il ne reproduit donc pas le taux de transition $B(E2; 2_2^+ \rightarrow 0_2^+)$ dans la bande de Hoyle, comme calculé dans le cadre des modèles théoriques AMD et THSR. Néanmoins, l'état 0_2^+ obtenu est localisé à moins de 1 MeV au-dessus de sa position mesurée, et le taux de transition $B(E2; 2_1^+ \rightarrow 0_2^+)$ calculé est en bon accord avec l'expérience. Par ailleurs, il a été montré que la bande excitée construite à partir de l'état 0_3^+ possède un fort caractère rotationnel avec des moments quadrupolaires spectroscopiques et des taux de transitions $E2$ intrabandes assez élevés. Dans le référentiel intrinsèque, cette bande manifeste une structure de chaîne linéaire prononcée qui correspond à la configuration $^8\text{Be}+\alpha$. Finalement, les facteurs de forme élastiques et inélastiques sont en bon accord avec les données expérimentales sur un intervalle de transferts de moments assez large. Concernant cet aspect en particulier, le présent modèle global manifeste un pouvoir prédictif qui peut concurrencer les modèles les plus performants et plus spécifiques pour l'étude des agrégats.

C.5. Conclusion

Dans cette thèse, nous avons déployé l'approche EDF relativiste à son état de l'art, avec restauration des symétries brisées à l'étape SR-EDF et mélange des états projetés selon la technique GCM, pour étudier le phénomène d'agrégation nucléaire. Cette approche permet un calcul cohérent et indépendant de tout paramètre libre, des spectres d'excitations collectives et des propriétés électromagnétiques des noyaux atomiques sur l'ensemble de la carte des nucléides. Nous avons appliqué notre modèle à l'étude du phénomène d'agrégation dans les isotopes du néon et dans l'isotope ^{12}C . Les résultats obtenus montrent un très bon accord avec les données expérimentales existantes et le niveau de précision atteint est comparable à celui obtenu en utilisant des modèles plus spécifiques à l'étude des agrégats. Cela montre que les approches de type EDF, dans leur implémentation au-delà du champ moyen, sont capables de décrire de façon unifiée les aspects liés au caractère de liquide quantique et au phénomène d'agrégation dans les noyaux atomiques. Les pistes envisagées pour améliorer notre approche incluent la prise en compte simultanée du degré de liberté triaxial, l'utilisation de mesures de localisation plus rigoureuses, de même que l'extraction des propriétés de particules individuelles à partir d'états collectifs corrélés [RPN16].

Bibliography

- [AAR16] S. E. Agbemava, A. V. Afanasjev, and P. Ring. Octupole deformation in the ground states of even-even nuclei: A global analysis within the covariant density functional theory. *Phys. Rev. C*, 93:044304, Apr 2016.
- [AARR14] S. E. Agbemava, A. V. Afanasjev, D. Ray, and P. Ring. Global performance of covariant energy density functionals: Ground state observables of even-even nuclei and the estimate of theoretical uncertainties. *Phys. Rev. C*, 89:054320, May 2014.
- [AB66] S. Ali and A. R. Bodmer. Phenomenological α - α potentials. *Nuclear Physics*, 80(1):99 – 112, 1966.
- [AER01] M. Anguiano, J. L. Egido, and L. M. Robledo. Particle number projection with effective forces. *Nuclear Physics A*, 696(3):467 – 493, 2001.
- [AJ94] S. Aberg and L.-O. Jönsson. Clustering aspects of nuclei with octupole and superdeformation. *Zeitschrift für Physik A Hadrons and Nuclei*, 349:205–211, 1994.
- [AM13] I. Angeli and K. P. Marinova. Table of experimental nuclear ground state charge radii: An update. *Atomic Data and Nuclear Data Tables*, 99(1):69 – 95, 2013.
- [APP⁺10] A. Astier, P. Petkov, M.-G. Porquet, D. S. Delion, and P. Schuck. Novel manifestation of α -clustering structures: New “ $\alpha + {}^{208}\text{Pb}$ ” states in ${}^{212}\text{Po}$ revealed by their enhanced $E1$ decays. *Phys. Rev. Lett.*, 104:042701, Jan 2010.
- [AS65] M. Abramowitz and I. A. Stegun. *Handbook of Mathematical Functions with Formulas, Graphs, and Mathematical Tables*. Dover Publications, New York, 1965.
- [AS90] F. Ajzenberg-Selove. Energy levels of light nuclei $A = 11$ -12. *Nuclear Physics A*, 506(1):1 – 158, 1990.
- [ASPG05] P. Arumugam, B. K. Sharma, S. K. Patra, and Raj K. Gupta. Relativistic mean field study of clustering in light nuclei. *Phys. Rev. C*, 71:064308, Jun 2005.

- [B⁺16] Bucher et al. Direct evidence of octupole deformation in neutron-rich ¹⁴⁴Ba. *Phys. Rev. Lett.*, 116:112503, Mar 2016.
- [BABH14] B. Bally, B. Avez, M. Bender, and P.-H. Heenen. Beyond mean-field calculations for odd-mass nuclei. *Phys. Rev. Lett.*, 113:162501, Oct 2014.
- [Bal14] B. Bally. *Description of odd-mass nuclei by multi-reference energy density functional methods*. PhD thesis, Université de Bordeaux, 2014.
- [BB67] D. M. Brink and E. Boeker. Effective interactions for Hartree-Fock calculations. *Nuclear Physics A*, 91(1):1 – 26, 1967.
- [BDF⁺90] P. Bonche, J. Dobaczewski, H. Flocard, P.-H. Heenen, and J. Meyer. Analysis of the generator coordinate method in a study of shape isomerism in ¹⁹⁴Hg. *Nuclear Physics A*, 510(3):466 – 502, 1990.
- [BDL09] M. Bender, T. Duguet, and D. Lacroix. Particle-number restoration within the energy density functional formalism. *Phys. Rev. C*, 79:044319, Apr 2009.
- [BE16] M. Borrajo and J. L. Egido. A symmetry-conserving description of odd nuclei with the Gogny force. *The European Physical Journal A*, 52(9):277, Sep 2016.
- [Bec10] C. Beck, editor. *Clusters in Nuclei, Vol. 1, Lecture Notes in Physics 818*. Springer-Verlag, Berlin, Heidelberg, 2010.
- [Bec12] C. Beck, editor. *Clusters in Nuclei, Vol. 2, Lecture Notes in Physics 848*. Springer-Verlag, Berlin, Heidelberg, 2012.
- [Bec14] C. Beck, editor. *Clusters in Nuclei, Vol. 3, Lecture Notes in Physics 875*. Springer-Verlag, Berlin, Heidelberg, 2014.
- [BFH03] M. Bender, H. Flocard, and P.-H. Heenen. Beyond-mean-field-model analysis of low-spin normal-deformed and superdeformed collective states of ³²S, ³⁶Ar, ³⁸Ar, and ⁴⁰Ca. *Phys. Rev. C*, 68:044321, Oct 2003.
- [BGG91] J.-F. Berger, M. Girod, and D. Gogny. Time-dependent quantum collective dynamics applied to nuclear fission. *Computer Physics Communications*, 63(1):365 – 374, 1991.
- [BGR56] G. Breit, R. L. Gluckstern, and J. E. Russell. Reorientation Effect in Coulomb Excitation. *Phys. Rev.*, 103:727–738, Aug 1956.
- [BH08] M. Bender and P.-H. Heenen. Configuration mixing of angular-momentum and particle-number projected triaxial Hartree-Fock-Bogoliubov states using the Skyrme energy density functional. *Phys. Rev. C*, 78:024309, Aug 2008.
- [BHR03] M. Bender, P.-H. Heenen, and P.-G. Reinhard. Self-consistent mean-field models for nuclear structure. *Rev. Mod. Phys.*, 75:121–180, Jan 2003.

- [BMMR02] T. Bürvenich, D. G. Madland, J. A. Maruhn, and P.-G. Reinhard. Nuclear ground state observables and QCD scaling in a refined relativistic point coupling model. *Phys. Rev. C*, 65:044308, Mar 2002.
- [BN96] P. A. Butler and W. Nazarewicz. Intrinsic reflection asymmetry in atomic nuclei. *Rev. Mod. Phys.*, 68:349–421, Apr 1996.
- [Boe48] J. De Boer. Quantum theory of condensed permanent gases I the law of corresponding states. *Physica*, 14(2):139 – 148, 1948.
- [BR85] J.-P. Blaizot and G. Ripka. *Quantum Theory of Finite Systems*. MIT Press, Cambridge, 1985.
- [BR12] G. F. Bertsch and L. M. Robledo. Symmetry Restoration in Hartree-Fock-Bogoliubov Based Theories. *Phys. Rev. Lett.*, 108:042505, Jan 2012.
- [BRR16] R. N. Bernard, L. M. Robledo, and T. R. Rodríguez. Octupole correlations in the ^{144}Ba nucleus described with symmetry-conserving configuration-mixing calculations. *Phys. Rev. C*, 93:061302, Jun 2016.
- [BRRM00] M. Bender, K. Rutz, P.-G. Reinhard, and J.A. Maruhn. Consequences of the center-of-mass correction in nuclear mean-field models. *Eur. Phys. J. A*, 7(4):467–478, 2000.
- [CBH⁺98] E. Chabanat, P. Bonche, P. Haensel, J. Meyer, and R. Schaeffer. A Skyrme parametrization from subnuclear to neutron star densities Part II. Nuclei far from stabilities. *Nuclear Physics A*, 635(1):231 – 256, 1998.
- [CFN⁺07] M. Chernykh, H. Feldmeier, T. Neff, P. von Neumann-Cosel, and A. Richter. Structure of the Hoyle State in ^{12}C . *Phys. Rev. Lett.*, 98:032501, Jan 2007.
- [CFN⁺10] M. Chernykh, H. Feldmeier, T. Neff, P. von Neumann-Cosel, and A. Richter. Pair Decay Width of the Hoyle State and its Role for Stellar Carbon Production. *Phys. Rev. Lett.*, 105:022501, Jul 2010.
- [CGH08] F. Chappert, M. Girod, and S. Hilaire. Towards a new Gogny force parameterization: Impact of the neutron matter equation of state. *Physics Letters B*, 668(5):420 – 424, 2008.
- [CGP⁺15] J. Carlson, S. Gandolfi, F. Pederiva, S. C. Pieper, R. Schiavilla, K. E. Schmidt, and R. B. Wiringa. Quantum Monte Carlo methods for nuclear physics. *Rev. Mod. Phys.*, 87:1067–1118, Sep 2015.
- [CMPN⁺05] E. Caurier, G. Martínez-Pinedo, F. Nowacki, A. Poves, and A. P. Zuker. The shell model as a unified view of nuclear structure. *Rev. Mod. Phys.*, 77:427–488, Jun 2005.
- [D⁺17] D. Dell’Aquila et al. High-Precision Probe of the Fully Sequential Decay Width of the Hoyle State in ^{12}C . *Phys. Rev. Lett.*, 119:132501, Sep 2017.

- [DBB⁺09] T. Duguet, M. Bender, K. Bennaceur, D. Lacroix, and T. Lesinski. Particle-number restoration within the energy density functional formalism: Non-viability of terms depending on noninteger powers of the density matrices. *Phys. Rev. C*, 79:044320, Apr 2009.
- [DG80] J. Dechargé and D. Gogny. Hartree-Fock-Bogolyubov calculations with the D1 effective interaction on spherical nuclei. *Phys. Rev. C*, 21:1568–1593, Apr 1980.
- [dJL98] F. de Jong and H. Lenske. Asymmetric nuclear matter in the relativistic Brueckner-Hartree-Fock approach. *Phys. Rev. C*, 57:3099–3107, Jun 1998.
- [DS10] T. Duguet and J. Sadoudi. Breaking and restoring symmetries within the nuclear energy density functional method. *Journal of Physics G: Nuclear and Particle Physics*, 37(6):064009, 2010.
- [DSNR07] J. Dobaczewski, M. V. Stoitsov, W. Nazarewicz, and P.-G. Reinhard. Particle-number projection and the density functional theory. *Phys. Rev. C*, 76:054315, Nov 2007.
- [Dug04] T. Duguet. Bare vs effective pairing forces: A microscopic finite-range interaction for Hartree-Fock-Bogolyubov calculations in coordinate space. *Phys. Rev. C*, 69:054317, May 2004.
- [Dug14] T. Duguet. *The Nuclear Energy Density Functional Formalism*, chapter in *Lecture Notes in Physics Vol. 879*. Springer, Berlin-Heidelberg, 2014.
- [EBR16] J. L. Egido, M. Borrajo, and T. R. Rodríguez. Collective and Single-Particle Motion in Beyond Mean Field Approaches. *Phys. Rev. Lett.*, 116:052502, Feb 2016.
- [Egi16] J. L. Egido. State-of-the-art of beyond mean field theories with nuclear density functionals. *Physica Scripta*, 91(7), 2016.
- [EHM09] E. Epelbaum, H.-W. Hammer, and Ulf-G. Meißner. Modern theory of nuclear forces. *Rev. Mod. Phys.*, 81:1773–1825, Dec 2009.
- [EKAV11] J.-P. Ebran, E. Khan, D. Peña Arteaga, and D. Vretenar. Relativistic Hartree-Fock-Bogoliubov model for deformed nuclei. *Phys. Rev. C*, 83:064323, Jun 2011.
- [EKL18] J.-P. Ebran, E. Khan, R.-D. Lasserri, and D. Vretenar. Single-particle spatial dispersion and clusters in nuclei. *Phys. Rev. C*, 97:061301, Jun 2018.
- [EKNV12] J.-P. Ebran, E. Khan, T. Nikšić, and D. Vretenar. How atomic nuclei cluster. *Nature*, 487:341–355, 2012.
- [EKNV13] J.-P. Ebran, E. Khan, T. Nikšić, and D. Vretenar. Localization and clustering in the nuclear Fermi liquid. *Phys. Rev. C*, 87:044307, Apr 2013.

- [EKNV14a] J.-P. Ebran, E. Khan, T. Nikšić, and D. Vretenar. Cluster-liquid transition in finite, saturated fermionic systems. *Phys. Rev. C*, 89:031303, Mar 2014.
- [EKNV14b] J.-P. Ebran, E. Khan, T. Nikšić, and D. Vretenar. Density functional theory studies of cluster states in nuclei. *Phys. Rev. C*, 90:054329, Nov 2014.
- [EKNV17] J.-P. Ebran, E. Khan, T. Nikšić, and D. Vretenar. Localization and clustering in atomic nuclei. *Journal of Physics G: Nuclear and Particle Physics*, 44(10):103001, 2017.
- [Eng07] J. Engel. Intrinsic-density functionals. *Phys. Rev. C*, 75:014306, Jan 2007.
- [F⁺05] H. O. U. Fynbo et al. Revised rates for the stellar triple- α process from measurement of ^{12}C nuclear resonances. *Nature*, 433:136–139, 2005.
- [FBS95] H. Feldmeier, K. Bieler, and J. Schnack. Fermionic molecular dynamics for ground states and collisions of nuclei. *Nuclear Physics A*, 586(3):493 – 532, 1995.
- [Fel90] H. Feldmeier. Fermionic molecular dynamics. *Nuclear Physics A*, 515(1):147 – 172, 1990.
- [FF14] M. Freer and H. O. U. Fynbo. The Hoyle state in ^{12}C . *Progress in Particle and Nuclear Physics*, 78:1–23, September 2014.
- [FHKE⁺18] M. Freer, H. Horiuchi, Y. Kanada-En'yo, D. Lee, and Ulf-G. Meißner. Microscopic clustering in light nuclei. *Rev. Mod. Phys.*, 90:035004, Aug 2018.
- [FLW95] C. Fuchs, H. Lenske, and H. H. Wolter. Density dependent hadron field theory. *Phys. Rev. C*, 52:3043–3060, Dec 1995.
- [FM14] S. Frauendorf and A.O. Macchiavelli. Overview of neutron-proton pairing. *Progress in Particle and Nuclear Physics*, 78:24 – 90, 2014.
- [Fom70] V. N. Fomenko. Projection in the occupation-number space and the canonical transformation. *Journal of Physics A: General Physics*, 3(1):8, 1970.
- [Fru07] T. R. Rodríguez Frutos. *Estudio de núcleos exóticos con teorías más allá campo medio*. PhD thesis, Universidad Autónoma de Madrid, 2007.
- [FS00] R. J. Furnstahl and B. D. Serot. Effective field theory and nuclear mean-field models. *Nuclear Physics A*, 663-664:513c – 516c, 2000.
- [FSF⁺13] Y. Fukuoka, S. Shinohara, Y. Funaki, T. Nakatsukasa, and K. Yabana. Deformation and cluster structures in ^{12}C studied with configuration mixing using Skyrme interactions. *Phys. Rev. C*, 88:014321, Jul 2013.
- [FTH⁺06] Y. Funaki, A. Tohsaki, H. Horiuchi, P. Schuck, and G. Röpke. Inelastic form factors to alpha-particle condensate states in ^{12}C and ^{16}O : What can we learn? *The European Physical Journal A - Hadrons and Nuclei*, 28(3):259–263, Jun 2006.

- [Fun15] Y. Funaki. Hoyle band and α condensation in ^{12}C . *Phys. Rev. C*, 92:021302, Aug 2015.
- [FV82] J. Friedrich and N. Voegler. The salient features of charge density distributions of medium and heavy even-even nuclei determined from a systematic analysis of elastic electron scattering form factors. *Nuclear Physics A*, 373(2):192 – 224, 1982.
- [FVR86] J. Friedrich, N. Voegler, and P.-G. Reinhard. Central depression of the nuclear charge distribution. *Nuclear Physics A*, 459(1):10 – 34, 1986.
- [FW05] H. Falakshahi and X. Waintal. Hybrid Phase at the Quantum Melting of the Wigner Crystal. *Phys. Rev. Lett.*, 94:046801, Jan 2005.
- [G⁺13] L. P. Gaffney et al. Studies of pear-shaped nuclei using accelerated radioactive beams. *Nature*, 497:199–204, 2013.
- [GHGP09] S. Goriely, S. Hilaire, M. Girod, and S. Péru. First Gogny-Hartree-Fock-Bogoliubov Nuclear Mass Model. *Phys. Rev. Lett.*, 102:242501, Jun 2009.
- [Gin97] J. N. Ginocchio. Pseudospin as a relativistic symmetry. *Phys. Rev. Lett.*, 78:436–439, Jan 1997.
- [GME⁺02] M. Greiner, O. Mandel, T. Esslinger, T. W. Hänsch, and I. Bloch. Quantum phase transition from a superfluid to a Mott insulator in a gas of ultracold atoms. *Nature*, 415:39–44, 2002.
- [GRT90] Y. K. Gambhir, P. Ring, and A. Thimet. Relativistic mean field theory for finite nuclei. *Annals of Physics*, 198(1):132 – 179, 1990.
- [GS13] M. Girod and P. Schuck. α -Particle Clustering from Expanding Self-Conjugate Nuclei within the Hartree-Fock-Bogoliubov Approach. *Phys. Rev. Lett.*, 111:132503, Sep 2013.
- [GW57] J. J. Griffin and J. A. Wheeler. Collective Motions in Nuclei by the Method of Generator Coordinates. *Phys. Rev.*, 108:311–327, Oct 1957.
- [Ham62] M. Hamermesh. *Group Theory and its applications to Physical problems*. Dover Publications Inc., New York, 1962.
- [HBC⁺00] P.-H. Heenen, P. Bonche, S. Cwiok, W. Nazarewicz, and A. Valor. *Riken Review*, 26:31, 2000.
- [HG07] S. Hilaire and M. Girod. Large-scale mean-field calculations from proton to neutron drip lines using the D1S Gogny force. *The European Physical Journal A*, 33(2):237–241, Aug 2007.
- [HHR82] K. Hara, A. Hayashi, and P. Ring. Exact angular momentum projection of cranked Hartree-Fock-Bogoliubov wave functions. *Nuclear Physics A*, 385:14–28, August 1982.

- [HI68] H. Horiuchi and K. Ikeda. A Molecule-like Structure in Atomic Nuclei of $^{16}\text{O}^*$ and ^{20}Ne . *Progress of Theoretical Physics*, 40(2):277–287, 1968.
- [HIK12] H. Horiuchi, K. Ikeda, and K. Kato. Recent Developments in Nuclear Cluster Physics. *Progress of Theoretical Physics Supplement*, 192:1–238, 2012.
- [HJS49] O. Haxel, J. H. D. Jensen, and H. E. Suess. On the "Magic Numbers" in Nuclear Structure. *Phys. Rev.*, 75:1766–1766, Jun 1949.
- [HK64] P. Hohenberg and W. Kohn. Inhomogeneous Electron Gas. *Phys. Rev.*, 136:B864–B871, Nov 1964.
- [HKL01] F. Hofmann, C. M. Keil, and H. Lenske. Density dependent hadron field theory for asymmetric nuclear matter and exotic nuclei. *Phys. Rev. C*, 64:034314, Aug 2001.
- [HT38] L. R. Hafstad and E. Teller. The Alpha-Particle Model of the Nucleus. *Phys. Rev.*, 54:681–692, Nov 1938.
- [Hub59] J. Hubbard. Calculation of Partition Functions. *Phys. Rev. Lett.*, 3:77–78, Jul 1959.
- [HW53] D. L. Hill and J. A. Wheeler. Nuclear Constitution and the Interpretation of Fission Phenomena. *Phys. Rev.*, 89:1102–1145, Mar 1953.
- [IMIO11] T. Ichikawa, J. A. Maruhn, N. Itagaki, and S. Ohkubo. Linear Chain Structure of Four- α Clusters in ^{16}O . *Phys. Rev. Lett.*, 107:112501, Sep 2011.
- [ITH68] K. Ikeda, N. Takigawa, and H. Horiuchi. The Systematic Structure-Change into the Molecule-like Structures in the Self-Conjugate $4n$ Nuclei. *Progress of Theoretical Physics Supplement*, E68:464–475, 1968.
- [KALR10] S. Karatzikos, A. V. Afanasjev, G.A. Lalazissis, and P. Ring. The fission barriers in Actinides and superheavy nuclei in covariant density functional theory. *Physics Letters B*, 689(2):72 – 81, 2010.
- [KE07] Y. Kanada-En'yo. The Structure of Ground and Excited States of ^{12}C . *Progress of Theoretical Physics*, 117(4):655–680, 2007.
- [KEH95] Y. Kanada-En'yo and H. Horiuchi. Clustering in Yrast States of ^{20}Ne Studied with Antisymmetrized Molecular Dynamics. *Progress of Theoretical Physics*, 93(1):115–136, 1995.
- [KEH01] Y. Kanada-En'yo and H. Horiuchi. Structure of Light Unstable Nuclei Studied with Antisymmetrized Molecular Dynamics. *Progress of Theoretical Physics Supplement*, 142:205–263, 2001.
- [KEHO95] Y. Kanada-En'yo, H. Horiuchi, and A. Ono. Structure of Li and Be isotopes studied with antisymmetrized molecular dynamics. *Phys. Rev. C*, 52:628–646, Aug 1995.

- [KEKO12] Y. Kanada-En'yo, M. Kimura, and A. Ono. Antisymmetrized molecular dynamics and its applications to cluster phenomena. *Progress of Theoretical and Experimental Physics*, 2012(1):01A202, 2012.
- [Kim04] M. Kimura. Deformed-basis antisymmetrized molecular dynamics and its application to ^{20}Ne . *Phys. Rev. C*, 69:044319, Apr 2004.
- [Kim07] M. Kimura. Molecular orbitals and $\alpha + ^{18}\text{O}$ molecular bands of ^{22}Ne . *Phys. Rev. C*, 75:034312, Mar 2007.
- [Koh99] W. Kohn. Nobel Lecture: Electronic structure of matter - wave functions and density functionals. *Rev. Mod. Phys.*, 71:1253–1266, Oct 1999.
- [KS65] W. Kohn and L. J. Sham. Self-Consistent Equations Including Exchange and Correlation Effects. *Phys. Rev.*, 140:A1133–A1138, Nov 1965.
- [Lat74] L. Lathouwers. An extension of Wong's theory for complex generator coordinates. *Nuclear Physics A*, 228(1):125 – 140, 1974.
- [Lat76] L. Lathouwers. The generator coordinate representation in an natural state formalism. *Annals of Physics*, 102(2):347 – 370, 1976.
- [LB13] C. J. (Kim) Lister and J. Butterworth. Nuclear physics: Exotic pear-shaped nuclei. *Nature*, 497:190–191, 2013.
- [LDB09] D. Lacroix, T. Duguet, and M. Bender. Configuration mixing within the energy density functional formalism: Removing spurious contributions from nondiagonal energy kernels. *Phys. Rev. C*, 79:044318, Apr 2009.
- [LKR97] G. A. Lalazissis, J. König, and P. Ring. New parametrization for the Lagrangian density of relativistic mean field theory. *Phys. Rev. C*, 55:540–543, Jan 1997.
- [LMGZ04] W. Long, J. Meng, N. Van Giai, and S.-G. Zhou. New effective interactions in relativistic mean field theory with nonlinear terms and density-dependent meson-nucleon coupling. *Phys. Rev. C*, 69:034319, Mar 2004.
- [LNVR05] G. A. Lalazissis, T. Nikšić, D. Vretenar, and P. Ring. New relativistic mean-field interaction with density-dependent meson-nucleon couplings. *Phys. Rev. C*, 71:024312, Feb 2005.
- [LRGM10] W. H. Long, P. Ring, N. Van Giai, and J. Meng. Relativistic Hartree-Fock-Bogoliubov theory with density dependent meson-nucleon couplings. *Phys. Rev. C*, 81:024308, Feb 2010.
- [Mar41] H. Margenau. Interaction of alpha-particles. *Phys. Rev.*, 59:37–47, Jan 1941.
- [May48] M. G. Mayer. On Closed Shells in Nuclei. *Phys. Rev.*, 74:235–239, Aug 1948.

- [MEK⁺18a] P. Marević, J.-P. Ebran, E. Khan, T. Nikšić, and D. Vretenar. Quadrupole and octupole collectivity and cluster structures in neon isotopes. *Phys. Rev. C*, 97:024334, Feb 2018.
- [MEK⁺18b] P. Marević, J.-P. Ebran, E. Khan, T. Nikšić, and D. Vretenar. Cluster structures in ¹²C from global energy density functionals. *ArXiv e-prints*, October 2018.
- [Men16] J. Meng, editor. *Relativistic Density Functional for Nuclear Structure, International Review of Nuclear Physics - Vol. 10*. World Scientific Publishing Co, Singapore, 2016.
- [MFH84] S. Marcos, H. Flocard, and P.-H. Heenen. Calculation of the Peierls-Yoccoz translational mass for Hartree-Fock wave functions. *Physics Letters B*, 134:287–289, January 1984.
- [MKF75] T. Matsuse, M. Kamimura, and Y. Fukushima. Study of the Alpha-Clustering Structure of ²⁰Ne Based on the Resonating Group Method for ¹⁶O+ α Analysis of Alpha-Decay Widths and the Exchange Kernel. *Progress of Theoretical Physics*, 53(3):706–724, 1975.
- [MKS⁺06] J. A. Maruhn, M. Kimura, S. Schramm, P.-G. Reinhard, H. Horiuchi, and A. Tohsaki. α -cluster structure and exotic states in a self-consistent model for light nuclei. *Phys. Rev. C*, 74:044311, Oct 2006.
- [MPR97] J. Meng, W. Pöschl, and P. Ring. Relativistic Hartree-Bogoliubov description of the lithium isotopes. *Zeitschrift für Physik A Hadrons and Nuclei*, 358(2):123–124, Feb 1997.
- [MR96] J. Meng and P. Ring. Relativistic Hartree-Bogoliubov Description of the Neutron Halo in ¹¹Li. *Phys. Rev. Lett.*, 77:3963–3966, Nov 1996.
- [MSTY⁺98] J. Meng, K. Sugawara-Tanabe, S. Yamaji, P. Ring, and A. Arima. Pseudospin symmetry in relativistic mean field theory. *Phys. Rev. C*, 58:R628–R631, Aug 1998.
- [MTZ⁺06] J. Meng, H. Toki, S. G. Zhou, S. Q. Zhang, W. H. Long, and L. S. Geng. Relativistic continuum Hartree Bogoliubov theory for ground-state properties of exotic nuclei. *Progress in Particle and Nuclear Physics*, 57(2):470 – 563, 2006.
- [Nak12] T. Nakatsukasa. Density functional approaches to collective phenomena in nuclei: Time-dependent density functional theory for perturbative and non-perturbative nuclear dynamics. *Progress of Theoretical and Experimental Physics*, 2012(1):01A207, 2012.
- [Nef12] T. Neff. Clusters and halos in light nuclei. *Journal of Physics: Conference Series*, 403(1):012028, 2012.

- [NF04] T. Neff and H. Feldmeier. Cluster structures within Fermionic Molecular Dynamics. *Nuclear Physics A*, 738:357 – 361, 2004. Proceedings of the 8th International Conference on Clustering Aspects of Nuclear Structure and Dynamics.
- [NGV⁺07] P. Navrátil, V. G. Gueorguiev, J. P. Vary, W. E. Ormand, and A. Nogga. Structure of $A = 10 - 13$ Nuclei with Two- Plus Three-Nucleon Interactions from Chiral Effective Field Theory. *Phys. Rev. Lett.*, 99:042501, Jul 2007.
- [NIV17] T. Nikšić, M. Imbrišak, and D. Vretenar. "Sloppy" nuclear energy density functionals. II. Finite nuclei. *Phys. Rev. C*, 95:054304, May 2017.
- [NMV14] T. Nikšić, P. Marević, and D. Vretenar. Microscopic analysis of shape evolution and triaxiality in germanium isotopes. *Phys. Rev. C*, 89:044325, Apr 2014.
- [NNNDC] Brookhaven National Laboratory NNDC National Nuclear Data Center. <http://www.nndc.bnl.gov>.
- [NPVR14] T. Nikšić, N. Paar, D. Vretenar, and P. Ring. DIRHB-A relativistic self-consistent mean-field framework for atomic nuclei. *Computer Physics Communications*, 185(6):1808 – 1821, 2014.
- [NQH⁺16] P. Navrátil, S. Quaglioni, G. Hupin, C. Romero-Redondo, and A. Calci. Unified ab initio approaches to nuclear structure and reactions. *Physica Scripta*, 91(5):053002, 2016.
- [NRV⁺10] T. Nikšić, P. Ring, D. Vretenar, Y. Tian, and Z. Y. Ma. 3D relativistic Hartree-Bogoliubov model with a separable pairing interaction: Triaxial ground-state shapes. *Phys. Rev. C*, 81:054318, May 2010.
- [NTH71] A. Nakada, Y. Torizuka, and Y. Horikawa. Determination of the Deformation in ^{12}C from Electron Scattering. *Phys. Rev. Lett.*, 27:745–748, Sep 1971.
- [NV16] T. Nikšić and D. Vretenar. "Sloppy" nuclear energy density functionals: Effective model reduction. *Phys. Rev. C*, 94:024333, Aug 2016.
- [NVB00] P. Navrátil, J. P. Vary, and B. R. Barrett. Large-basis ab initio no-core shell model and its application to ^{12}C . *Phys. Rev. C*, 62:054311, Oct 2000.
- [NVFR02] T. Nikšić, D. Vretenar, P. Finelli, and P. Ring. Relativistic Hartree-Bogoliubov model with density-dependent meson-nucleon couplings. *Phys. Rev. C*, 66:024306, Aug 2002.
- [NVNL14] K. Nomura, D. Vretenar, T. Nikšić, and B.-N. Lu. Microscopic description of octupole shape-phase transitions in light actinide and rare-earth nuclei. *Phys. Rev. C*, 89:024312, Feb 2014.

- [NVR06a] T. Nikšić, D. Vretenar, and P. Ring. Beyond the relativistic mean-field approximation: Configuration mixing of angular-momentum-projected wave functions. *Phys. Rev. C*, 73:034308, Mar 2006.
- [NVR06b] T. Nikšić, D. Vretenar, and P. Ring. Beyond the relativistic mean-field approximation. II. Configuration mixing of mean-field wave functions projected on angular momentum and particle number. *Phys. Rev. C*, 74:064309, Dec 2006.
- [NVR08] T. Nikšić, D. Vretenar, and P. Ring. Relativistic nuclear energy density functionals: Adjusting parameters to binding energies. *Phys. Rev. C*, 78:034318, Sep 2008.
- [NVR11] T. Nikšić, D. Vretenar, and P. Ring. Relativistic nuclear energy density functionals: Mean-field and beyond. *Progress in Particle and Nuclear Physics*, 66(3):519 – 548, 2011.
- [NW83] K. Neergård and E. Wüst. On the calculation of matrix elements of operators between symmetry-projected Bogoliubov states. *Nuclear Physics A*, 402(2):311 – 321, 1983.
- [NYH⁺75] F. Nemoto, Y. Yamamoto, H. Horiuchi, Y. Suzuki, and K. Ikeda. Structure of Intrinsic States of $K^\pi = 0^+$ Bands in ^{20}Ne : Study of Transient Character. *Progress of Theoretical Physics*, 54(1):104–118, 1975.
- [OY66] N. Onishi and S. Yoshida. Generator coordinate method applied to nuclei in the transition region. *Nuclear Physics*, 80(2):367 – 376, 1966.
- [OYN04] H. Ohta, K. Yabana, and T. Nakatsukasa. Variation after parity projection calculation with the Skyrme interaction for light nuclei. *Phys. Rev. C*, 70:014301, Jul 2004.
- [PBSH16] B. Pritychenko, M. Birch, B. Singh, and M. Horoi. Tables of E2 transition probabilities from the first 2^+ states in even-even nuclei. *Atomic Data and Nuclear Data Tables*, 107:1 – 139, 2016.
- [PR09] L. Próchniak and S. G. Rohoziński. Quadrupole collective states within the Bohr collective Hamiltonian. *Journal of Physics G: Nuclear and Particle Physics*, 36(12):123101, 2009.
- [R⁺18] M. Kumar Raju et al. Reorientation-effect measurement of the first 2^+ state in ^{12}C : Confirmation of oblate deformation. *Physics Letters B*, 777:250 – 254, 2018.
- [RB11] L. M. Robledo and G. F. Bertsch. Global systematics of octupole excitations in even-even nuclei. *Phys. Rev. C*, 84:054302, Nov 2011.
- [RE10] T. R. Rodríguez and J. L. Egido. Triaxial angular momentum projection and configuration mixing calculations with the Gogny force. *Phys. Rev. C*, 81:064323, Jun 2010.

- [RGER02] R. R. Rodríguez-Guzmán, J. L. Egido, and L. M. Robledo. Correlations beyond the mean field in magnesium isotopes: angular momentum projection and configuration mixing. *Nuclear Physics A*, 709(1):201 – 235, 2002.
- [RGER03] R. R. Rodríguez-Guzmán, J. L. Egido, and L. M. Robledo. Quadrupole collectivity of neutron-rich neon isotopes. *The European Physical Journal A - Hadrons and Nuclei*, 17(1):37–47, May 2003.
- [RGL97] P. Ring, Y. K. Gambhir, and G. A. Lalazissis. Computer program for the relativistic mean field description of the ground state properties of even-even axially deformed nuclei. *Computer Physics Communications*, 105(1):77 – 97, 1997.
- [RGR14] R. R. Rodríguez-Guzmán and L. M. Robledo. Microscopic description of fission in uranium isotopes with the Gogny energy density functional. *Phys. Rev. C*, 89:054310, May 2014.
- [Rin96] P. Ring. Relativistic mean field theory in finite nuclei. *Progress in Particle and Nuclear Physics*, 37:193 – 263, 1996.
- [RJ84] H. J. Rose and G. A. Jones. A new kind of natural radioactivity. *Nature*, 307:245–247, 1984.
- [RMUO11] P.-G. Reinhard, J. A. Maruhn, A. S. Umar, and V. E. Oberacker. Localization in light nuclei. *Phys. Rev. C*, 83:034312, Mar 2011.
- [RMVC⁺11] X. Roca-Maza, X. Viñas, M. Centelles, P. Ring, and P. Schuck. Relativistic mean-field interaction with density-dependent meson-nucleon vertices based on microscopical calculations. *Phys. Rev. C*, 84:054309, Nov 2011.
- [Rob07] L. M. Robledo. Particle number restoration: its implementation and impact in nuclear structure calculations. *International Journal of Modern Physics E*, 16(2):337–351, 2007.
- [Rob09] L. M. Robledo. Sign of the overlap of Hartree-Fock-Bogoliubov wave functions. *Phys. Rev. C*, 79:021302, Feb 2009.
- [Rob10] L. M. Robledo. Remarks on the use of projected densities in the density-dependent part of Skyrme or Gogny functionals. *Journal of Physics G: Nuclear and Particle Physics*, 37(6):064020, 2010.
- [Rob14] L. M. Robledo. Clustering in atomic nuclei: a mean field perspective. *Journal of Physics: Conference Series*, 569(1):012038, 2014.
- [RPN16] T. R. Rodríguez, A. Poves, and F. Nowacki. Occupation numbers of spherical orbits in self-consistent beyond-mean-field methods. *Phys. Rev. C*, 93:054316, May 2016.

- [RRR18] L. M. Robledo, T. R. Rodríguez, and R. R. Rodríguez-Guzmán. Mean field and beyond description of nuclear structure with the Gogny force: A review. *ArXiv e-prints*, July 2018.
- [RS72] M. Reed and B. Simon. *Methods of Modern Mathematical Physics*. Academic Press, 1972.
- [RS80] P. Ring and P. Schuck. *The Nuclear Many Body Problem*. Springer, Berlin, 1980.
- [RZZ⁺18] Z. X. Ren, S. Q. Zhang, P. W. Zhao, N. Itagaki, J. A. Maruhn, and J. Meng. Stability of the linear chain structure for ^{12}C in covariant density functional theory on a 3D lattice. *ArXiv e-prints*, May 2018.
- [SBB⁺13] J. Sadoudi, M. Bender, K. Bennaceur, D. Davesne, R. Jodon, and T. Duguet. Skyrme pseudo-potential-based EDF parametrization for spuriousity-free MR EDF calculations. *Physica Scripta*, 2013(T154):014013, 2013.
- [SDK⁺07] M. V. Stoitsov, J. Dobaczewski, R. Kirchner, W. Nazarewicz, and J. Terasaki. Variation after particle-number projection for the Hartree-Fock-Bogoliubov method with the Skyrme energy density functional. *Phys. Rev. C*, 76:014308, Jul 2007.
- [Ser01] Milena Serra. *Field Theoretical Description of Exchange Terms and Pairing Correlations in Nuclear Systems*. PhD thesis, Technische Universität München, 2001.
- [SKW⁺17] R. Smith, Tz. Kokalova, C. Wheldon, J. E. Bishop, M. Freer, N. Curtis, and D. J. Parker. New Measurement of the Direct 3α Decay from the ^{12}C Hoyle State. *Phys. Rev. Lett.*, 119:132502, Sep 2017.
- [Sky56] T. H. R. Skyrme. CVII. The Nuclear Surface. *Philosophical Magazine*, 1(11):1043–1054, 1956.
- [Sky58] T.H.R. Skyrme. The effective nuclear potential. *Nuclear Physics*, 9(4):615 – 634, 1958.
- [SM70] I. Sick and J. S. McCarthy. Elastic electron scattering from ^{12}C and ^{16}O . *Nuclear Physics A*, 150(3):631 – 654, 1970.
- [SP08] O. Sorlin and M.-G. Porquet. Nuclear magic numbers: New features far from stability. *Progress in Particle and Nuclear Physics*, 61(2):602 – 673, 2008.
- [SS68] P. Strehl and Th. H. Schucan. Study of monopole transitions in ^{12}C , ^{24}Mg , ^{28}Si , ^{32}S and ^{40}Ca by inelastic electron scattering. *Physics Letters B*, 27(10):641 – 643, 1968.

- [SSBN10] A. Staszczak, M. Stoitsov, A. Baran, and W. Nazarewicz. Augmented Lagrangian method for constrained nuclear density functional theory. *The European Physical Journal A*, 46(1):85–90, Oct 2010.
- [Sto05] N. J. Stone. Table of nuclear magnetic dipole and electric quadrupole moments. *Atomic Data and Nuclear Data Tables*, 90(1):75 – 176, 2005.
- [SW86] B. D. Serot and J. D. Walecka. The Relativistic Nuclear Many Body Problem. *Adv. Nucl. Phys.*, 16:1–327, 1986.
- [THSR01] A. Tohsaki, H. Horiuchi, P. Schuck, and G. Röpke. Alpha Cluster Condensation in ^{12}C and ^{16}O . *Phys. Rev. Lett.*, 87:192501, Oct 2001.
- [THSR17] A. Tohsaki, H. Horiuchi, P. Schuck, and G. Röpke. Colloquium: Status of α -particle condensate structure of the Hoyle state. *Rev. Mod. Phys.*, 89:011002, Jan 2017.
- [TKH04] Y. Taniguchi, M. Kimura, and H. Horiuchi. New Constraint of Clustering for AMD and Its Application to the Study of the 2α - ^{12}C Structure of ^{20}Ne . *Progress of Theoretical Physics*, 112(3):475–487, 2004.
- [TMR09a] Y. Tian, Z. Y. Ma, and P. Ring. A finite range pairing force for density functional theory in superfluid nuclei. *Physics Letters B*, 676(1):44 – 50, 2009.
- [TMR09b] Y. Tian, Z. Y. Ma, and P. Ring. Separable pairing force for relativistic quasiparticle random-phase approximation. *Phys. Rev. C*, 79:064301, Jun 2009.
- [TMR09c] Y. Tian, Z. Y. Ma, and P. Ring. Axially deformed relativistic Hartree Bogoliubov theory with a separable pairing force. *Phys. Rev. C*, 80:024313, Aug 2009.
- [TRP05] B. G. Todd-Rutel and J. Piekarewicz. Neutron-Rich Nuclei and Neutron Stars: A New Accurately Calibrated Interaction for the Study of Neutron-Rich Matter. *Phys. Rev. Lett.*, 95:122501, Sep 2005.
- [Val61] J. G. Valatin. Generalized Hartree-Fock Method. *Phys. Rev.*, 122:1012–1020, May 1961.
- [VALR05] D. Vretenar, A. V. Afanasjev, G. A. Lalazissis, and P. Ring. Relativistic Hartree-Bogoliubov theory: static and dynamic aspects of exotic nuclear structure. *Physics Reports*, 409(3):101 – 259, 2005.
- [Vau73] D. Vautherin. Hartree-Fock Calculations with Skyrme’s Interaction. II. Axially Deformed Nuclei. *Phys. Rev. C*, 7:296–316, Jan 1973.
- [VER13] N. L. Vaquero, J. L. Egido, and T. R. Rodríguez. Large-amplitude pairing fluctuations in atomic nuclei. *Phys. Rev. C*, 88:064311, Dec 2013.

- [VMK88] D. A. Varshalovich, A. N. Moskalev, and V. K. Khersonskii. *Quantum Theory of Angular Momentum*. World Scientific, Singapore, 1988.
- [WAK⁺17] M. Wang, G. Audi, F. G. Kondev, W. J. Huang, S. Naimi, and X. Xu. The AME2016 atomic mass evaluation (ii). Tables, graphs and references. *Chinese Physics C*, 41(3):030003, 2017.
- [Wal04] J. D. Walecka. *Electron Scattering for Nuclear and Nucleon Structure*. Cambridge University Press, Cambridge, 2004.
- [Wei35] C. F. v. Weizsäcker. Zur Theorie der Kernmassen. *Zeitschrift für Physik*, 96(7):431–458, Jul 1935.
- [Won70] C. W. Wong. The generator-coordinate theory as a flexible formulation of the many-body Schrödinger equation. *Nuclear Physics A*, 147(3):545 – 562, 1970.
- [Won98] Samuel S. M. Wong. *Introductory Nuclear Physics, Second Edition*. John Wiley, New York, 1998.
- [WR11] M. Warda and L. M. Robledo. Microscopic description of cluster radioactivity in actinide nuclei. *Phys. Rev. C*, 84:044608, Oct 2011.
- [YBH15] J. M. Yao, M. Bender, and P.-H. Heenen. Beyond-mean-field study of elastic and inelastic electron scattering off nuclei. *Phys. Rev. C*, 91:024301, Feb 2015.
- [YL07] C. Yannouleas and U. Landman. Symmetry breaking and quantum correlations in finite systems: studies of quantum dots and ultracold Bose gases and related nuclear and chemical methods. *Reports on Progress in Physics*, 70(12):2067, 2007.
- [ZLN⁺16] J. Zhao, B.-N. Lu, T. Nikšić, D. Vretenar, and S.-G. Zhou. Multidimensionally-constrained relativistic mean-field study of spontaneous fission: Coupling between shape and pairing degrees of freedom. *Phys. Rev. C*, 93:044315, Apr 2016.
- [ZLYM10] P. W. Zhao, Z. P. Li, J. M. Yao, and J. Meng. New parametrization for the nuclear covariant energy density functional with a point-coupling interaction. *Phys. Rev. C*, 82:054319, Nov 2010.
- [ZMR03] S.-G. Zhou, J. Meng, and P. Ring. Spherical relativistic Hartree theory in a Woods-Saxon basis. *Phys. Rev. C*, 68:034323, Sep 2003.
- [ZRX⁺12] B. Zhou, Z. Ren, C. Xu, Y. Funaki, T. Yamada, A. Tohsaki, H. Horiuchi, P. Schuck, and G. Röpke. New concept for the ground-state band in ²⁰Ne within a microscopic cluster model. *Phys. Rev. C*, 86:014301, Jul 2012.
- [ZYL⁺16] E. F. Zhou, J. M. Yao, Z. P. Li, J. Meng, and P. Ring. Anatomy of molecular structures in ²⁰Ne. *Physics Letters B*, 753:227 – 231, 2016.

Abbreviations

| | |
|--------|--|
| AM | Angular Momentum |
| AMD | Antisymmetrized Molecular Dynamics |
| AMP | Angular Momentum Projection |
| BCS | Bardeen-Cooper-Schrieffer |
| BMF | Beyond Mean-Field |
| DFT | Density Functional Theory |
| DD-ME | Density-Dependent Meson-Exchange |
| DD-PC | Density-Dependent Point-Coupling |
| EDF | Energy Density Functional |
| FMD | Fermionic Molecular Dynamics |
| GCM | Generator Coordinate Method |
| HFB | Hartree-Fock-Bogoliubov |
| HWG | Hill-Wheeler-Griffin |
| MR-EDF | Multi-Reference Energy Density Functional |
| PN | Particle Number |
| PNP | Particle Number Projection |
| RHB | Relativistic Hartree-Bogoliubov |
| RMF | Relativistic Mean-Field |
| SCMF | Self-Consistent Mean-Field |
| SR-EDF | Single-Reference Energy Density Functional |
| THSR | Tohsaki-Horiuchi-Schuck-Röpke |

List of Figures

| | | |
|-----|---|----|
| 1 | Schematic representation of clustering in atomic nuclei. | 3 |
| 2 | Various nuclear shapes that are taken into account within the study. | 5 |
| 1.1 | Performance of DD-PC1 functional with two different BMF models. | 20 |
| 1.2 | Self-consistent ground-state densities of ^{20}Ne isotope: comparison between the non-relativistic and relativistic functional. | 29 |
| 1.3 | Harmonic oscillator potentials with three different depths and radial wave-functions of the corresponding p -waves. | 30 |
| 1.4 | Systematic RHB predictions of nuclei with small radial dispersions of the valence neutrons single-particle states. | 31 |
| 1.5 | Mean value of the energy gap between consecutive occupied single-neutron levels as a function of quadrupole deformation parameter in ^{20}Ne | 33 |
| 1.6 | EDF-based analog of the conventional Ikeda diagram. | 34 |
| 2.1 | Schematic representation of the spontaneous symmetry breaking. | 40 |
| 3.1 | Convergence of the RHB energies in ^{20}Ne with the size of harmonic oscillator basis. | 61 |
| 3.2 | Convergence of the AMP energies in ^{20}Ne with the number of discretization points in projection integral for even-positive spin-parities. | 62 |
| 3.3 | Convergence of the AMP energies in ^{20}Ne with the number of discretization points in projection integral for odd-negative spin-parities. | 63 |
| 3.4 | Convergence of the AMP and PNP energies in ^{20}Ne with the number of discretization points in projection integrals for even-positive spin-parities. | 64 |
| 3.5 | Convergence of the AMP and PNP energies in ^{20}Ne with the number of discretization points in projection integrals for odd-negative spin-parities. | 65 |
| 3.6 | Convergence of the AMP and PNP energies of the 2_1^+ state in ^{20}Ne for a very large number of discretization points in projection integrals. | 67 |
| 3.7 | Excitation energies of collective states in ^{20}Ne as a function of the number of considered norm overlap eigenstates. | 68 |
| 4.1 | Self-consistent RHB binding energies of even-even $^{20-34}\text{Ne}$ isotopes, in the $\beta_2 - \beta_3$ plane. | 73 |
| 4.2 | Intrinsic nucleon densities of ^{20}Ne . Densities corresponding to the self-consistent minimum and to the symmetry-restored minimum are shown. | 75 |
| 4.3 | Angular momentum-, particle number-, and parity-projected energy surfaces of even-even $^{20-34}\text{Ne}$ isotopes for $J^\pi = 0^+$ in the $\beta_2 - \beta_3$ plane. | 76 |

| | | |
|------|--|-----|
| 4.4 | Two-neutron separation energies of $^{22-34}\text{Ne}$ isotopes on SR-EDF and MR-EDF level in comparison with the experimental data. | 77 |
| 4.5 | Amplitudes of collective wave functions squared $ g(\beta_2, \beta_3) ^2$ of the ground states of $^{20-34}\text{Ne}$ isotopes in the $\beta_2 - \beta_3$ plane. | 78 |
| 4.6 | Ground-state deformation parameters β_2 and β_3 of $^{20-34}\text{Ne}$ isotopes on the SR-EDF and MR-EDF level. | 79 |
| 4.7 | Angular momentum-, particle number-, and parity-projected energy surfaces of even-even $^{20-34}\text{Ne}$ isotopes for $J^\pi = 2^+$ in the $\beta_2 - \beta_3$ plane. . . . | 81 |
| 4.8 | Angular momentum-, particle number-, and parity-projected energy surfaces of even-even $^{20-34}\text{Ne}$ isotopes for $J^\pi = 4^+$ in the $\beta_2 - \beta_3$ plane. . . . | 81 |
| 4.9 | Angular momentum-, particle number-, and parity-projected energy surfaces of even-even $^{20-34}\text{Ne}$ isotopes for $J^\pi = 1^-$ in the $\beta_2 - \beta_3$ plane. . . . | 82 |
| 4.10 | Angular momentum-, particle number-, and parity-projected energy surfaces of even-even $^{20-34}\text{Ne}$ isotopes for $J^\pi = 3^-$ in the $\beta_2 - \beta_3$ plane. . . . | 82 |
| 4.11 | Calculated excitation energies of 2_1^+ and 4_1^+ states and transition strengths $B(E2; 2_1^+ \rightarrow 0_1^+)$ in even-even $^{20-34}\text{Ne}$ isotopes compared with data. . . . | 83 |
| 4.12 | Calculated low-energy spectra of $^{22,24}\text{Ne}$ and $^{32,34}\text{Ne}$ isotopes. | 84 |
| 4.13 | Amplitudes of collective wave functions squared $ g(\beta_2, \beta_3) ^2$ of the low-energy levels in ^{22}Ne | 85 |
| 4.14 | Amplitudes of collective wave functions squared $ g(\beta_2, \beta_3) ^2$ of the low-energy levels in ^{24}Ne | 85 |
| 4.15 | Amplitudes of collective wave functions squared $ g(\beta_2, \beta_3) ^2$ of the low-energy levels in ^{32}Ne | 86 |
| 4.16 | Amplitudes of collective wave functions squared $ g(\beta_2, \beta_3) ^2$ of the low-energy levels in ^{34}Ne | 86 |
| 4.17 | Calculated low-energy spectrum of ^{20}Ne compared with the available experimental data and with predictions of two other theoretical models. . . | 88 |
| 4.18 | Amplitudes of collective wave functions squared $ g(\beta_2, \beta_3) ^2$ of the low-energy levels of ^{20}Ne | 89 |
| 4.19 | Characteristic intrinsic nucleon densities of collective states of the ground-state band and the $K^\pi = 0^-$ band in ^{20}Ne | 91 |
| 5.1 | Self-consistent RHB energy surface and angular momentum-, particle number- and parity-projected energy surfaces of ^{12}C isotope in $\beta_2 - \beta_3$ plane. . . . | 97 |
| 5.2 | Potential energy curves of ^{12}C isotope as functions of axial quadrupole deformation β_2 for parity-conserving ($\beta_3 = 0$) configurations. | 98 |
| 5.3 | Calculated low-energy spectrum of ^{12}C compared with the available experimental data. | 99 |
| 5.4 | Amplitudes of collective wave functions squared $ g(\beta_2, \beta_3) ^2$ of the low-energy levels in ^{12}C | 100 |
| 5.5 | Characteristic intrinsic nucleon densities of the first three 0^+ and 2^+ collective states in ^{12}C | 102 |
| 5.6 | Form factors of electron scattering from ^{12}C for $0_1^+ \rightarrow 0_1^+$ and $0_1^+ \rightarrow 0_2^+$ transitions in comparison to experimental and theoretical data. | 104 |

List of Tables

| | | |
|-----|--|----|
| 1.1 | List of phenomenological parameters of DD-PC1 functional. | 18 |
| 2.1 | Properties of nuclear symmetries that are broken and restored within our calculation: rotational, particle number, and parity invariance. | 41 |
| 4.1 | Self-consistent RHB values of deformation parameters, binding energies, and charge radii in ground states of $^{20-34}\text{Ne}$ isotopes. | 74 |
| 4.2 | Calculated ground-state band spectroscopic quadrupole moments in the even-even $^{20-34}\text{Ne}$ isotopes. | 80 |

Titre : Vers une description unifiée des états nucléaires de type liquide quantique et cluster à l'aide de fonctionnelles de la densité relativistes

Mots clés : Fonctionnelles de la Densité Relativistes, Restauration des Symétries, Méthode de la Coordonnée Génératrice, Modèles Collectifs, Agrégats Nucléaires.

Résumé : Dans cette thèse, nous développons un modèle collectif de la structure du noyau préservant les symétries, basé sur la théorie des fonctionnelles de la densité relativistes. Les états de référence à déformation quadrupole/octupole et à symétrie axiale sont générés en résolvant les équations de Hartree-Bogoliubov relativistes. Nous employons la fonctionnelle avec couplage ponctuel covariant DD-PC1 dans le canal particule-trou de l'interaction effective, tandis que la force d'appariement non-relativiste séparable dans l'espace des impulsions est utilisée dans le canal particule-particule. Les corrélations collectives relatives à la restauration des symétries brisées sont prises en compte en projetant les états de référence à la fois sur les bonnes valeurs du moment angulaire, de la parité et du nombre de particules. L'étape suivante consiste à combiner les états à symétries restaurées à l'aide du formalisme de la méthode de la coordonnée génératrice. Ceci nous permet d'obtenir des prédictions spectroscopiques détaillées, incluant les énergies d'excitation, les moments multipolaires électromagnétiques et les taux de transition, ainsi que les facteurs de forme élastique et inélastique.

La méthode décrite est globale et peut être employée pour l'étude de la structure de nucléides très divers. Comme première application de ce modèle, nous étudierons la formation de clusters dans les noyaux légers. Le clustering nucléaire peut être considéré comme étant un phénomène de transition entre les phases liquide quantique et solide des noyaux finis. En contraste avec l'image conventionnelle du liquide quantique homogène, la localisation spatiale des particules α donne une image du noyau atomique similaire à une molécule. Nous réalisons en particulier une analyse complète de la collectivité quadrupole-octupole et des structures de cluster dans les isotopes du néon. Une attention particulière est accordée au cas de l'isotope ^{20}Ne , dans lequel il semble que les structures de cluster apparaissent dès l'état fondamental. Nous étudions également la structure à basse énergie de l'isotope ^{12}C . Nous concentrons notre analyse sur la structure en bandes construite à partir d'états 0^+ qui manifestent une grande variété de formes, notamment les configurations triangulaires de la bande de Hoyle ainsi que des chaînes linéaires 3α dans des états de plus haute énergie.

Title : Towards a unified description of quantum liquid and cluster states in atomic nuclei within the relativistic energy density functional framework

Keywords : Relativistic Energy Density Functional, Restoration of Symmetries, Generator Coordinate Method, Collective Models, Nuclear Clustering.

Abstract : In this thesis we develop a symmetry-conserving collective model for nuclear structure studies based on the relativistic energy density functional framework. Axially-symmetric quadrupole- and octupole-deformed reference states are generated by solving the relativistic Hartree-Bogoliubov equations. In the particle-hole channel of the effective interaction we employ the covariant point-coupling DD-PC1 functional, while the non-relativistic pairing force separable in momentum space is used in the particle-particle channel. Collective correlations related to restoration of broken symmetries are accounted for by simultaneously projecting reference states on good values of angular momenta, parity, and particle numbers. In the next step, symmetry-restored states are mixed within the generator coordinate method formalism. This enables us to obtain detailed spectroscopic predictions, including excitation energies, electromagnetic multipole moments and transition rates, as well as both the elastic and inelastic form factors.

The described framework is global and it can be employed in various nuclear structure studies across the entire nuclide chart. As a first application, we will study formation of clusters in light nuclei. Nuclear clustering is considered to be a transitional phenomenon between quantum-liquid and solid phases in nuclei. In contrast to the conventional homogeneous quantum-liquid picture, spatial localization of α - particles gives rise to a molecule-like picture of atomic nuclei. In particular, we carry out a comprehensive analysis of quadrupole-octupole collectivity and cluster structures in neon isotopes. A special attention is paid to the case of self-conjugate ^{20}Ne isotope, where cluster structures are thought to form already in the ground state. Finally, we study the low-lying structure of ^{12}C isotope. We focus on the structure of bands built on 0^+ states that are known to manifest a rich variety of shapes, including the triangular configurations of the Hoyle band and 3α linear chains in higher states.

